

The  
University  
Of  
Sheffield.

**An Investigation of Molybdenum Disulphide Dry Film Lubricant Coatings  
used in Aero-Engine Fan Disc Applications**

**By:**

Marcello Cadeddu

A thesis submitted in partial fulfilment of the requirements for the degree of  
Doctor of Philosophy

The University of Sheffield  
Faculty of Engineering  
Department of Mechanical Engineering

April 2021

## Summary

*Turbofan jet engines are widely used as a means of propulsion in the aviation industry. The fan is a key part of the engine, providing a large proportion of the overall thrust, and is subjected to the harshest loading conditions in the engine. Fan blades are connected to the disc through a dovetail joint, where a low friction molybdenum disulphide surface coating is used. This coating enables the blade to move within the joint to achieve its least stressed location in response to service conditions. Should this coating fail, the fan blade is no longer able to move, and the blade root is subject to fatigue. One notable incident occurred in Australia in 2001, where the aforementioned fatigue of the fan blade led to a contained failure, highlighting the need to ensure this coating is well understood and works effectively. A literature review at the start of this work identified that there were gaps in knowledge surrounding the coating system used by Rolls Royce on fan blades, and that the exact mechanism and failure modes of the coating as it undergoes fretting are currently unknown. As such, the aim of this research project is to determine the functional tribological behaviour of molybdenum disulphide coatings when applied to titanium on titanium contacts, in the context of an aero-engine fan blade dovetail joint.*

*A failed blade root was tribologically assessed, along with biaxial samples coated with the molybdenum disulphide coating and tested on a Rolls-Royce developed representative test platform. From these components, the functional behaviour of the coating was assessed, and a failure analysis was performed. Following this, the response of the coating to a range of load and surface conditions was investigated, firstly through coated ball on flat samples on a tribometer, and secondly via a purpose built test platform, where contact conditions representative of the fan root slot were achieved. For each of the two stages of testing, in-situ force measurement allowed changes in the coefficient of friction throughout the test to be determined, with this dataset then coupled with full surface characterisation of the samples post-test. Finally, an ultrasonic based method was proposed to monitor wear in-situ on a fan blade root slot contact, and trialled on the aforementioned purpose built rig.*

*The wear mechanism of the coating was found to depend both on contact pressure as well as the surface topography. At moderate to high contact pressures, when wear debris was retained in the contact, a durable, low friction glaze layer was observed to form on the surface. This layer occurred as a consequence of compaction and sintering of wear debris, generated during the initial interaction between the two surfaces. With time, this layer was observed to lose ductility, and breakdown, forming a cracked, platelet structure, before ultimately being removed. Surface waviness was also found to play an important role in the formation of this glaze layer, with peaks in the surface profile concentrating contact stresses, improving compaction and sintering of wear debris. In cases where the contact pressure was lower, the coating was found to undergo wear, without the formation of the glaze layer. In such cases, the contact pressure was found to be too low to promote compaction and sintering of wear debris, and friction remained high. Finally, ultrasound was demonstrated to be a useful tool for monitoring wear of molybdenum disulphide coatings in-situ, however significant further work is required to develop the technique into a reliable condition monitoring tool.*

## Nomenclature

ATSB	Australian Transport Safety Bureau
BSE	Back Scattered Electron
CoF	Coefficient of Friction
DFL	Dry Film Lubricant
EDM	Electrical Discharge Machining
EDX	Energy Dispersive X-Ray Analysis
EDXF	Energy Dispersive X-ray Fluorescence
EDXS	Energy-Dispersive X-ray Spectroscopy
EOB	Edge Of Blade
FEM	Finite Element Method
HCF	High Cycle Fatigue
HVOF	High Velocity Oxidation Fuel
LCF	Low Cycle Fatigue
LVDT	Linear Variable Differential Transformer
MoS <sub>2</sub>	Molybdenum Disulphide
MURI	Multi-University Research Initiative
RR	Rolls Royce
SE	Scattered Electron
SEM	Scanning Electron Microscope
STAMINA	STANDING wave Measurement of INterfaces and lAyers)
TTS	Tribological Transformed Structure
UMT	Universal Mechanical Tester
°C	Temperature, degrees Centigrade
µm	Length, micrometres
GPa	Pressure, Gigapascals
Hz	Frequency, Hertz
kV	Voltage, kilo-volts
m/s	Velocity, metres per second
mm	Length, Millimetres
MPa	Pressure, Megapascals
N	Force, Newtons
nm	Length, nano-metres
A	Amplitude
c	Velocity of sound in a material
f	Frequency
L	Thickness
R	Reflection coefficient
t	Time
z	Acoustic impedence

$\alpha$	Attenuation coefficient
$\rho$	Density
$\Phi$	Phase shift
$\omega$	Angular frequency

# Contents

Summary .....	ii
Nomenclature .....	iii
Contents .....	v
Foreword .....	ix
Dedication .....	x
1 Introduction .....	1
1.1 Project Motivation .....	1
1.2 Aims and objectives .....	3
1.3 Structure of the thesis .....	4
1.4 Research Highlights .....	5
2 Literature review .....	6
2.1 Background .....	6
2.1.1 Dovetail joints operating conditions .....	6
2.1.2 Rolls-Royce coating system .....	8
2.1.3 Tribology at the disc-blade interface .....	9
2.2 Fretting .....	11
2.2.1 Fretting regimes .....	11
2.2.2 Fretting of titanium alloys .....	13
2.2.3 Fretting in dovetail joints .....	16
2.2.4 Methods to mitigate fretting .....	16
2.3 Molybdenum Disulphide .....	18
2.3.1 Solid film lubrication and coating techniques .....	18
2.3.2 Sliding behaviour .....	19
2.3.3 Fretting behaviour .....	21
2.3.4 Rolls Royce Commissioned Studies .....	23
2.3.5 Alternative Coating Systems .....	25
2.4 Summary .....	26
3 Analysis of a failed fan blade and Rolls Royce test samples .....	27
3.1 Surface characterisation techniques .....	27
3.1.1 Scanning Electron Microscope Imaging .....	28
3.1.2 Optical interferometry .....	28
3.1.3 Elemental analysis .....	28
3.1.4 Sectioning and preparation of samples .....	29
3.2 Ex-service Trent800 blade investigation .....	30

3.2.1	Visual inspection and sample choice .....	31
3.2.2	Surface Morphology .....	32
3.2.3	Topography measurements .....	34
3.2.4	Elemental analysis.....	34
3.2.5	Residual thickness measurement.....	36
3.2.6	Overall considerations.....	36
3.3	Biaxial Specimens Investigation .....	37
3.3.1	Test configuration and conditions.....	37
3.3.2	Sectioning of samples .....	38
3.3.3	Blade specimen .....	39
3.3.4	Disc Specimen.....	47
3.4	Discussion .....	49
3.4.1	Trent800.....	49
3.4.2	Biaxial Specimens.....	50
3.4.3	Overall validity of the study.....	51
3.5	Summary .....	53
4	Ball-on-flat tests .....	54
4.1	Tests samples.....	56
4.1.1	Geometry and coating procedure .....	56
4.1.2	Sample topography .....	57
4.2	Methodology .....	59
4.2.1	Test equipment and procedure .....	59
4.2.2	Test parameters .....	63
4.2.3	Data analysis .....	64
4.3	Results .....	65
4.3.1	Influence of pressure on surface morphology .....	65
4.3.2	Influence of pressure on coefficient of friction evolution.....	70
4.3.3	Influence of surface topography.....	74
4.4	Multi-asperity contact model .....	79
4.4.1	Motivation and objectives.....	79
4.4.2	Suitability of existing models .....	80
4.4.3	Model development and implementation.....	81
4.4.4	Results.....	84
4.5	Discussion .....	87

4.5.1	Comparison with Trent800 investigation.....	87
4.5.2	Lubrication capabilities.....	91
4.5.3	Contact model.....	94
4.5.4	Surface topography and failure.....	96
4.5.5	Test arrangement.....	98
4.6	Summary.....	99
5	Scaled-disc testing.....	100
5.1	University of Sheffield fan blade test rig.....	100
5.1.1	Rig configuration.....	100
5.1.2	Control systems and data acquisition.....	103
5.1.3	Contact arrangement.....	103
5.1.4	Data processing.....	104
5.2	Test Methods.....	105
5.2.1	Rolls-Royce SCITEK.....	105
5.2.2	University of Sheffield fan blade rig.....	106
5.3	Results.....	107
5.3.1	SCITEK.....	107
5.3.2	University of Sheffield fan blade rig.....	110
5.4	Discussion.....	120
5.4.1	SCITEK.....	120
5.4.2	University of Sheffield fan blade rig.....	121
5.4.3	Comparisons of test rigs.....	123
5.4.4	Conditions affecting sintered layer.....	124
5.5	Summary.....	125
6	Coating condition monitoring.....	126
6.1	Conventional ultrasound methods.....	126
6.2	STAMINA.....	127
6.3	Wear measurement.....	129
6.4	Experimental plan.....	130
6.5	Trial Results.....	132
6.6	Analysis.....	133
6.7	Conclusion.....	137
7	Conclusions.....	138
7.1	Future Directions.....	142
	References.....	144

A.	Appendix- Tables from Marcello’s draft.....	150
A.1.	Literature Review .....	150
A.1.1.	Section 2.2.3 Fretting in dovetail joints .....	150
A.1.2.	Section 2.3.5- Alternatives.....	151
A.2.	Section 5.4 Discussion.....	153
A.3.	Section 5.3 Results .....	154
A.4.	Section 5.4 Discussion.....	166
B.	Appendix- Modelling Theory .....	166
B.1.	Hertz Theory.....	166



## Foreword

*This thesis contains the work of Marcello Cadeddu, who died as a consequence of a genetic heart condition prior to its completion. At the time of his death, all the experimental and simulation work planned for the PhD project was completed, with the majority of the thesis also written up. Where sections of the thesis were yet to be completed, experimental data had been post-processed and figures completed, with a skeleton narrative for a given section also drafted. In order to provide a coherent body of work, these plans have been used to complete the missing sections, with any additions based on Marcello's notes shown in italics in the thesis. In all cases the planned section structure and narrative has been maintained, with the original notes the section was based upon included in the appendices.*

*The additions made based on Marcello's notes are specifically detailed below:*

- *Section 1.4 added to Chapter 1 to provide the highlights from the thesis.*
- *A summary (2.4) added to the literature review (Chapter 2) to bring the work discussed in the chapter together*
- *Minor additions due to fragmented sentence structure in Section 3.3.4*
- *Results section (5.3.2) added to Chapter 5 based on processed data in Appendix A, with text added to explain results.*
- *Ultrasound measurements converted to thickness to contextualise results.*
- *Chapter 7 is new text but is based on discussions and conclusions from each of the chapters. A discussion chapter is omitted as no notes were present to form the basis of such a chapter, and each chapter has lengthy discussion sections individually.*

## Dedication

Marcello's family and I would like to thank Rolls Royce, and in particular Glen Pattinson, for the opportunity given to Marcello to undertake this project.

We also give thanks to the University of Sheffield and in particular Professors Neil Sims, Rob Dwyer-Joyce and Matthew Marshall, along with Kimberley Hyde and Matt Harmon for the work that they all carried out so that Marcello's research could be collated and recognised. I also thank Matt sincerely for the support he gave to Marcello during the development of the project and for his support given to me and the family subsequently.

Heartfelt thanks go to friends and colleagues who stood by us in our grief.

Finally, and most importantly, thanks to you Marcello, once again you have made us proud of you. You have never gone away; we carry you in our hearts and thoughts always.

Rest in peace.

With immense love,

Veronica

A nome mio e di tutta la famiglia, un ringraziamento alla Rolls Royce e a Glen Pattinson per l'opportunità data a Marcello di intraprendere questo progetto.

Un ringraziamento alla University of Sheffield, in modo particolare ai professori Neil Sims, Rob Dwyer-Joyce e Matthew Marshall, a Kimberley Hyde e a Matt Harmon per tutto il lavoro svolto affinché questa tesi venisse portata a termine e riconosciuta. Ringrazio sentitamente Matt per il supporto dato a Marcello durante lo svolgimento del progetto e per il sostegno dato a me e alla famiglia

.

Grazie di cuore agli amici e colleghi che si sono stretti a noi in questo grande dolore.

Ma soprattutto, grazie a te Marcello, ci hai reso ancora una volta fieri di te. Non sei mai andato via, ti portiamo sempre nel cuore e nei pensieri.

Riposa in pace.

Con immenso amore,

Veronica

# 1 Introduction

## 1.1 Project Motivation

Turbofan gas turbine jet-engines are largely used for civil aviation applications. They offer higher fuel efficiency and lower noise with respect to other gas turbine configurations such as the turboprop or the turbojet. An example of turbofan is represented in Figure 1-1.

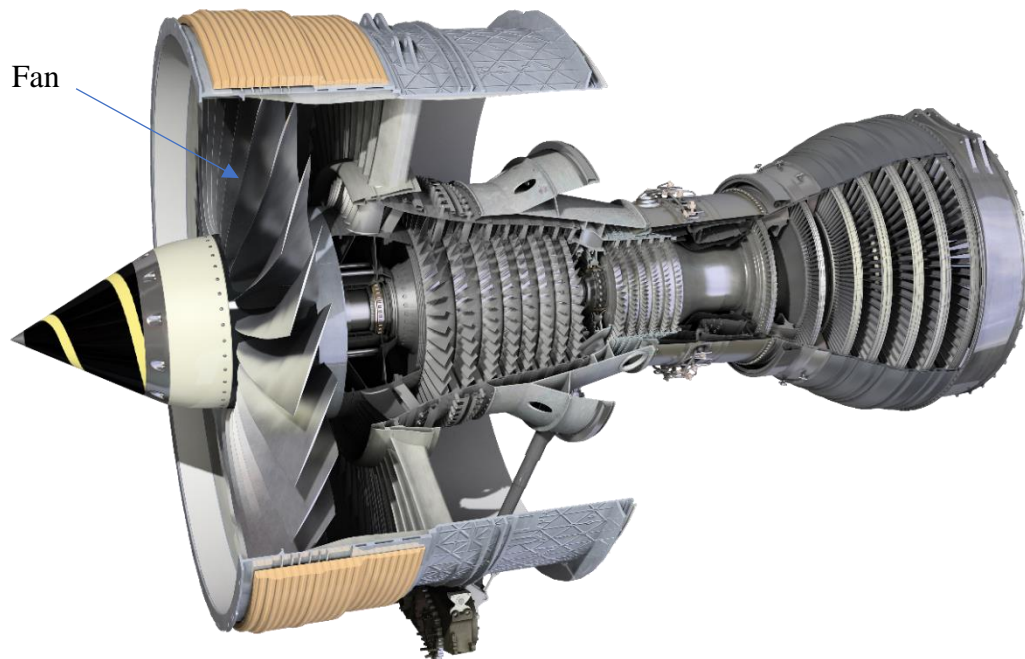


Figure 1-1: Section of Trent800 engine [1]

The fan is a key component of a turbofan engine. It consists of multiple fan blades (typically between 22 and 26) connected to the fan disc, which is driven by the low-pressure turbine through the fan shaft. Both the blades and the disc are manufactured from a Titanium alloy (Ti-6Al-4V) for its excellent strength-to-density ratio. The air entrained by the fan is partly fed to the core of the engine through higher pressure compressor stages, combustor, turbine and nozzle, and partly accelerated rearwards to drive the airplane forward. In modern turbofans such as the Rolls-Royce Trent™, 80 % of the total thrust is generated by the fan directly [1]. As a result, the fan is the largest rotating stage of the engine and it is subjected to the harshest loading conditions. Thus, it is vital to ensure its integrity and safety. A fundamental aspect of this is to guarantee a secure connection between the fan blades and the disc, which is typically realised with a dovetail joint assembly, as schematically represented in Figure 1-2.

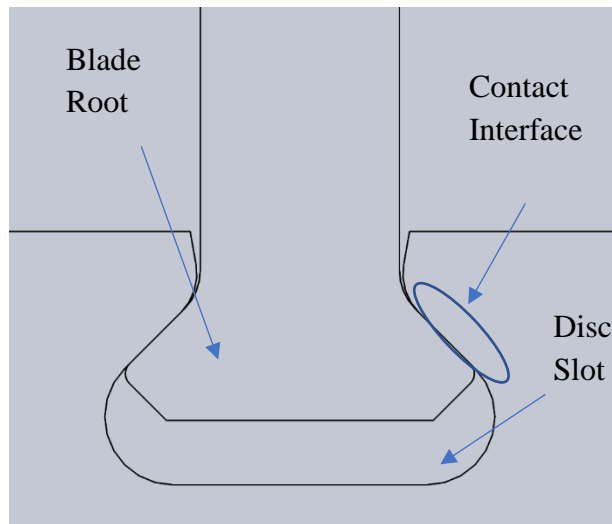


Figure 1-2: Schematic representation of the dovetail joint connection between fan blade root and fan disc.

During engine operation, the centrifugal load and the vibrations subject the blade-disc contact interface to a combination of Low Cycle Fatigue (LCF) and High Cycle Fatigue (HCF) loading [2]–[4]. Under these conditions, premature joint failure may occur due to fretting fatigue [5], [6].

The LCF is produced by the disc expansion and contraction caused by the centrifugal loading. As the disc expands, the fan blades slip radially outwards until they reach an equilibrium position at constant revolution speed; this phenomenon is often referred to as “seating” or “bedding” and is a key part of the blade root design. Correct and consistent seating prevents overstressing the fan root and improves engine balancing. Whilst the interface is loaded at constant revolution speed, air-flow instability and engine vibrations subject the contact to several low displacement HCF cycles. These load conditions, known as fretting fatigue, promote crack nucleation and therefore potential premature failure. Finally, the completion of LCF takes place as the rotational speed is reduced, the disc contracts and the blades return to their original position. From a tribological point of view, achieving a low friction contact at the interface between the disc root and the fan root is essential for a correct functionality of the joint [7], [8]. Otherwise, the blade can lock in a position which increases damage to the blade, as it is subjected to high stress fatigue cycles. A lubricated interface facilitates the blade seating and it mitigates crack nucleation by allowing the blade to migrate to its least stressed position at the different points in the loading cycle.

Due to the high friction of self-mated titanium surfaces and the unsuitability of liquid lubrication, solid lubricant coating systems are applied onto the blade root to reduce the coefficient of friction (CoF) [9]. The solution adopted by aero-engine manufactures such as Rolls-Royce consists of a plasma-sprayed metallic bond coat layer (Cu-Ni-In) on which a Molybdenum Disulphide (MoS<sub>2</sub>) Dry Film Lubricant (DFL) layer is applied.

Despite their excellent lubrication properties, DFL coatings wear and degrade. On the 31st of January 2001 at Melbourne International Airport, a Rolls-Royce RB211 Trent 892 fan blade was released from the disc during take-off of a Boeing 777-300 as a consequence of a fatigue failure of two major sections of the root (see Figure 1-3). The failure was contained within the engine casing, no fire developed, and the take-off was safely aborted with no injuries reported. Subsequently, the failed fan blade was examined by the Australian Transport Safety Bureau and it determined that the failure originated from inappropriate DFL lubrication [10].

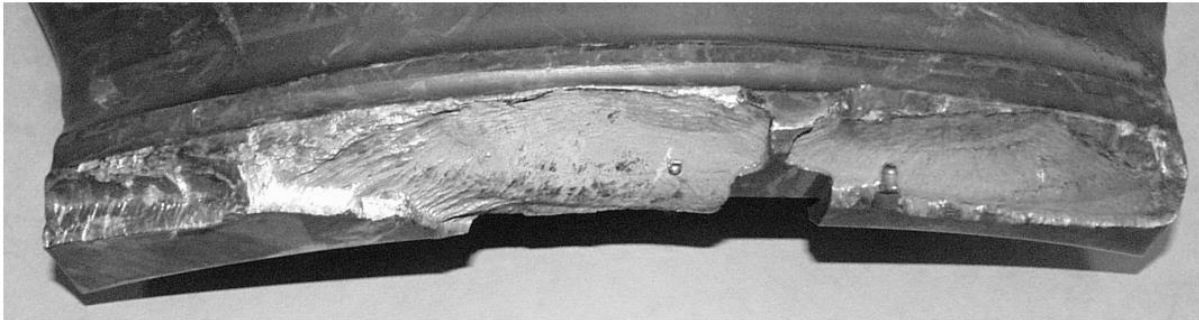


Figure 1-3: Side view of failed Trent 892 fan blade root: the picture shows the loss of two major sections of the root [10].

Maintaining a low friction contact in the dovetail assembly is therefore essential with respect to the integrity of the fan and in-flight safety. This is achieved by Rolls Royce through a preventive re-lubrication schedule which entails regeneration of the coating system during shop visits and on-wing lubricant top-ups at the airports. As this process represents a significant cost, there is a desire within the industry to increase maintenance intervals.

Several studies have addressed the fan blade contact problem, investigating the MoS<sub>2</sub> based DFL behaviour as well as exploring the use of alternative solutions. Details can be found in Chapter 2. However, the behaviour of the MoS<sub>2</sub> coatings is yet to be fully comprehended. A deeper understanding of the mechanism providing low friction and the failure modes of the coating is of interest, but is not yet investigated in the literature as the studies are from outside of the aerospace sector. Such a study would aid coating manufacturers in improving the design. Hence, the motivation for this PhD project has arisen.

## 1.2 Aims and objectives

The overall aim of this investigation is to understand the life of the Rolls-Royce fan blade coating system. Particularly, the role of the bond coat layer is of interest, as it has been proven to improve coating life remarkably but has been poorly investigated in the literature. To achieve this aim there are a number of objectives:

1. Explore in-service components and establish functional tribology behaviour and failure modes
2. Undertake simple tests to investigate coating and response to key operational variables

3. Incorporate different test scales to include more representative geometries and to corroborate findings of simpler tests
4. Explore the possibility of condition monitoring and if the remaining useful life can be estimated

### **1.3 Structure of the thesis**

Following this introductory section, a review of the previous researches related to the fan blade contact available in the literature is presented in Chapter 2. The review includes an overview of the dovetail joints, fretting behaviour and its influence on the blade-disc interface, as well as the current knowledge of MoS<sub>2</sub> as a solid lubricant. The previous tests pertinent to the RR fan blade contact are also included.

Chapter 3 reports the surface inspection of the ex-service fan blade, which focusses on the difference in the surface morphology in different areas of the contact interface. This allows the observation of the tribological transformation of the coating due to engine operation. Further, the inspection of 2D replicas of the blade root tested at the University of Oxford with the biaxial rig is reported. Scanning Electron Microscope (SEM) imaging, topographical measurements and elemental analysis are the main surface characterisation techniques adopted for the surface analysis.

An experimental assessment of the mechanical behaviour and failure mode of the coating under simulated operating conditions is carried out. Specifically, the effects LCF loading are assessed, as they are known to subject the coating to material removal. Chapter 4 includes the ball-on-flat tests experimental methodology and results. The coating is tested at room temperature, over a range of a range of pressures up to 825 MPa. The influence of the surface topography for the specific test configuration is discussed with support of a contact modelling technique. The tests are then scaled up to a simplified 2D scaled geometry of the components on a bespoke test rig in Chapter 5. The platform set-up and the experimental methodology are explained, followed by the test results. Throughout both sets of tests, the coefficient of friction is monitored throughout and it is related to the surface analysis findings. The influence of contact pressure, contact configuration and the relative displacement amplitude are the key parameters under study.

In Chapter 6, the test rig is ultrasonically instrumented, and a preliminary test is carried out. The ultrasonic signal is related to the progression of the wear damage. Conventional pulse-echo measuring techniques were used to assess the coating state. Further development of the method into an in-situ measurement tool would help improve the maintenance scheduling.

A summary of the whole thesis is included in Chapter 7 along with directions for how this work can be taken forward.

## 1.4 Research Highlights

*This work has resulted in several key highlights:*

- *Tribological analysis of a failed blade root from Rolls Royce indicated that contact pressure played a key role in the way the coating performs*
- *A new Fan Blade rig was built and validated by comparing results to a Rolls Royce test platform (SCITEK). This rig can be used to further evaluate the lubrication mechanism of the coating to optimise its performance. This new rig utilises curved specimens to produce a line contact due to the specimens being self-aligning and required contact pressures can be generated by modest load application.*
- *The main lubrication mechanism was identified to be the wear and compaction of DFL particles with some bond coat particles into a glazed layer. This glazed layer was responsible for low CoF in test results. This mechanism was identified in ball-on-flat tests first and then corroborated with tests using the new Fan Blade rig.*
- *Surface topography plays a key role in the formation of the glazed layer. Rougher test specimens resulted in much larger contact pressures on the asperity tips compared to the nominal contact pressure. This could be used to texture a fan blade to promote glaze formation and improve lubrication performance of the blade*
- *An ultrasound method has demonstrated it could be used to measure the thickness of the coating. This still needs significant laboratory work to gather more data and improve the method.*

## 2 Literature review

This chapter presents the previous studies related to fan blade investigation, damage mechanisms, the materials used and alternatives that have been explored. The first part includes an overview of the dovetail joints, the MoS<sub>2</sub> based coating system used by RR, as well as a brief discussion of the tribology at the disc-blade interface. As fretting is the surface damage mode affecting the dovetail functionality, this is reviewed along with its effects on Ti-6Al-4V joints and the methods to prevent it. The use of MoS<sub>2</sub> as a DFL is then reported. The MoS<sub>2</sub> properties, deposition methods and the mechanical behaviour are reviewed, with a focus on the fretting mechanism. Attention is drawn to the aspects that have not yet been fully addressed or understood, highlighting the motivation for this project.

### 2.1 Background

#### 2.1.1 Dovetail joints operating conditions

A dovetail joint connects the fan blades to the fan disc, simplifying assembly, disassembly, and inspection procedures. The blade root is slotted within the fan disc slot and secured in position with the use of a shear key and a leaf spring (Figure 2-1).



Figure 2-1: Fan assembly (left). Fan blade dovetail connection (top right) and fan blade root (bottom right) [1]

During operation, the joints are subjected to centrifugal load, air-flow and vibrational effects, as schematically illustrated in Figure 2-2. These loading conditions are complex, and are often modelled as a combination of LCF and HCF [3].



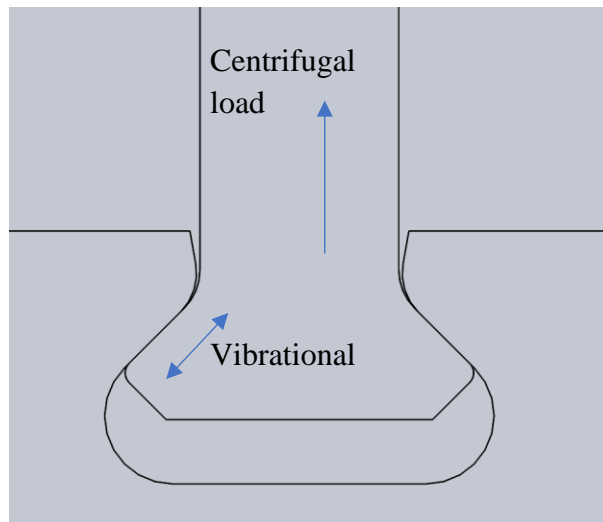


Figure 2-2: Schematics of the forces acting on the dovetail joint.

The LCF is produced by the fan rotation. At maximum thrust, the fan blade tip speed reaches 450 m/s subjecting each blade to a centrifugal load equivalent to the weight of 100 tonnes [7]. The blade is forced to move radially as a result of the disc expansion, seating into its least stressed position. The relative seating slip is estimated to range from 25  $\mu\text{m}$  [11] to 300  $\mu\text{m}$  [12]. Vibrations and air-flow instability (HCF) produce further relative movement, whose oscillatory displacement amplitude and frequency are estimated to be around a few micrometres and hundreds of Hertz respectively [11], [13]. The typical civil flight cycle consists of a main LCF period during take-off and landing and many HCF cycles. Whereas, military flights experience more severe LCF loading due to several accelerations and decelerations [9]. A simplified civil flight cycle is also represented in Figure 2-3.

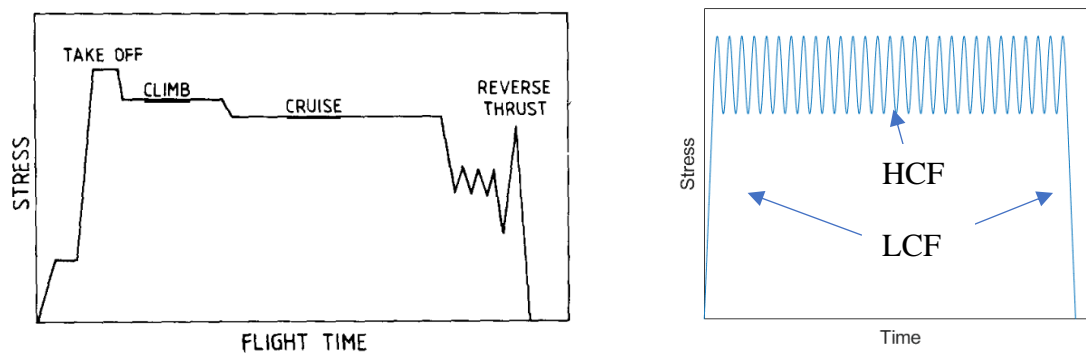


Figure 2-3: Simplified civil flight cycle (left) [9] and LCF-HCF representation

As mentioned in the introduction, the blade-disc interface needs appropriate lubrication in order to mitigate the effects of both LCF and HCF. The DFL coating system used by Rolls-Royce to achieve so is described in the next section, then the tribological behaviour of the system is discussed in Section 2.1.3 below.

### 2.1.2 Rolls-Royce coating system

The current solution adopted by RR consists of using a MoS<sub>2</sub> DFL layer applied to both the disc slot and the blade root. Prior to coating application, both components undergo a grit-blasting and shoot-peening procedure. The former is performed to degrease the surface and remove any dirt, while the latter improves the fretting fatigue life by introducing a residual compressive stress on the surface. A Cu-Ni-In Metco58 bond coat layer (Oerlikon Metco, MSRR9507/31) is then plasma sprayed onto the blade to improve adhesion and retention of the DFL. This Cu-Ni-In coating limits nucleation and propagation of cracks as it can resist larger amounts of plastic deformation [14], [15]. This is a relatively soft coating (see Table 1) compared to the base alloy and reduces the shear loads transmitted to the substrate thereby increasing the components ability to withstand fretting [16]. Finally, a commercially available DFL coating PL237 (Indestructible Paints, MSRR9274DFL) is sprayed on both components, air dried for 10 minutes and oven cured for 60 minutes at  $190 \pm 5$  °C. According to the manufacturer's specifications, the PL237 is designed to provide good protection against fretting up to 300°C.

Material	Ti-6Al-4V	Cu-Ni-In
Elastic modulus (GPa)	119	60
Poisson ratio	0.29	0.15
Yield stress (MPa)	970	
Vickers hardness	360 HV <sub>0.3</sub>	170 HV <sub>0.3</sub>

Table 1: Mechanical properties of Ti-6Al-4V and CuNiIn [11]

The final layer thickness achieved is 100-150 µm for the bond coat and around 20 µm for the DFL. The coating system (as applied) used in the root is shown in Figure 2-4, schematically illustrated using a block diagram to show the disc and blade as well as the coating layers applied to them, along with a cross-section micrograph of the blade root surface provided by Rolls Royce.

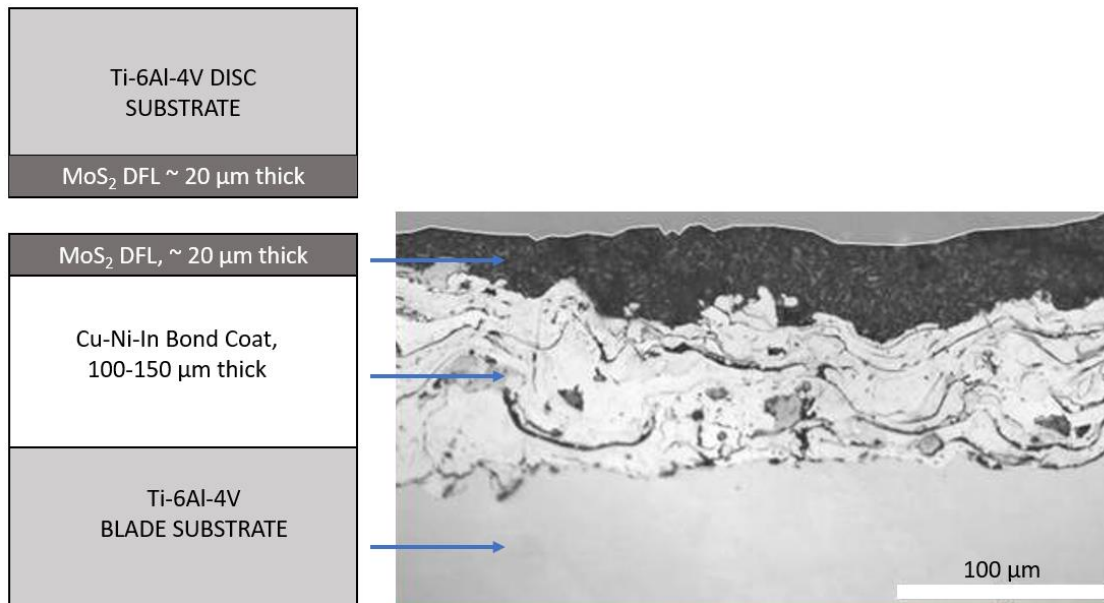


Figure 2-4: Schematics of the fan blade coating system (left). Cross-section micrograph of a coated fan blade root (right)

The maintenance schedule comprises re-lubrications at the airport and during workshop visits. On-wing maintenance is carried out typically every 1200 engine cycles to top up the DFL with the PL470 repair kit (indestructible paints). The blades are taken out from the disc and all the coated surfaces are cleaned with a brush to remove loose debris. After this process, molybdenum disulphide is added with an applicator and air cured. The bond coat is fully stripped and replaced around every 4500 engine cycles.

### 2.1.3 Tribology at the disc-blade interface

The effect of LCF and HCF subject an uncoated disc-blade interface to small relative amplitude oscillatory movement whilst it is loaded. Such conditions are referred to as fretting: a renowned surface damage mechanism [17]. Fretting is a complex phenomenon with as many as fifty parameters affecting behaviour and surface damage modes [18], among which normal load and displacement amplitude appear to be very important. In order to introduce the fretting effects on the dovetail applications, a short summary of the fretting behaviour is proposed below.

At low amplitudes and high contacting loads partial slip (mixed slip) fretting regime can take place, with some parts of the interface slipping whilst other are sticking. Such a mechanism induces crack nucleation and propagation, resulting in fretting fatigue: a reduction of the plain fatigue endurance of a component [19]. At higher displacement amplitudes (and lower load) gross sliding occurs, where no part of the interface is sticking. As the main mechanism under gross sliding is removal of material, this regime is also referred to as fretting wear.

The HCF loading has been observed to cause fretting fatigue on uncoated fan blade roots [20]. It is generally agreed that adhesion is a key driving factor of fretting fatigue on Titanium alloys [16], and by reducing the CoF a transition from partial slip to gross slip occurs. Therefore, a

low coefficient of friction (provided by coatings) on the dovetail interface can effectively halt crack nucleation. A further advantage of good lubrication is ensuring that the blade can correctly seat into position as the disc slot expands and contracts under LCF. A correct blade seating affects LCF directly by reducing the overall stresses on the blade root and HCF indirectly by reducing engine vibrations produced by unbalanced fan rotation.

The use of DFL coatings is beneficial for both LCF and HCF effects on the dovetail contact. However, they are subjected to wear [21] and eventually lose their lubrication properties. As a result, the root surface is no longer protected and cracks form and propagate until the section can no longer withstand the load and fails. The life cycle of a coating fan blade root is summarised in the chart in Figure 2-5.

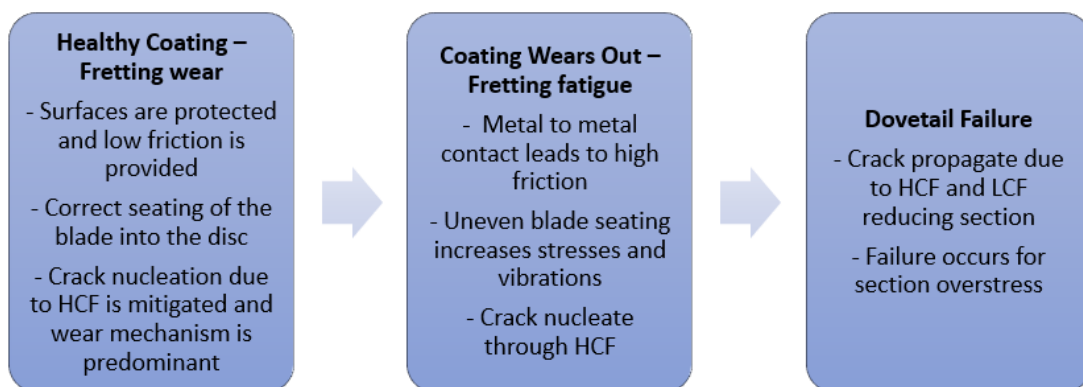


Figure 2-5: Dovetail interface life cycle

This life cycle is consistent with the failure of the Trent892 blade in Melbourne [10]. The Australian Transport Safety Bureau divided the fractured root surface in three parts: HCF cracks nucleation and propagation in proximity of the shear key, an area of further propagation due to LCF, and an area of final ductile overload failure (Figure 2-6).

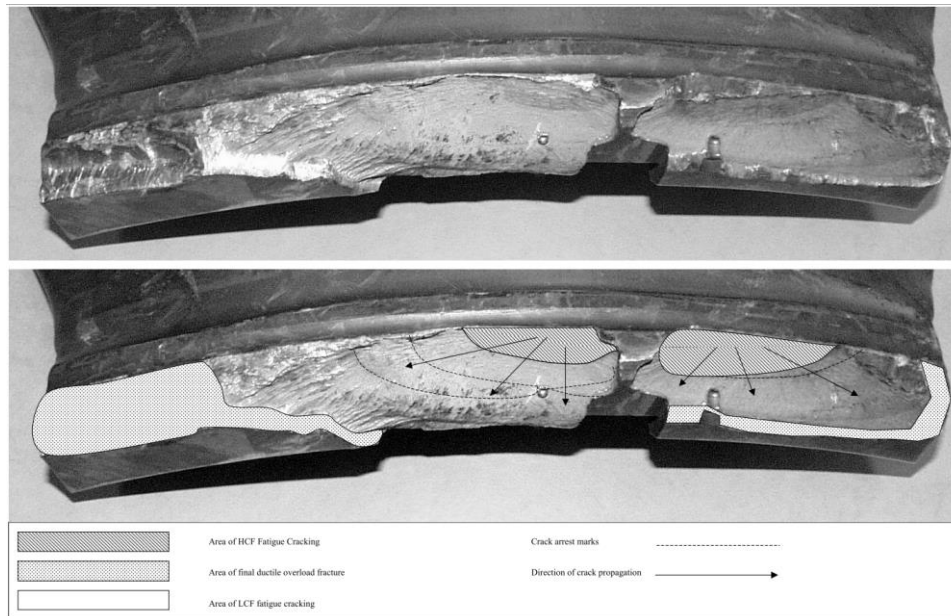


Figure 2-6: Examination of the fractured fan blade failure mode according to the ATSB [10].

## 2.2 Fretting

The concept of fretting was first proposed in the early 20<sup>th</sup> century. Since then, fretting has been found to affect a wide range of applications, including railways, power generation, and biomedical implants. The ASM Handbook on failure analysis and prevention [17] defines fretting as follows: "A special wear process that occurs at the contact area between two materials under load and subject to minute relative motion by vibration or some other force."

Although strong progress has been made by researchers to understand fretting, the phenomenon is yet to be fully comprehended. Factors such as contact geometry, forces, displacement amplitude, reciprocating frequency and environmental conditions were found to affect fretting behaviour [19]. The different surface damages and failure modes associated with fretting are often referred to as fretting fatigue, fretting wear and fretting corrosion, though ambiguity might arise between different damage mechanisms [22].

### 2.2.1 Fretting regimes

A key parameter for the study of fretting is the displacement amplitude. Firstly, there is an upper limit displacement above which the fretting behaviour transitions into reciprocating wear. As proposed by Chen et al. [23], volumetric wear is independent of the displacement amplitude under reciprocating wear conditions. Whereas, it reduces proportionally to the displacement amplitude within fretting conditions. The displacement threshold that marks the transition has been experimentally identified within the 150-300  $\mu\text{m}$  interval, no theoretical value has been proposed [19].

Changes in behaviour have also been observed within fretting conditions dependent of the displacement amplitude and the normal load. As proposed by Mindlin's theory [24], these changes are due to the elastic nature of the contact. At the smallest displacements (and highest loads), no relative slip occurs at the interface, whereas at larger displacements (and lowest loads) sliding is achieved across the whole contact area. Intermediate scenarios may also occur where a portion of the contact interface sticks, whilst the rest experiences micro-slip. It is common in the literature to categorise these fretting conditions into the three regimes: stick regime, mixed stick-slip behaviour, and gross slip regime [25]–[27]. These were also associated to different damage mechanisms, as summarised below:

1. Stick regime: It occurs at high loads and small displacement amplitude. No relative motion is achieved at the contact interface. Small amount of damage by wear is observed.
2. Gross slip regime: This takes place at low loads and large displacement amplitude. The largest amount of wear is observed in this regime (thus being also referred to as fretting wear), which involves debris production and ejection [11].
3. Mixed stick-slip regime (partial slip): This is a transitional situation, where parts of the interface are sticking, and part is slipping. The main mechanism of damage is crack nucleation and propagation produced by the large stress gradient induced below the surface [11], [28]. As the fatigue endurance limit is drastically reduced under these conditions (by 40-60% in the worse cases [4]), it also referred to as fretting fatigue.

Fretting experiments of materials are usually performed across a range of displacements to fully characterise the performance and estimate the life in all of the regimes. Although several parameters to determine the fretting regimes have been proposed (such as the dissipated energy ratio, the system free transition criterion, and the differential criterion [29]) the combination of displacement and normal load is the most largely used. Commonly, fretting maps are produced as the example in Figure 2-7 to aid the identification of the mechanism produced by a given combination of load and displacement.

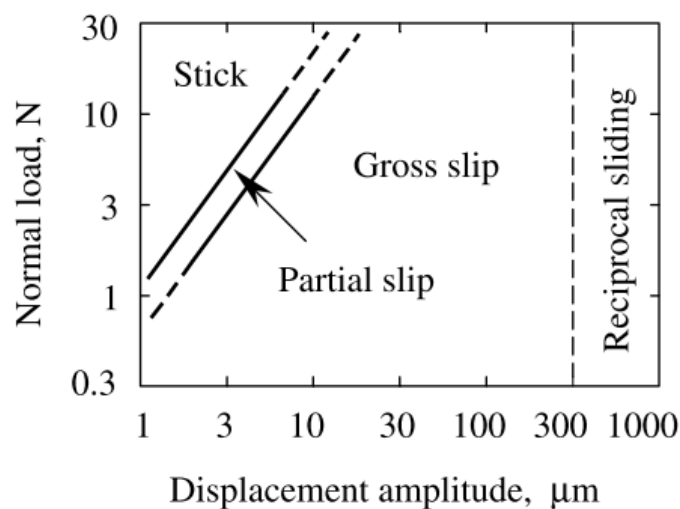


Figure 2-7: Example of fretting map. The map identifies the fretting regimes depending on displacement amplitude and normal load [30]

The fretting regime is typically inferred by analysing the fretting loops. These consist of plotting the tangential force against the displacement amplitude as the example in Figure 2-8.

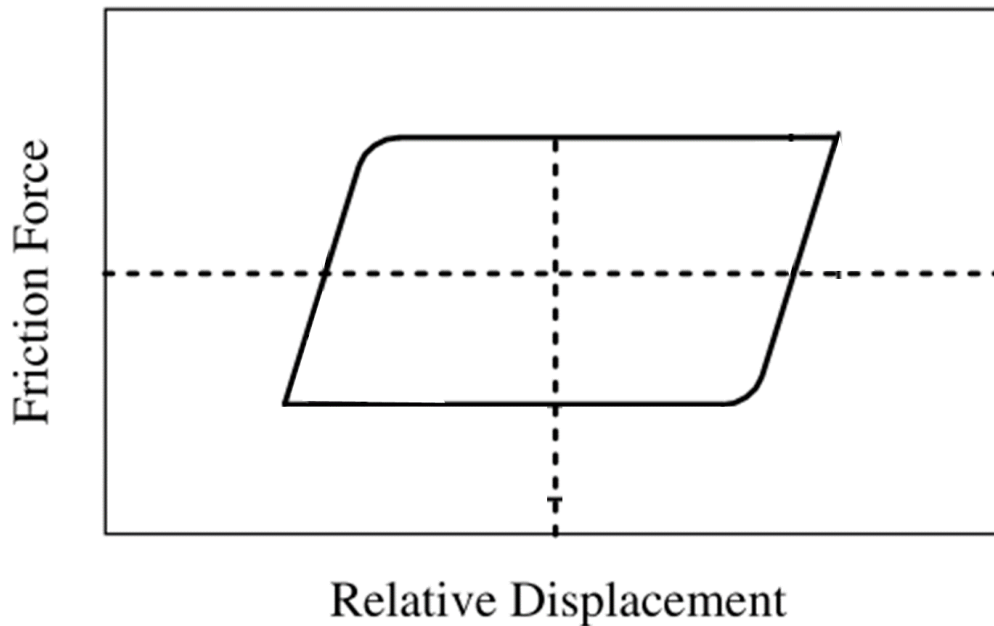


Figure 2-8: Example of fretting loop

In the gross slip regime, the loop has a polygonal shape, which changes into an ellipse in the mixed regime, and collapses in a line when no relative motion occurs in the stick regime. These are shown schematically in Figure 2-9.

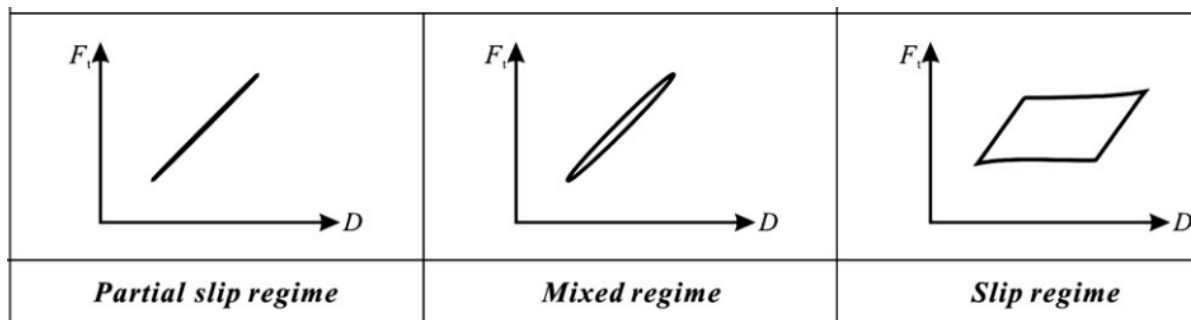


Figure 2-9: Changes of the fretting loop shape at different fretting modes [31]

### 2.2.2 Fretting of titanium alloys

Titanium alloys have been studied extensively due to their variety of applications within the industry, from the aerospace sector to biomedical implants. Particularly, the alpha-beta alloy, Titanium 6Al-4V (UNS designation R56400), is a common choice as it provides excellent mechanical properties and high corrosion resistance, whilst having a relatively low density. However, the tribological properties of self-mated titanium alloys are well-known to be inadequate for many applications due to high CoF, propensity to gall, and high surface damage

deriving from hard oxide debris production [32]. The tribological behaviour of Ti-6Al-4V has been largely investigated, with several studies focusing on its fretting performance.

Hager et al. [27] performed a number of tests on ellipse-on-flat contact arrangements over a range of normal loads and imposed displacement amplitude (at 30 Hz frequency). They produced the fretting map of Figure 2-10, which displays a linear relationship between the critical load and displacement that marks the transition between mixed stick to gross slip.

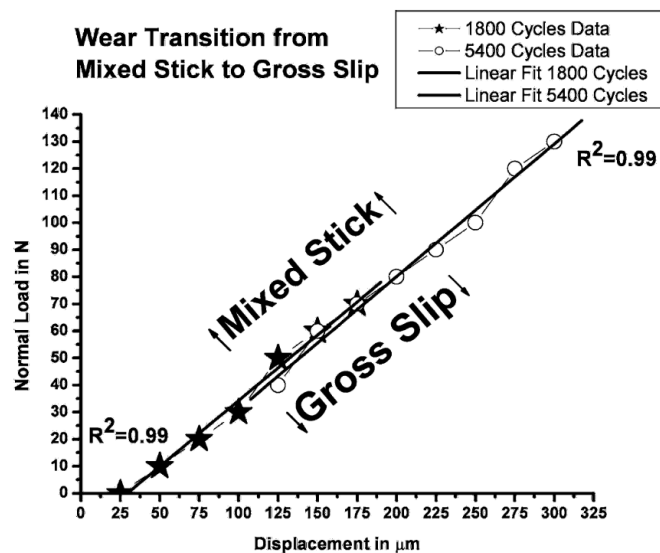


Figure 2-10: Fretting map for Ti-6Al-4V [27]

An observation of the effects of the fretting regime on the wear scar morphology was made by Mohd Tobi et al. [26], by inspecting the cross-section of a flat specimen tested on a cylinder-on-flat contact arrangement. Under a partial fretting regime, cracking occurred at the extremes of the contact, in correspondence of the slip zones (Figure 2-11-a) whilst a thin layer of debris formed under gross-sliding conditions (Figure 2-11 -b). The above mechanism is in line with the fretting response of steels and other metals.

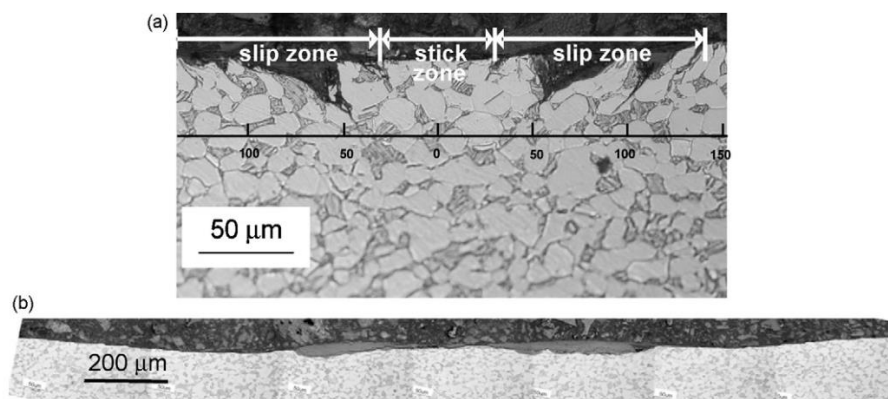


Figure 2-11: Wear scar of Ti-6Al-4V under mixed regime (a) and gross-sliding regime (b) [26]



The formation of a surface layer under gross sliding regime, which is often referred to as tribological transformed structure (TTS), has been observed by many other researchers. Everitt et al. have characterised the mechanical properties of a Ti-6Al-4V TTS by nanoindentation [33], finding that its hardness is around two times the hardness of the bulk properties, whereas the elastic modulus differences are not significant. Fouvry et al. [11] have related the formation of the TTS (Figure 2-12) to a sharp increase of the CoF as debris agglomeration occurred during the first few hundred cycles of their tests. Then, a steady high-friction behaviour occurs.

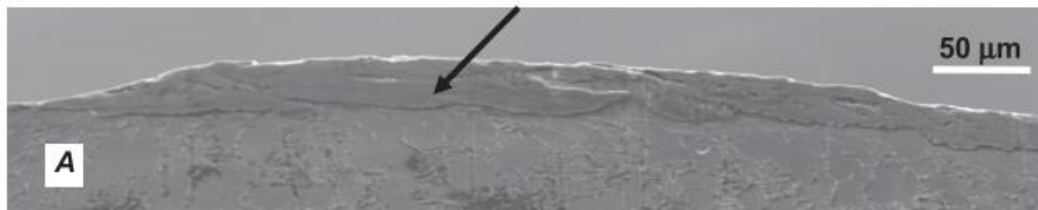


Figure 2-12: Agglomerated third body particles on a fretted Ti-6Al-4V surface [11]

The combination of factors driving the different fretting regimes and their resulting damaging mechanisms have been largely investigated, whereas the capability of quantifying the damage predictively still poses a major challenge to researchers. Many damage models have been developed to study the effects of crack nucleation and crack initiation under mixed slip regimes [34], [35]. The prediction of the wear mechanism is more difficult due to the complexity of the phenomenon, which involves: high-stress gradients, activation of the TTS, the changes in the contact geometry and the involvement of third-body particles [36]. Some work has focused on incorporating both the effects of mixed slip and gross slip regimes, as a vast number of components are subjected to both damage modes as a result of a combined HCF and LCF loading. These studies perform tests at variable displacement amplitude. Cortez et al. [37] showed that a cumulative damage linear model, namely, the Miner–Palmgren rule could be used as a satisfactory indicator of fatigue life prediction. This rule establishes a cumulative summation parameter that predicts that failure might occur when the unitary value is exceeded. The parameter is calculated as the sum of the ratios between the effective number of cycles under a given condition and the corresponding cycles to failure under the same conditions. Namjoshi and Mall [3] also addressed the computation of variable displacement amplitude fretting fatigue prediction. By assessing the fretting behaviour of Ti-6Al-4V over several HCF/LCF cycles ratio, they showed that cumulative life was predicted more accurately using non-linear models.

More recent work performed by Paulin et al. [36] aimed to predict the wear damage using a wear parameter, derived as a combination of the cumulative energy dissipated in the contact and the imposed sliding amplitude. The model was proved to be accurate over a range of displacement amplitudes. In a later study, the same approach [20] was proved to be capable of including friction, wear and crack nucleation of Ti-6Al-4V interfaces, which can be therefore be exploited in FEM fretting modelling of components.

### **2.2.3 Fretting in dovetail joints**

The effects of fretting in aero-engine components has been a major cause of concern, with HCF being reported as the largest causes of failure [38]. Many academic and industrial studies, including initiatives such the High Cycle Fatigue (HCF) and the Multi-University Research Initiative (MURI) in the USA, have thus focused on the fretting behaviour of aero-engine components. The study of fretting fatigue at component level involves a careful assessment of the stress distribution at the interface, which is essential to develop fretting life prediction models [39], [40]. Several methodologies have been applied to estimate the contact stresses in the dovetail joints [41]–[43], and relate it to crack initiation and propagation [39], [40], [44]. Finite element analysis, semi-analytics methods and energy-based models were used to model the contact.

Given the complexity of the dovetail geometry, most of the studies have been carried out on a simplified 2D geometry of the joint. An interesting test setup is the 2D biaxial test rig. A biaxial test rig applies loads to two opposing blade specimens representing the centrifugal forces in an engine. The opposing blade specimens are mounted onto a central disk specimen which is also subjected to load which simulates the disk expansion. HCF loads are also applied via mechanical shaker units which represent blade vibration [45].

In order to meet increasingly higher power demands fan blades have increased in size and evolved over time. Modern blades have complex dovetail connections to offset the increased weight and centrifugal loading (increase in stresses and fretting at the blade root) that have resulted from this increase in size. The latest designs involve geometrical features such as skew angle, cone angle and twist on the blade. The complex geometry and loading conditions make the study of the assembly complicated, which is usually performed by finite element models (FEM). A detailed analysis of how centrifugal load and aerodynamic forces act on the blade was made by Anandavel et al. [46], to develop a 3-D FEM of the assembly. Anandavel et al. [46] skewed the dovetail assembly and included aerodynamic with vibration loading, which mimics the 3D bulk loading the blade-disk interface experiences during normal operation. This work concluded that the 3D assembly led to an increase by a factor of 2 to the peak pressure experienced by the assembly as well as changing the location of the peak pressure compared to the 2D assembly.

Given the importance of dovetail joints to the longevity of the fan and therefore the engine overall, Rolls Royce have carried out several in-house studies to ensure the fan is optimised for performance and lifespan. These have typically been 2D simulations of stresses and are detailed in Section 2.3.4.

### **2.2.4 Methods to mitigate fretting**

Several techniques have been investigated and found to be effective in mitigating the effects of fretting. At the design stage, a careful consideration of the geometry of the interface is paramount for improving fretting fatigue due its influence on the factors that cause fretting

such as the pressure distribution [47]. For dovetail attachments, the use of chamfers and undercutting is often adopted to improve fretting life [48]. Such design is currently applied by RR in the Trent 800 fan blades. Chamfers and undercuts reduce fretting and improve life by removing one of the contacting surfaces in areas where fretting is at its worst. This has the effect of allowing the blade root to deform rather than fret in these areas.

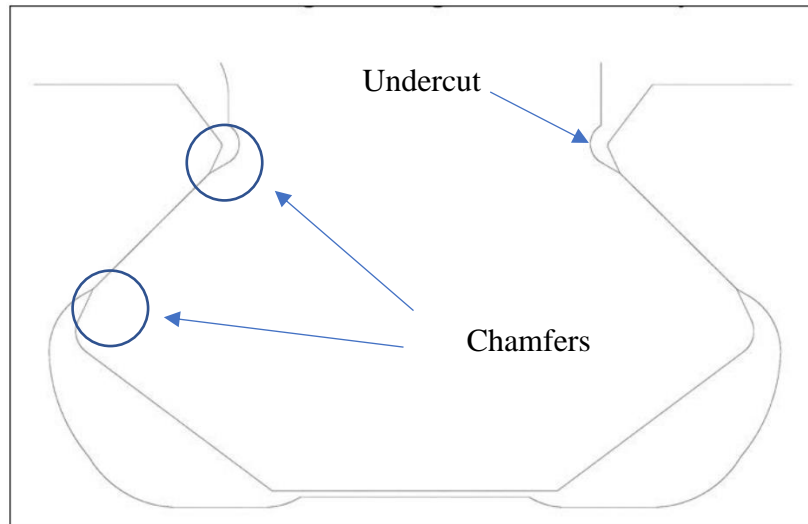


Figure 2-13: Use of chamfers, undercutting and relief radius on a dovetail joint [48].

Selecting a material with better fretting resistance can also be considered during the design stage. However, this is not always a viable solution due to incompatibility of the bulk properties with the structural requirements (as it is the case for the fan assembly). Several surface engineering treatments and modifications techniques have been developed to improve the fretting performance to overcome this circumstance. Surface treatments that induce a residual compressive stress on the surface have been proved to halt crack growth and therefore increase fretting fatigue life [49], [50]. Shot-peening, laser shock peening, ultrasonic impact treatment and water jet cavitation peening are among the techniques used.

A reduced adhesive action at the interface has also been found to be beneficial, as it alleviates the fretting wear damage [51]. The use of liquid lubricants and greases are not a suitable alternative in fretting contexts, given the typical low speed relative motion [52]. The use of DFLs can improve the life of dovetail assembly since low coefficients of friction have been found to decrease the probability of crack initiation [8]. Further, solid film lubricants have higher load carrying capacity than oil lubricants [53]. For these reasons, the use of MoS<sub>2</sub> and graphite coatings have been used by airlines [54]. A low friction contact across the blade-disc interface is also beneficial to ensure correct blade seating. This improves not only balancing of the fan and therefore reduces vibrations (and HCF related fretting effects), but also limits overstress in the blade root. As the use of a MoS<sub>2</sub> coating is part of the current solution adopted by Rolls Royce to protect the fan blade interface, the next section includes a review of its lubrication mechanism and of the previous findings regarding its fretting behaviour.

## 2.3 Molybdenum Disulphide

### 2.3.1 Solid film lubrication and coating techniques

The principle of solid lubrication relies on interposing a thin film of low shear strength between two sliding surfaces to reduce friction [55]. Given its low shear strength, molybdenum disulphide has been used as a solid lubricant since it was first applied in the aerospace industry, with most recent studies extending its use to electronics applications [56], [57]. Molybdenum disulphide (chemical formula  $\text{MoS}_2$ ) is silvery in colour and shiny, similar in appearance to graphite. The low shear strength has been related to its lamellar hexagonal structure [55]. This characteristic is due to the layered structure that consists of molybdenum atoms sheet bonded between two sheets of sulphur atoms (see Figure 2-14) [58]. The Mo-S covalent bonds within the layers are strong, whereas the van der Waals interactions between the sulphur sheet at the interface between the two layers is weak [59].

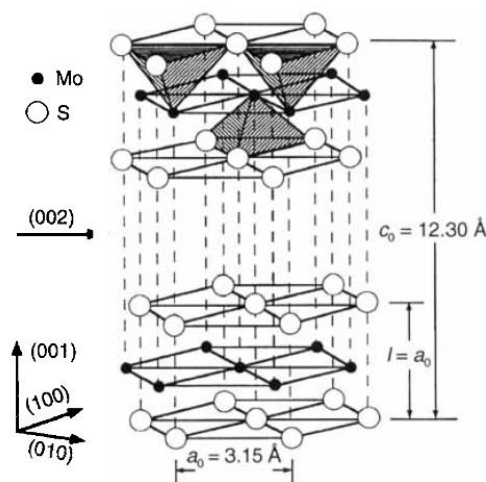


Figure 2-14: Schematics of the crystallographic structure of  $\text{MoS}_2$  ([58]).

$\text{MoS}_2$  coatings can be applied by means of several techniques, with the most common being burnishing, sputtering and spraying. Burnishing consists on producing films by mechanically working  $\text{MoS}_2$  particles onto a surface (rubbing). Burnished films have uniform coating thickness (typically within 0.1-10  $\mu\text{m}$ ) and weak surface adhesion, but they are economical and easy to apply ([58]). These issues can be mitigated by using a combination of hot pressing and laser texturing to lead to improvements in performance compared to burnishing [60]. Sputtering deposition, also known as a physical vapour deposition, allows for the application of very thin films to surfaces. As sputtered  $\text{MoS}_2$  exhibits excellent lubrication (CoF as low as 0.01) and remarkable life in vacuum or dry conditions, these films have been applied as solid lubricants in satellites and spacecraft [55]. Finally, magnetron sputtering can lead to even better performance, especially when combined with a harder substrate material [61].

Solid lubricant particles can also be dispersed in an adhesive of resin system, which can be then sprayed onto the surface to lubricate. Sprayed  $\text{MoS}_2$  films (also referred to as  $\text{MoS}_2$  bonded films) offer a better lubrication and wear resistance than other solid films deposited with other

techniques [62], Rolls Royce therefore use this technique. However, there are a number of factors that influence the performance of bonded films (such as pre-treatment of substrate, conditioning of film, nature of substrate, method of application etc.) and these can be optimised for different applications [62].

### **2.3.2 Sliding behaviour**

Although the fretting behaviour of MoS<sub>2</sub> coating films has been largely investigated [60], [61], [63], the wear mechanism and failure modes are not fully understood. A good review of how the MoS<sub>2</sub> lubricates and fails from a macroscopic point of view was proposed by Fusaro et al. [64], which reported the results of previous studies. These suggested that MoS<sub>2</sub> compacts and sinters on the contact forming a thin and coalesced film, whose oxidation leads to embrittlement, blistering and scaling of the film. In order to extend those results the effect of the substrate surface roughness [64] and the environment [65] were investigated. The behaviour within three different atmospheres was analysed (moist air, dry air and dry argon) with moist air being the environment where the shortest life and the highest coefficient of friction was observed. In moist air the failure was due to oxidation causing blistering and break-up of the film. Whereas in dry and vacuum environments, the failure is due to gradual depletion of the film by lateral flow. The effect of the roughness was evaluated by testing on three different surfaces (polished, sanded and sandblasted) and the results suggested that rougher substrates provided increased life, but similar coefficient of frictions. Regarding the macroscopic behaviour, the work confirmed that MoS<sub>2</sub> compacts and sinters to form a thin layer that provides good lubrication and wear resistance. The extrusion of this film leads to loss of ductility, embrittlement and ultimately failure of the film with loss of material in form of a black, powdery material. Fusaro et al. [64] also showed that the CoF was split into four distinct phases as shown in Figure 2-15. First there is a run-in phase where compaction of the layer, material transfer between counter faces and generation of particles occurs. Next, a stable period of low friction occurs before the film starts to break down causing variations in friction coefficient. This friction stability is often attributed to worn particles replenishing lubrication in the contact from reservoirs and that only a thin layer of lubricant is required [66]. Finally, failure occurs when there is no longer enough MoS<sub>2</sub> to separate the surfaces with a corresponding rapid increase in friction coefficient.

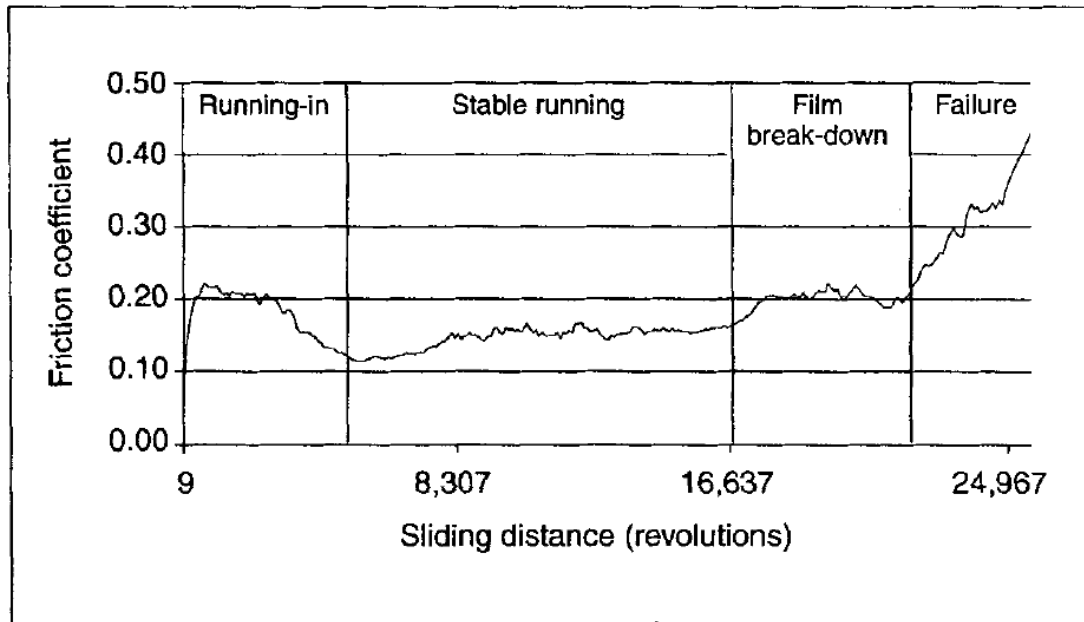


Figure 2-15: Typical stages in friction performance of MoS<sub>2</sub> [64]

As noted, substrate texture is a key variable, with Hu et al. investigating its influence on the reciprocating sliding behaviour of MoS<sub>2</sub> on a steel substrate [60]. The texture consisted of an evenly spaced grid of surface depressions as shown in Figure 2-16. Two different deposition techniques were used: hot pressing and burnishing.

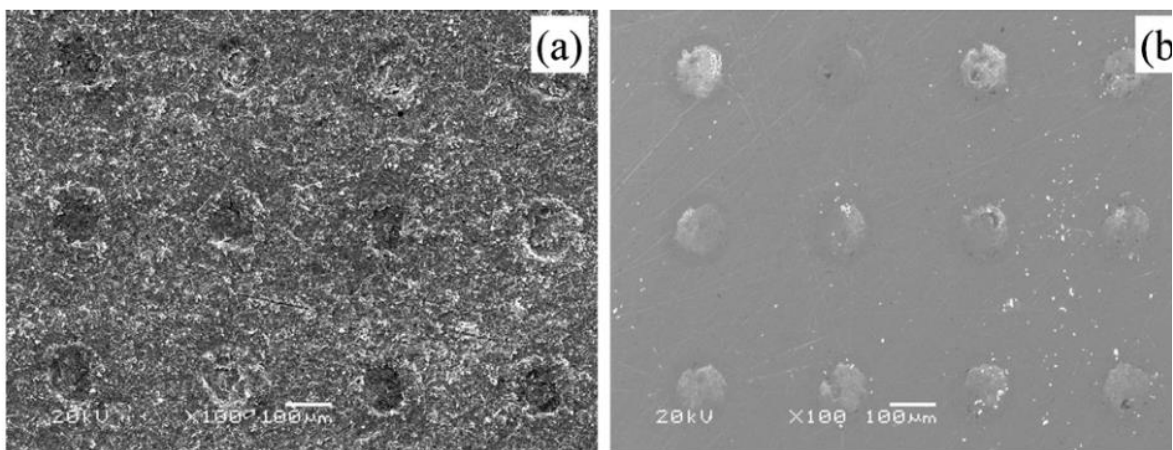


Figure 2-16: SEM micrographs of MoS<sub>2</sub> coatings by hot pressing (a) and burnishing (b) on the textured surface [60]

The texture improved the wear life by providing MoS<sub>2</sub> reservoirs to replenish the contact with lubricant particles, and 15% to 20% of area coverage with depressions was found to be optimal. The experiments also highlighted that the hot-pressing deposition offers significantly longer life than burnishing, and they related this property to a better adhesion to the substrate and a larger coating thickness.

### 2.3.3 Fretting behaviour

Xu et al. investigated the influence of substrate material and preparation of bonded MoS<sub>2</sub> particles [67]. The particles, within the size of 0.5-1 μm, were dispersed in a novolac-epoxy resin and applied at different thicknesses on a range of different steels substrates. They observed that mixed and partial slip regime were difficult to form, even at very low displacements (5 μm) after the coating application, as opposed to the bare steel interface where the transition occurred around 40 and 20 μm respectively. They described the damage mechanism as follows: a first low damage stage where plastic flow and scratch occurred (Figure 2-17a), followed by a micro-crack nucleation and propagation phase (Figure 2-17b and c), and finally, failure due to delamination of particles (Figure 2-17d). The CoF recorded was around 0.1 throughout the whole test duration, with a rapid increase at the end of test (Figure 2-17e).

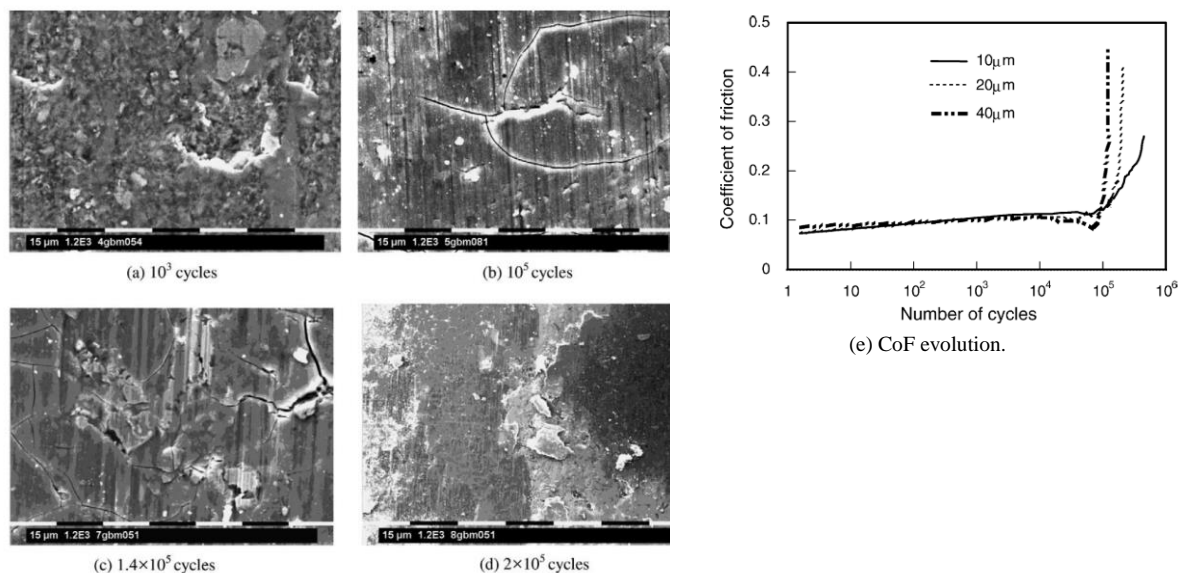


Figure 2-17: Progression of the wear damage observed by Xu and al. [67]. a) to d) show SEM images of the 20 μm test, e) CoF evolution at different displacements.

Following this investigation, Xu performed further experiments with other researchers to better address the subject [68]. They proposed the role of oxidation of MoS<sub>2</sub> to MoS<sub>3</sub> as responsible for the CoF increments during the wear progression. Oxidation is equally important in fretting. They also observed that the cracks formed preferentially along the direction parallel to the fretting movement (as shown in the example in Figure 2-18) and they correlated this effect to the tendency of MoS<sub>2</sub> particles to orientate likewise.

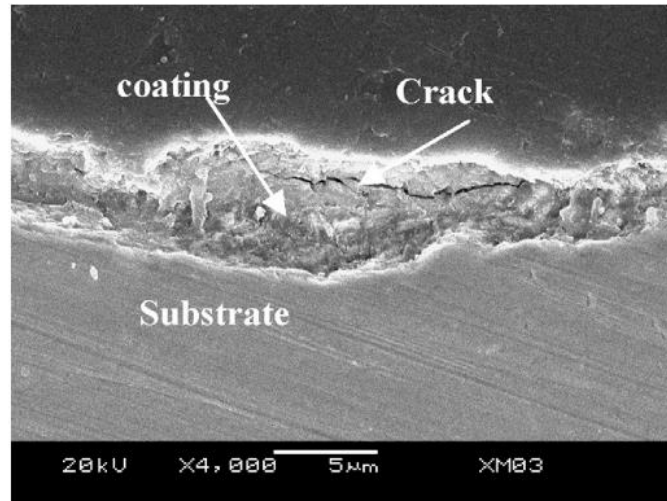


Figure 2-18: Cross-section of the wear scar along the fretting direction [68]

Further, they compared the performance of bonded MoS<sub>2</sub> particles to PTFE and graphite bonded solid coatings. The results indicated the PTFE as best performing solution, as shown in Figure 2-19.

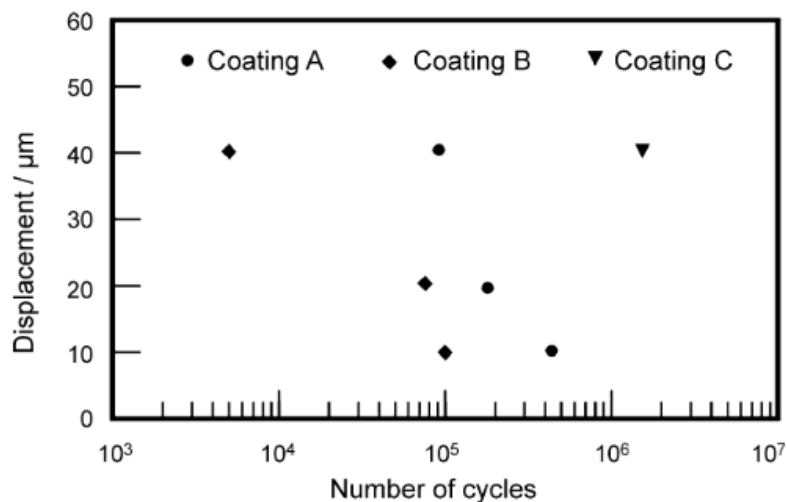


Figure 2-19: Variation of fretting life at different displacement amplitude for 3 different coatings: Coating A) MoS<sub>2</sub>, B) Graphite C) PTFE

Yinping et al. also performed testes on bonded MoS<sub>2</sub> particles, covering a large range of loads and frequencies. They found that the wear rate and the friction coefficient were the highest at the lowest contacting loads, and then decreased as the load increased, and become load-independent after a certain load threshold was exceeded. The same qualitative behaviour occurred for the wear rate as a function of reciprocating frequency. Whereas the coefficient of friction started at the lowest value at low frequency, and then reached a plateau region at a higher value. Their graphs are reported in Figure 2-20.



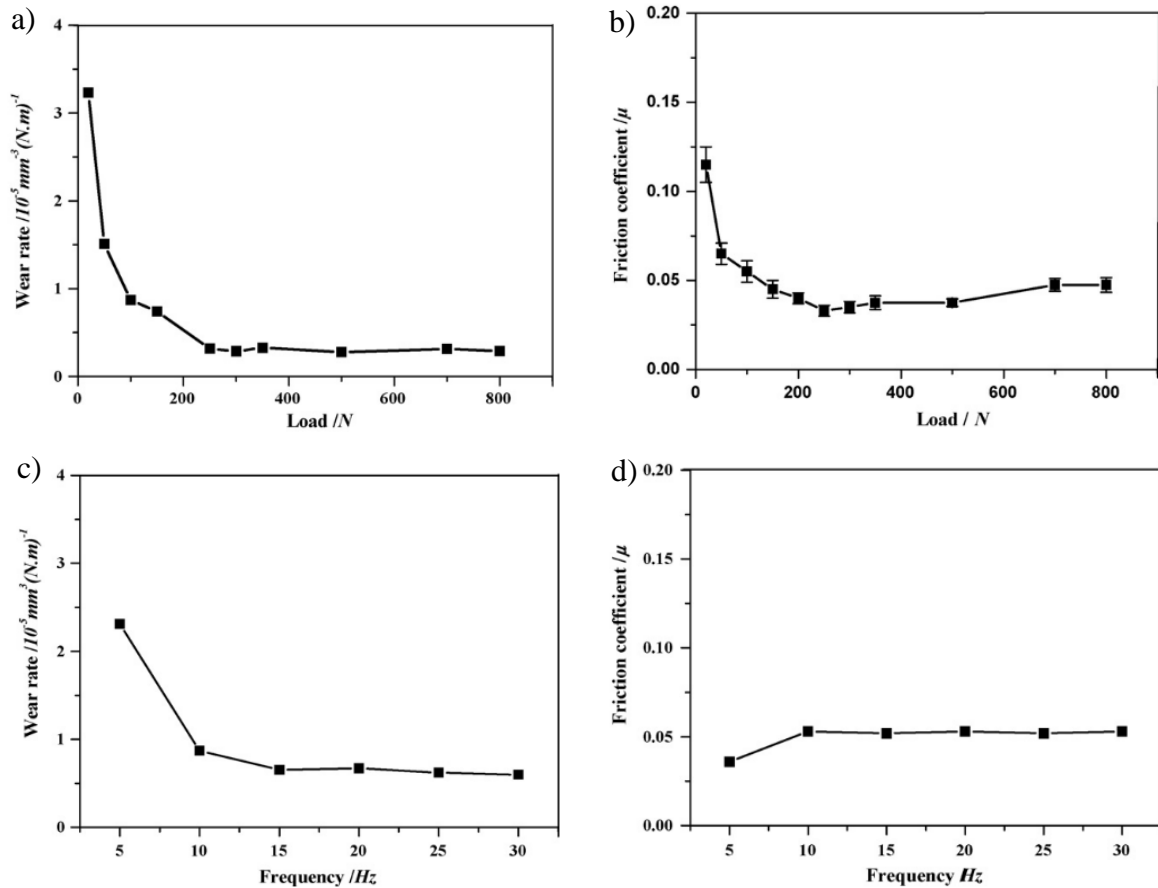


Figure 2-20: Effects of load and frequency on the wear rate and CoF of bonded MoS<sub>2</sub>

### 2.3.4 Rolls Royce Commissioned Studies

Section 2.2.3 provides details on why lubrication is important for Rolls Royce engines. Therefore, they have carried out extensive testing to optimise the coating. Beale [7] provides a review of Rolls Royce testing carried out and the procedure for selecting new material/coating combination. First a simpler flat-on-flat configuration ‘in-line Dartec rig’ is used (as shown in Figure 2-21). The test is concluded when the CoF reaches 0.3 and the number of cycles determines the coating life. The best performing coatings/materials are taken forward to more complex (and therefore more representative) test rigs such as bi-axial rigs. In this test the test specimens are manufactured to simulate the blade root/dovetail coupling and the movement applied is specified to be typical of the movement in service. Typical results for different coatings are shown in Figure 2-22.

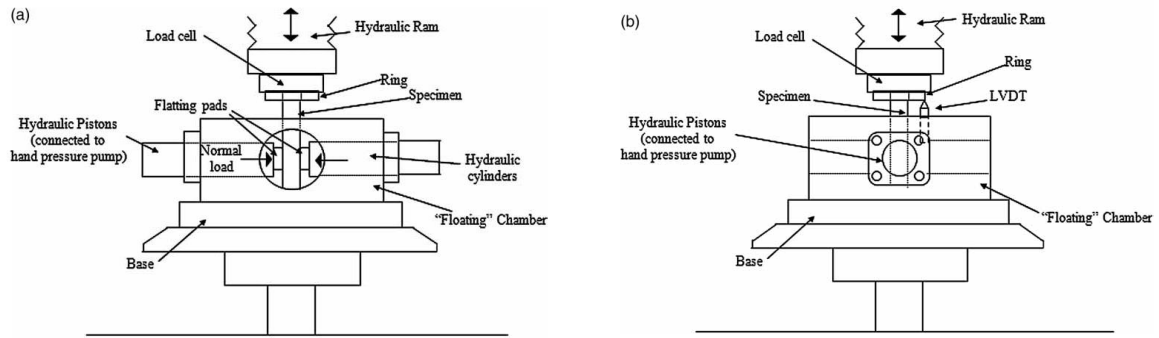


Figure 2-21: Schematic of Dartec rig a) front view b) side view [69]

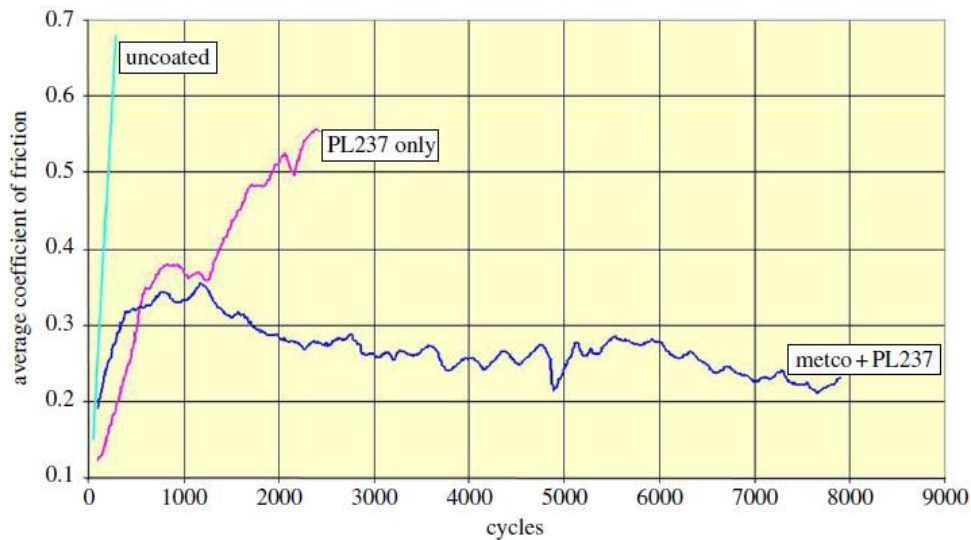


Figure 2-22: Example of results from biaxial test rig for different coatings [7]

Kim and Korsunsky have investigated the effects of imposed displacement and initial coating thickness on the Dartec rig [70]. Consistently with many other works, they found that the life of the coating is increased with a larger initial thickness. With regards of the effects of the imposed displacement, their experiments suggested that the CoF evolution (expressed as *maximum tangential force*,  $Q_{max}/Normal\ Force, P$ ) against the accumulated reciprocating distance is similar in the range 0.4-0.6 mm.

There has also been some investigations using Ti-6Al-4V alloys [71], [72] to determine the location of the transition from mixed to gross slip as well as the evolution of the slip regimes. However, these studies used uncoated pads and therefore are less relevant to this study given its focus on the coating.

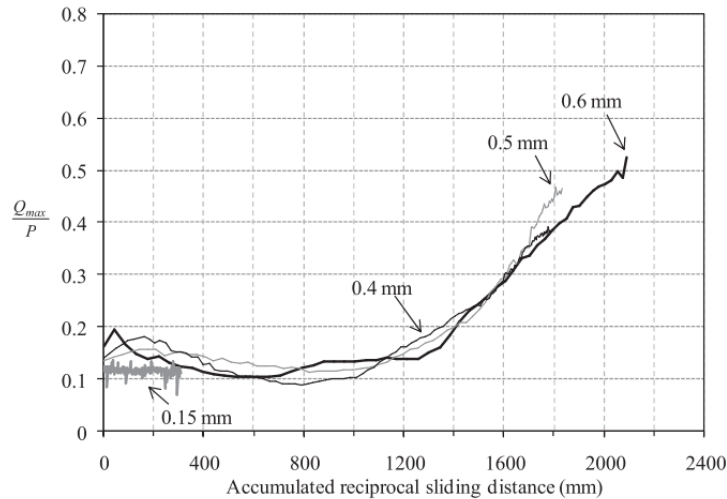


Figure 2-23:  $Q_{\max}/P$  as a function of accumulated distance.

### 2.3.5 Alternative Coating Systems

Given the availability of an in-house test rig, coupled with a desire by Rolls-Royce to increase service life, alternative coating systems have also been investigated.

Kim and Korsunsky [69] have tested the durability of a hybrid Ni-MoS<sub>2</sub> coating on the Dartec rig. Multi-layer films (composed of 75 % of MoS<sub>2</sub> and 25 % Ni) were applied onto the Ti-6Al-4V specimens' substrate by either plasma spraying or High Velocity Oxidation Fuel (HVOF) thermal spraying. The overall thickness was around 100-150  $\mu\text{m}$ . The pads were coated with a 30-50  $\mu\text{m}$  thick plasma sprayed MoS<sub>2</sub> coating. The performance of this coating system was found to offer a longer life endurance than the conventional system. This is due to the Ni forming a harder film which increases resistance to fretting [73].

More generally, Mechano-chemical deposition techniques was investigated by Korsunsky et al. [8] as alternative deposition technique. They explain that this technique combines the characteristics of mechano-chemistry and shot-peening and they proved that it can be effectively used to create a well-adhered layer with significantly improved tribological properties.

The tribological properties of Ti-MoS<sub>2</sub> coatings were investigated [56] at both macroscopic scale (using an in situ tribometer) and microscopic scale (using a nanoindentation instrument). Different humidity's were also tested. Differences were observed between the two scales, with **ploughing** observed at the microscopic scale but not the macro scale. Comparisons to other coatings were not carried out.

Aluminium Bronze can also be plasma sprayed onto Ti-6Al-4V to improve fretting performance and tests between Al-Bronze and Cu-Ni-In showed that the Al-bronze sustained

slightly less wear to other coatings tested [32]. These tests were performed without a solid lubrication layer so were not wholly representative of the RR coating system.

Overall, no satisfactory alternative coating system was identified or insight into modifying parameters of the current system to achieve an improvement in service life, and thus the motivation for this project remains.

## 2.4 Summary

*Fan blade dovetail joints have been shown to be an extremely complex area of an aero engine. The geometry is intricate, and they are subjected to a variety of loading conditions. In order to reduce the stress on the fan blade, it can move radially to find its least stressed position, prolonging the life of the blade. For this to occur Rolls Royce use a DFL coating in the blade-disc interface.*

*The main failure mechanism relates to fretting at the blade-disc interface. Initially, the coating is subjected to fretting wear and once the coating wears out, fretting fatigue dominates due to metal-metal contact and uneven blade seating until joint failure. Fretting affects a wide range of applications but is still not fully understood. Therefore, there is a need to carry out laboratory testing on simpler geometries to understand the mechanisms and key parameters that affect fretting behaviour. Titanium alloys and MoS<sub>2</sub> have been extensively tested, mostly using ball-on-flat tests or other unrepresentative configurations. These test configurations provide some fundamental knowledge and suggest directions for more representable geometry/loading condition testing. Ideally, theories and assumptions are tested on simpler test scales before stepping up test complexity and testing the outcomes on more representable test platforms. Additionally, there is a large body of literature on titanium alloys and MoS<sub>2</sub> but surprisingly little research has been carried out on the bond coat and the role it plays in the lubrication mechanism of the blade-disc interface.*

*Modelling has also been shown to be important to bridge the gap between 2D test platforms and real dovetail joints due to the complexity of the joints. The mechanism behind MoS<sub>2</sub> providing low friction and the failure mode has not yet been fully investigated for the aerospace sector so there currently is a gap in the literature to fully understand the coating for this application.*

*To prevent joint failure, re-lubrication typically occurs every 1200 engine cycles to top up the DFL coating and full coating replacement occurs every 4500 engine cycles. These service intervals are short enough to ensure the coating does not fail so the coating is topped up regardless of its condition. This means that there is scope to increase the service interval, leading to reduced costs, provided there was a way of monitoring the coating performance in-situ to identify when it should be replaced.*

### 3 Analysis of a failed fan blade and Rolls Royce test samples

The aim of this chapter was to examine the tribological transformations that the Rolls Royce coating system undergoes due to use and to investigate the mechanical behaviour and failure modes. The analysis is performed by inspecting the surfaces of used components. Among the several studies that have addressed the fan blade contact, the only study relevant to the Rolls Royce coating system was the forensic analysis undertaken by the Australian Transport Safety Bureau (ATSB), following the fan blade release in Melbourne [10]. They described a fan blade root of the intact engine as presenting a mixture of residual DFL and galled areas along the full root length, on both the suction and pressure side. The appearance of the root surface, shown in Figure 3-1, was reported to be typical in the fan assemblies of both engines. The damage, orientated in the direction of radial sliding, was associated with the blade seating and identified as the cause of the other blade failure.



Figure 3-1: Rolls-Royce RB211 Trent 892 blade dovetail root inspected by the ATSB [10].

In this chapter, a Trent 800 blade root of unknown loading history is studied. A set of samples tested to failure on the biaxial rig at Oxford University, not previously subjected to tribological investigation are also examined. Although this is a representative test, it is considered to be sufficiently complex to represent the engine conditions [39]. The investigation consisted of a combined analysis of the following techniques: imaging, topographical measurements, elemental analysis and residual coating thickness measurements. These methodologies are presented in the following section of this chapter. The inspection of the Trent800 blade root is then reported. Three areas of different appearance identified through visual inspection were compared to investigate the different mechanisms taking place. By relating the spatial patterns across the root surface between coating behavior and contact pressure, the latter is identified as a key tribological parameter. The biaxial samples' analysis is then reported, where the role of pressure, test conditions and re-lubrication history is considered. The findings are then collated in the discussion section.

#### 3.1 Surface characterisation techniques

The surface characterisation techniques presented in this section will be used throughout the whole thesis to assess the coating state. The technologies and devices used are listed, along

with a brief explanation of results processing and interpretation. The default settings and procedure are also reported, which will be used unless otherwise stated.

### **3.1.1 Scanning Electron Microscope Imaging**

Scanning Electron Microscope (SEM) imaging is used to acquire high magnification micrographs of a surface. There are two main techniques to scan a sample: using the Secondary Electron (SE) detector or the Back Scattered Electron (BSE) detector [74]. The secondary electrons are generated by the inelastic interaction of the electrons with the surface. These electrons have low energy and originate from the surface under measurement, carrying information relative to the surface topography. The BSE acquisition relies on the count of electrons scattered due to elastic collision with the surface. As the scattering capability increases with the atom size (which depends on the atomic number), the BSE image provides qualitative information on the surface composition. A Philips XL-30 and a Hitachi TM3030 SEM device were used. The TM3030 also features a mixed SE/BSE scan conveying both topographical and elemental information, which was always used with this microscope. The detector used is indicated in each micrograph in any other case, along with a scale bar and other information.

### **3.1.2 Optical interferometry**

Optical interferometry is a non-invasive contactless technique used to measure the topography of a surface [75]. A Contour-GT and an Alicona InfiniteFocusSL instruments were used at 5x magnification, both capable of a vertical resolution of 100 nm. These devices output a topographical map of a surface and offer several post-processing techniques to extract parameters such as surface roughness, waviness, and line profiles. The specific post-processing technique is explained in more details on each relevant application.

### **3.1.3 Elemental analysis**

Quantitative information of a surface composition can be obtained with an SEM using Energy-Dispersive X-ray Spectroscopy (EDXS), which allows to distinguish the elements of a surface by their unique electromagnetic emission spectrum [76]. Typically, the data can be processed to produce a distribution map for each phase, or an overall weight percentage composition. Energy Dispersive X-ray Fluorescence (EDXF) was also used, which relies on the same fundamental principles of EDXS. Specifically, a Fischerscope XAN 250 device was used with a beam excitation voltage of 30 kV and no filters. The drawback of this instrument is the capability to detect only the elements whose atomic number ranges between 13 (Aluminium) to 92 (Uranium), excluding the possibility to identify oxygen (atomic number 9). Therefore, oxidation effects cannot be detected.

Both these technologies rely on the penetration of the beam into a sample (interaction volume), whose depth is in the order of a few micrometres. When the thickness of the coating is smaller

than the beam penetration depth, the measurements is affected by the substrate composition too. This must be taken into account when interpreting the results.

### 3.1.4 Sectioning and preparation of samples

The examination of the coating subsurface is of interest to gather further information that is not directly accessible from the top of the surface, such as coating residual thickness. This is achieved by cross-sectioning a component and imaging it perpendicular to the coated surface. A cross-sectional access to the surface also improves EDXS measurements reliability, overcoming uncertainties related to the beam penetration into the substrate.

Depending on shape and dimension of the component, the cut is made by either using EDM wire cut erosion or abrasive cutting machine. As this process might damage the coating, the samples are visually inspected to assess the depth to which the damage affected the surface, which is then measured and recorded. An example of a sample sectioned with abrasive cut is shown in Figure 3-2, where the damage is highlighted.

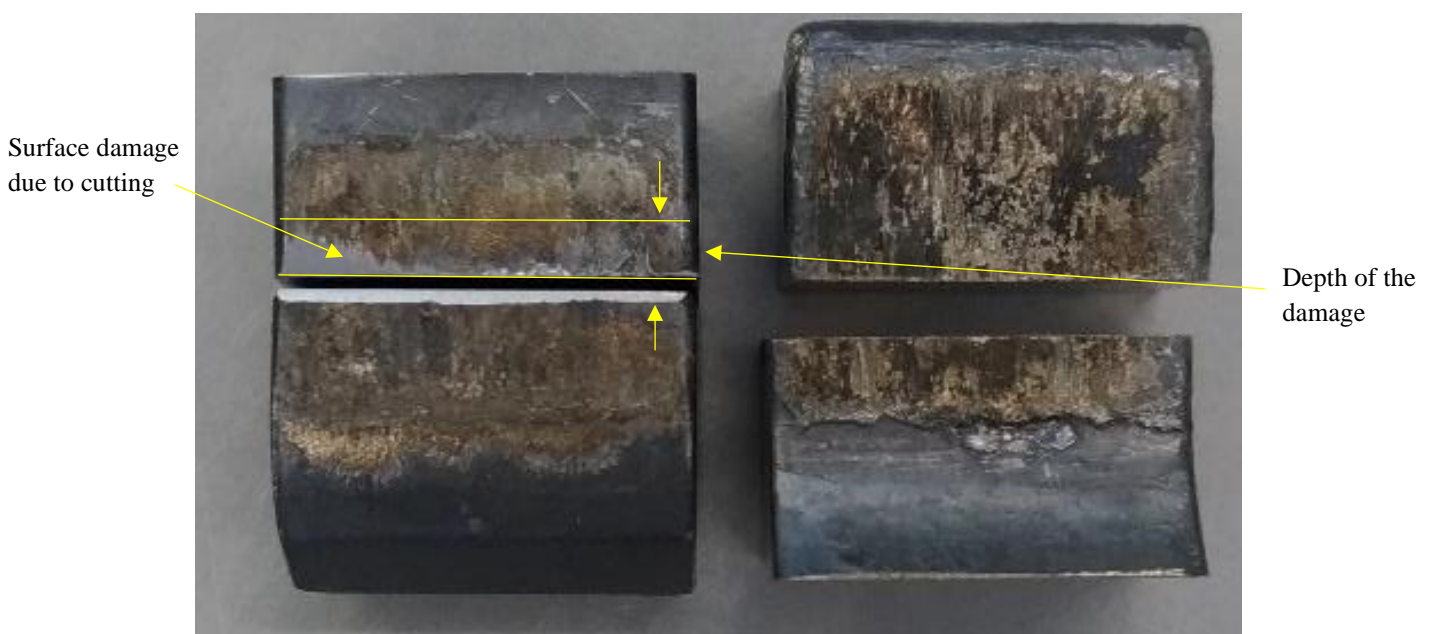


Figure 3-2: Outcome of abrasive cross-sectional cut.

The surface exposed with the cut is positioned facing the bottom of a mounting mould, which is then filled with a clear epoxy resin under vacuum conditions and air-cured to allow for settling. After curing, the sample is removed from the mould and undergoes a coarse grinding procedure. The thickness of the sample is measured every 2 minutes with a caliper in order to stop the process when the cumulative thickness removed is equal to or larger than the damage depth. Finally, the surface is further ground and polished, according to the sample preparation process shown in Table 2.

Process	Abrasive & Lubricant	Load per sample	Speed (rpm)	Time (min)
Grinding – Stage 1	P400 SiC – Water	35 N	300	1
Grinding – Stage 2	P800 SiC – Water	35 N	300	1
Grinding – Stage 3	P1200 SiC – Water	35 N	300	1
Polishing – Stage 1	9 $\mu$ m Diamond Suspension	35 N	300	6
Polishing – Stage 2	Colloidal Silica Suspension	35 N	300	4

Table 2: Sample preparation process

It is of interest to estimate the position of the final section on the top view of the surface. The measurement during cutting and overall thickness removed are then used to estimate the location of the final section. The surface profile is then extracted from the topographical data at that location and superimposed onto the cross-sectional image. An example of the outcome of the process is shown in Figure 3-3. As shown in the figure, the agreement between the coating profile image confirms a satisfactory section location estimation and surface preservation.

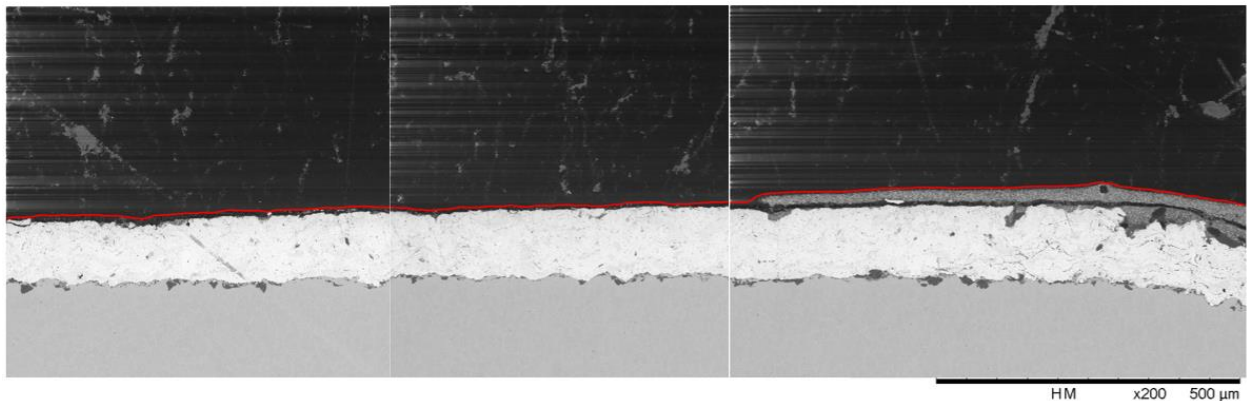


Figure 3-3: Example of surface profile (red line) superimposed on a cross-sectional image

### 3.2 Ex-service Trent800 blade investigation

An ex-service Rolls-Royce Trent800 fan blade root has been inspected. Prior to entering into service, the blade was coated with the RR coating system (as described in Section 2.1.2). The loading history and the number of cycles of the component were not available for this study. Regardless of the past service history, different behaviour is expected to occur as a function of contact pressure around the root slot. According to the RR FEM model [12], the contact area can be divided into two broad regions in terms of average contact stress (Figure 3-4).



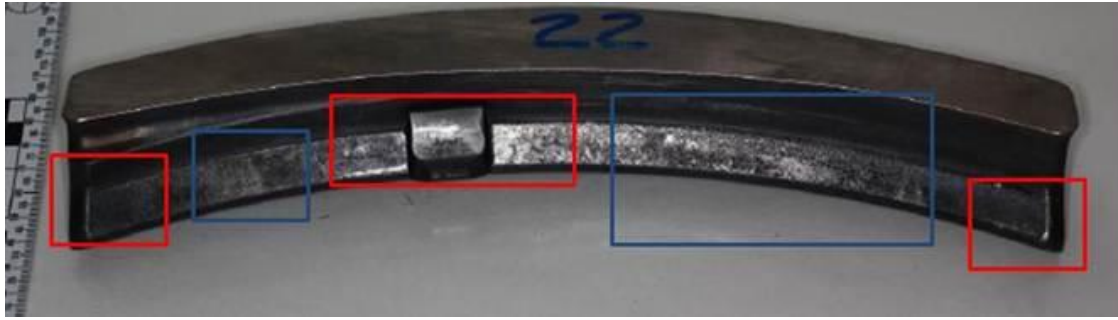


Figure 3-4: Stress regions of the fan blade root (Blue 150 MPa, Red 300 MPa averagely).

High contact pressure areas (around 300 MPa) were identified from the RR FEM model [12] and are situated close to the trailing and leading edge and in the proximity of the shear key, whereas stresses averaging 150 MPa are experienced in the rest of the surface.

### 3.2.1 Visual inspection and sample choice

Three different appearances of the coated surface were identified through visual inspection of the root surface. The typical appearance of each area is marked in the picture below (Figure 3-5).



Figure 3-5: Different features observed in the root

Area 1 looks grey in colour and was observed to occur exclusively in the edges of the contact, whereas Area 2 is dark-grey and was found all over the surface of the root. Area 3 was found mainly in the high load region and looks black; loose powdery debris was also found on the root surface similar in appearance to the coated surface in the same region. Table 3 shows a summary of the features of each area and their spatial patterns.

Area 1 (edge of the contact)	Area 2 (Low load)	Area 3 (High load)
<ul style="list-style-type: none"> <li>• Grey</li> <li>• Least common</li> <li>• Found in the contact area edges</li> </ul>	<ul style="list-style-type: none"> <li>• Dark-grey</li> <li>• Most common area</li> <li>• Present mainly in the low loaded areas</li> </ul>	<ul style="list-style-type: none"> <li>• Black in colour</li> <li>• Quite common</li> <li>• Found mainly in the high loaded areas</li> </ul>

Table 3: Different areas observed in the used fan blade root

In order to analyse the areas identified visually, five samples were cut out of the component from different locations using electro discharge machine (EDM). The samples were sourced from both the intrados and extrados of the root at different axial locations, allowing to provide adequate coverage of each of the three areas to perform the analysis. Figure 3-6 shows the location of the samples.



Figure 3-6: Fan blade cut positions (marked in red). Intrados (above) and extrados (below).

The three areas were then analysed with SEM, optical interferometer and energy dispersive X-ray fluorescence (EDXRD).

### 3.2.2 Surface Morphology

A Philips XL-30 SEM was used to image the three areas. The beam voltage was 20kV and the magnification was 200x. The SE and BSE micrographs of the typical structure of the three areas are shown in Figure 3-7 and a comparison to an as applied layer in

Figure 3-8.

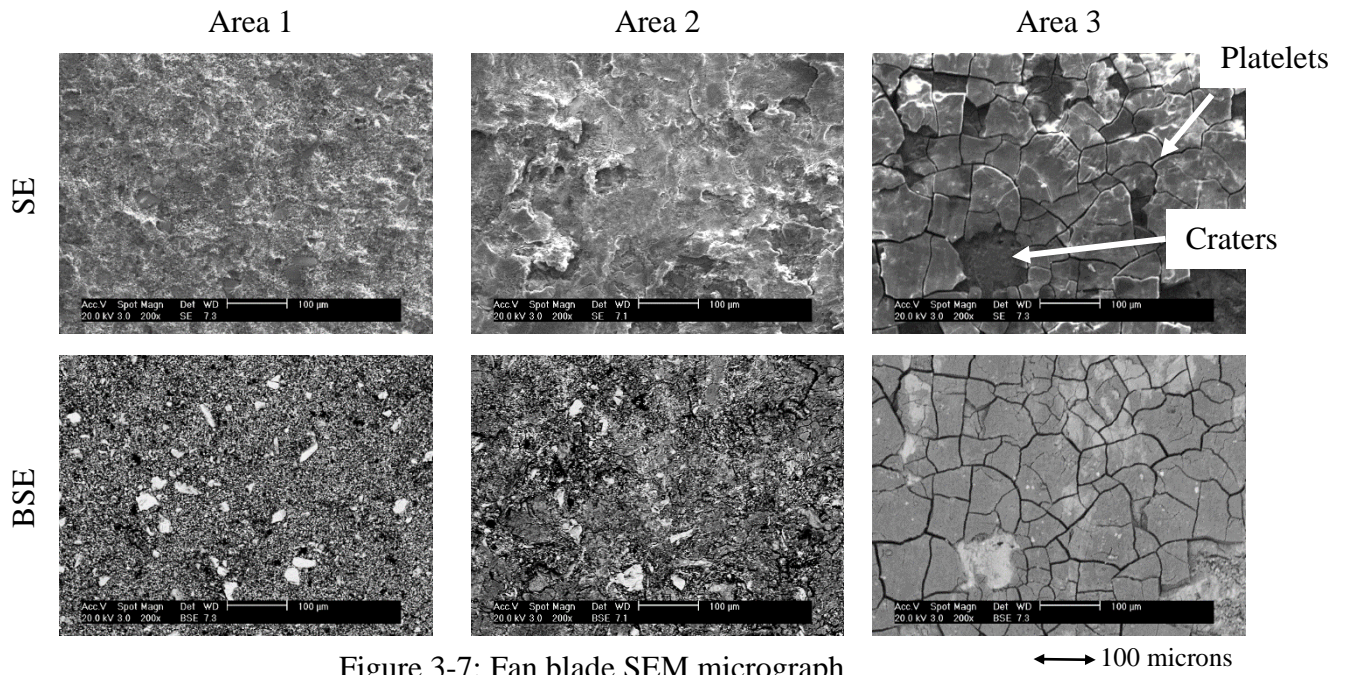


Figure 3-7: Fan blade SEM micrograph

←→ 100 microns

As shown in the figure, it can be noticed that Area 1 appears to be the least damaged and it is believed to be unloaded or very lowly loaded. Similarities were found between high magnification micrographs of Area 1 and of the typical as applied structure of  $\text{MoS}_2$ , with only light changes in structure. Area 2 looks slightly more damaged, appearing to have been gently compacted and worked. This can be seen as a progression of Area 1. Area 3 shows a different structure where two different features can be identified: a cracked top layer presenting a platelet structure which has detached in some places leaving craters behind. This layer is believed to have formed by the  $\text{MoS}_2$  particles compaction and sintering due to the contact pressure, with this structure similar to as detailed in the previous studies of the coating highlighted in the literature review.

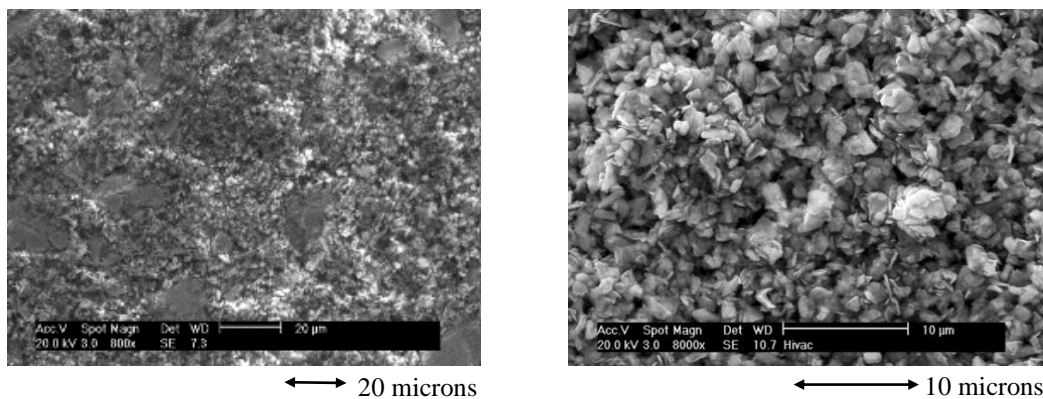


Figure 3-8: Fan blade area 1 micrograph (left),  $\text{MoS}_2$  as applied [77]. NB Micrographs have different magnification

### 3.2.3 Topography measurements

The characteristic surface topography of each area acquired with the Contour GT is illustrated in Figure 3-9. The profile of Area 1 and 2 appeared similar, presenting a quite regular surface, with peak-to-valley heights of up to approximately 20  $\mu\text{m}$ . The measurements in Area 3 showed that the thickness of the platelets was of up to 40  $\mu\text{m}$ .

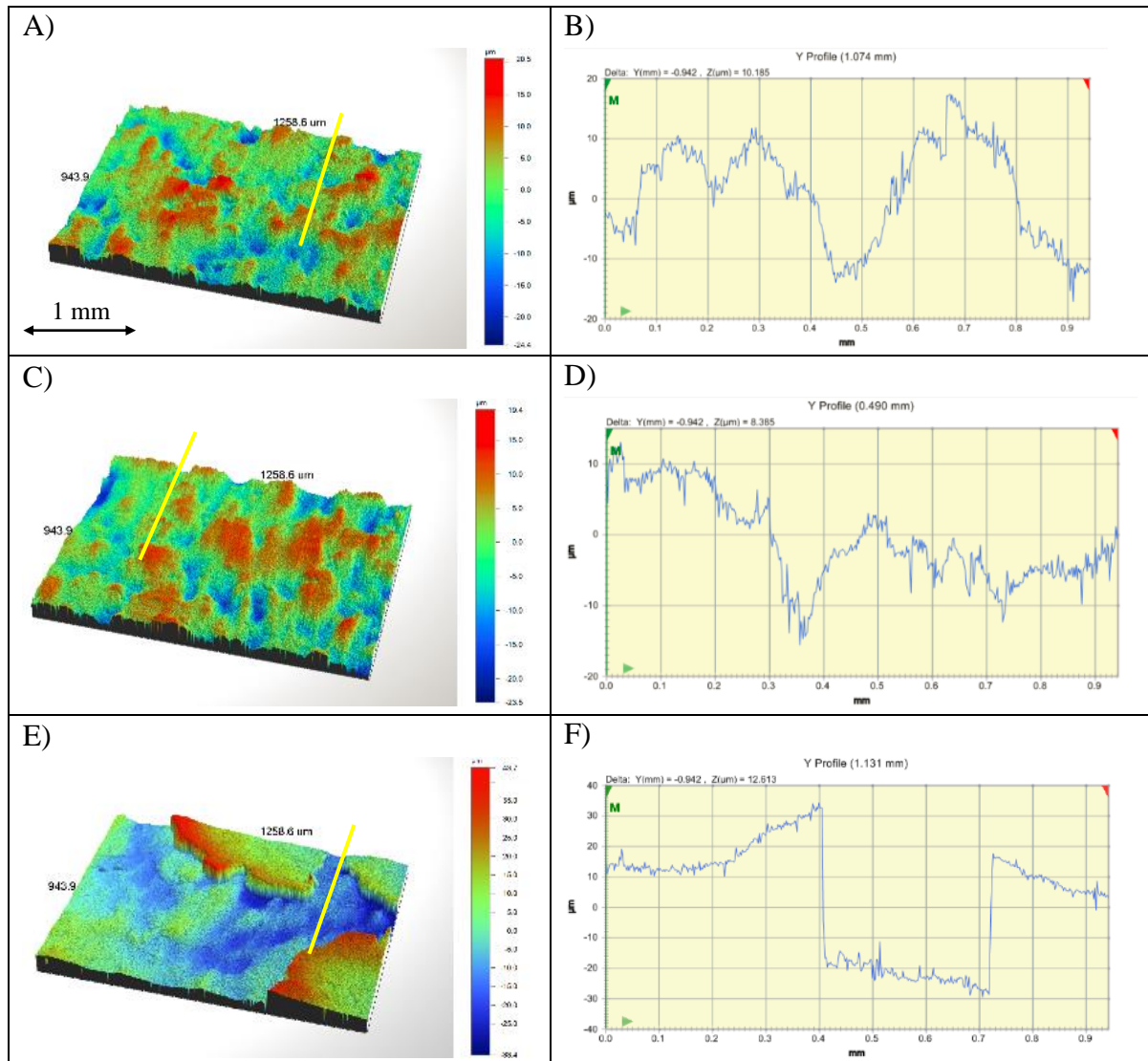


Figure 3-9: A) Area 1 surface topography B) Area 1 surface profile C) Area 2 surface topography D) Area 2 surface profile E) Area 3 surface topography F) Area 3 surface profile. N.B. Vertical scales are different

### 3.2.4 Elemental analysis

The Fischerscope was used to perform elemental analysis measurement on the samples (Figure 3-10). The results are presented by grouping Copper (Cu), Nickel (Ni) and Indium (In) weight percentages into an overall bond coat weight percentage measure, and Molybdenum (Mo) and Sulphur (S) into an overall DFL weight percentage. Other elements detected were: Antimony

(Sb), Silver (Ag), Cobalt (Co), and Iron (Fe). Among these, antimony had the highest percentage, averaging 9.48% across all the measurements. Antimony is a common additive found in MoS<sub>2</sub> based DFL formulations in the form of antimony trioxide (Sb<sub>2</sub>O<sub>3</sub>), including in commercial products used by RR such as Molikote™ 3400A (TMC product). Some early research suggested that Sb<sub>2</sub>O<sub>3</sub> can improve the MoS<sub>2</sub> life by acting as a sacrificial anti-oxidant and preventing the MoS<sub>2</sub> oxidation [78], although some later studies found no direct evidence of this [79].

Small percentages of iron (not higher than 0.3%) might be contained in Ti-6Al-4V according to the UNS designation R56400, whereas silver might be a contaminant coming from the engine bolt coatings [80]. However, iron, silver, and cobalt weight percentages combined did not exceed 0.35% in any measurements and were therefore neglected for the analysis. It should also be noted that the measurements in Area 3 were taken from both the platelets and the craters to highlight the differences.

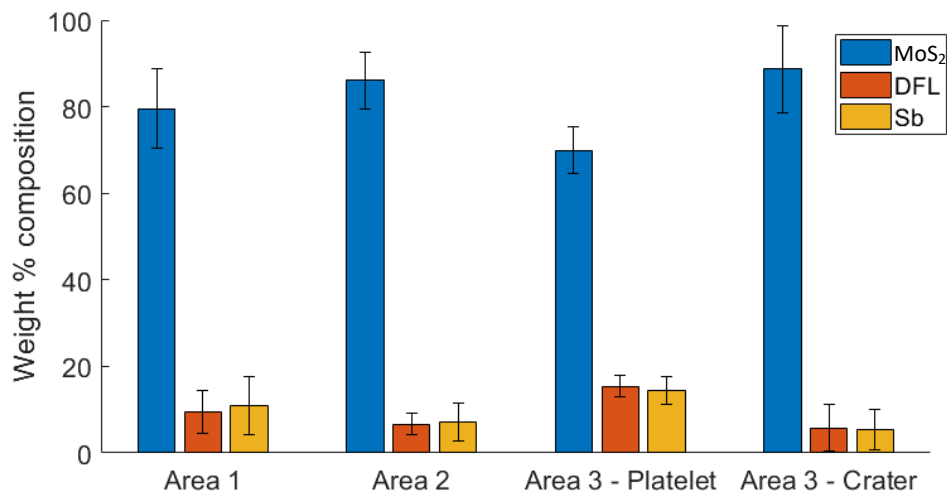


Figure 3-10: Elemental analysis of the fan blade root areas.

As shown in Figure 3-10, the platelets and the craters presented the highest and the lowest percentages of DFL respectively, Area 1 had an intermediate value and Area 2's composition was close to the craters of Area 3. For completeness, the mean compositions are also reported in Table 4.

	Area 1	Area 2	Area 3 (Platelets)	Area 3 (Craters)
Bond coat	79.59%	86.10%	69.91%	88.71%
Coating	9.48%	6.65%	15.42%	5.74%
Sb	10.83%	7.16%	14.49%	5.47%

Table 4: Average composition of the areas

### 3.2.5 Residual thickness measurement

Coating residual thickness measurements were performed to determine the differences of the coating stratigraphic composition. Wear and transfer of DFL occurring due to service can be inferred. The comparison of Area 2 against Area 3 is of interest, as the differences are produced by the differences in contact pressure. The images are shown in Figure 3-11.

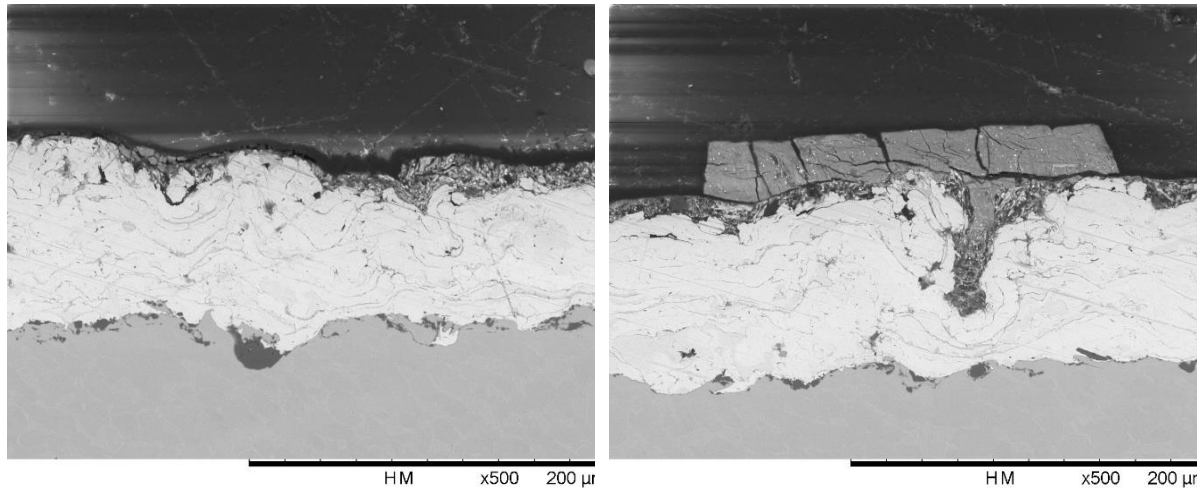


Figure 3-11: Cross-sectional micrography of blade surface: low load area 2 (left), high load area 3 (right).

As shown in the figure, the residual layer thickness of Area 2 compared to the 20 μm nominal thickness of the as-applied DFL, indicates a clear material removal in the low stress areas. The original coating structure also appeared intact across the whole section, except in the highest surface peaks where it has been tribologically transformed. The lowest coating residual thickness was also observed there. The cross-section of Area 3 shows an analogous coating subsurface, where an extra top layer covering part of the surface can be observed. As the thickness and dimension of this layer are comparable to the typical platelet dimensions, this clearly represents the black-layer observed in the high stress areas.

### 3.2.6 Overall considerations

By analysing the data gathered the following considerations can be inferred:

- Area 1: This is the least common area which was found only in the edges of the coated region, it is silvery in colour and shiny. High magnification micrographs show that the typical as applied structure of the MoS<sub>2</sub> has been preserved. Thus, it is believed that this region was either unloaded or subjected to very low-pressure contact.
- Area 2: This dark-grey area was found all over the root, being mostly present in the low loaded areas. The surface appeared gently compacted. Removal of material seemed to be occurring due to mild sliding wear, consistently with an average DFL percentage lower than the out of contact areas.

- Area 3: This area is typical of highly stressed regions, although it was also found in low-pressure regions. It can be noticed that the surface is black and presents a platelet structure, with some parts having been removed by delamination leaving craters. The platelets presented the highest DFL percentage found in all the roots. Further, their thickness (up to 50  $\mu\text{m}$ ) was larger than the nominal DFL thickness (20  $\mu\text{m}$ ), and they were located on top of a surface comparable to Area 2 for both elemental composition and cross-sectional structure. High MoS<sub>2</sub> concentration, large thickness and the stratigraphic structure of the platelets imply that material transfer has occurred from low loaded regions or from the disc. It was however not possible to determine the exact origin of the layer, likely formed by compaction and sintering of DFL particles subjected to higher pressure. Extrusions and oxidation of this sinter layer likely led to embrittlement, with consequent crack formation and loss of material by delamination of small platelets. This process is consistent with the failure mechanism of MoS<sub>2</sub> described in [64], [65].

### 3.3 Biaxial Specimens Investigation

#### 3.3.1 Test configuration and conditions

The biaxial test rig simulates the contact between the fan blade root and the fan disc using a two-dimensional replica of the Rolls-Royce dovetail joint. Each test requires a set of three samples: one plate with two dovetail shaped slots that represents the disc, and two bars with one extreme shaped as the blade root. These are shown in Figure 3-12.

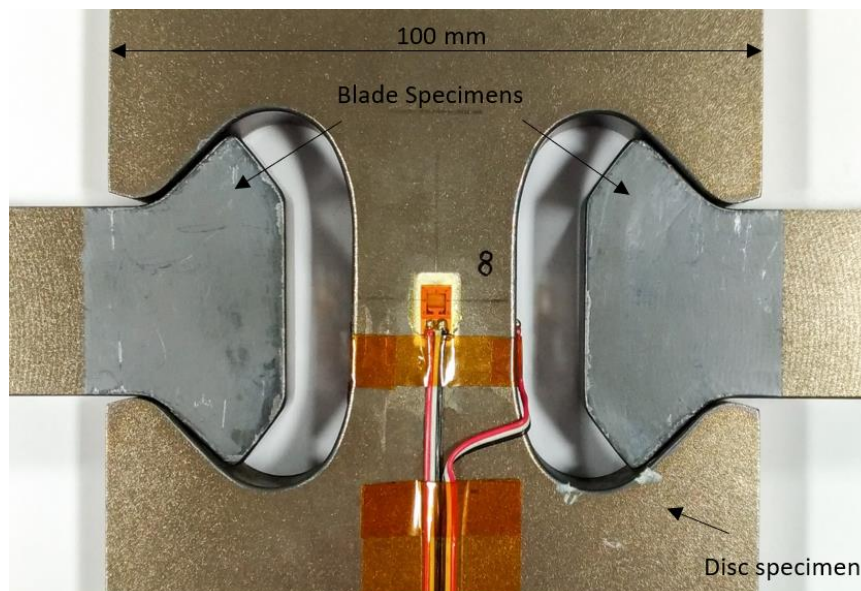


Figure 3-12: Trent800 style biaxial test rig specimens tested at Oxford University [39]

The schematics in Figure 3-13 shows the structure of the test rig. The disc is connected to and loaded by the LCF disc actuator and, simultaneously, the LCF blade actuator exerts a tensile load on the two blade samples. In this manner, the expansion of the disc and the loading on the

blade due to centrifugal effects are simulated. While the LCF loads are held, the HCF mechanical shakers simulate the effects of in-flight vibrations. The LCF loads are then released as completion of the LCF cycle. This will be also referred to as major cycle hereon, whereas the vibration cycles will be referred to as minor cycles. The major cycle is repeated until failure is detected by a set of strain gauges bonded to the specimen, with the failure criteria being the visual identification of cracks in one or both of the samples.

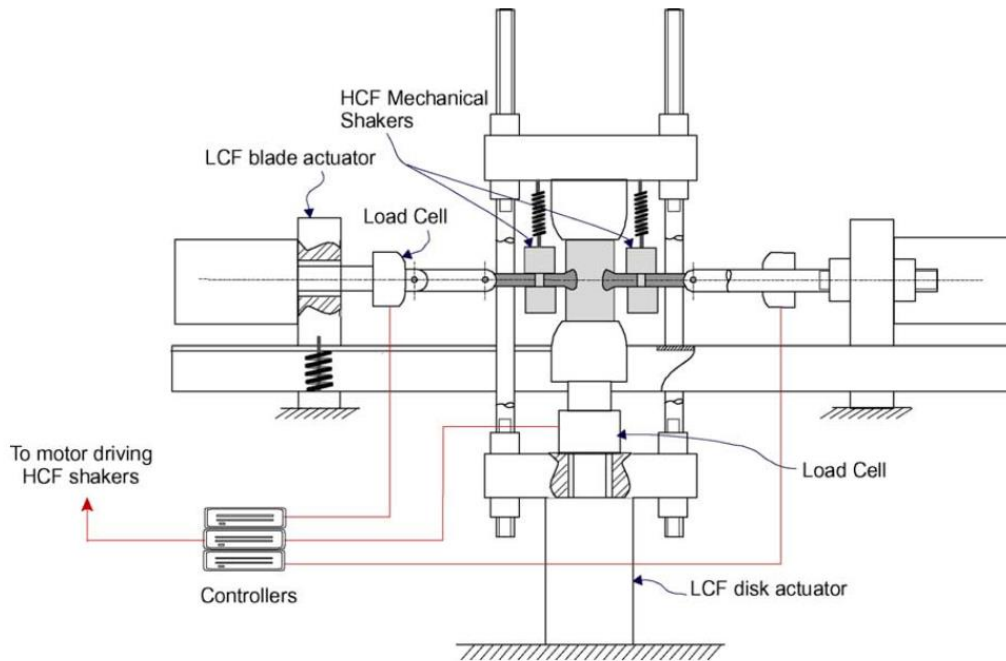


Figure 3-13: Biaxial test rig schematics [45]

The components analysed were Trent800 style specimens made of Ti-6Al-4V alloy. The disc was coated with PL237 DFL and the blade was coated with Metco58 and PL237 DFL as per the coating procedure described in section 2.3.1. The LCF load was 120 kN on the disc specimen and 80 kN on the blade specimens, and 7200 vibration cycles (minor cycles) were performed per each major cycle.

The contact pressure under these conditions was estimated to be approximately 250 MPa, depending on CoF at the interface [7]. Relubrication on the blade was performed at 5000, 8000 and 10000 cycles and failure occurred at cycle number 12281. These are nominal intervals based on observation of coefficient of friction and are not linked to real service intervals. The coefficient of friction data for this test was not available.

### 3.3.2 Sectioning of samples

As the biaxial rig is designed to achieve equal loading on each of the four blade/disc interfaces, only one mating pair was inspected. The components were EDM cut as indicated in

Figure 3-14 in order to allow for inspection of the surfaces indicated by the red arrows.



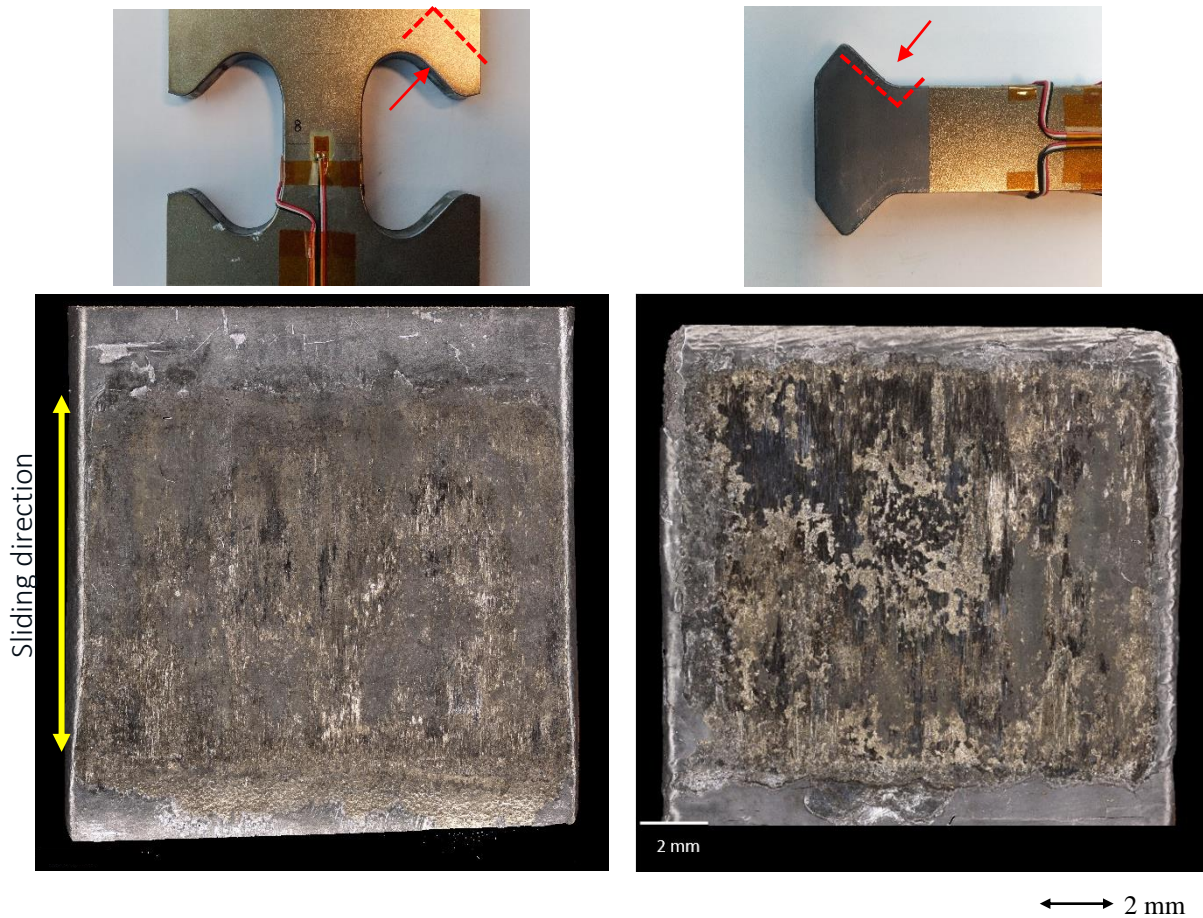


Figure 3-14: Sectioning of the samples: disc (left) and blade (right).

Similarly to the blade root investigation, a visual inspection of the surface was performed. The contacting surface of the blade specimen shows light wear marks orientated along the sliding direction and heterogeneity in its morphological composition. Four areas were identified in the blade. These were imaged with the SEM and measured with the Alicona. The samples were then sectioned and prepared according to the procedure in §3.1.4. The disc shows less heterogeneity compared to the blade specimen. There were three areas identified that were of interest. As with the blade these were imaged by SEM.

### 3.3.3 Blade specimen

The areas under analysis of the contacting surface are shown

Figure 3-15 (BA, BB, BC and BD), the estimated locations of the cross-sections are also marked.

Figure 3-16 shows an SEM image of the whole blade surface. This image is included as it shows the differences between the chosen regions more clearly than in

Figure 3-15.

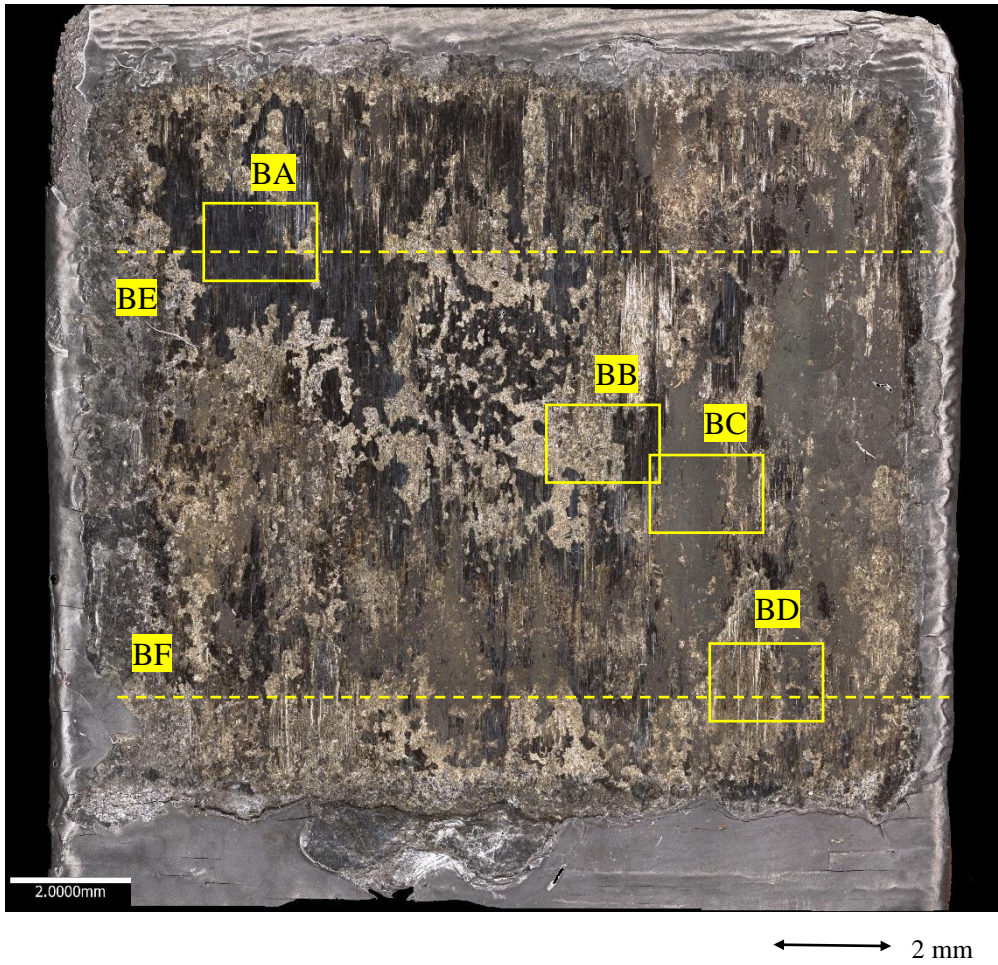


Figure 3-15: Blade specimen surface. BA, BB, BC and BD indicate the four different areas. The dashed line indicates the location and the direction of observation of the cross-sectional images

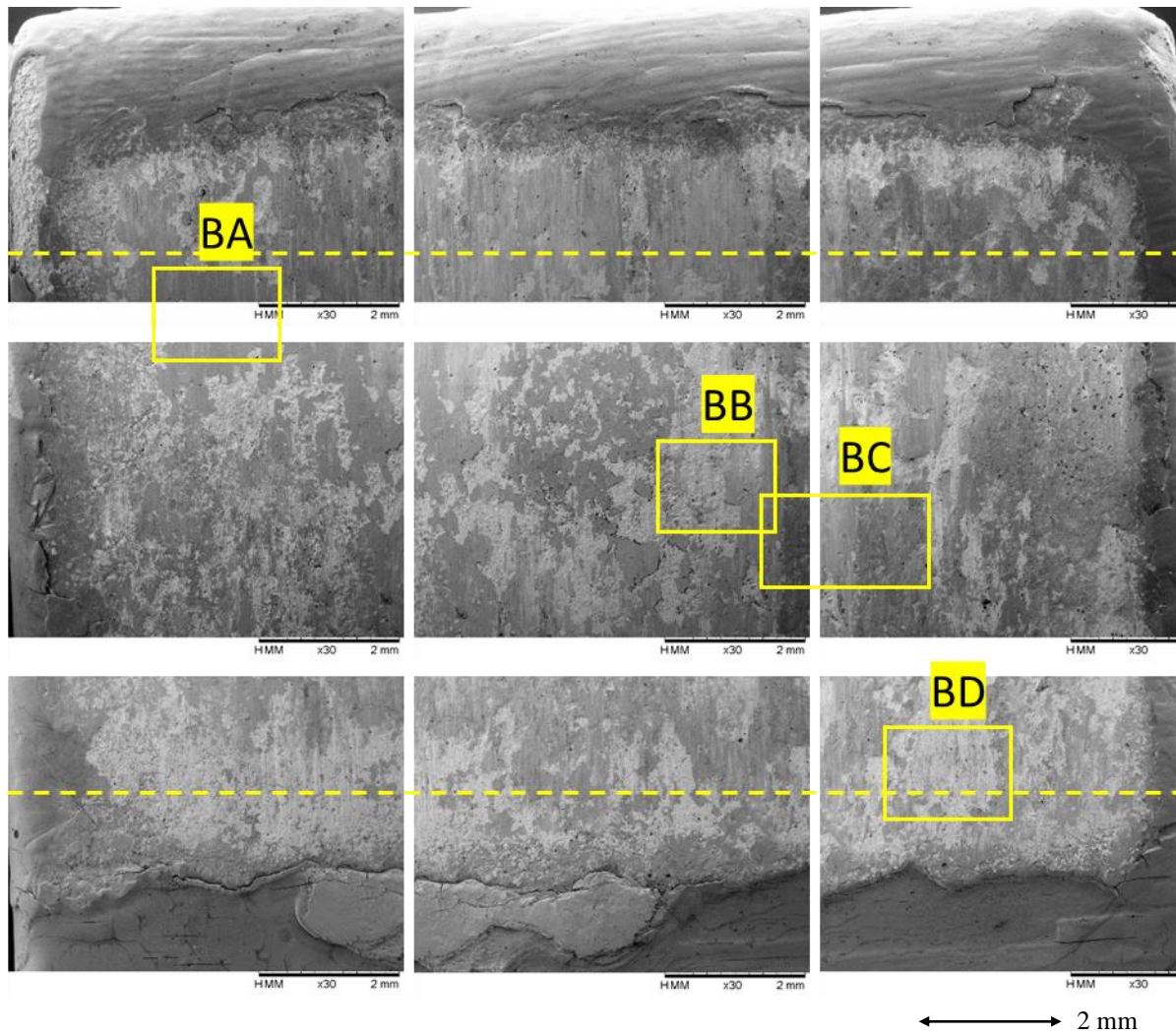


Figure 3-16: SEM images of whole blade surface

The SEM micrograph in BA is shown in

Figure 3-17, along with a cross section profile as well as surface profiles. The surface profile location is shown as the red line in

Figure 3-17a. A dull black layer can be observed from the top view, presenting light cracks and small regions of detachment. The cross-section shows the layer is composed of small DFL agglomerates that have been mechanically deposited together. These agglomerates might originate from the fragmentation of previously formed layers which have been re-sintered in a new layer with fresh DFL particles. Regardless, given the large coverage of the DFL layer it is proposed that BA provides good lubrication. Additionally, the surface profile shows that the black layer has a smoother surface compared to the region of gold appearance. This gold region is discussed further in BB (Figure 3-18)

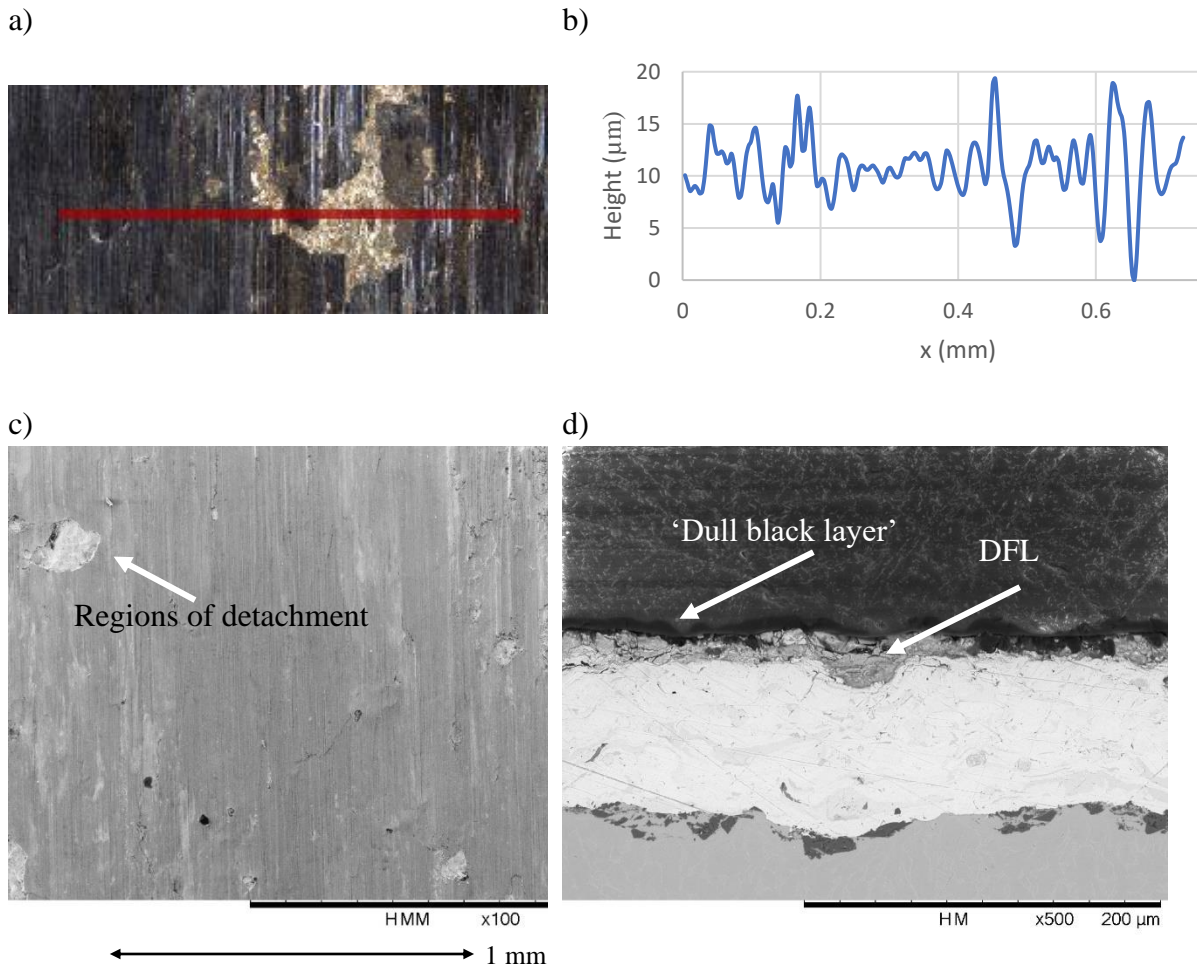


Figure 3-17: BA a) surface, b) surface profile, c) SEM d) cross section

BB is shown in Figure 3-18. A small part of this area shows a platelet structure resembling BA. In the rest of the surface, the bond coat is believed to have been exposed due to detachment of these platelets. This is in line with the cross-sectional view, which shows no evidence of DFL as opposed to BA. A thin black layer appears to have formed on top of the bond coat surface, likely due to oxidation. High CoF is expected here due to the tribological properties of the bond coat.

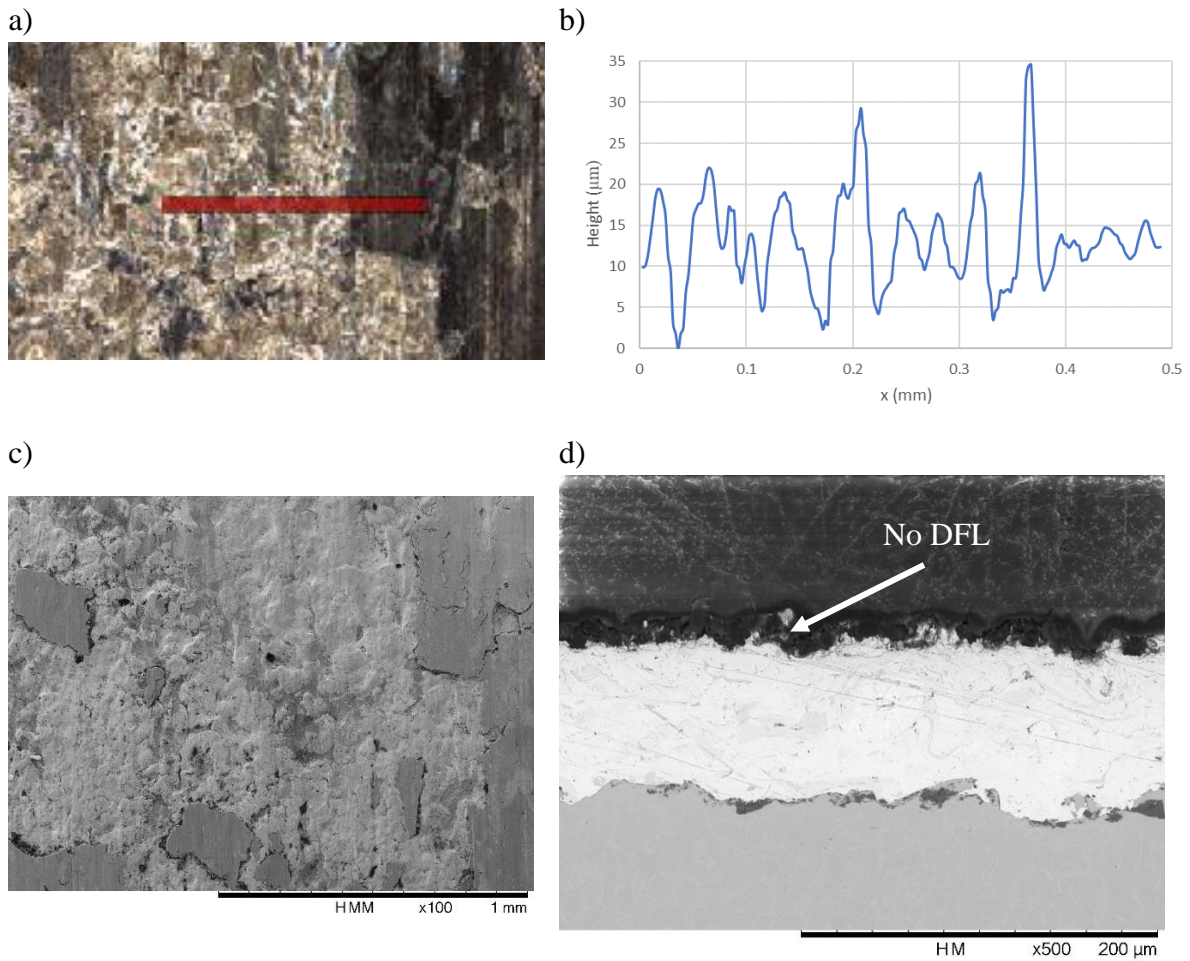


Figure 3-18: BB a) surface, b) surface profile, c) SEM d) cross section

BC is shown in Figure 3-19. On the cross-section, this area shows a fragmented structure analogous to BA. However, the surface images (

Figure 3-17a and Figure 3-19a) appear markedly different, appearing less homogeneous and with slightly different colour. As it is mainly composed of DFL, this part is also thought to provide good lubrication. The profile shows that this region is relatively smooth compared to BB.

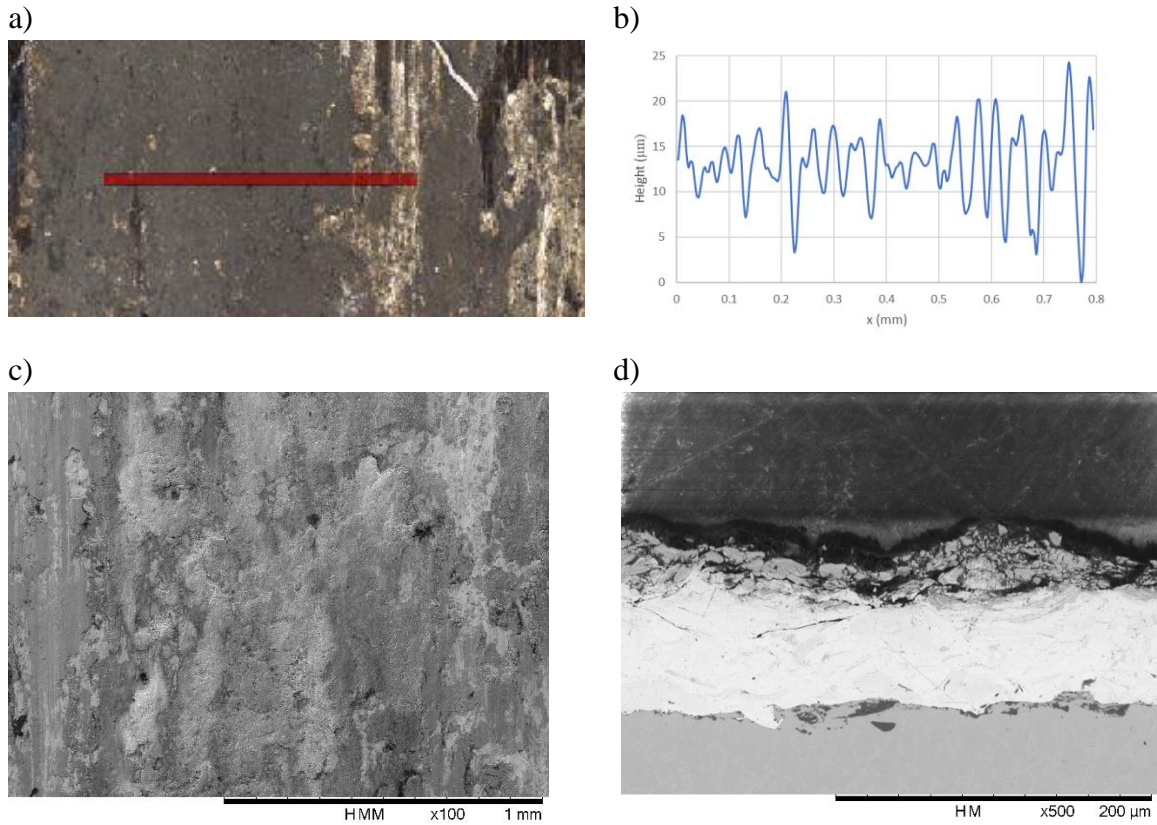


Figure 3-19: BC a) surface, b) surface profile, c) SEM d) cross section

Finally, BD is shown in Figure 3-20. The thinner bond coat residual thickness is observed here, with evidence of interlayer cracking. Adhesion of the surface has occurred here following DFL depletion, with subsequent bond coat detachment. Clearly, this was the worst lubricated area.

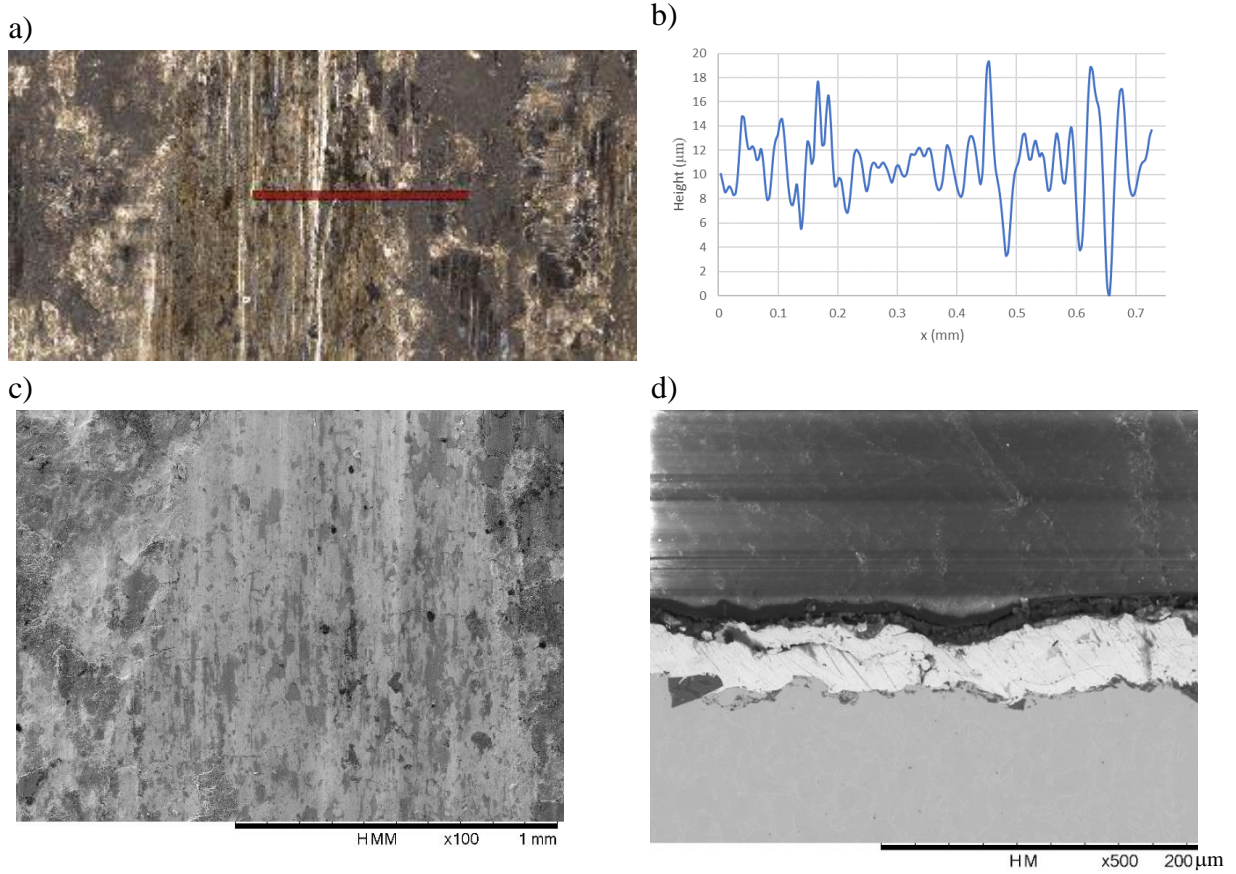


Figure 3-20: BD a) surface, b) surface profile, c) SEM d) cross section

The inspection of the blade also allowed further observations to be made. Firstly, the out-of-contact area in the Edge of Blade (EOB) zone presented extended signs of cracks as shown in Figure 3-21 on the unworn coating.

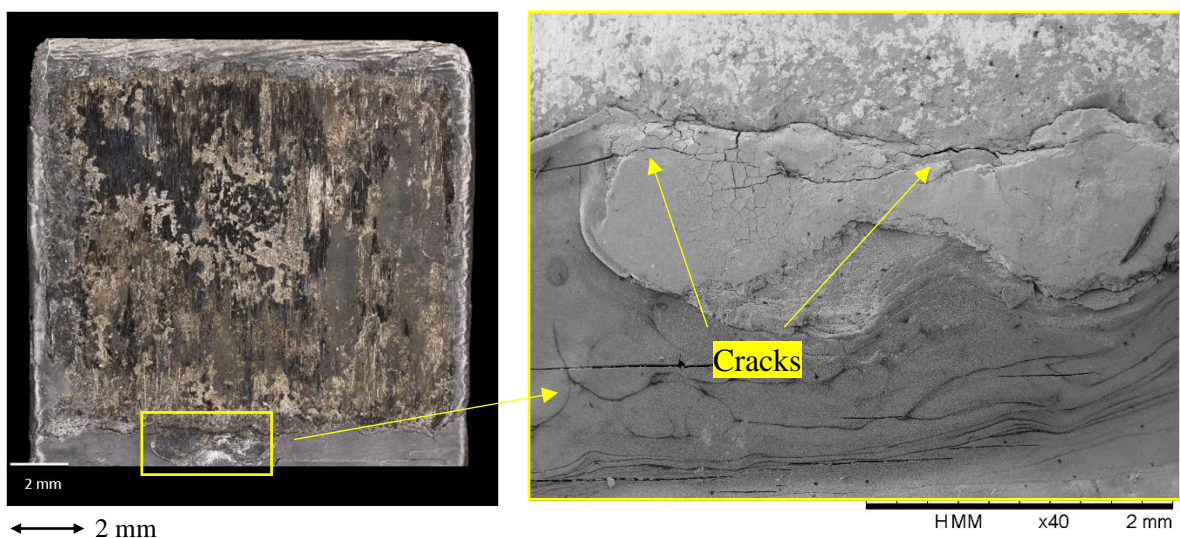


Figure 3-21: SEM micrograph of the out-of-contact area near the EOB

Assessing the cross-section at the contact edges also aided the analysis. As shown in Figure 3-22, the side edges of the blade, fewer DFL layers than expected (first layer and 3 re-lubrications) can be observed. Further, in this area the poor adhesion of the relubrication layers is evident. An inconsistency with regards of the coating thickness is also noticeable.

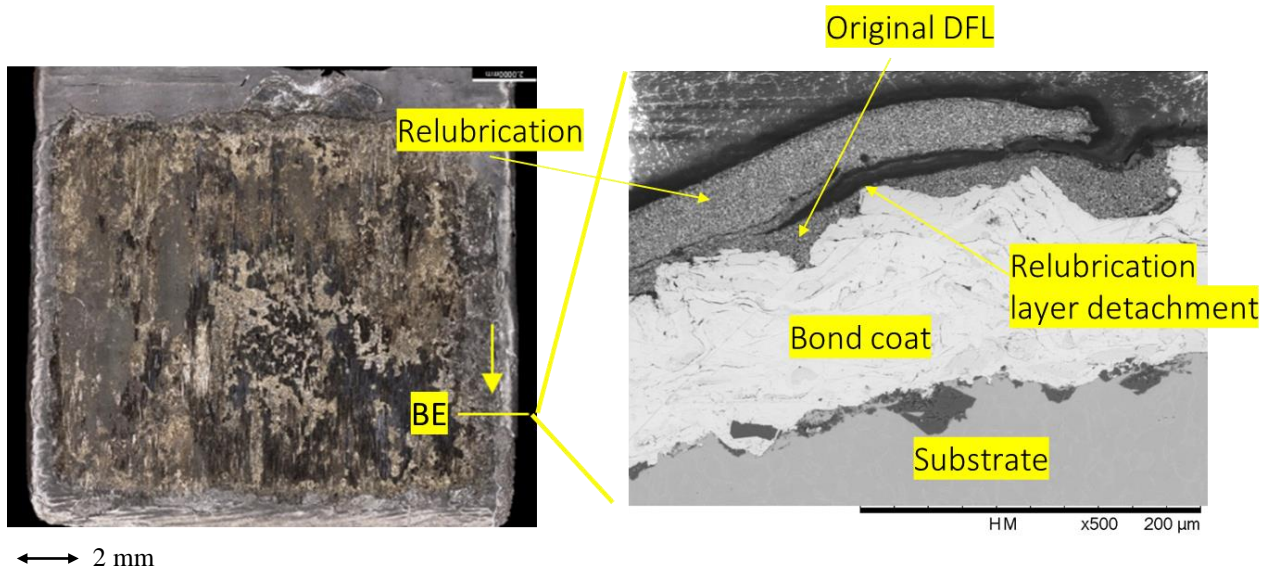


Figure 3-22: Cross-section from contact edges

Figure 3-23 shows how the surface profiles across the whole blade which shows how the roughness changes between each of the different areas clearly. The profiles support the previous findings that the black layer is smoother compared to other areas and that BD has the thinnest bond coat.

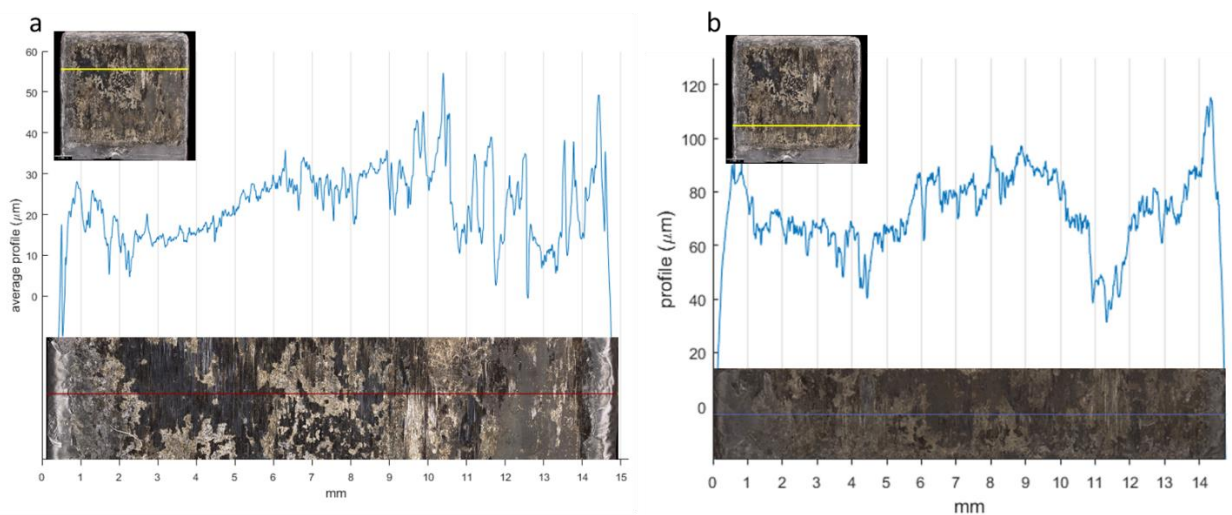


Figure 3-23: Surface profiles across whole blade a) BE b) BF, note change in y-axis scale



### 3.3.4 Disc Specimen

As for the blade specimen, three areas were identified that were of interest due to the appearance of the disc sample. A cross section was also taken and two points on the cross section analysed. The location of these areas and points is shown in Figure 3-24.

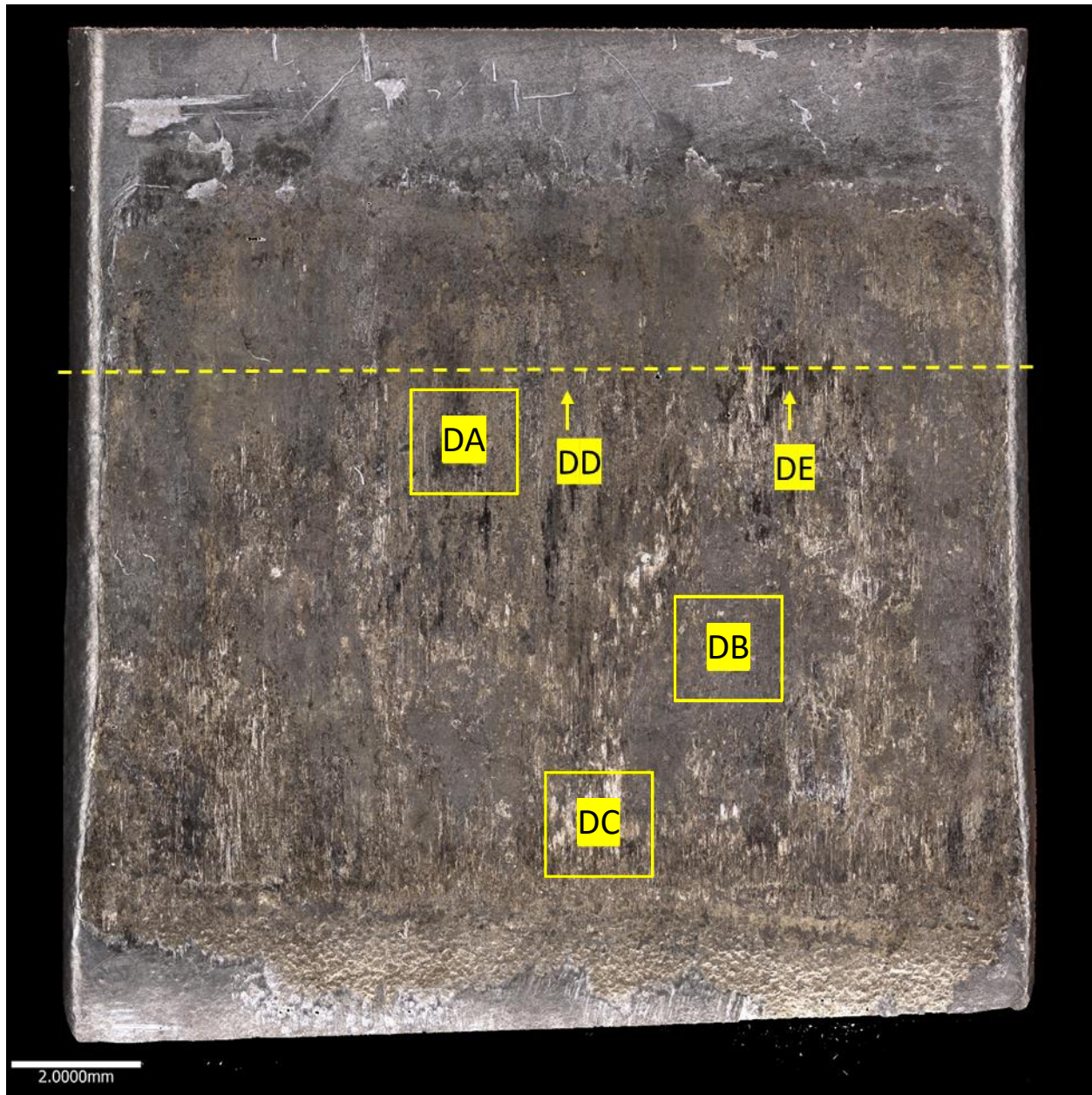


Figure 3-24: Overview of disc specimen

Figure 3-25 shows the SEM images of the surface as well as the surface profile DA. The areas chosen have similar appearance to areas on the blade and therefore the conclusions drawn for the blade are also true for the disc. In DA some small craters and platelets can be seen. This is similar to BA (

Figure 3-17). The surface profile shows that the areas that appear black are smoother than the other areas, as seen on the blade surface profiles.

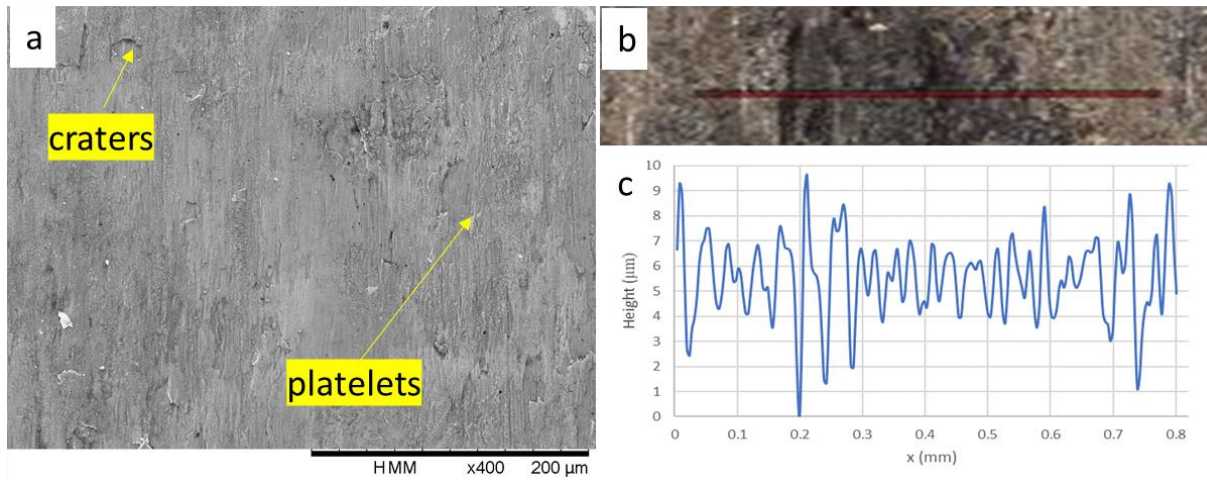


Figure 3-25: DA a) SEM, b) surface c) surface profile

DB looks similar in appearance via microscope and SEM to BC (Figure 3-19). There are large amounts of DFL still present at the surface.

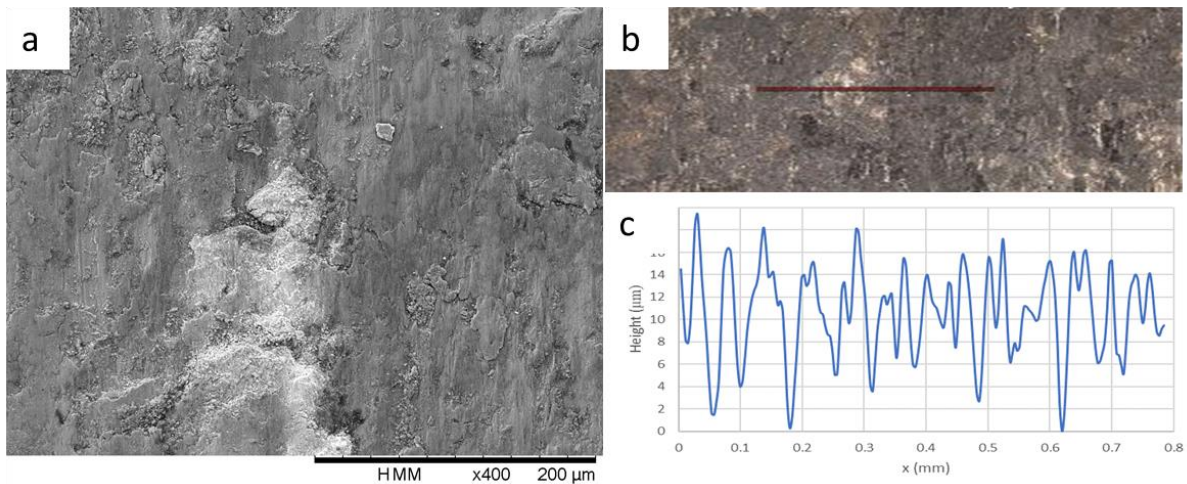


Figure 3-26: DB a) SEM, b) surface c) surface profile

DC here (Figure 3-27) has a similar appearance to BB (Figure 3-18). However, the DFL layer on BB has broken down whereas there is still some DFL layer present in DC. This is shown by the differences in SEM images between the two areas and the fact that the gold appearance on the micrograph image (

Figure 3-24) is not as bright or extensive as in Figure 3-18a. It is important to note that there is no bond coat on the disc and therefore once the DFL breaks down completely the surface appearance would be different to the blade as it will be the alloy that is exposed rather than the bond coat. However, there is also likely to be some material transfer from the blade (especially

as the bond coat leads to a high CoF) to the disc, so some bond coat could end up present on the disc. How much this occurs would require further analysis.

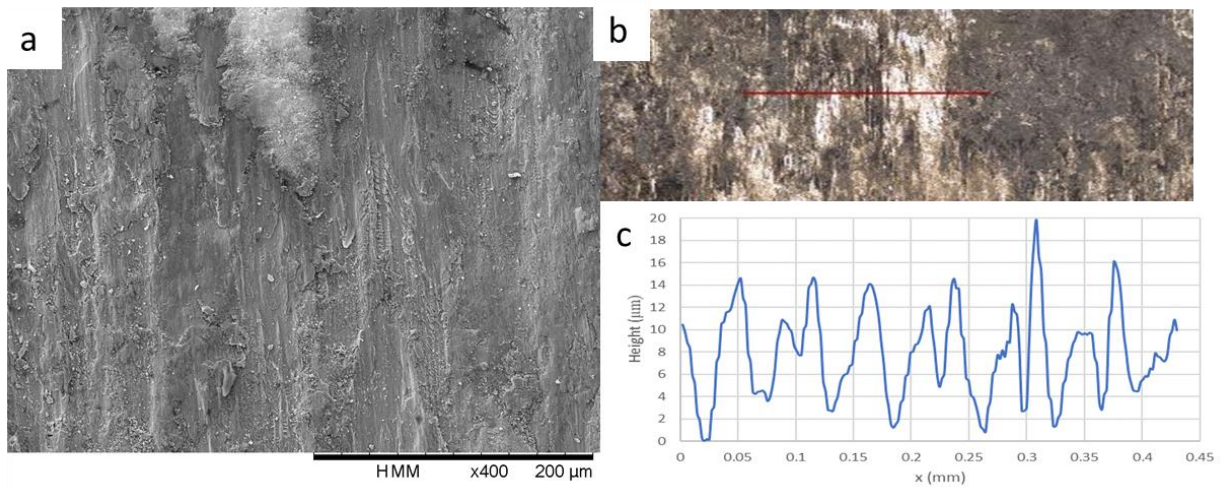


Figure 3-27: DC a) SEM, b) surface c) surface profile

The cross-section of the disc is shown in Figure 3-28. Both points on the cross section show significant reduction in the DFL layer. The locations of the cross sections are shown on

Figure 3-24. At point DD the DFL layers is still present, but not as a consistent layer. It has broken down and a black layer has formed at the surface with some debris trapped within the black layer. Whether this material is from the disc or material transfer from the blade would require further analysis. There is also cracking and more significant surface damage in the alloy than at Point DE. At point DE the DFL layer is present but is very thin (only a few microns thick) and the black layer is present here, but is thinner than at point DD.

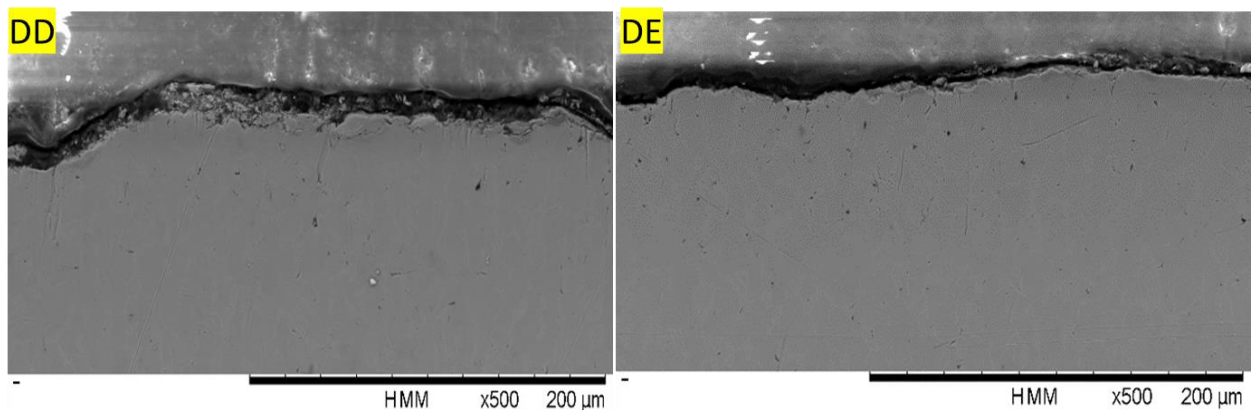


Figure 3-28: Cross sections of disc DD and DE

### 3.4 Discussion

#### 3.4.1 Trent800

The Trent800 blade root analysis showed two main tribo-mechanisms of the as-applied coating structure due to in-service contact, which were classified as follows: mild plastic flow of DFL

(Area 2) and sintering into a black layer (Area 3). Upon visual inspection, these were found to be prevalent in low and high pressure areas respectively. Although both features could be found across the whole blade length, the simplified low/high average pressure distribution (Figure 3-4) used only illustrates the pressure-behaviour patterns to a certain extent. In fact, it offers a broad indication of the stress concentration regions in the axial direction (shear key location, intrados and intrados extremes), but it neglects the gradient along the radial direction and the stress concentrations at the contact edges (EOB). These contact edges are also subjected to contact stress intensification and were found to have a large layer coverage. The idea that high pressure promotes the layer formation is therefore strengthened, although proving a direct cause-effect from the analysis is challenging.

Nevertheless, the mechanism observed is in line with the MoS<sub>2</sub> behaviour previously reported by Fusaro et al. [17], [16]. Their study reported that DFL particles compacted and sintered under high pressure into a reflective back layer, however, no pressure value was proposed. The influence of pressure needs to be better addressed, to study whether the behaviour transitions gradually or at a specific pressure threshold. Assessing the CoF changes due to coating structure modifications would also be of interest. As Singer et al. have reported that MoS<sub>2</sub> friction decreases at higher pressure [81], it is possible that the layer formation might be associated with a CoF drop; this is a point of future study.

Overall, the blade is deemed to be in a functional lubrication state as the whole contacting surface was covered by DFL and no signs of metallic exposure were observed. A significant residual life is also expected. In Area 2, the cross-section showed the thinnest residual layer on the bond coat peaks, however, a large reservoir of DFL was still retained in the valleys. In Area 3, even though the DFL layer seemed to detach easily in the form of platelets (in line with the black debris found on the component), the surface underneath was still covered by an Area 2 like layer.

### **3.4.2 Biaxial Specimens**

The inspection of the biaxial specimens was performed upon test termination due to assembly failure. As the surface cracks in the out-of-contact area, the failure occurred due to fracture of the blade root in proximity of the EOB. This is a recurrent failure mode reported for both the biaxial testing and the fan blades dovetails [10], [82]. Failure of the blade dovetail occurred due to fracture of the substrate, again this is typical. It is therefore clear that the inspected surface was not lubricated adequately.

The biaxial blade sample also showed directionality of the damage along the major loading direction and showed a mix of different areas. It has been proposed that these areas included features similar to the root surface (Area BA and Area BC), where the coating has undergone changes due to plastic flow and mechanical compression. Bond coat exposure (Area BB) and bond coat detachment (Area BD) occurred in other areas. These features likely represent the damage progression of the other regions (and therefore of the mechanism observed in the root),

where DFL starvation led to high friction and adhesive behavior. Similar distinct areas were also identified on the disc.

Although some parts of the blade specimen were deemed to be providing good lubrication, the high CoF and adhesive spots have likely brought the contact to transition from gross-sliding to mixed slip behaviour and led to fretting fatigue failure of the assembly. As no Ti-6Al-4V exposure was detected in the blade, the bond coat coming into contact due to DFL depletion clearly provides a surface protection effect sufficient to prevent full substrate exposure. The role of contact pressure distribution is evident on the biaxial analysis too. As it can be observed on the topographical map in Figure 3-29, the most severe wear took place in the EOB area, where the contact stress is known to be the highest. This strengthens the motivation to investigate pressure effects experimentally.

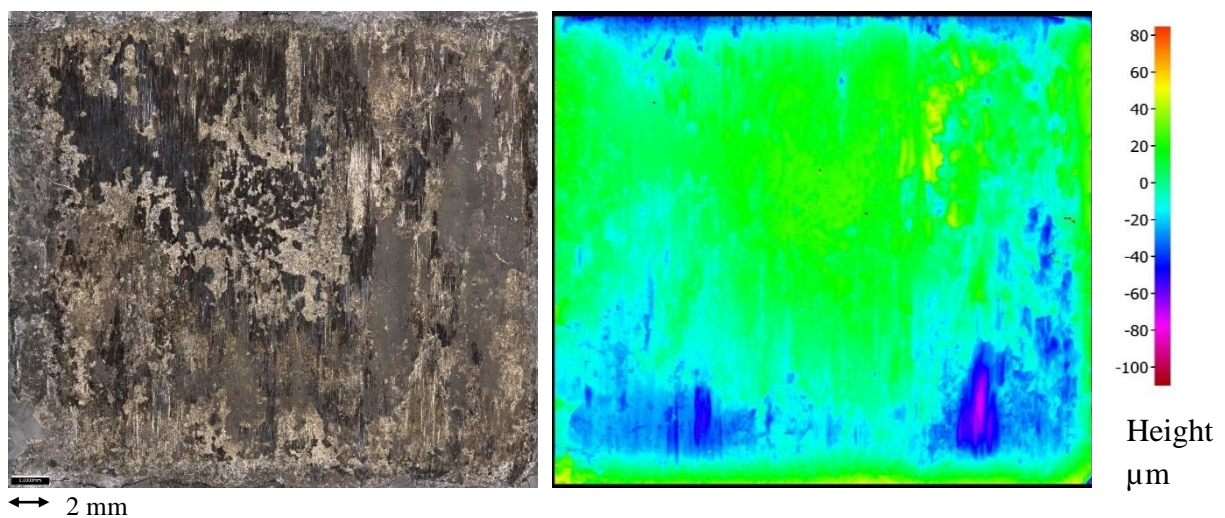


Figure 3-29: Biaxial blade sample (left) and its profile map (right)

Throughout the test, the blade has been re-lubricated three times. Understanding the interaction between the different DFL layers was challenging, given that the inspection took place only after the test termination. At this point, the residual coating layer was observed to have a fragmented structure (Area BA), indicating that the layer might have formed from a combination of debris removed from the oldest layer, embedded into new DFL particles.

Nevertheless, the signs of the detachment at the contact edges (

Figure 3-22) suggests that weak DFL interlayer adherence might be an issue. There is, however, a possibility that such detachment has resulted during the specimen sectioning and preparation process, although every effort has been made to rule this out. The inconsistent relubrication layer thickness has also been pointed out as a noteworthy matter.

### 3.4.3 Overall validity of the study

The investigation undertaken has given insight into the mechanical behaviour of the coating system and its failure mode. Familiarisation with the surface transformation produced in service will aid the understanding of the tests undertaken in the rest of this work, allowing an assessment of the extent of the behaviour that can be reproduced experimentally. However, it

must be highlighted that the work was based on the visual inspection of the components. Given the qualitative nature of the area categorisation and selection the images representative of each area, the process was subjective and dependent on the best judgment of the author. The process to estimate the cross-section locations in the surface images may be also be subjected to inaccuracies. Further, an uncomplete loading history of the Trent800 blade, the impossibility to observe the surfaces at intermediate stages did not allow for a comprehensive analysis.

However, the pressure has been proved to be a key parameter in driving the behavior of the system as there were evident spatial patterns with the tribo-changes of the coating. The influence of pressure is therefore investigated experimentally in the rest of the thesis, with the main objective is to assess the CoF of the various surface features (particularly the sintered layer) and the life capabilities.

### 3.5 Summary

The investigation carried out in this chapter can be summarised as follows:

1. A Trent800 blade root and a set of samples tested with the biaxial test rig were examined. The analysis aimed to investigate the RR coating system tribological changes due to service or simulated representative conditions.
2. Three different areas of the Trent root were compared: out-of-contact, low- and high-pressure. DFL particles sintered on the high-pressure areas, forming a MoS<sub>2</sub> rich layer. The layer showed a cracked platelet structure as a result of embrittlement and oxidation. Mild extrusion and compaction were observed in the low-stress areas, where the thinnest DFL residual thickness was measured. Overall, the root was deemed to be appropriately lubricated.
3. As the biaxial sample failed and high friction was reported at this point [39], the breakdown of the DFL layer and exposure of bond coat is thus linked with such a high friction event.
4. The largest wear volumes were observed in the highest-stress EoB region. Other considerations on thickness and adherence of relubrication layers have also been made.
5. The analysis suggested that the contact pressure is a key factor in driving the coating behavior. Therefore, this will be a key parameter under investigation in following experimental chapters.

## 4 Ball-on-flat tests

The forensic investigation of the ex-service fan blade has shown dissimilarities in the coating behaviour across the root surface, which were deemed to be related to the contact pressure. A substantial portion of areas subjected to the highest stresses were observed to be covered by MoS<sub>2</sub> particles compacted into a black-coloured, reflective layer. As previously discussed, a similar mechanism was observed by Fusaro et al. [64], [65] on a MoS<sub>2</sub> coated steel substrate, using a pin-on-disc sliding wear apparatus. A later study performed by Singer et al. [81] on a sputtered-deposited MoS<sub>2</sub> in dry air found that contact pressure affects friction, according to  $CoF \propto L^{-1/3}$  where  $L$  denotes the normal load. Though these findings provide insight into the coating behaviour, it is important to note that they might not apply to the fan blade root application as they were carried out under tribological conditions not representative of the application (e.g. different substrate, environmental conditions, and relative movement between the specimens). As pointed out in the literature review chapter, the role of many parameters such as substrate properties and contact conditions can affect the behaviour significantly.

The most recent investigation related to the fan blade contact was performed by Barman et al. [83] at the University of Nottingham for Rolls-Royce. Their tests were carried out fretting a PL237 R2 coated Ti-6Al-4V specimen on a cylinder-on-flat configuration at 2.5 Hz with a 300 µm displacement amplitude. They characterised the lubrication mechanism (Figure 4-1) into three main phases. A running-in phase (Stage I) where the CoF increases very sharply at the beginning of the test to then decrease slightly. A second phase (Stage II), consisting of a sudden drop of CoF at the beginning (to 50% of that observed during running-in phase) followed by a gradual increase in CoF. Finally, a third phase was observed, with a sharp rise in the CoF, where the coating was deemed to have failed. Erratic behaviour in CoF is observed during the onset of the third phase due to titanium exposure within the contact. As this investigation is closely related to the work undertaken in this thesis, it will be largely referred to hereafter.



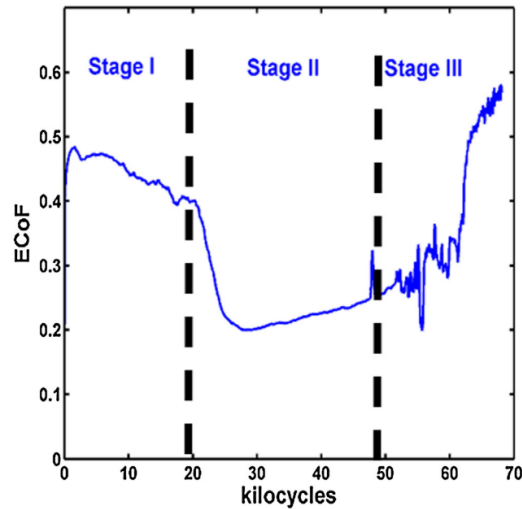


Figure 4-1: CoF evolution of self-mated PL237 R2 coated Ti-6Al-4V specimens under fretting conditions observed by Barman et al. at the University of Nottingham [83]. The graph shows three different stages of the CoF evolution

The aim of this chapter is to extend the study conducted by Barman et al. to the case when the bond coat METCO58 layer is applied on one of the two surfaces, to fully replicate the coating architecture currently used on Rolls-Royce fan blades.

The main objective was to explore the influence of contact pressure, aiming to reproduce the mechanism observed in the Trent fan blade root surface. Furthermore, the influence of the surface topography of the samples is explored. The motivation of this originates from the pre-test analysis of the test samples, which highlighted irregular distribution of asperities height and concentration within each sample as well as differences among samples. The study entails repeating tests under the same conditions and the analysis of the results includes the estimation of the contact pressure at macro-asperity level by using a bespoke contact model.

Additionally, tests were also performed on a specimen with no bond coat applied. This allowed further investigation of the surface topography effects as the bond coat was observed to increase the surface waviness. Furthermore, this test set-up offered a comparison with the work performed by Barman et al.

A coupon scale ball-on-flat geometry was chosen for the experiments. This contact configuration is largely adopted in tribological testing as it provides an economically convenient solution, while overcoming the problem of specimen misalignments (typical of other contact geometries) and allowing to achieve high contact pressure with limited normal loads. A post-test inspection of the samples is performed with the SEM, along with the assessment of the DFL lubrication performance. Finally, a life estimation of the component is presented, based on observation of the evolution of the CoF during the tests.

## 4.1 Tests samples

### 4.1.1 Geometry and coating procedure

A sphere and a plate specimen were required for each test as represented in Figure 4-2.

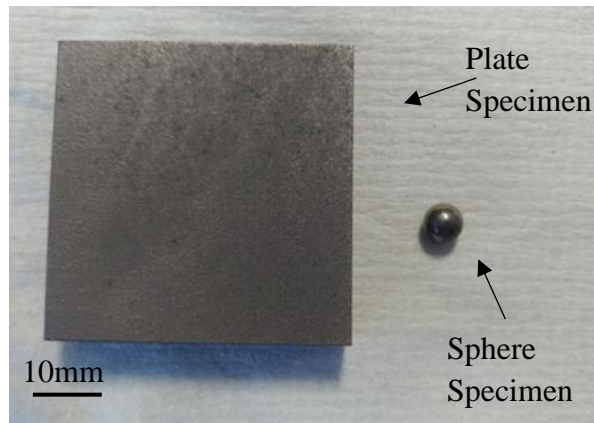


Figure 4-2: Plate and sphere specimens.

The plate specimens were manufactured from a 10 mm grade 5 Ti-6Al-4V block whose Young's modulus and Poisson's ratio are  $E = 110$  GPa and  $\nu = 0.315$  respectively. The block was manufactured using EDM wire erosion into 45 x 45 mm coupons: suitable dimensions for the rig clamping fixture. The surface was coated, like the fan blade root, with a plasma sprayed layer of METCO58 and a PL237 R2 DFL top coat layer, following a shot peening and grit blasting substrate preparation process. For more details on the coating procedure the readers are referred to Section 2.1.2. A cross-section of the flat specimen is shown in Figure 4-3.

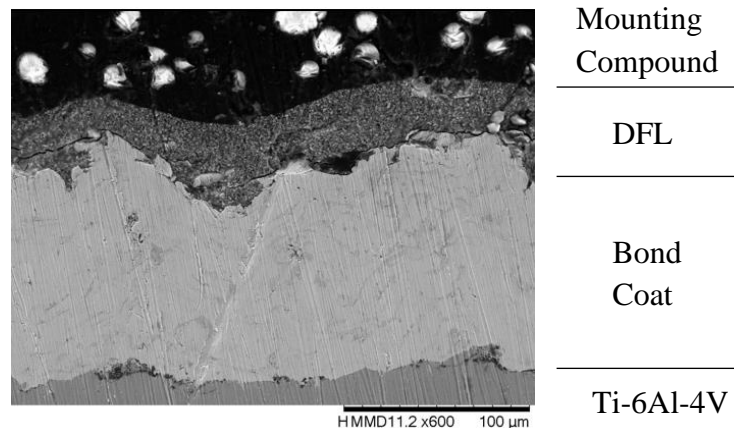


Figure 4-3: SEM image of the plate specimen cross-section. The image shows the different layers (from bottom to top): Ti-6Al-4V, Bond Coat METCO58, DFL PL237 R2, and the mounting compound

The spheres used were 6.35 mm (0.25") in diameter, a commercial dimension compatible with the rig ball specimen holder. The material was grade 5 Ti-6Al-4V. The surface grit blasted and shot peened, and then coated with PL237 R2.

Two batches of specimens were used, manufactured separately. Albeit they were manufactured to the same specifications, the two batches were found to have dissimilarities in surface topography as shown in the following section.

#### 4.1.2 Sample topography

The topography of the test samples was quantified to assess its effects on the contact geometry and on the contact pressure at the interface. In fact, all real surfaces present a certain degree of irregularity, which causes the real area over which two bodies are contacting to be much smaller than the nominal one. The load is supported by few asperities, and the local contact pressure at these asperities being much higher. The surfaces can be seen as composed of a number of length scales of roughness superimposed on top of each other [84], with the irregularities at a microscale typically being referred to as micro-asperities (roughness) and those at larger scale (waviness) being referred to as macro-asperities.

The surface of the flat specimens was measured with an Alicona optical interferometer profilometer, using a 5x magnification lens. They showed a wavy profile with macro-asperities of irregular size and concentration. A surface profile measured is shown in Figure 4-4, as an example.

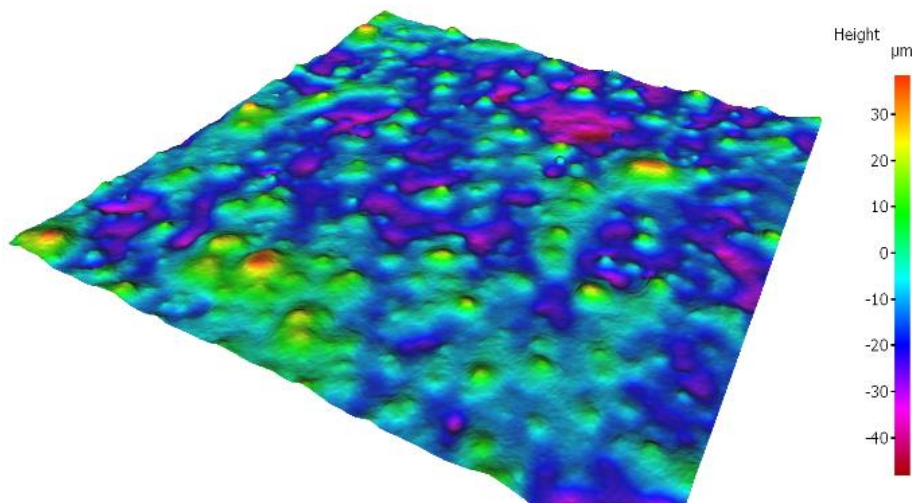


Figure 4-4: Surface of a plate sample, showing irregular topography.

The data acquired was processed with the MeasureSuite Alicona software to quantify surface parameters. The Surface Profile tool of the MeasureSuite allows the user to select a single-line profile. This, referred to as the primary profile, can be decomposed into a waviness profile and a roughness profile. This allows quantification of the surface irregularities at a different scale. Figure 4-5 shows an example of such decomposition, where the blue line shows the different profiles.

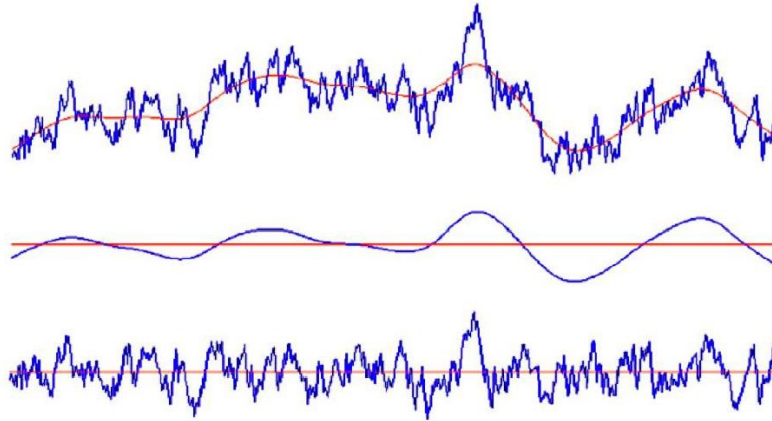


Figure 4-5: Decomposition of primary profile (top) into waviness (centre) and roughness (bottom)

The irregularities are quantified with the root mean square roughness ( $Rq$  for roughness and  $Wq$  for waviness) defined as below:

$$Rq = \sqrt{\frac{1}{n} \sum_1^n y_{r,i}^2} \quad Wq = \sqrt{\frac{1}{n} \sum_1^n y_{w,i}^2}$$

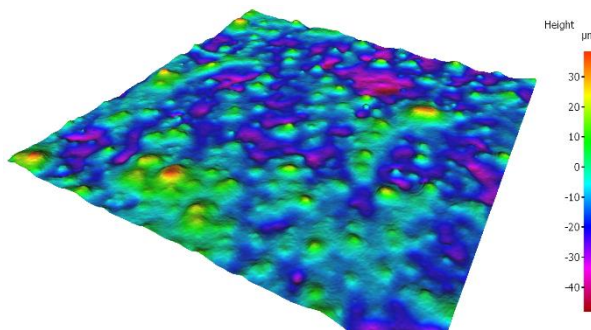
where  $n$  is the number of data points composing the profile, and  $y_{r,i}$  and  $y_{w,i}$  are the deviation of the  $i$  –  $th$  data point from the mean roughness and waviness profile respectively. The measurements were performed on four samples (including the sample in Figure 4-4) sourced from the two batches provided. The results are presented in Table 5 and the respective topography maps can be found in Figure 4-6.

	Roughness $Rq$ ( $\mu\text{m}$ )	Waviness $Wq$ ( $\mu\text{m}$ )
1 <sup>st</sup> Batch – Specimen 1	2.40	10.18
1 <sup>st</sup> Batch – Specimen 2	3.03	11.24
2 <sup>nd</sup> Batch – Specimen 1	3.21	4.72
2 <sup>nd</sup> Batch – Specimen 2	2.44	5.69

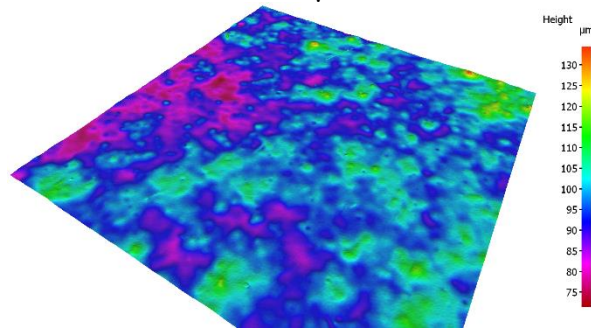
Table 5: Roughness and Waviness measurements of flat samples

The values indicate that the samples have similar roughness (around 3  $\mu\text{m}$ ), whereas the waviness tends to be twice as large in the 1<sup>st</sup> batch. This must be accounted for when analysing the results.

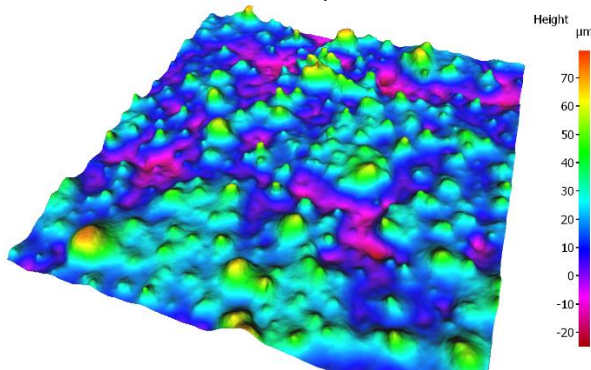
1<sup>st</sup> Batch – Specimen 1,  $Rq = 2.40 \mu\text{m}$   $Wq = 10.18 \mu\text{m}$



2<sup>nd</sup> Batch – Specimen 1,  $Rq = 3.21 \mu\text{m}$   $Wq = 4.72 \mu\text{m}$



1<sup>st</sup> Batch – Specimen 2,  $Rq = 3.03 \mu\text{m}$   $Wq = 11.24 \mu\text{m}$



2<sup>nd</sup> Batch – Specimen 2,  $Rq = 2.44 \mu\text{m}$   $Wq = 5.69 \mu\text{m}$

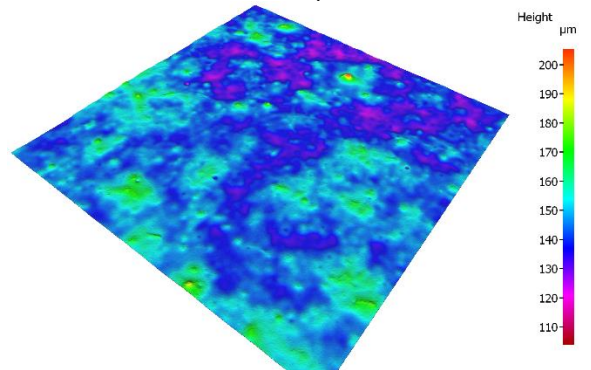


Figure 4-6: Topography maps of plate specimens, with respective  $Rq$  and  $Wq$ . It can be noted that the samples sourced from the 1<sup>st</sup> batch (left) present a wavier surface of the 2<sup>nd</sup> batch (right)

## 4.2 Methodology

### 4.2.1 Test equipment and procedure

The ball on flat reciprocating tests were performed on either a Bruker CETR Universal Mechanical Tester (UMT) as shown in Figure 4-7 or a UMT-3 device, depending on availability. Both test platforms can be used to achieve the same test set-up by fitting the appropriate load cell, fixtures and reciprocating stage.

A ball specimen is connected through a ball holder fixture to the upper part of the machine, the carriage, which can move along the vertical direction ( $z$ ), whereas the plate specimen is connected to the lower drive reciprocating stage. The test begins by lowering down the carriage until the two specimens are brought into contact at a desired set-point load measured by a load cell. Then, the lower drive reciprocates the plate specimen along the  $x$  direction whilst a constant normal load is maintained. The test is terminated at a set number of reciprocating cycles and the load is then released. The normal load ( $F_z$ ), the tangential load ( $F_x$ ), the vertical position of the carriage ( $z$ ) and the linear drive position ( $x$ ) are recorded throughout the duration of the test.

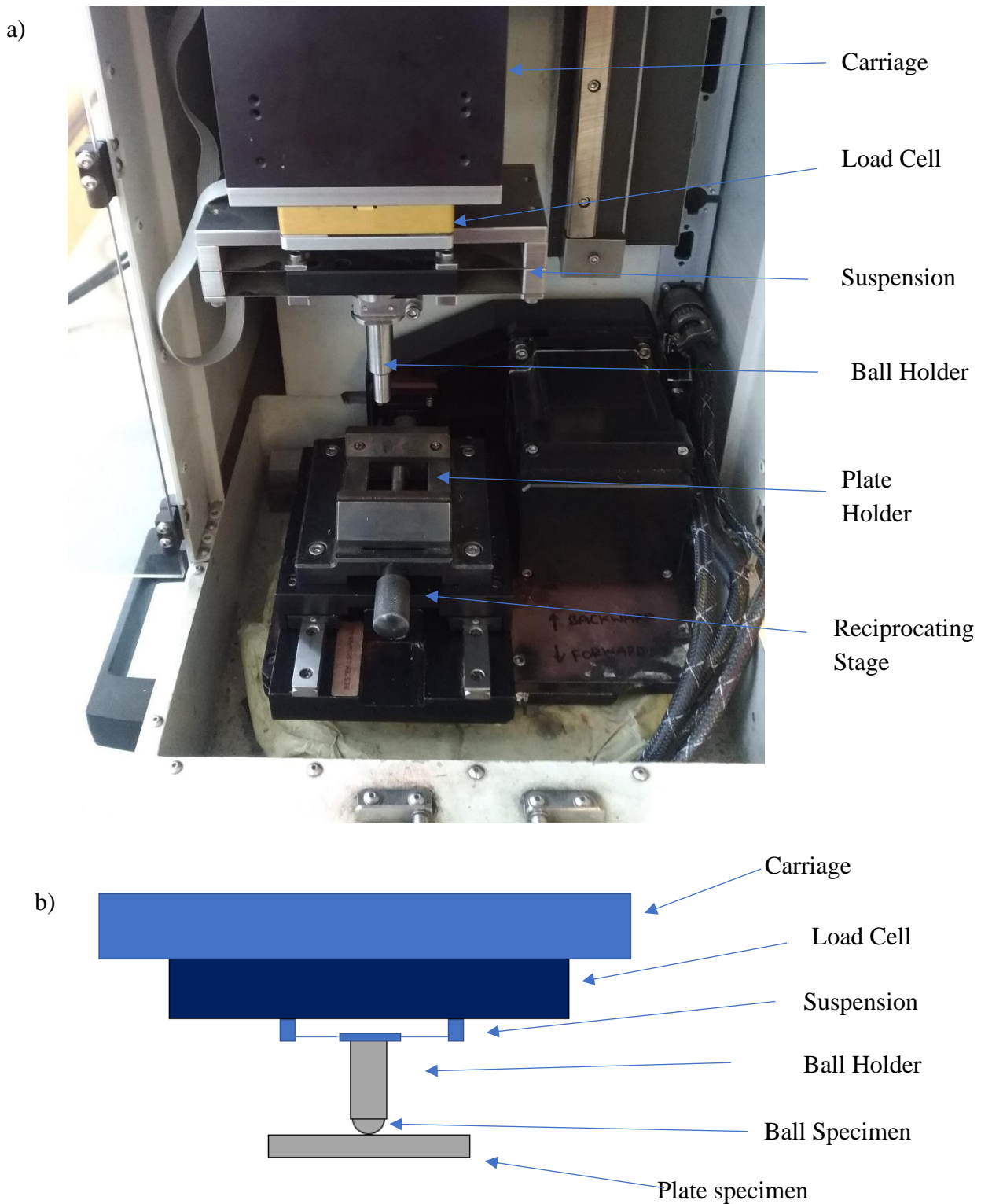


Figure 4-7: CETR UMT device, fit with reciprocating stage, load cell and ball holder. a) Front view picture, b) Side view schematics.

To ensure accuracy and reliability in estimating the coefficient of friction during the reciprocating phase, the normal load fluctuation caused by surface irregularities and positioning of the plate specimen should be maintained within the strictest tolerance possible.

The UMT features a control system that processes the load cell signal in real-time and adjusts the vertical position of the carriage. Although this system limits the load fluctuations, its response was observed not to be satisfactory for low contacting loads. A suspension can be placed in between the load cell and the specimen holder to compensate for the surface irregularities by deforming elastically, and therefore, improving the stability of the normal load control. Figure 4-8 shows that the normal load fluctuation is reduced when the suspension is used, especially at low load.

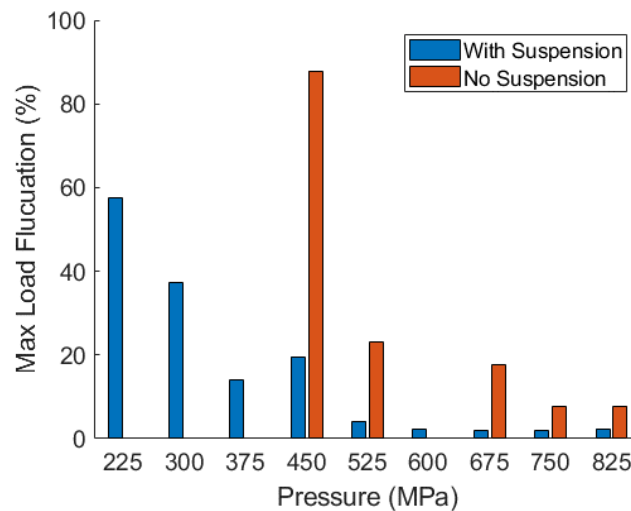


Figure 4-8: Maximum normal load fluctuation (as percentage of normal load) against the equivalent Hertzian contact pressure for the ball-on-flat samples used in these tests

The introduction of the suspension in the system is beneficial for the vertical load control, however, it can be problematic due to a lower stiffness of the rig along the reciprocating movement direction, which may result in a large deviation between the slip amplitude of the contact and the displacement measured. In fact, the displacement is measured by the LVDT located on the lower drive reciprocating stage, to which the plate specimen is connected. At high frictional loads, the two specimens stick at the contact interface, causing both the bodies to be displaced jointly by the lower drive as schematically illustrated in Figure 4-9. In this situation, the friction force required to initiate motion is greater than the forced applied by the linear drive.

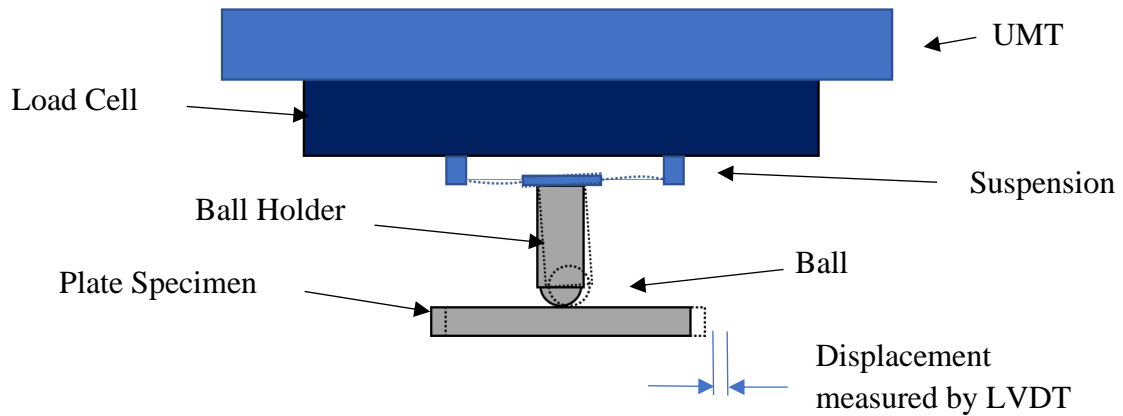


Figure 4-9: Simplified schematics of the UMT set-up (side view). The dotted line shows the system after some displacement is imposed to the plate specimen by the lower drive (not represented)

The force-displacement output can be monitored by plotting the tangential load against the displacement for a given cycle, in the form of fretting loops. For an ideal perfectly rigid test rig, the displacement measured is equal to the slip amplitude in the contact and the fretting loop has a squared shape. In reality, the loop is in the form presented in Figure 4-10, where  $\Delta^*$  is the imposed displacement amplitude, the contact slip amplitude is indicated by  $\delta^*$ , and the slope of the sides of the loop ( $S$ ) is proportional to the stiffness of the rig.

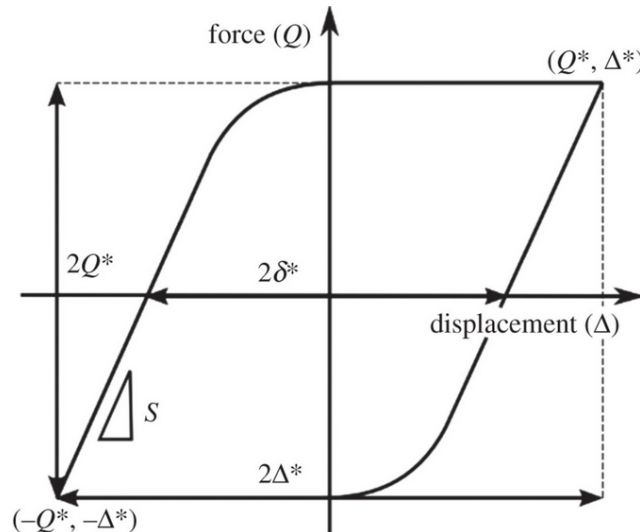


Figure 4-10: Example of real fretting loop [85]. The slope of the sides is proportional to the test rig stiffness

As the normal load is increased the friction force required to initiate the motion increases too. As a result, the slip amplitude decreases further, and the use of suspension is no longer convenient due to its marginal effect on the vertical load control. For this reason, the suspension was used only to perform the lower pressure tests.



#### 4.2.2 Test parameters

The displacement amplitude and the reciprocating frequency were set to 300  $\mu\text{m}$  and 2.5 Hz respectively. These values are commonly used in the literature as representative of high cycle fatigue loading of the engine's fan blade contact [70], [83]. The first set of tests aimed to analyse the effect of contact pressure. The tests were performed on samples from the smoother batch to limit the influence of surface irregularity on the results. With regards of the contact pressure, a Rolls-Royce FEM model of the blade/disc interface estimates a contacting pressure ranging from 150 to 800 MPa, and to cover the whole range the following pressure values were chosen: 150, 225, 300, 375, 450, 525, 600, 675, 750, 825 MPa [12]. The theoretical contact radius and normal load to be applied to achieve the above pressures on a ball-on-flat configuration were calculated using Hertz elastic theory [86] which yielded the values in the table below (Table 6).

Average Contact Pressure [MPa]	Load [N]	Radius of Contact (mm)
150	0.159	0.0184
225	0.537	0.0276
300	0.537	0.0276
375	2.487	0.0459
450	4.297	0.0551
525	6.824	0.0643
600	10.186	0.0735
675	14.504	0.0827
750	19.895	0.0919
825	26.481	0.1011

Table 6: Average Hertzian Contact Pressure (MPa), normal load (N), and Radius of Contact (mm)

The calculation was made by neglecting the mechanical properties of the coating layer, to aid comparison with Barman et al.'s work. The tests duration was initially set to perform 70,000 reciprocating cycles, as failure typically occurs before then [83]. Based on the results analysis of these tests, a longer test was also performed to further assess the failure mechanism.

The study of the effect of contact pressure is followed by the assessment of the impact of the surface topography. This consisted of performing four tests at the same conditions (450 MPa, 70,000 cycles), selecting 2 random samples from each batch. It can be observed that the contact radii calculated in Table 6 (whose value ranged from 10 to 100  $\mu\text{m}$ ) are within the same order of magnitude as the diameter of the asperities measured in the pre-test analysis of the samples (around 10 to 50  $\mu\text{m}$ ). Therefore, this suggests that a limited number of asperities are involved in the contact, and it will be investigated later in the post-test analysis of the samples. Finally, tests with no bond coat are performed at 300, 450, 600 and 750 MPa for comparison.

### 4.2.3 Data analysis

The data recorded by the UMT software was processed using MATLAB®. The vertical load signal was analysed to ensure that good load control was achieved. The maximum tangential force ( $Q^*$ ) was extracted for each cycle from the tangential force raw data ( $F_x$ ). As the ratio  $Q^*/P$  (with  $P$  being the nominal overall normal load) corresponds to the coefficient of friction if a gross-slip regime is achieved [71], it is important to analyse the friction data and the fretting loop simultaneously. However, the loops were observed to be distorted into an unusual twisted shape at certain points of the tests as in the example in Figure 4-11.

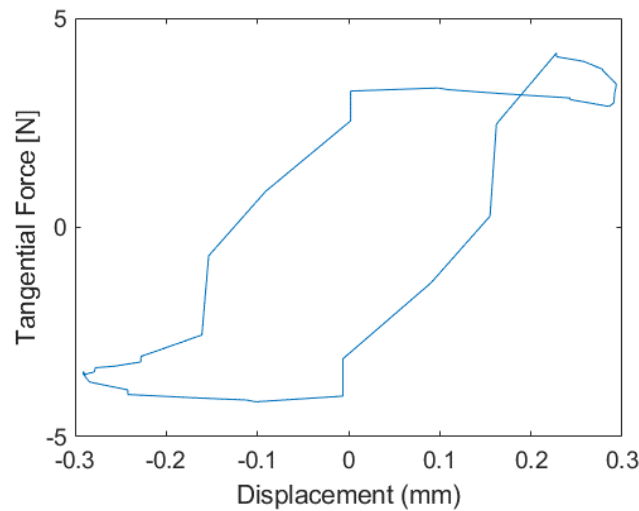


Figure 4-11: Example of distorted fretting loop. The loop does not show the typical shape represented in the example in Figure 4-10

The change was observed to be due to asynchronous recording of the force signal with respect to the recorded position, as shown in Figure 4-12. Theoretically, the tangential force should invert its sign right after the motion is reverted at the extremes of the reciprocating stroke (maximum and minimum displacement position). At those points, the sliding velocity reaches zero and inverts its direction, causing the direction of the friction force that must be overcome to resume motion to invert too. Furthermore, the direction of the force should always be opposite to the sliding direction (the opposite scenario would imply that energy is being produced in the contact, rather than being dissipated into heat).

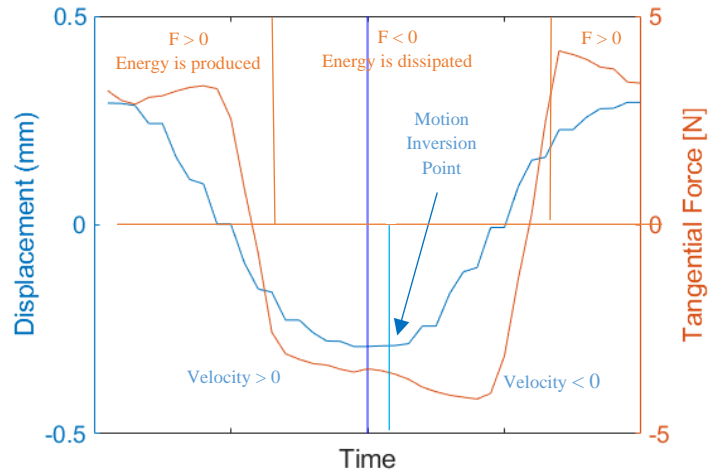


Figure 4-12: Time domain data of the twisted loop of Figure 4-11

Being an unrealistic scenario, the shift is deemed to be due to anomalous functioning of the software (asynchronous timing between the force and displacement recordings). This is supported by the fact that anomalies were observed only in the tests performed in one of the two UMT platforms used. The signals were synchronised to produce properly shaped fretting loop plots as in Figure 4-13. The synchronisation was thus performed by indexing the minimum force of a cycle and making it coincident to the maximum displacement amplitude.

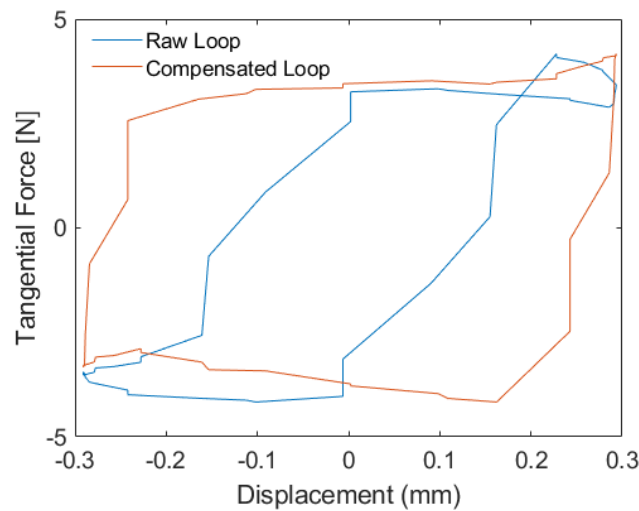


Figure 4-13: Fretting loop before and after compensation.

## 4.3 Results

### 4.3.1 Influence of pressure on surface morphology

The results of the influence of pressure reported here include the SEM images of the wear scar on the plate specimens and the coefficient of friction ( $Q^*/P$ ) throughout the duration of each test. The images were taken with a Hitachi TM3030 SEM using a mixed BSE/SE beam at 15

kV voltage. A micrograph at 50x magnification of the surface tested at intermediate pressure (525 MPa) is reported in Figure 4-14 to describe the post-test surface appearance. MoS<sub>2</sub> particles detached due to shearing of the coating were partly extruded and compacted into a film onto the wear track and partly displaced out of the contact in the form of loose debris. Observation of the wear track at higher magnification of 500x (Figure 4-15) showed an irregular shaped MoS<sub>2</sub> layer. Patches of only as-applied DFL structure were found along with some areas with loose debris, especially at the edges of the contact. Furthermore, light-grey areas were observed, which were found to be exposed bond coat due to DFL depletion from the upper surface of the highest asperities.

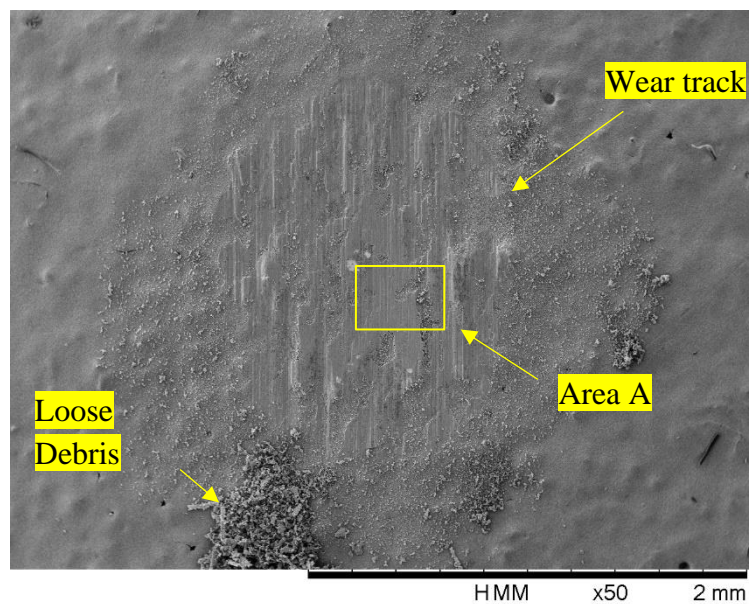


Figure 4-14: SEM micrograph (50x) of the plate specimens at 70,000 cycles. Average Hertzian contact pressure 575 MPa

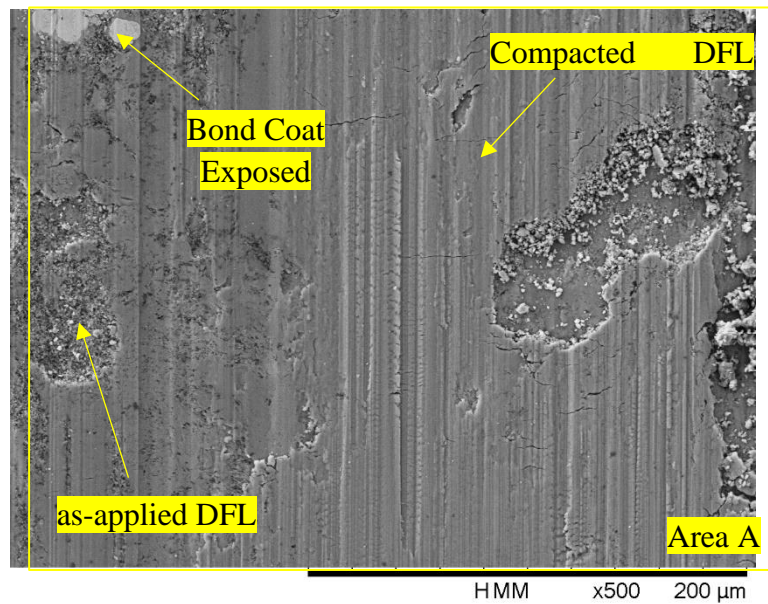


Figure 4-15: SEM micrograph (500x) of the plate specimens at 70,000 cycles (Area A from Figure 4-14). Average Hertzian contact pressure 575 MPa. The image shows the different areas: exposed bond coat, as-applied DFL, and DFL layer

Variations in the wear scar morphology with pressure can be observed in Figure 4-16 where the micrographs of the lowest (225 MPa) and the highest pressure (825 MPa) tests are included. At low pressure, the as-applied structure is largely preserved across the wear scar, whereas only small patches are preserved at the highest pressure. The amount of debris displaced out of the wear track and the exposed bond coat surface are larger at higher pressure.

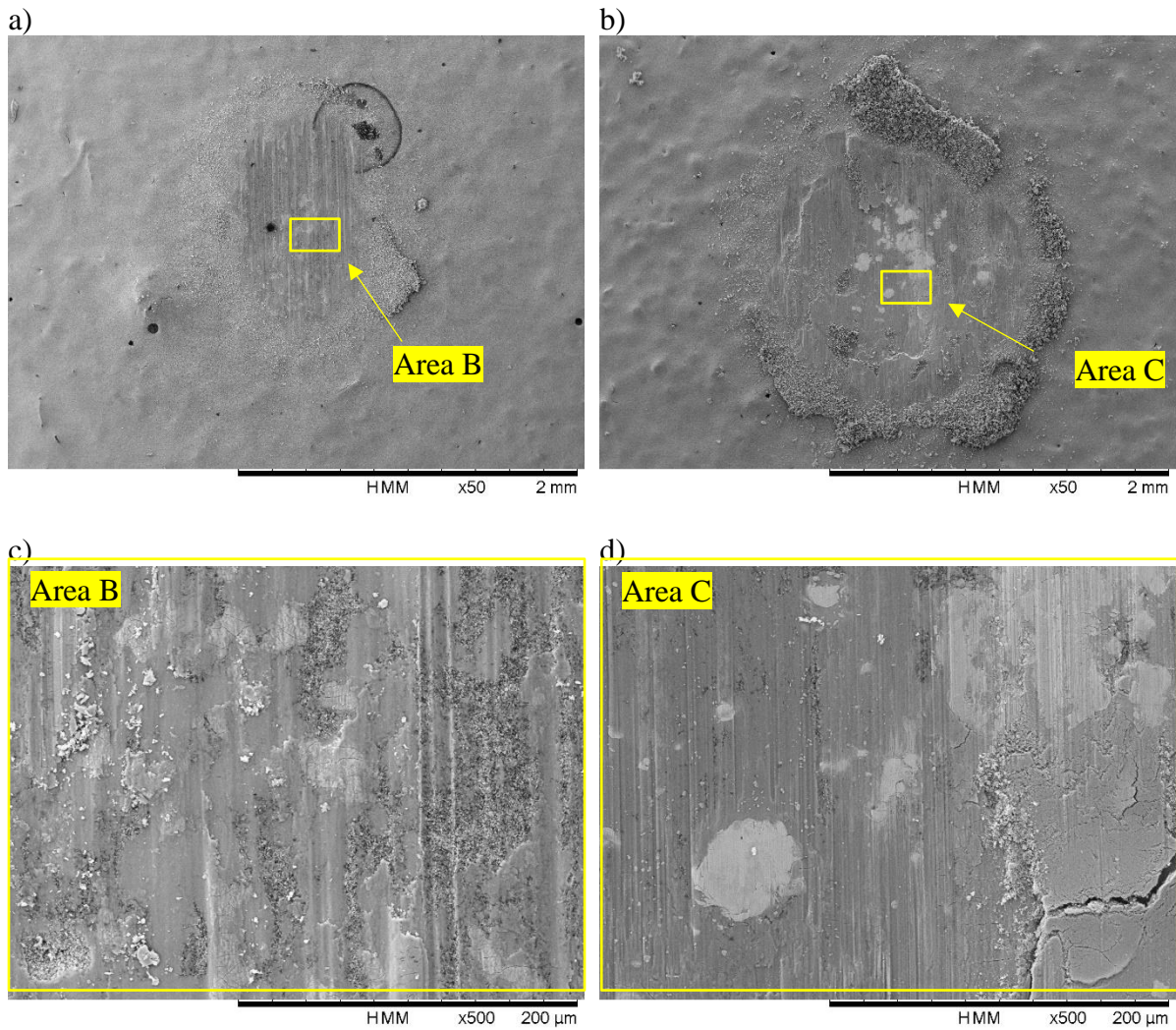


Figure 4-16: SEM micrographs of the plate specimens at the end of the test (70,000 cycles). a) 225 MPa 50x, b) 825 MPa 50x, c) zoom of area B at 500x, d) zoom of area C at 500x.

The morphology of the DFL layer also changes with pressure. High magnification micrographs show gentle extrusion and compaction of the film and light scratches along the reciprocating direction for the low-pressure test, which progressively turns into a highly compacted layer and fractures at higher pressure. A limited portion of the layer shows extensive cracking (as shown in Figure 4-17 from the 750 MPa test), though not at the level observed in the high stressed areas of the Trent800 root (see Section 3.2).

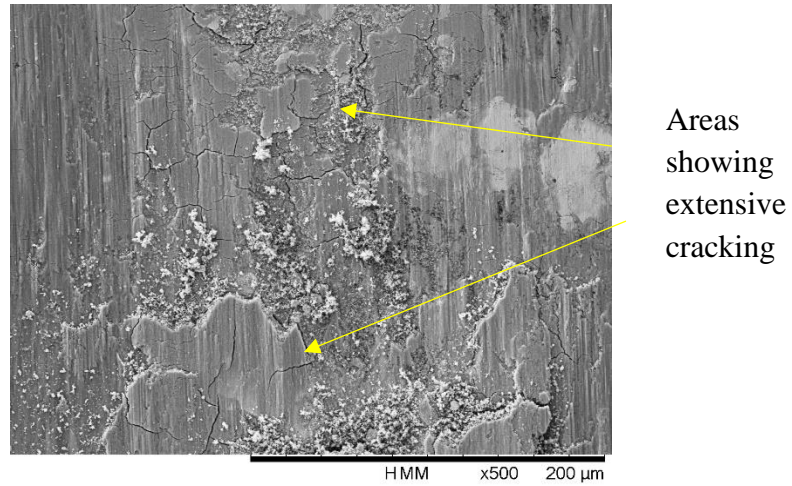


Figure 4-17: Area in the wear track of the test at 750MPa showing extensive cracking

The SEM images of all the plate samples wear scars are reported in Figure 4-18, where the features discussed and the general progression of the mechanism with pressure is evident.

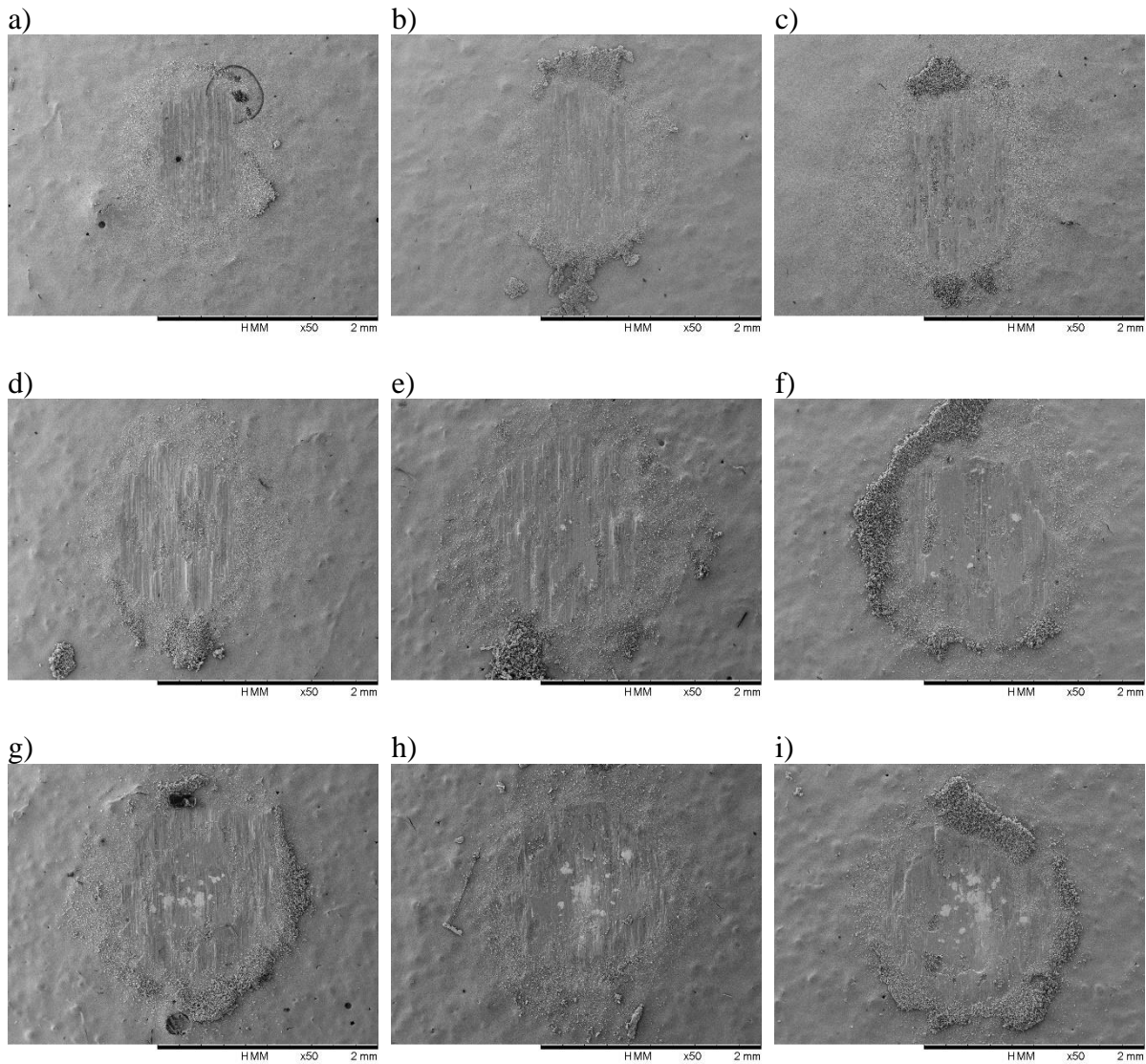


Figure 4-18: SEM images of the plate samples at 70,000 cycles. a) 225 MPa, b) 300 MPa, c) 375 MPa, d) 450 MPa, e) 525 MPa, f) 600 MPa, g) 675 MPa, h) 750 MPa, i) 850 MPa

#### 4.3.2 Influence of pressure on coefficient of friction evolution

The CoF evolution of the tests is shown in Figure 4-19. This was calculated as  $Q^*/P$ . As mentioned, the  $Q^*/P$  is representative of the CoF only if gross-sliding regime is achieved. The fretting loops are presented later in this section to verify the condition is met.



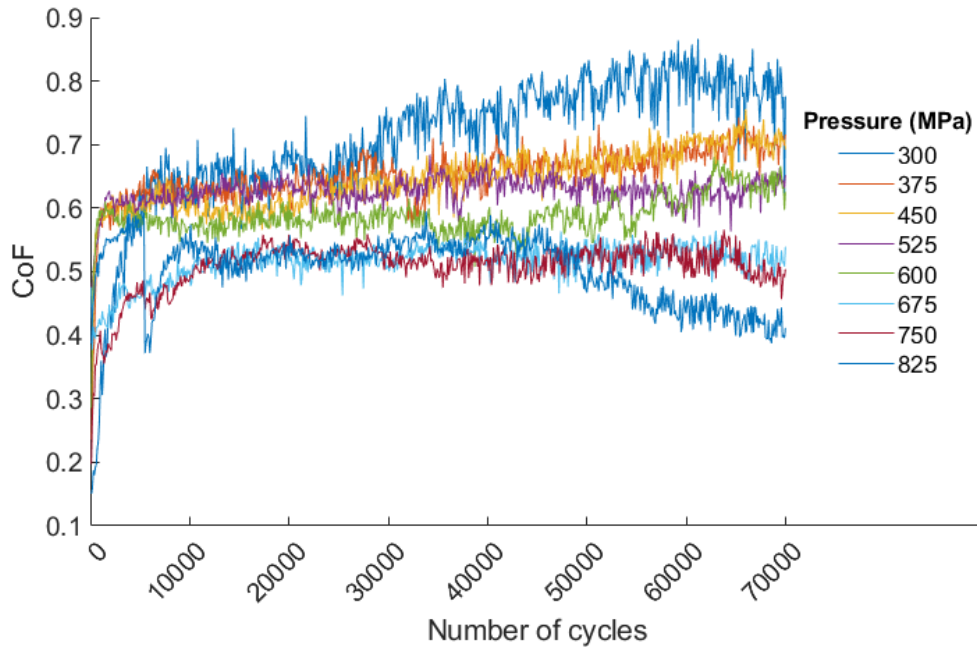


Figure 4-19: CoF evolution: influence of pressure

The 225 MPa test showed high noise and values larger than one. This is believed to be due to weak load control capability causing large tangential force variations, and it is not included in the following discussion. As a similar result would be achieved at 150 MPa, the test was not carried out.

The progression of the other tests is qualitatively similar, with a sharp rise of the CoF at the beginning (starting from approximately 0.1), followed by a secondary stage where an almost steady state is held until the test is terminated. The CoF ranged from approximately 0.4 to approximately 0.8 during this phase. Furthermore, there is a slight increasing trend of the CoF at the lowest pressure during the second stage that gradually changes to constant at intermediate pressure and then shows weak signs of decrease at 825 MPa.

By plotting the CoF value at 70,000 cycles (as average of the last 50 cycles) a clear decreasing trend of CoF at the end of test with increased pressure becomes evident (Figure 4-20).

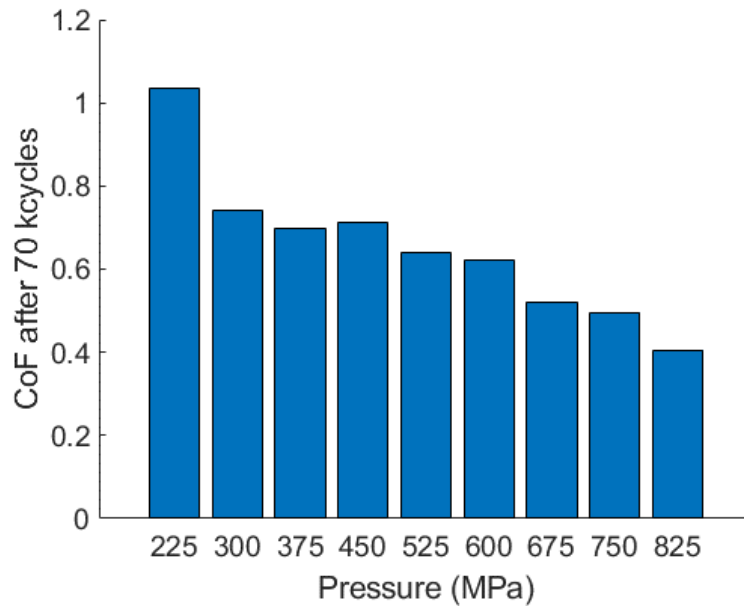


Figure 4-20: CoF at the end of test (average of last 50 cycles). A clear decreasing trend is observed

It should be noted that the CoF evolution does not contain a tertiary phase, which was observed by Barman et al. [83], and took place after the steady friction phase as a sudden increase in friction. Although this not occurring is consistent with a large residual amount of DFL on the wear track, it is important to assess the life of the coating as a function of pressure. Hence, the test duration was increased, aiming to reach failure. The first trial test was run at 450 MPa average Hertzian contact pressure, as the test equipment was particularly stable at such loading conditions both in terms of load control and fixtures compliance (as discussed in section 4.2.1). The CoF evolution is shown in Figure 4-21, where the red vertical lines in the graphs represent the points in time where the motion was interrupted (for 1-2 seconds), whilst the load was held. This was done to overcome the limitations of the software recording capabilities.

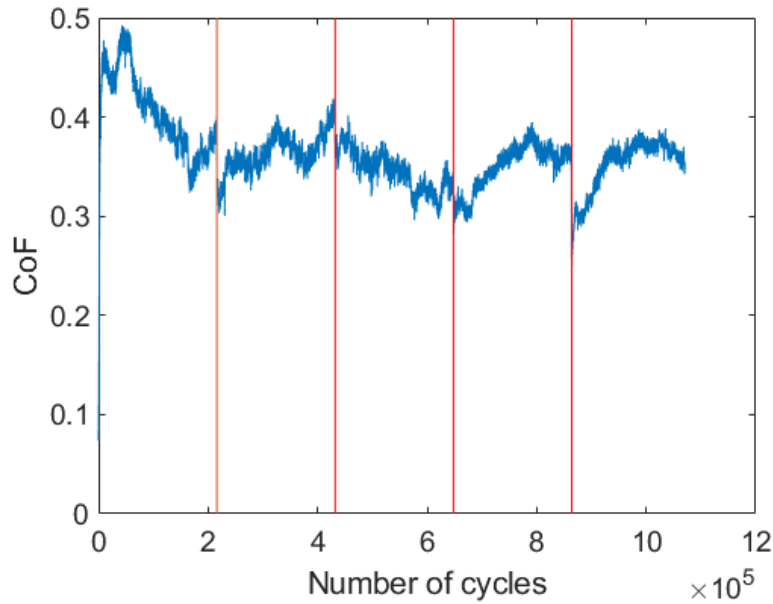


Figure 4-21: CoF evolution of a test performed at 450 MPa

As shown in the figure, the CoF is maintained constant within the steady phase and it shows no signs of incipient failure, despite the increased test duration (over 1 million cycles). It is believed that prolonging the test further would not likely produce failure, and is likely to be unachievable with the contact configuration adopted, as will be detailed in the discussion section of this chapter. Moreover, a full characterisation across the whole pressure range would be time consuming and unlikely to yield a different outcome. For this reasons, further testing with the UMTs was not carried out.

The fretting loops of the tests are included in Figure 4-22. These are plotted at the beginning of the test (1,000 cycles), and then again at the end of the tests (70,000). The loops show that gross slip regime is achieved at the beginning of the test in all cases except the 825 MPa test which shows full sticking behaviour. Towards the end of the tests, a gross slip regime is still achieved in all cases (except in the 725 MPa and 825 MPa tests), meeting the assumption required to calculate the CoF as the  $Q^*/P$ .

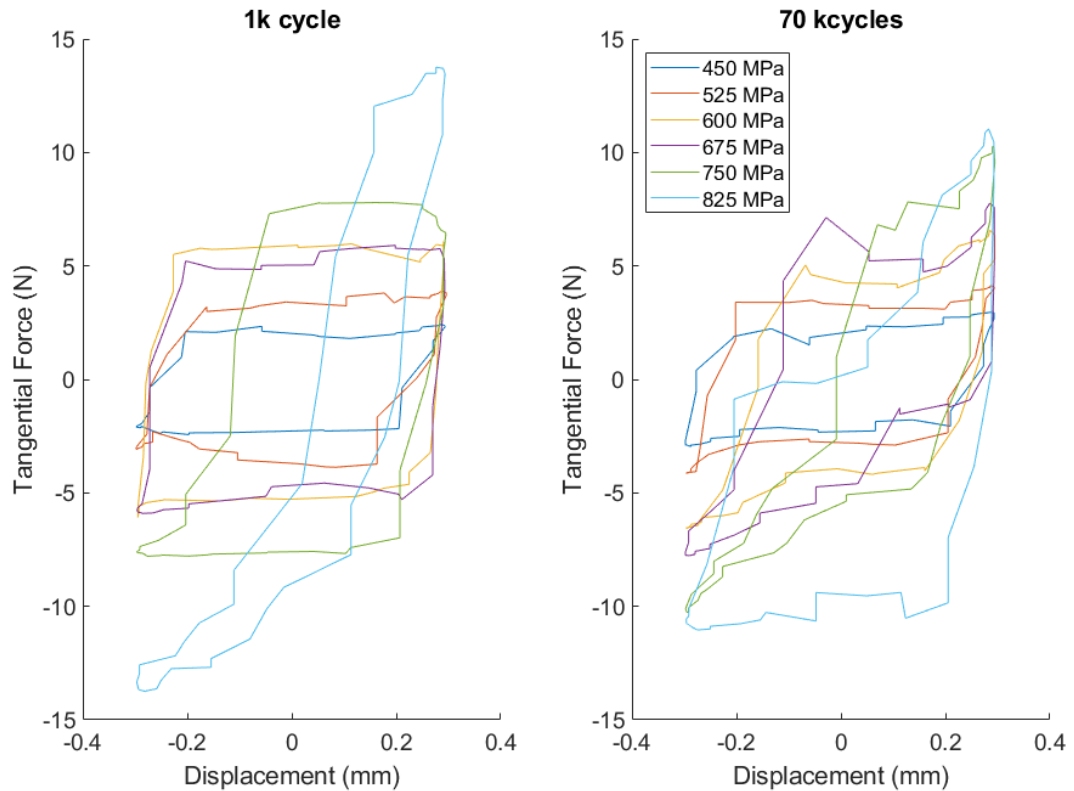


Figure 4-22: Fretting loops of the tests. The loops show that gross slip regime is achieved at the beginning of the tests in all cases except at 825 MPa at 1,000 cycles and the 750 MPa and 825 MPa 70,000 cycles

### 4.3.3 Influence of surface topography

The surfaces images of the 450 MPa test repeats are shown in Figure 4-23, with the specimens A and B being sourced from the high waviness batch and C and D from the low waviness batch. The images show differences in the shape and in the composition of the wear scar, with rougher specimens producing a more irregularly-shaped wear scar and showing a larger degree of bond coat exposure when compared to the smoother samples.

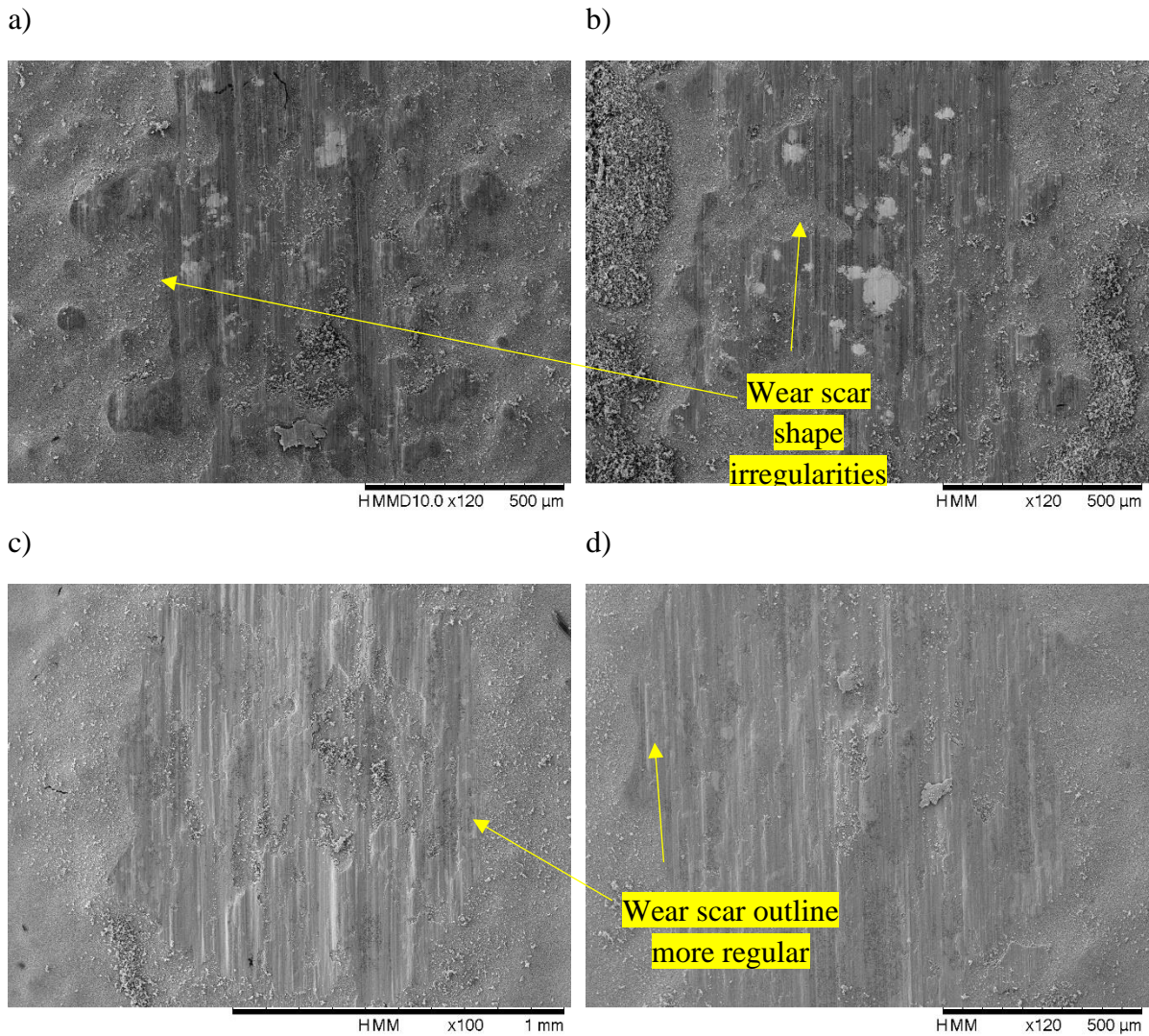


Figure 4-23: SEM micrographs of test repeated at 450MPa for 70,000. a) Test A Batch 1, b) Test B Batch 1, c) Test C Batch 2, d) Test C Batch 2

Differences in the CoF evolutions are also noticeable (Figure 4-24). From a qualitative point of view, the evolution of the CoF of the four tests were similar, where the values observed during the steady phase were approximately within 0.45 to 0.7.

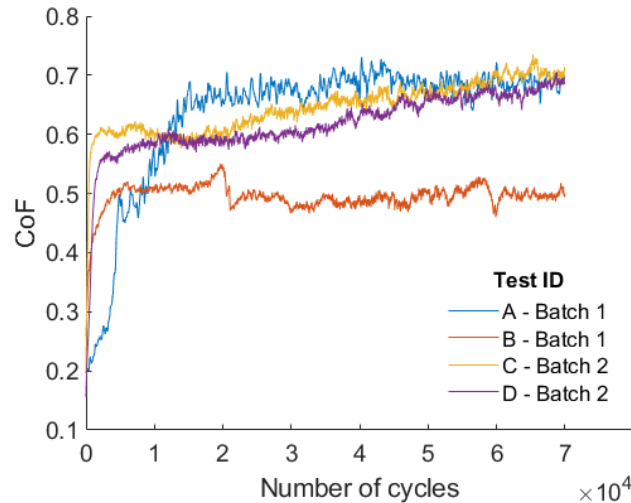


Figure 4-24: CoF evolution of tests repeated at 450MPa for 70,000. Test IDs refer to Figure 4-23

The dissimilarities in the wear scars can be correlated to the location where the sphere first contacts the plate sample. Depending on the size and concentration of macro-asperities in the specific spot, the contact interface will involve a different number of asperities, influencing the pressure distribution and the resulting mechanical behaviour. This effect is more marked in the rougher areas. An additional test was run for 10,000 cycle at 300 MPa to explore the mechanism at the early stages of the contact on a rough sample. The surface shows that the contact occurred on the tip of the highest asperities, whilst the remaining surface did not come in contact (Figure 4-25). Although the nominal pressure of the test (average Hertzian pressure) was relatively low, DFL compaction occurred to the extent observed on smoother samples tested at higher nominal pressure. This is thought to be due a local pressure increase caused by the waviness, and it is investigated later.

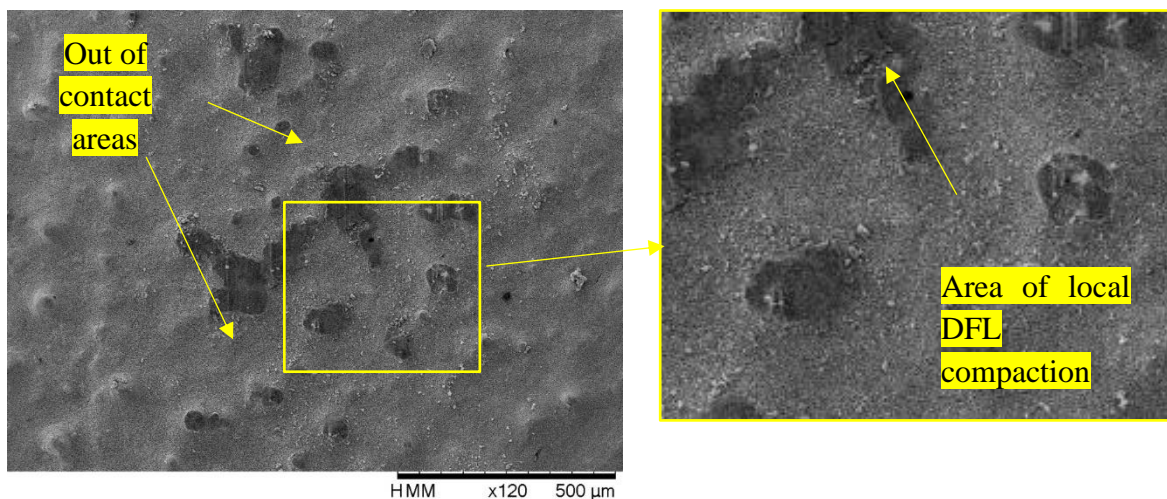


Figure 4-25: Surface of test at 300 MPa after 10,000 cycles performed on a wavy sample

Further investigation of the surface topography was performed by testing the plate samples with no METCO 58 application, which offered the smallest waviness among all the samples available. Four different test pressures were selected (300, 450, 600 and 750 MPa), for consistency with previous testing. The wear scars were more regularly shaped, presenting an elliptical form as shown Figure 4-26. A large volume of debris at the contact edges was observed, likely linked to weaker debris entrainment capabilities due to the smaller waviness of the samples with no bond coat.

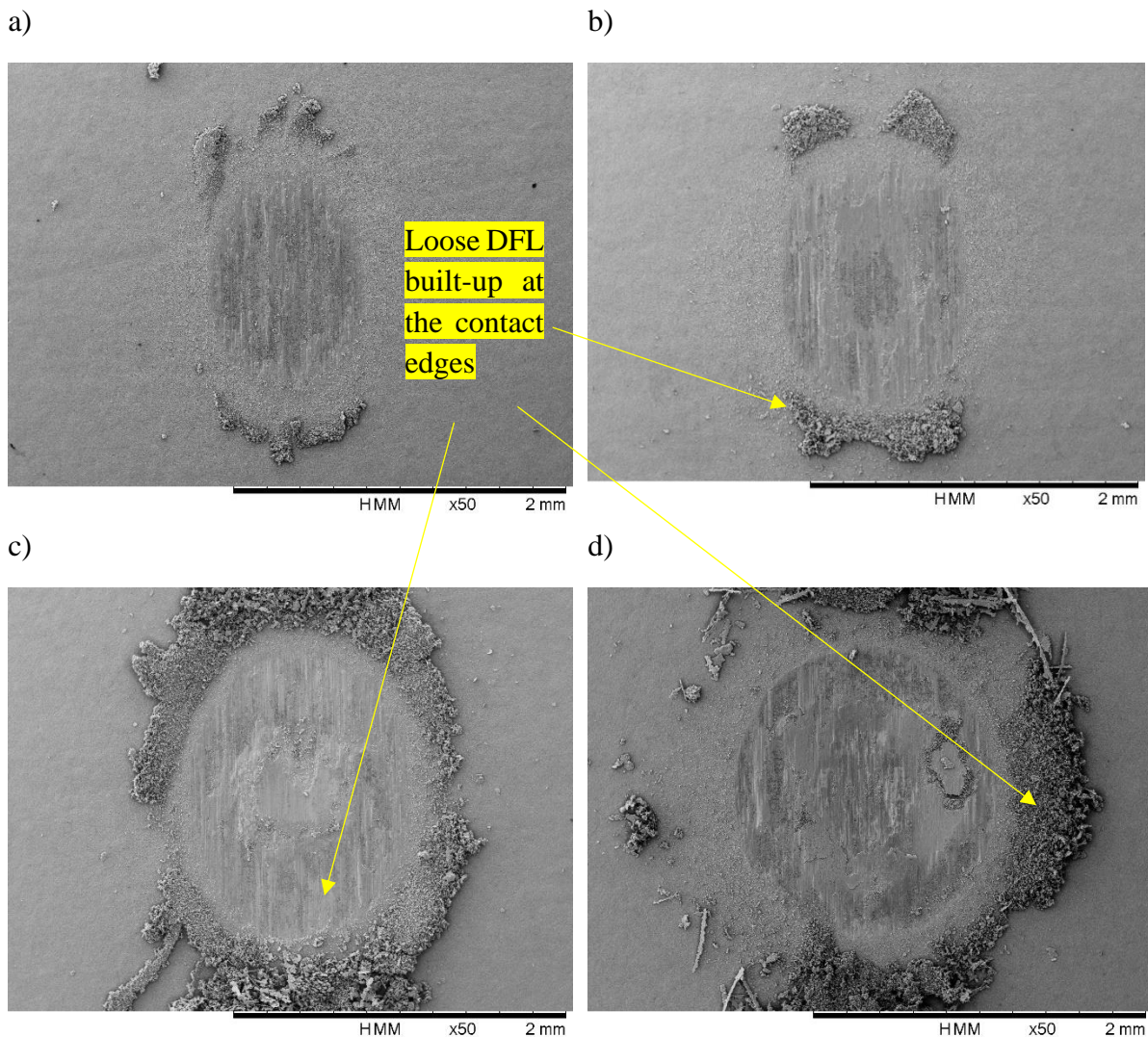


Figure 4-26: SEM micrographs of the tests performed on samples without bond coat. a) 300 MPa b) 450 MPa c) 600 MPa d) 750 MPa

With increasing load, a similar layer formation mechanism and relationship with pressure can be observed in these samples, exhibiting larger wear debris coverage and higher compaction. At 750 MPa, titanium exposure is observed in the centre of the wear scar as light-grey, bright areas. The tests without METCO 58 generally presented lower CoF during the test than those conducted at the same pressure with METCO 58, except of the case at 750 MPa (Figure 4-27).

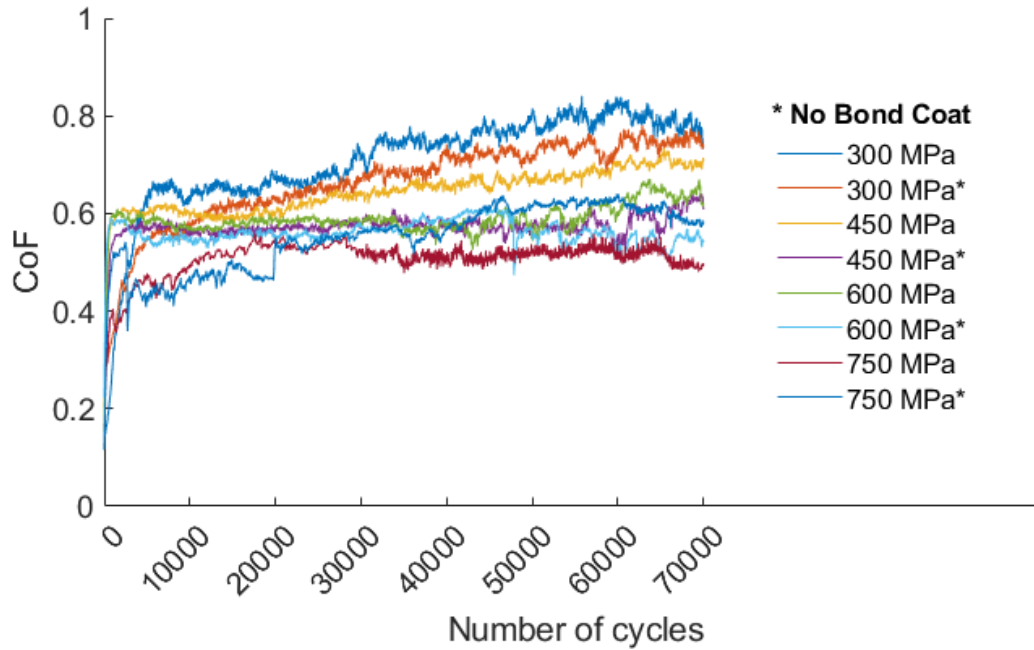


Figure 4-27: CoF evolution: influence of the bond coat. Lower CoF was recorded on the samples with no bond coat (apart from the 750 MPa test)

A summary of the results of the tests presented in this section is shown in Figure 4-28, which includes the CoF at end of each test. The test instances that were run more than once are represented with the average values of the repeats. The graph highlights the decreasing CoF trend with increased pressure. Generally, a lower CoF is observed for the samples without bond coat, and a slight difference between the two batches with different bond coats (450 MPa tests) is also noticeable. Although a larger number of tests would be required to assess the statistical significance of these results, further testing was not performed. As proposed in the discussion section, exploring the coating behaviour further on a different contact configuration is thought to be more beneficial for the fan blade contact investigation. This statement is supported by the work performed in the next section, which studies the influence of the topography on the contact mechanics of the ball-on-flat contact configuration.



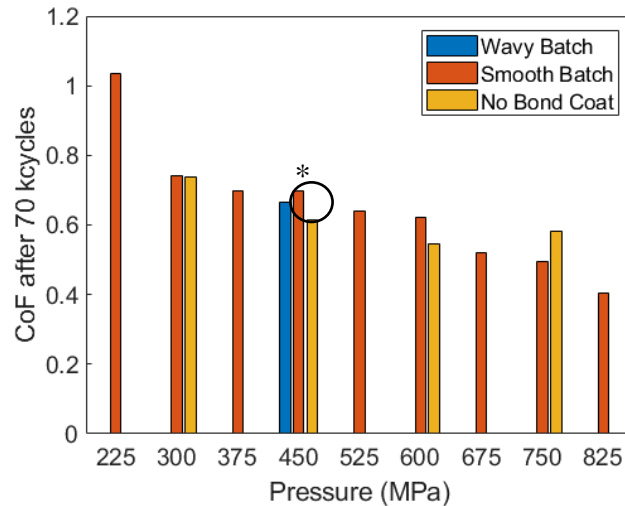


Figure 4-28: Summary of the CoF at the end of test. The bar marked with an asterisk represents the average CoF for the case where repeat tests were performed.

## 4.4 Multi-asperity contact model

### 4.4.1 Motivation and objectives

The results of the tests from different sample batches presented in section 4.3.3 indicated that the wear scar shape and composition is influenced by the surface topography of the plate sample. Particularly, that the concentration of the macro-asperities and their size within the area where the contact with the sphere takes place affected the test outcome. Typically, Hertzian theory [87] is adopted to estimate the contact pressure in non-conformal contacts (and it was used in this chapter for the test design): relying on the assumption of surfaces being perfectly smooth. Clearly, such an assumption does not apply in most of the instances reported here, where only the most prominent parts of the surface (macro-asperity tips) are acting as the load bearing surface (particularly at the beginning of the tests, as shown in Figure 4-25).

The scope of this section is to account for the surface topography and provide an estimation of the contact pressure, locally, on the macro-asperities. Emphasis is put on one instance of additional testing performed (Figure 4-29) where different mechanical behaviour among the macro-asperities of the coating was observed. This case is of interest as it allows investigation of the pressure-behaviour relationship, and it has been chosen as the main case study and for the model development. After presenting a brief review of potential multi-asperity contact modelling approaches, the development and implementation of a bespoke model is presented, along with the results on two different test surfaces.

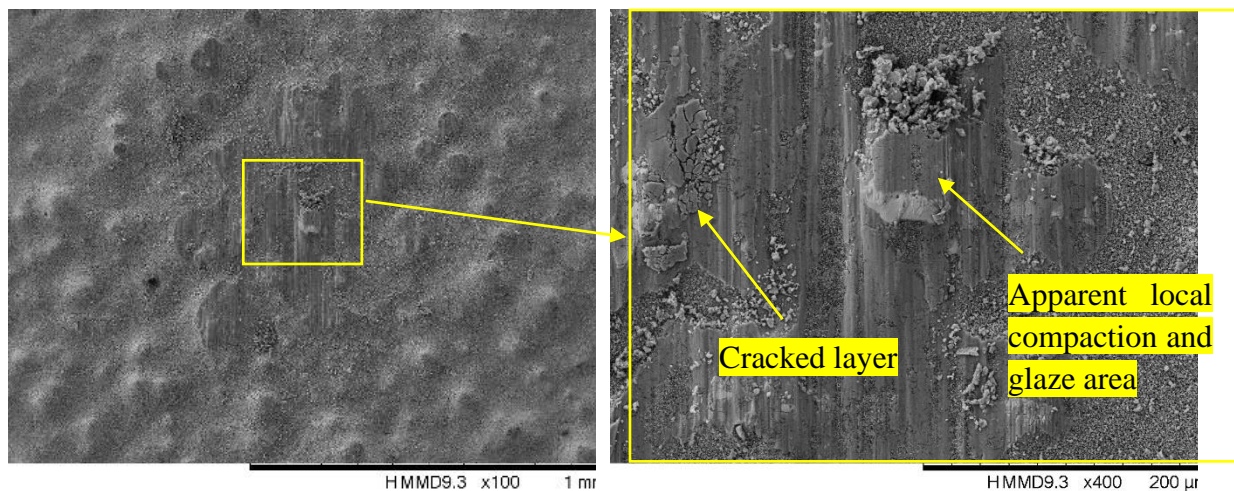


Figure 4-29: SEM image of bonded test specimen tested at 300MPa for 70'000 (left: 100x magnification, right: detail at 400x magnification). The surface shows strong heterogeneity of the surface composition

#### 4.4.2 Suitability of existing models

Several researchers have worked on the contact mechanics of real surfaces to understand the effects of topography and derive models to calculate the contact pressure at asperity level. Following the work of Bowden and Tabor [88] that estimated orders of magnitude difference between the nominal and the real contact pressure, Archard [89] and Bush et al. [90] developed the first asperity contact models to better address the subject. These were followed by the work of Greenwood and Williamson [91], which is widely applied and cited in the literature. They modelled the surface asperities with spheres of equal radii and Gaussian height distribution, estimating a near linear load to real contact area relationship.

Many other multiple asperity models have been developed after Greenwood and Williamson's work, covering different scales of roughness. Regardless of the scale considered, most of the techniques replace the contact between two rough surfaces with a smooth-rough interface, since this was proved by Greenwood and Tripp [92] to be a realistic supposition. The asperities of the rough body are then modelled as spheres (or paraboloids) allowing for the decomposition of the contact into many non-conforming contact spots. The Hertzian theory was applied in all the models discussed hitherto to solve these contact spots. Some more complex multiple asperity contact models have also been proposed, aimed to incorporate effects of adhesion [93], [94] applying single asperity adhesive solutions (for example the models of Johnson et al. [84] and Derjaguin et al. [95]) or plastic models (Abbot and Firestone model [96]) to the individual contact spots. Further information on multiple asperity contact model techniques can be found on the review papers published by Bhushan [97] and by Ramesh et al. [98].

The majority of the multi-asperity methods are based on statistical distribution modelling of asperities' location and dimensions, and they then output the real contact area for a given load. In order to investigate the influence of topography in the ball-on-flat tests, an estimation of the contact pressure at the interface is needed. This needs to be calculated from the topographical

data of the tests' surfaces, to produce a contact map where the estimated pressure is displayed for each asperity. A viable approach would be FEA modelling, as the example published by Cole and Sayles [99]. However, given the computational complexity of such an approach, the implementation of a bespoke contact model has thus been chosen as an alternative approach.

The model was developed to process the flat specimen's topographical data and produce a contact pressure map of the tested surfaces, estimating the average contact stress on the contacting macro-asperities for a given relative position of the two specimens. The contacting asperities are extracted from the 3D data of the plate specimen and are approximated with hemispherical caps, to which Hertz theory and the Jackson and Green model [100] are applied to provide results in the elastic and plastic region respectively.

The latter model is a recent study that provides dimensionless equations to study plasticity in macro contacts (such as rolling elements) as well as micro contacts. In fact, due to the complexity of modelling plasticity analytically, elastic-plastic and plastic behaviour are usually studied by performing finite element analysis (FEA) on a point contact interface [100]–[102]. Jackson and Green also based their study on FEA simulations of a point contact, and they fitted the results to obtain the dimensionless equations, which showed to be in good agreement with many other plastic models (validated against experimental results) and are valid for any set of material properties, hence its application in this case.

#### **4.4.3 Model development and implementation**

The main assumptions of the model are:

- The contacting asperities are modelled as hemispherical caps to exploit the use of existing single-asperity contact models. This means that the estimated pressure is more representative of the pressure at the beginning of the tests, when the asperities are more likely to have hemispherical shape, as no wear took place.
- The curvature of the sphere specimen ( $r = 3.175$  mm) is neglected as it is two orders of magnitude larger than the average macro-asperity size (10s of  $\mu\text{m}$ ). This allows the decomposition of the contact into a number of sphere-on-flat contact spots (one for each of the contacting asperities).
- The roughness component of the two surfaces is neglected and the role of the waviness only is considered (macro-asperities). It should therefore be noted that such estimation does not reflect the actual pressure at micro-asperity level [98].
- The summits of the asperities are at the same height and they are assumed to be subjected to the same deformation.

The post-test 3D raw data of surface profile is imported into MATLAB® and is then pre-processed to produce the x and y grids and the correspondent surface height matrix z, replacing the missing data points by interpolation and compensating for tilting of the specimen during

the measurement. The surface plot of the case studied after pre-processing is shown in Figure 4-30.

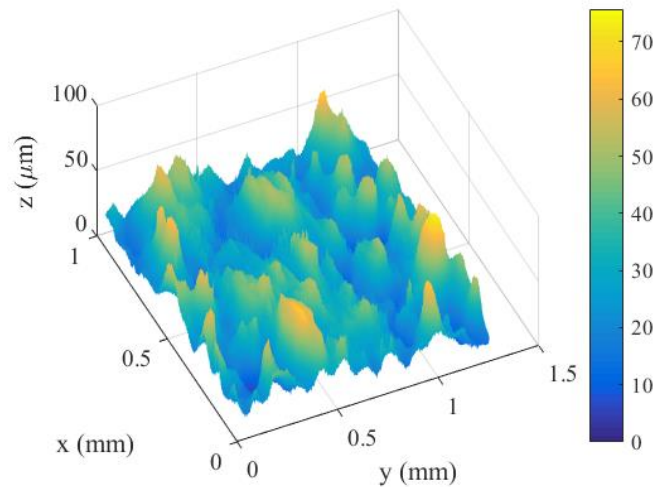


Figure 4-30: Measured surface profile after post processing. Sample sourced from wavy batch, tested at 300 MPa average Hertzian pressure for 70,000 cycles

The following step of the model is the extraction of the asperities which contact with the sphere for a given position of the ball respective of the plate sample. A perfectly spherical countersurface is located at a desired location on the plate surface and an arbitrary interference between the two is applied. An example of this step is illustrated in Figure 4-31.

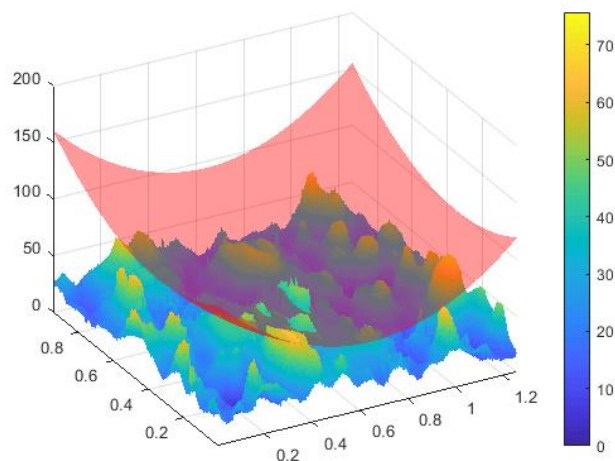


Figure 4-31: Sphere shaped counter surface being used to extract the macro-asperities

The intersection between the counter surface and the test surface is then superimposed onto the SEM image of the test surface. The comparison of the intersection with the wear scar, ensures a correct match between the topographical data and the image. An example of the result is shown in Figure 4-32, which is representative of the sphere being located at the lowest point of the reciprocating stroke.

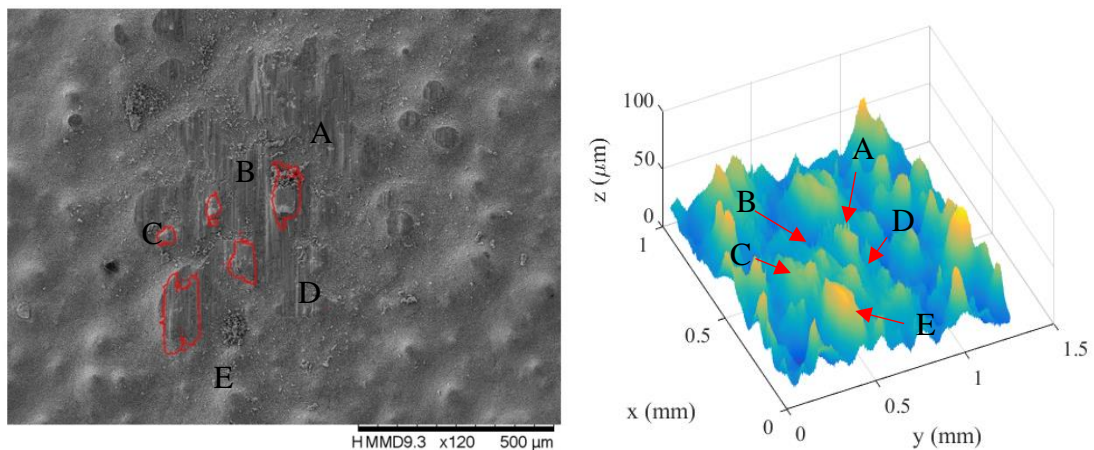


Figure 4-32: Base of the extracted asperities superimposed onto SEM image

The contacting asperities are extracted by selecting all the surface data points above the sphere countersurface. A volume optimization criterion which minimizes the difference between the real surface and a hemisphere is then used on each contacting asperity. The variables under optimization are the coordinates of the asperities' centres and their radii. Allowing the radii to differ among the asperities permits pressure variations, since equal radii asperities would support an equal share of the load, yielding the same stress. The contacting asperities and the modelled hemisphere (red) are then represented in Figure 4-33. The fitting error is also indicated, expressed as a percentage difference between the volume of the modelled and real asperities, showing limited values.

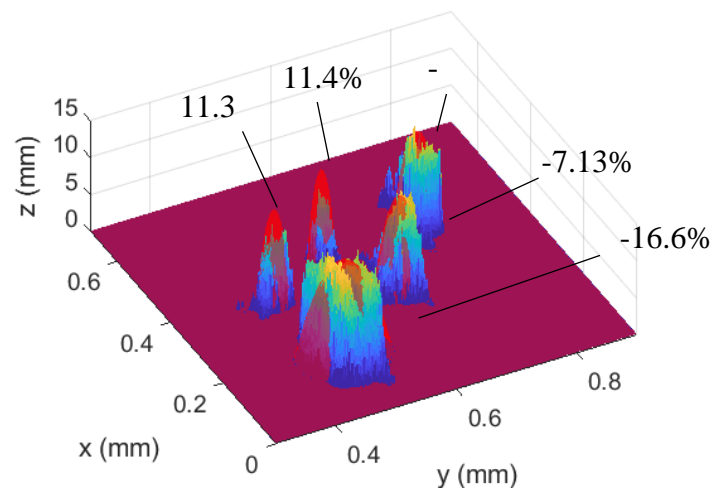


Figure 4-33: Asperities fitting

To calculate the pressure on each of the asperities the load sharing between the asperities must be computed. This is achieved by following steps:

- 1) An arbitrary deformation of the asperities is imposed (which is assumed to be the same on each of the contacting asperities).

- 2) The load necessary to produce that deformation is computed for each asperity according to Hertz or Jackson and Green equations.
- 3) The sum of the loads on each asperity is compared to the overall normal load applied to calculate the “load error”.
- 4) The deformation is adjusted, and the programs reiterates from step 1) until the load error is smaller than 0.1%.

Finally, the pressure on each asperity is calculated using the loads calculated during step 2) at the last iteration of the algorithm.

#### 4.4.4 Results

The results of the application of the model to two different case studies is reported here. Clearly, the surfaces under examination complied with the following requirements:

- The samples were all sourced from the wavy batch where the macro-asperities were pronounced, as opposed to the smoother batch
- The asperities were spaced apart from each other (low density). This facilitated extraction of the asperities from the surface that would tend otherwise to be detected as a single entity.
- The samples were tested at low pressure (300 MPa) as the pre-test topography was better preserved due to lower wear, allowing for clearer identification of the asperities.

Figure 4-34 shows a post-test SEM image as an example of an unsuitable surface to be analysed with the contact model (test pressure 450MPa). The asperities summits have worn down such that they have merged into a single contact patch, causing the algorithm to fail to extract the contour of the individual asperities. The model was not designed for such a case, as its aim is to investigate when discrete contact occurs.

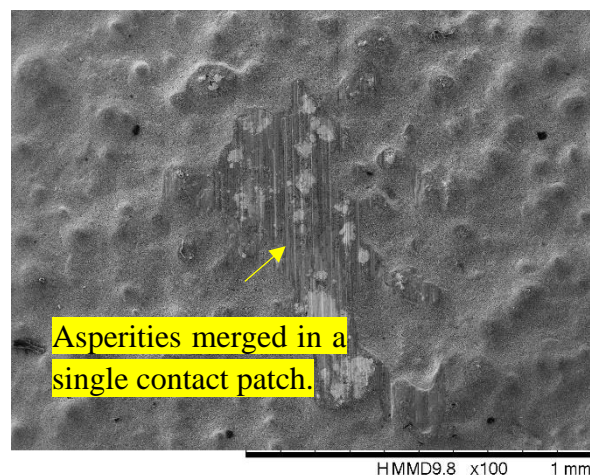


Figure 4-34: Wear scar shape not suitable for contact modelling

The results include the SEM images with the contour of the extracted contacting asperities, a pressure map and a table including the estimated pressure and contact radius for each asperity.

The Hertzian parameters reported are mean contact pressure, load supported and contact radius. The same parameters are reported for the Jackson and Green [103], [104] results, along with the dimensionless penetration parameter  $\omega^*$ , defined as the ratio between the actual penetration and the penetration at which the material would first exceed the yield stress. The overall deformation calculate with the plastic model is also reported.

The SEM image and the contact map produced for test 1 are shown in Figure 4-35, and included in Table 7. The overall deformation calculated with the Jackson and Green model was 0.463  $\mu\text{m}$ .

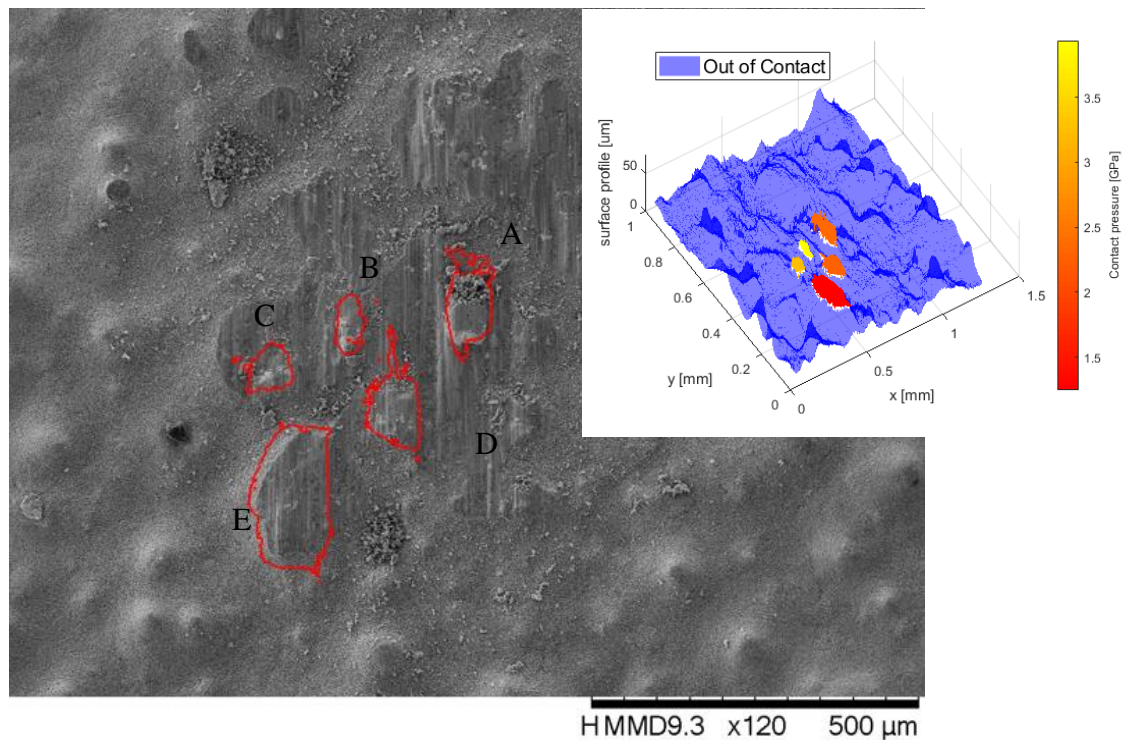


Figure 4-35: Test 1 - SEM image and Hertzian Contact Map. Sample tested for 70'000 cycles at 300MPa average Hertzian pressure. Asperities are labelled from A to E to report the results in Table 7

	Radius of Asperity ( $\mu\text{m}$ )	Hertz Model			Jackson and Green Model			
		Pressure (GPa)	Load (N)	Radius ( $\mu\text{m}$ )	Pressure (GPa)	Load (N)	Radius ( $\mu\text{m}$ )	$\omega^*$
A	63.6	2.34	0.243	5.75	1.98	0.235	6.14	15.50
B	22.5	3.94	0.145	3.42	2.14	0.107	3.98	43.84
C	33.2	3.24	0.176	4.15	2.11	0.145	4.68	29.71
D	66.9	2.28	0.249	5.89	1.97	0.243	6.26	14.76
E	224.9	1.25	0.457	10.81	1.60	0.541	10.37	4.39

Table 7: Contact model results of Test 1

The SEM image and the contact map produced for test 2 are shown in Figure 4-36, and included in Table 8. The overall deformation calculated with the Jackson and Green model was 0.453  $\mu\text{m}$ .

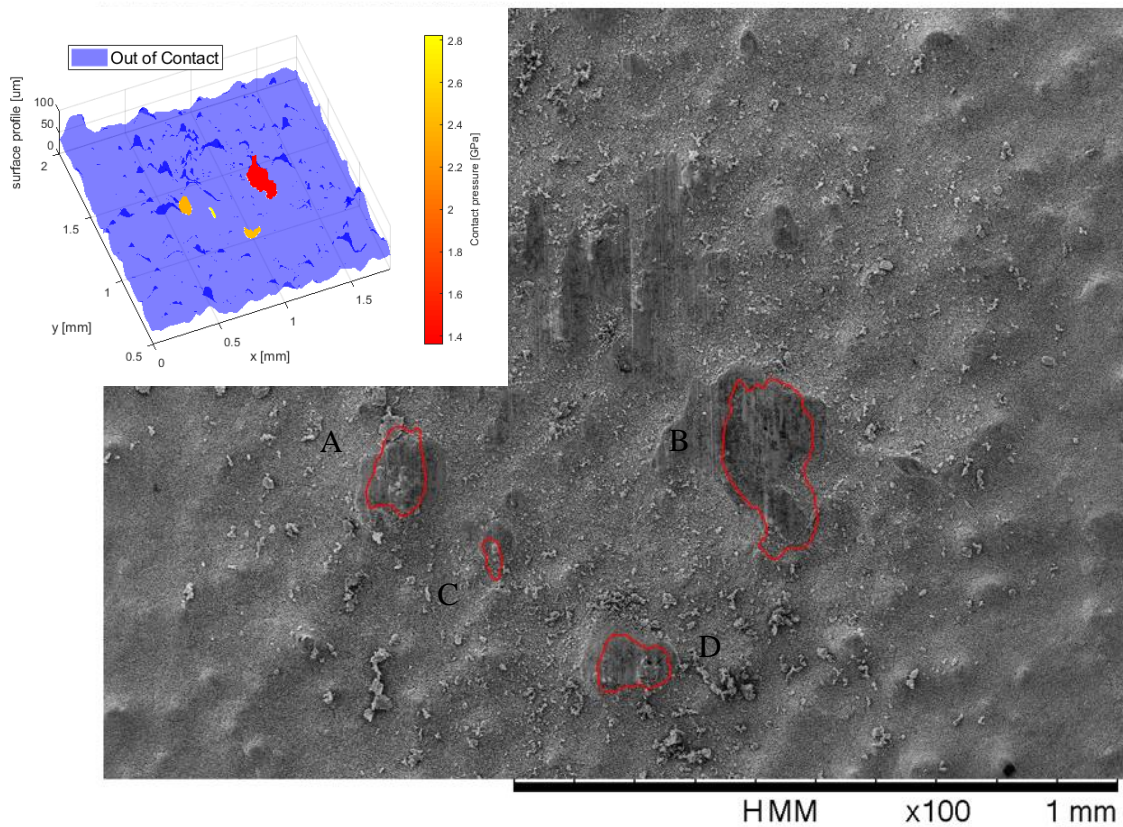


Figure 4-36: Test 2 - SEM image and Hertzian Contact Map. Sample tested for 10'000 cycles at 300MPa average Hertzian pressure. Asperities are labelled from A to E to report the results in Table 8



	Radius of Asperity ( $\mu\text{m}$ )	Hertz Model			Jackson and Green Model			
		Pressure (GPa)	Load (N)	Radius ( $\mu\text{m}$ )	Pressure (GPa)	Load (N)	Radius ( $\mu\text{m}$ )	$\omega^*$
A	73.4	2.27	0.295	6.43	1.85	0.282	6.97	17.86
B	226.0	1.29	0.518	11.29	1.54	0.602	11.14	5.80
C	37.1	3.19	0.210	4.58	1.96	0.170	5.25	35.26
D	51.2	2.72	0.247	5.37	1.92	0.217	5.99	25.64

Table 8: Contact model results of Test 2.

The model estimated a large variability of contact stress between the asperities, which ranged from 1.25 GPa to 3.97 GPa when the elastic model was used. The large gap from the nominal pressure computed at global level (300 MPa) suggests that Hertz theory does not provide a plausible estimation. Evidently, this derives from the assumption of smoothness of the surface not being met. The elastic-plastic results yielded a narrower and likely more realistic stress range, from 1.60 to 1.97 GPa. Both the models highlight a large discrepancy between the contact stress among the asperities and highlight why behaviour globally witnessed for high contact pressures was evident locally at low contact pressures for rougher surfaces.

## 4.5 Discussion

### 4.5.1 Comparison with Trent800 investigation

The main mechanism observed in the ball-on-flat reciprocating tests was the formation of a surface layer generated by extrusion and compaction of loose MoS<sub>2</sub> particles, by which MoS<sub>2</sub> is known to provide good lubrication. As the motivation of this study originated from the forensic investigation of the fan blade root, it is interesting to compare the tests outcome with the blade observation. Overall, there were similarities in the mechanism of MoS<sub>2</sub> particles being gently extruded and compacted under lower pressure and producing a more highly compacted layer as the load was increased. At the highest test pressures, fracture of the layer occurred, though this was more marked in the blade resulting in a platelet structure.

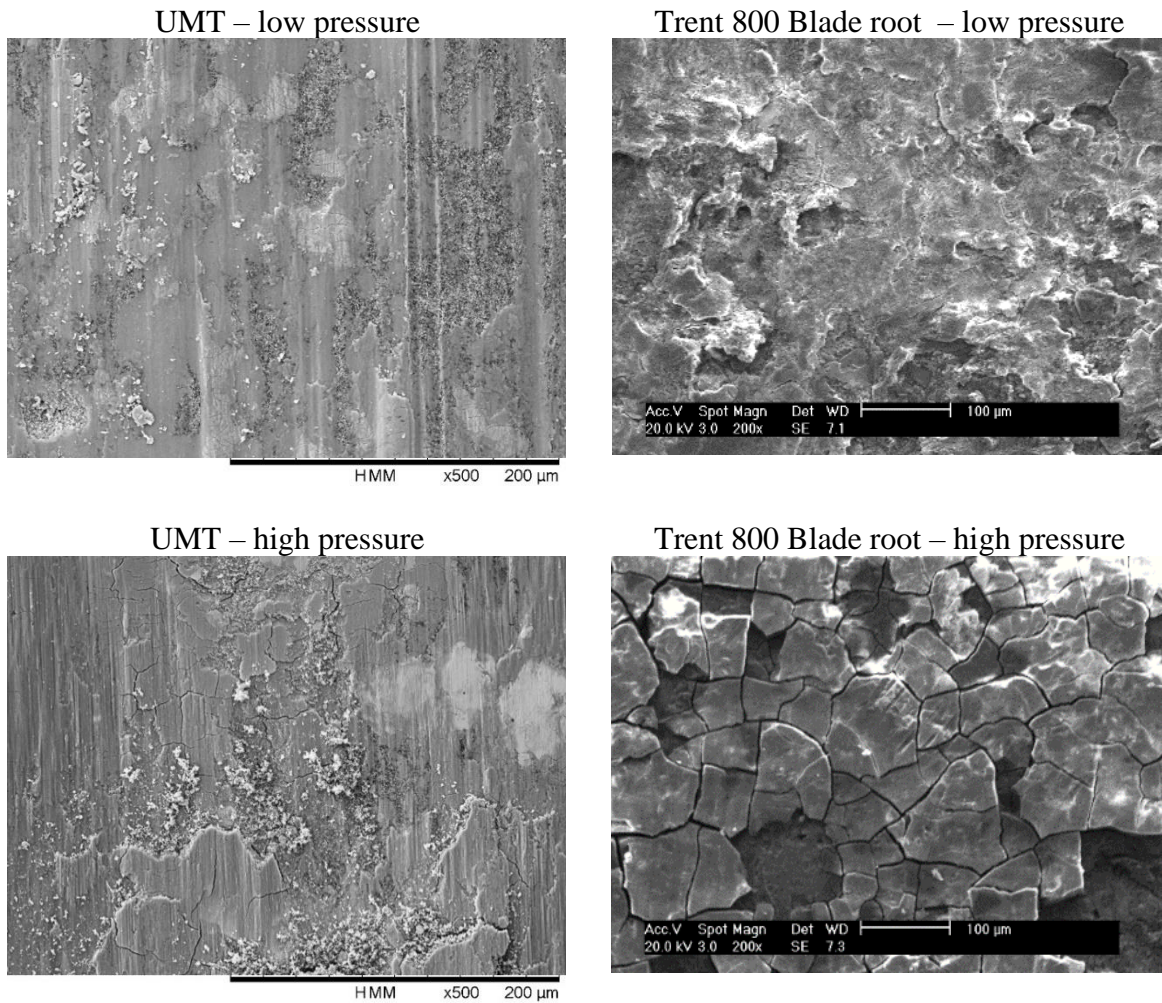


Figure 4-37: Comparison between UMT tests and Trent800 blade root surface. N.B. Images have different scales.

When comparing the surface of the tests to the surface of the component, it is worth pointing out the differences between the two contact configurations. The contact on the dovetail root occurs over a larger surface with large areas subjected to small pressure gradients, where a fairly constant pressure is achieved. As a result, a uniform morphology of the surface is produced in such areas. The ball-on-flat contact occurs on a much smaller area and the pressure calculated is the average value of the theoretical distribution proposed by Hertz theory. This Hertzian pressure profile peaks at the centre of the contact at 1.5 times the average pressure values and reduces to zero at the contact edges according to the distribution shown in Figure 4-38.

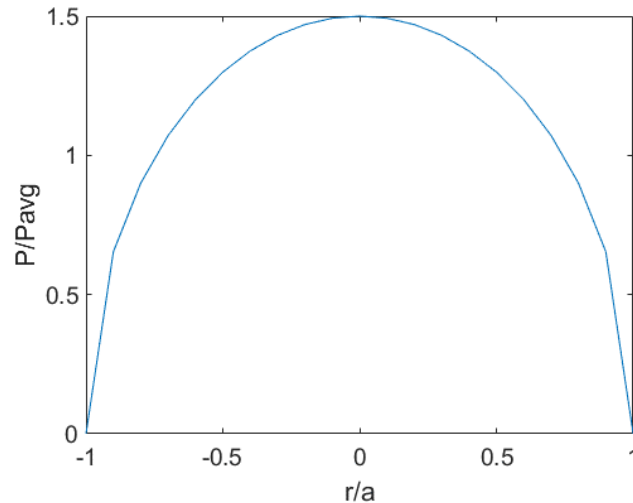


Figure 4-38: Contact pressure distribution estimated by Hertz.  $P$  is the contact pressure at a given position,  $P_{avg}$  is the average Hertzian pressure,  $r$  is the distance from the centre of the wear scar,  $a$  is the semi-width of the contact

With such a distribution, the morphology is more heterogeneous across the wear scar, with features typical of high contact pressure (such as glaze layer and cracks) being more likely to be found within the central areas of the contact. As it has been shown, the pressure distribution is also affected by topography as the peaks of the surface act as bearing surfaces and are subjected to higher pressure. This effect is more marked on the ball-on-flat surface, given the small ratio between the contact area and the average macro-asperity size, and it can be predominant on particularly rough surfaces. It is also thought that the topography also affects the CoF measured in the experiments, as mentioned later in more detail.

The differences discussed explain why a high-pressure test includes both high and low-pressure features, as opposed to a more global behaviour observed in the root surface. The material removal due to wear also influences the two contact configurations differently. The ball-on-flat contact is subjected to a higher contact pressure drop as the ball is flattened during the test, as shown in Figure 4-39. The more conforming contact interface of the dovetail joint retains its shape and the contact pressure profile.

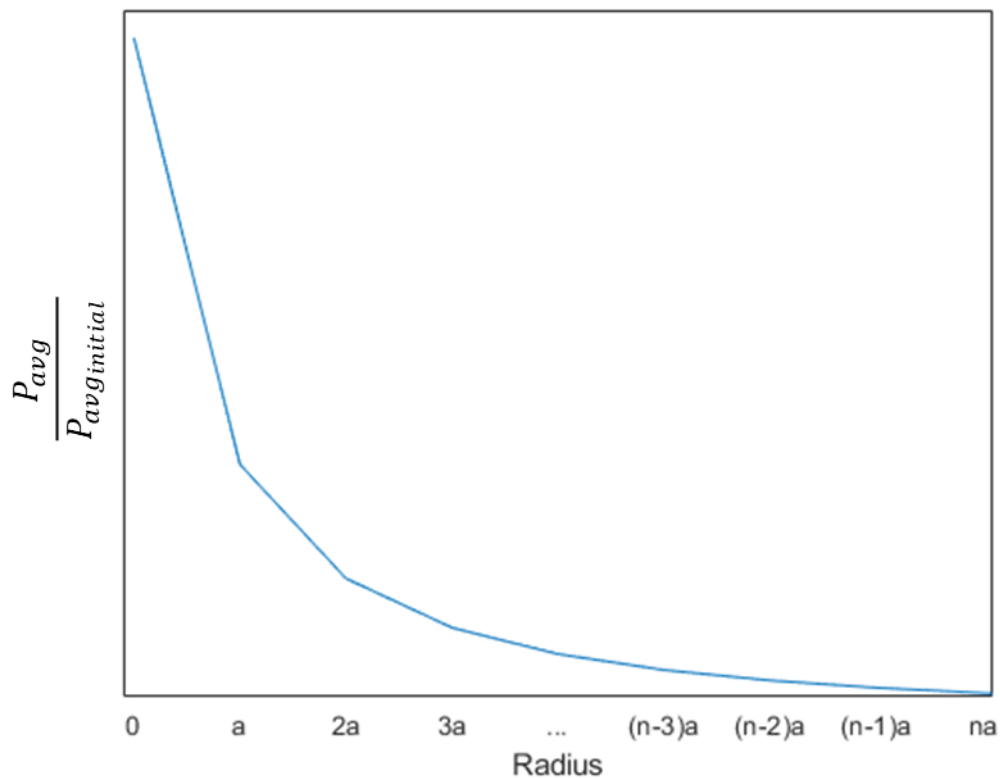


Figure 4-39: Pressure drop as contact radius increases for a ball-on-flat test

Other secondary sources that contribute to producing different features between the tests and real components might be:

- The reciprocating displacement achieved in the tests is representative of the relative movement of the root respective to the disc slot due to bedding of the blade (LCF), whilst the effects of vibrations (HCF) are not simulated.
- The larger contact area of the blade-disc interface offers higher MoS<sub>2</sub> particles entrainment, whereas ejection from the tests wear track is observed; this is indicated by the debris built-up at the contact area periphery.
- The environmental conditions are not representative of the in-flight temperature and humidity. These have been discussed to have a detrimental effect on the coating behaviour, mostly due to higher rate of oxidation of MoS<sub>2</sub> particles [65]. The blade was likely re-lubricated whereas the specimens were not.

Considering all the above, the results of the ball-on-flat tests must be contextualised prior to drawing any conclusion applicable to the fan blade contact.

#### 4.5.2 Lubrication capabilities

The main objective of the experimental work in this chapter was to assess the dependence of coating behaviour as function of pressure. Particularly, the capability of providing a low coefficient of friction for the longest operating time possible. This is a key aspect with regards to the suitability of the product. The test results have shown an inverse CoF-load relationship (as observed by Singer et al. [81] on the sliding behaviour of thin MoS<sub>2</sub> films) in the fretting behaviour of the fan blade coating system. It should be reminded that gross slip regime must be achieved to assume that the  $Q^*/P$  ratio is equivalent to the CoF. The fretting loops have shown that this condition was met in the tests up to 600 MPa, meaning that the highest-pressure tests (750 and 825MPa) might not be significant.

Given the variability of the CoF measured while repeating the tests, it was difficult to establish an empirical relationship and, perhaps, this is not crucial for the scope of this project. A qualitative understanding of the relationship between mechanical behaviour and lubrication capabilities would be more of interest to aid coating designers in identifying the driving parameters of the lubrication mechanism.

Due to the pressure distribution and the effect of the topography, the wear scars were composed of the following: as-applied DFL, DFL layer (extruded and compacted to different extents), loose DFL particles, and exposed bond coat. Each of these areas will require a different tangential force to overcome friction, depending on the lubrication mechanism triggered. The net tangential force measured during the tests (which is used to calculate the CoF) is representative of the global behaviour of the surface, being the sum of the tangential force required in each locality.

For this reason, a direct association of a CoF value to a specific area is not straightforward. However, the proportion of the areas upon which the surface is made up is thought to be relatable to the overall CoF. In fact, a larger proportion of the DFL layer, particularly in its highly compacted form, was observed in the wear track of the higher-pressure test (as shown in Figure 4-16), a lower overall CoF was then recorded for this test. This is consistent with the mechanism that was first observed by Fusaro et al. [64], [65], and confirmed later by other research, for which MoS<sub>2</sub> must be compacted under high pressure to create a low-friction film.

However, the CoF measured in this experimental work is significantly larger than the values reported in the literature for MoS<sub>2</sub> based films, which are around 0.1 – 0.4 [58], [67] (or even lower than 0.1 when testing is performed in vacuumed or dry environments [62], [105]). The CoF evolution measured in tests conducted (especially at lower pressure) is comparable to the bare Ti-6Al-4V data measured by Fridrici et al. [106]. Figure 4-40 shows their findings, including the CoF evolution of Ti-6Al-4V coated with a Cu-Ni-In bond coat only.

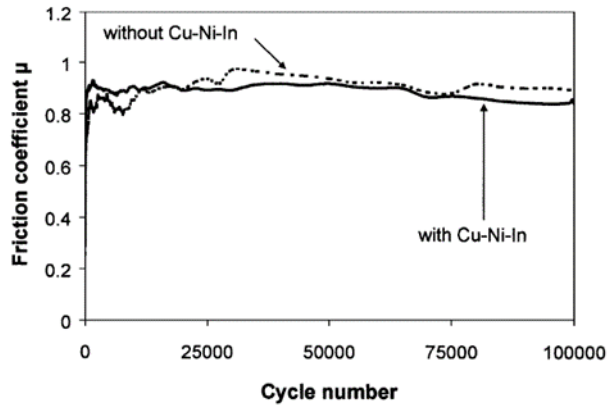


Figure 4-40: CoF evolution of bare Titanium and Cu-Ni-In coated Titanium. The graphs show CoF values comparable to those recorded in the tests

There are two key reasons which are likely to produce an overestimation of the CoF. Firstly, the mechanical compliance of the specimen's substrate/bond coat causes a bow wave to form during relative motion, as schematically illustrated in Figure 4-41.

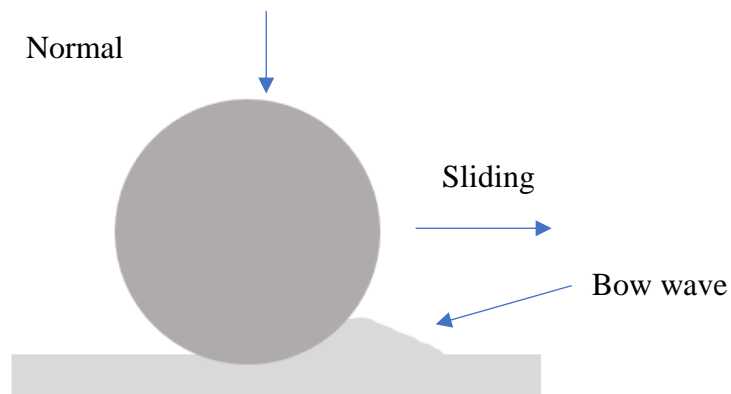


Figure 4-41: Example of a bow wave

A study found that approximately 70 % of the tangential force measured on a ball-on flat aluminium-steel interface is due to the bow wave, and only the remaining 30 % is attributed to friction [107]. Assuming the same proportion is applicable for the fan blade coating, that would account for an overestimation by a factor of 2.33. If the tangential force data is corrected by such factor, the results are closer to the values observed in the literature (Figure 4-42).

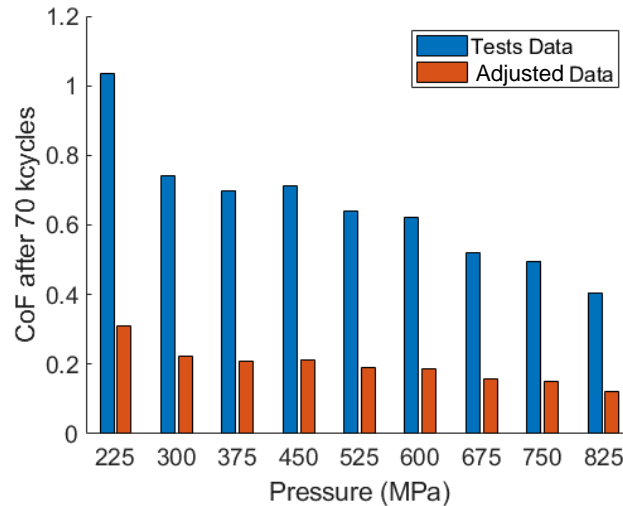


Figure 4-42: CoF evolution adjusted by a 3/10 factor as a compensation for the tangential force absorbed for the bow wave generation

Secondly, a limited low-friction layer coverage is achieved due to a combination of factors: the contact pressure distribution, the effect of surface topography and poor debris entrainment. The latter reduces the amount of MoS<sub>2</sub> particles required to form the layer, whilst the contact pressure distribution limits the area subjected to high stress, which is necessary to promote the layer formation. High waviness enhances both aspects, by limiting the contacting surface to the asperities' peaks and retaining debris in the out-of-contact valleys.

Although the findings indicated that higher contact pressure is beneficial for triggering a lower friction contact, this information is not sufficient to fully characterise the coating behaviour as the life should be assessed too. The CoF evolution was observed to have two phases: a running-in phase where the CoF rose steeply over the first few thousands of cycles and a secondary phase where an approximately steady CoF was maintained until the end of the tests at 70,000 cycles. This was the case regardless of the application of the bond coat to the plate specimen.

According to Barman et al. [83], a tertiary phase also takes place which exhibits a sharp rise of the CoF caused by DFL depletion. This took place at around 65,000 cycles in the test they performed (whereas it did not in the equivalent test of this investigation). Extending the duration of the tests over 70,000 cycles as in the test performed at 450 MPa, still did not cause any signs of failure. Specifically, due to the enduring nature of the surface previously detailed, and its failure to form a continuous sintered layer, friction both never reached its lowest value nor rose rapidly as the sintered layer eventually failed.

Finally, it must be noted that the gross slide regime should occur for the  $Q^*/P$  ratio to represent the CoF. This was shown to be the case for most of the tests, except for the 750 and 825 MPa instances towards the end of the test. For this reason, any consideration deriving from the analysis of the CoF of those tests should be taken with care as it might not reflect the lubrication capabilities. Further, the influence of the surface topography in driving the lubrication

mechanism and its effects on the difficulties in achieving failure needs to be addressed. The rest of the discussion focuses on these aspects, starting from the contact model results.

### 4.5.3 Contact model

The tests performed to assess the pressure influence were purposely selected from the smoother batch, to limit the effect of the surface topography (particularly due to the bond coat waviness) on the wear mechanism. These tests produced a more regular and homogeneous wear scar than those performed on the wavier batch, on which local dissimilarities of the contact pressure caused by the irregularities of the surface were believed to occur.

The contact model was developed to estimate the contact pressure at macro-asperity level, estimating a Hertzian contact pressure ranging from 1.25 GPa to 3.94 GPa in the two examples provided. Although these pressure values are largely over the elastic limit of the material, they highlight that the application of the Hertz contact model at global level, which yielded an average pressure of 300 MPa for the tests under modelling, is not an accurate estimation.

The Jackson and Green elastic-plastic calculations yielded contact pressure ranging from 1.60 GPa to 2.14 GPa. Compared to the Hertzian results, the model yields lower pressure in the smaller radii asperities and higher pressure in the largest asperities. This is explained by the inverse penetration-contact force relation obtained by Jackson and Green for dimensionless penetration parameter ( $\omega^*$ ) larger than 1 (as it is the case in all the results obtained). The dimensionless graph in Figure 4-43 shows that the dimensionless contact force reduces as the penetration is increased. Since the absolute penetration is assumed to be equal to all the asperities, the asperities with smaller radius will have a larger dimensionless penetration and therefore they will support a lower load (lower pressure). Consequently, the larger asperities will support a larger load (higher pressure) to meet the condition that the sum of the load carried by each asperity must be equal to the overall normal load.



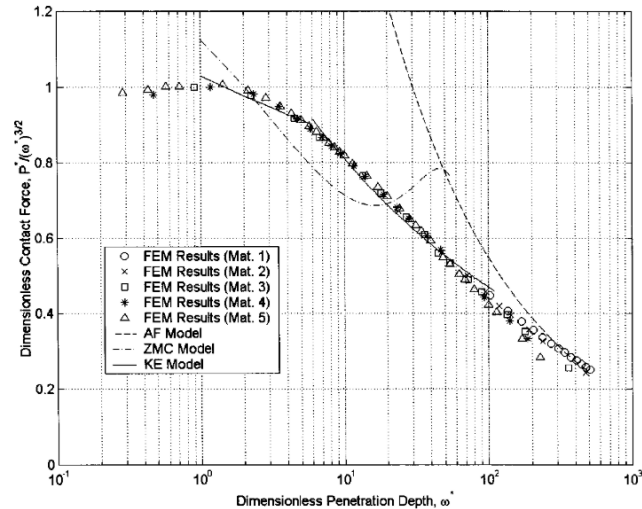


Figure 4-43: Relation between penetration and contact force (dimensionless) obtain by Jackson and Green with FEM simulations [100]

The overall deformation of the asperities calculated with the Jackson and Green model was around  $0.5 \mu\text{m}$ . Considering the typical peak-to-valley distance of the macro-asperities is two orders of magnitudes larger (a few tens of micrometres), the deformation result is consistent with the SEM images showing virgin DFL in the valleys of the surface because of the contact being limited to the asperity tips. The motivation of undertaking modelling at macro-asperity level was partly fuelled by the interest of relating asperities behaviour to contact pressure. Generally, the asperities where the lowest pressure was estimated (Figure 4-35E in Test 1 and Figure 4-36B in Test 2) showed slight changes in the DFL structures and no bond coat exposure. The highest pressure among all the tests was estimated in the macro-asperity B of Test 1, which showed both areas with exposed bond coat and areas with cracked layer (Figure 4-44) that were not observable in the other asperities under analysis. These findings are in line with the observation made previously, when discussing the influence of pressure and represent the behaviour seen on a smoother surface at higher pressure, now occurring locally for a rougher surface and a lower global pressure.

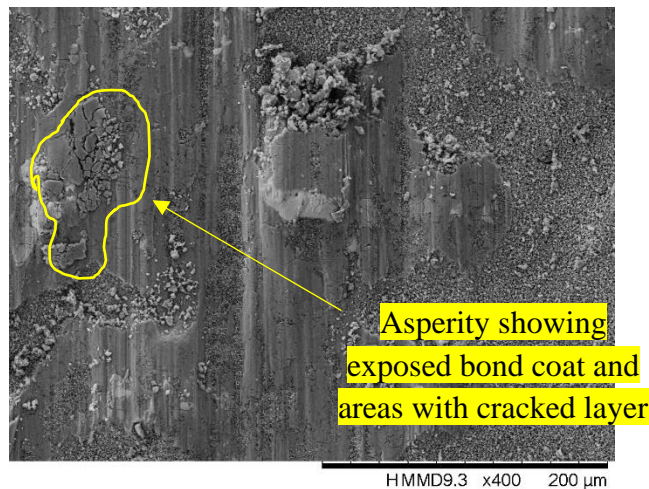


Figure 4-44: Asperities with the highest estimated contact pressure (highlighted in yellow). The asperity shows exposed bond coat and areas with cracked layer

The potential factors of misestimation of the contact model must also be pointed out. The calculation is representative of the pre-test contact pressure, before wear flattens the summit of the asperities, causing the contact pressure to drop. This agrees with the contact area observed in the images being larger than the theoretical values calculated with the contact models. This was the case at both local and global levels. Further, modelling the macro-asperities as sphere-on-flat point contacts is a convenient simplification to take advantage of existing single asperity models, avoiding more computationally expensive methods such as FEA simulations. However, some of the topographical features are dissimilar to hemispheres, having elliptical or irregular shape, and therefore are subjected to misestimations.

The mechanical properties of the Ti-6Al-4V were used, for consistency with the calculation carried out in the Nottingham work. This is a strong assumption given that the diameter of the modelled asperities is comparable to the thickness of the coating layers. The effect of shear stress due to the reciprocating motion and the compliance of the substrate are not taken into consideration.

#### 4.5.4 Surface topography and failure

It has been highlighted that significant local pressure disparities exist at the interface between the two samples. This triggers the MoS<sub>2</sub> lubrication mechanism differently and causes some areas to shear more easily than others. It has also been discussed that the overall CoF estimated is a net response of the overall surface and it is indicative of the average behaviour of the asperities. The variability of the tangential force observed during the tests repetition can be related to this effect, which is dependent on the initial topography of the surface. As mentioned, the absence of failure and the high CoF measured can both be linked to the sample's topography. On the smoother surfaces (samples without bond coat) the interface experiences a rapid pressure drop as the contact area is increased due to wear. As an example, the wear scar of the 450 MPa test width measured 1.123 mm (Figure 4-45), whilst the theoretical Hertzian

contact area (at the beginning of the test) was around ten times smaller (0.1286 mm). The resulting pressure drop is believed to arrest the progression of the wear damage and delay the onset of failure. Further, the limited contact pressure and the reduced debris availability restrain the sinter layer formation, hence the high CoF.

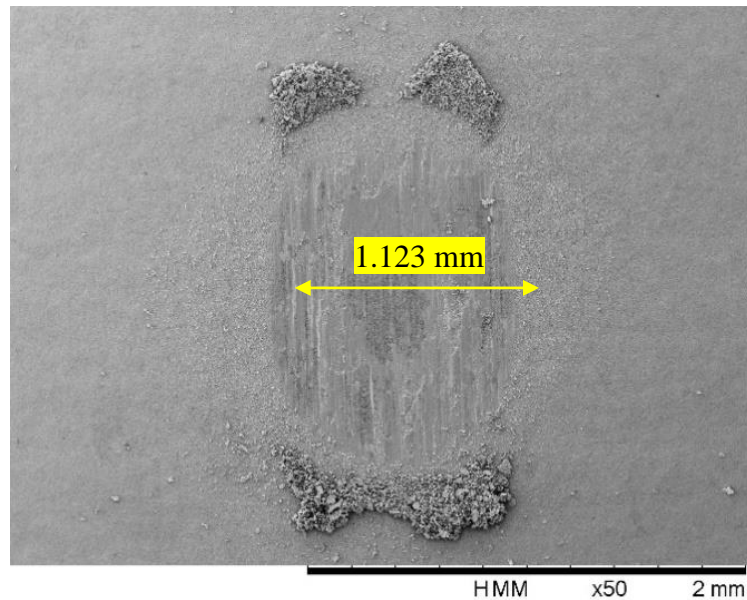


Figure 4-45: Approximate measurement of Fithe wear scar width

On a wavy sample, the interaction between the two surfaces takes place at the tip of the macro-asperities. The average pressure at these locations is higher than the corresponding value on a flat sample, promoting MoS<sub>2</sub> compaction and sintering into a layer. The pressure at the asperities drops at the beginning of the tests as the asperities summits are flattened, but not to the extent of a flat surface, as schematically represented in Figure 4-46.

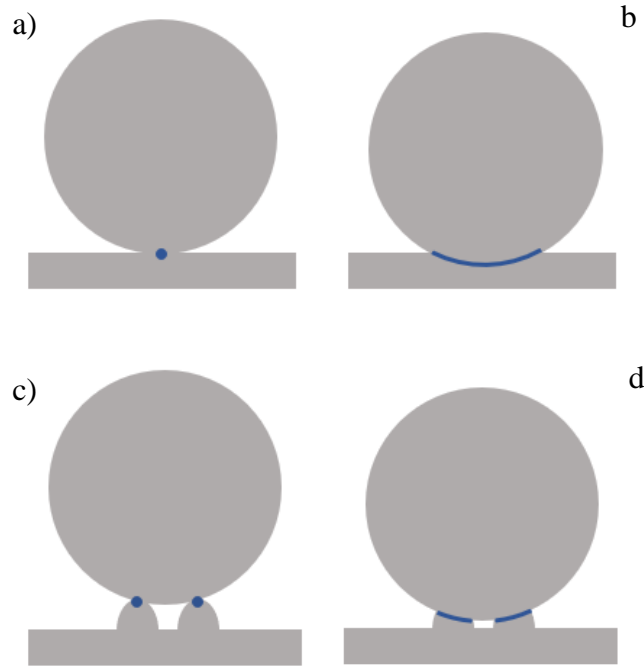


Figure 4-46: Schematics of the contact area change due to wear. a) Flat surface before wear, b) Flat surface after wear, c) Wavy surface before wear, d) Wavy surface after wear

Considering the high initial contact pressure and the moderate pressure drop, it is proposed that the pressure is still high enough to achieve failure at macro-asperity level. This is also suggested by the cracks observed in some asperities. As the material removal progresses, other parts of the surface come into contact and the interface comprises of a combination of asperities at different stages of their lubrication mechanism. As those that have failed will be harder to shear, a higher net CoF is measured in the samples with bond coat. When all the asperities are completely flattened, the progression of the mechanism is analogous to a smooth surface, reducing the contact pressure to a point that global failure cannot be achieved.

#### 4.5.5 Test arrangement

Although ball-on-flat is an advantageous tribological assessment, the previous discussion has highlighted its limitations for this specific investigation clearly. The limited contact area at the interface between the specimens was found to be inadequate due to the surface irregularities, causing poor test repeatability and preventing global failure from occurring. This was also thought to cause poor debris entrainment, which reduced availability within the wear track for the layer formation. Another limitation was the impracticality of analysing the countersurface due to inevitable damage of the sphere when removed from its holder. This is important as it would provide further insight into the mechanism.

The experiment's results provided awareness of the influence of the contact size and configuration, as well as an understanding of the contact pressure and topography influence on a ball-on-flat test configuration. Considering its limitations however, the investigation is

continued on a different test rig that allows testing at a larger scale on a more conformal contact, aiming to overcome the problems incurred in these experiments. Furthermore, the rig allows for ambient temperature control.

## 4.6 Summary

The mechanical behaviour and the lubrication capabilities of the fan blade coating system have been studied by performing ball-on-flat reciprocating tests. The findings can be summarized as follows:

- The main lubrication mechanism was observed to be the extrusion and compaction of DFL particles into a layer, consistent with most of the works reported in the literature. Broad similarities were observed between the tests and the Trent800, with the morphology of the DFL layer at higher pressure resembling the cracked-structure observed in the highly stressed areas of the Trent800 root surface.
- The  $Q^*/P$  ratio decreased as the contacting load was increased. As  $Q^*/P$  is representative of the CoF in the gross-slide regime, this confirmed that the lubrication effect was more efficient at higher contacting loads. This was associated to a larger coverage of DFL layer onto the wear track.
- The wear scars were observed to be a composition of: as-applied DFL, DFL layer, loose DFL particles, exposed bond coat, and out-of-contact areas. On rougher samples, dissimilar composition and mechanical behaviour occurred at macro-asperity level, which was thought to cause poor test repeatability.
- A contact model was developed to estimate the contact pressure on the macro-asperities. The pressure was estimated in the order of a few giga-pascal, highlighting potential unrepresentativeness of the test's conditions. Moreover, the pressure disparities among the macro-asperities observed was related to the behaviour dissimilarities.
- The work has given insight into the behaviour of the coating, particularly with regards of the effects of pressure and surface roughness. However, weak debris entrainment capabilities, small contact areas respect to asperity size, and difficulties in estimating coating life were recognised as limitation of the test configuration. Thus, the investigation is continued on a different test platform.

## 5 Scaled-disc testing

Studying the influence of the contact pressure on the fan blade coating system behaviour was the main purpose of the previous chapter. Better lubricity was observed at higher contact pressure as the coating was compacted into a low-friction layer. However, the ball-on-flat contact arrangement was identified as inappropriate for a comprehensive analysis of the tribological behaviour of the coating, suggesting a different configuration was needed. For this reason, a test platform has been developed at the University of Sheffield by the author as part of this research project to accommodate a blade and two scaled disc specimens, which fret against each on a simplified 2-D blade-disc interface. The machinery can reproduce low cycle fatigue loading and offers the possibility to test under controlled environmental conditions.

The test conditions were based on a combined analysis of the ball-on-flat tests findings and some additional data provided by Rolls-Royce. The work also includes a set of interrupted tests at critical points of the life, which allows for investigation of the wear progression. The Rolls Royce data was generated with an experimental set-up to investigate several coating systems, which includes the fan blade coating system. The analysis of this data is provided in section 5.3.1 and the test rig detailed in 5.2.1. The data provides validation of the new University of Sheffield based test-rig by comparing results from it to similar tests carried out by Rolls Royce.

### 5.1 University of Sheffield fan blade test rig

*To counter some of the limitations explored in Chapter 4 a new test rig has been built at The University of Sheffield. This rig aims to mimic the geometry and entrainment of debris to the contact of an actual fan blade interface closer than the ball-on-flat tests.*

#### 5.1.1 Rig configuration

The rig (Figure 5-1) has been built on a tensometer frame (NENE 1.2 kN) that can deliver oscillatory movement along the vertical direction through a hydraulic actuated system.

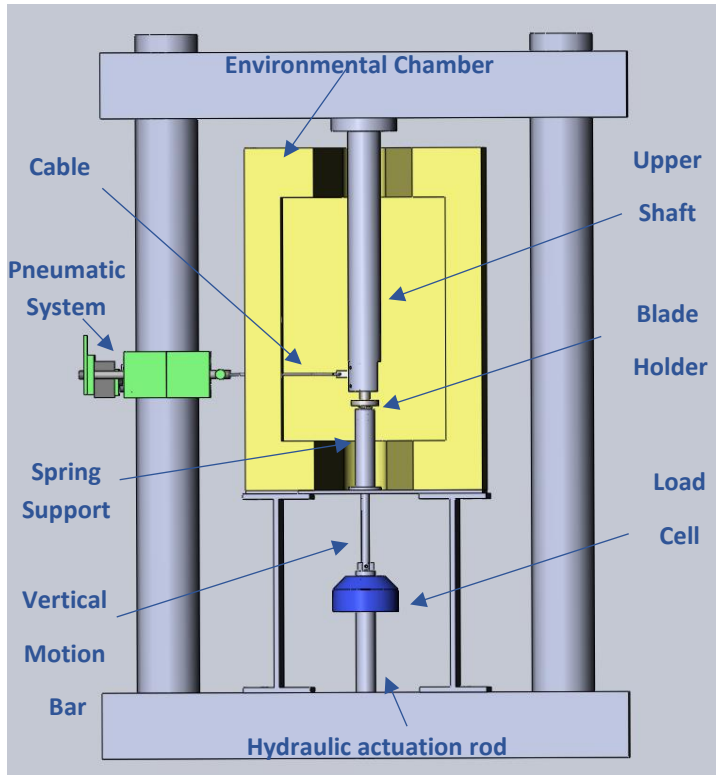


Figure 5-1 Fan blade test rig

A shaft (upper shaft) is connected to the top cross beam, which accommodates the two-disc specimens and it is held stationary during the tests. The bottom rod of the tensometer is driven by the hydraulic actuator and provides the movement to the blade holder, where the blade is connected to (Figure 5-2). A pneumatic system provides a load along the horizontal direction which is applied to the blade using a cable. Two I-beams are used to hold an environmental chamber that surrounds the specimens and part of the fixtures.

In order to simulate centrifugal load, the blade is pressed against the disc specimens at a constant load using the pneumatic system. The maximum horizontal load achievable is 1200 N. While the load is applied, the blade is fretted against the disc specimen to simulate the effect of the vibration. The environmental chamber provides temperature control within the range from -180 °C up to 600 °C.

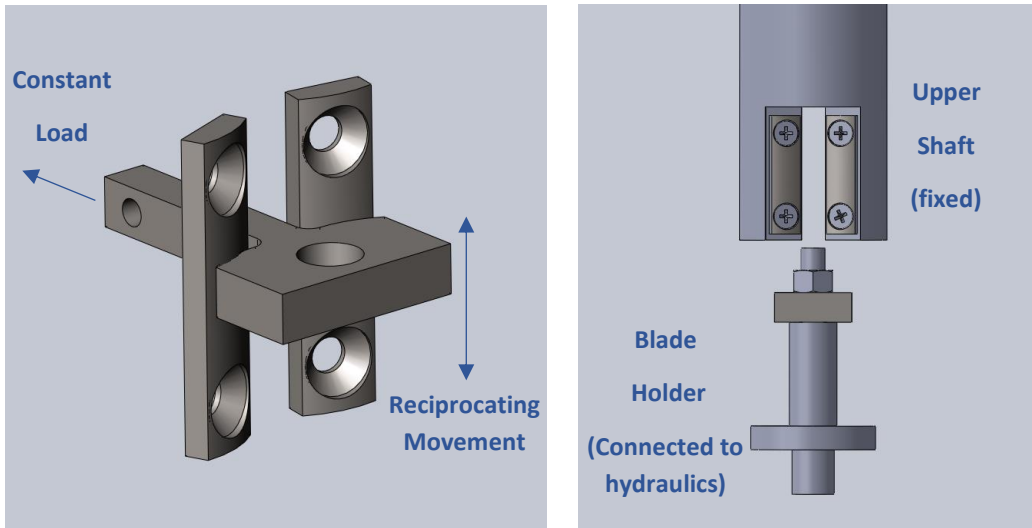


Figure 5-2 Specimens loading and relative movement (left), specimen connections (right)

The vertical motion is transferred from the hydraulic system to the blade holder with the system shown in Figure 5-3. A rigid connection between the parts would restrict the movements of the blade on the horizontal plane, and an articulated configuration is therefore used instead. This ensures effective transfer of the horizontal load exerted on the blade into the contact and improves the contact alignment.

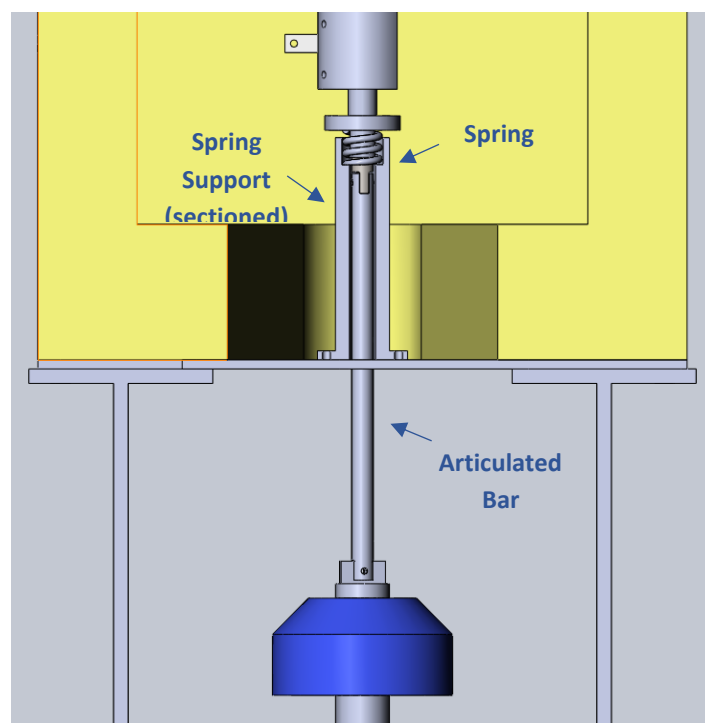


Figure 5-3 Vertical movement transmission system.

A return spring has been used to guarantee efficient vertical motion transmission from the hydraulic system to the blade specimen holder. Its purpose is to maintain the articulated



connection in a state of tension (rather than alternating tension and compression at each cycle), limiting the loss of displacement occurring in the clearances of the joints.

### 5.1.2 Control systems and data acquisition

The rig is operated through two different hardware, one for the horizontal load and another for the vertical motion. The pneumatic system is controlled through a LabView program with a closed loop system that adjusts the air pressure to minimise the load error with respect to the set point value. The reciprocating movement is controlled through the tensometer controller (MOOG). The position of the bottom rod is measured with a linear variable differential transformer (LVDT) and the vertical force with a load cell. A proportional integrative derivate integral loop provides position control of the system. The commanded position, feedback position and feedback force are recorded during the tests.

### 5.1.3 Contact arrangement

The disc and the blade specimens are shown in Figure 5-4 along with a top view of their relative position when assembled on the rig, realising a line contact (cylinder on cylinder). Although the contact geometry is different from the dovetail joint configuration, it was chosen as it limits misalignments and achieves high contact stress at moderate normal load values.

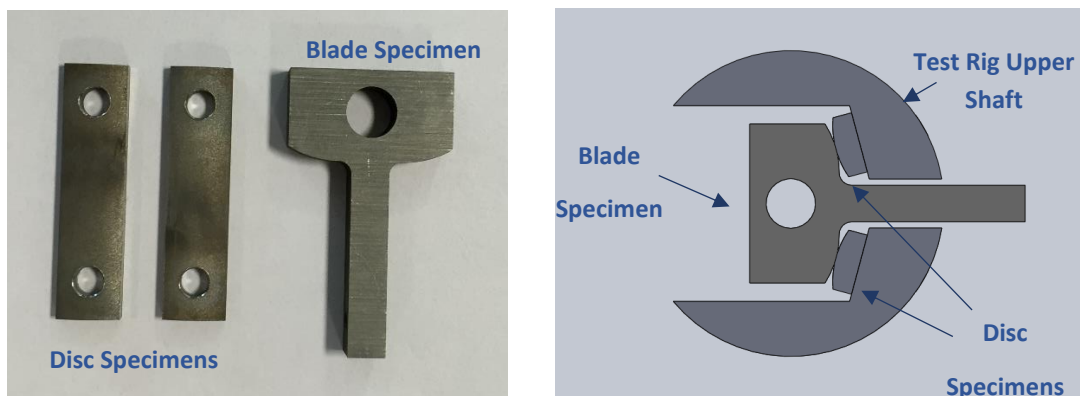


Figure 5-4: Disc and blade specimens (left), contact arrangement within rig (right)

Hertz theory was used to evaluate the relationship between geometry, material properties, normal load and contact pressure which is shown in Figure 5-5.

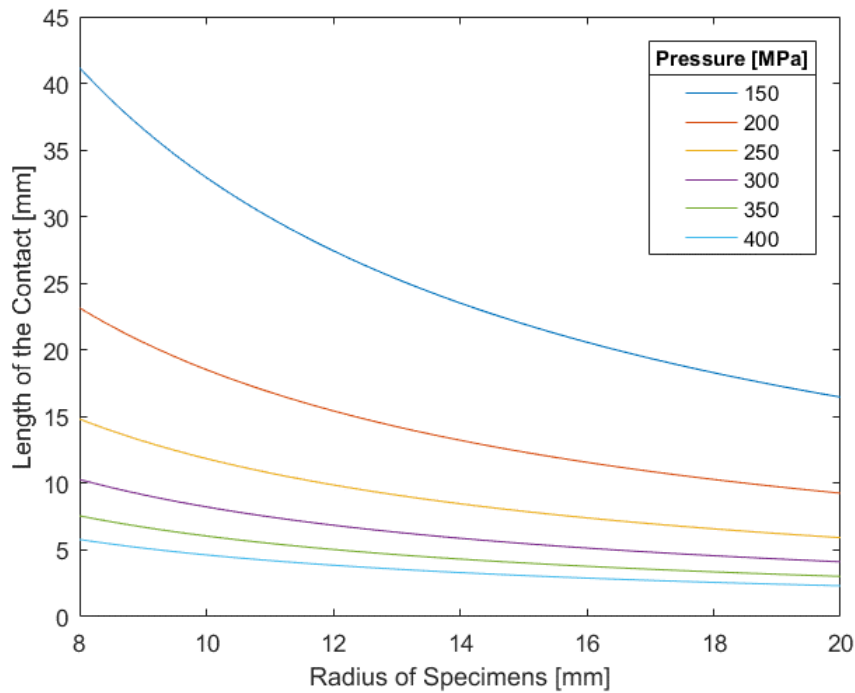


Figure 5-5 Geometry – Contact pressure relationship (Normal load 338N).

The graph was produced for the maximum pulling load (1200 N, corresponding to 338 N on each side of the contact) and for the radius of the blade and disc specimens having the same value. The graph shows that the contact pressure increases as length and radius decrease. The final length adopted was 6.35 mm (1/4”), being the best among the choices restricted by the commercial dimension available (titanium plate). By setting the radius to 15 mm it is possible to cover the whole test pressure range, with moderate values of the pulling load (maximum 694 N). This is beneficial as it avoids significant bending of the upper shaft and therefore limits misalignments along the vertical direction.

#### 5.1.4 Data processing

Data acquired in test must be processed to calculate the evolution of the coefficient of friction throughout the test. A free body diagram of the blade is shown in Figure 5-6.

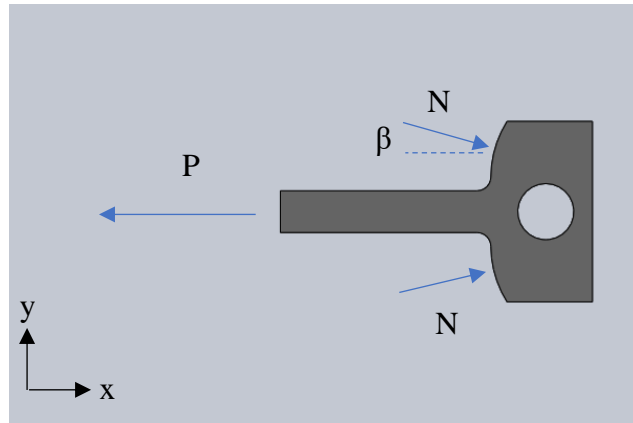


Figure 5-6 Blade specimens free body diagram (horizontal plane)

Resolving forces in the x-direction, the normal load,  $N$ , on the contact is related to the pulling load,  $P$ , exerted on the specimen  $P$  by the following relationship:

$$N = \frac{P}{2} \cos(\beta)$$

Equation 5-1

where it should also be noted that the components of the load,  $P$ , in the  $y$ -direction are considered equal and opposite. The force along the vertical direction measured by the load cell is due to friction between the specimen and the spring return force, which are both functions of the specimen displacement. In order to obtain the friction force, a reference signal must be taken before each test, by recording the spring response when no contact occurs between the specimens. Then, the test is carried out and a measurement signal is acquired (friction plus spring). The friction force is obtained by subtracting the reference from the measurement signal, after synchronisation of the two captured signals.

Finally, the coefficient of friction,  $\mu$ , is calculated for each cycle as the ratio of the friction force,  $F$ , (acting on one side of the blade) and the normal load.

$$\mu = \frac{F}{N}$$

Equation 5-2

## 5.2 Test Methods

### 5.2.1 Rolls-Royce SCITEK

An experimental investigation of anti-fretting coatings behaviour has been carried out at Rolls-Royce as part of an internal research for the compressor blade contact. The reason for its inclusion in this thesis is to provide validation of the new University of Sheffield based test rig by being able to compare results as the SCITEK rig is even closer to a realistic contact. Comparisons between the test rigs will be discussed in section 5.4.

The experimental plan was set out to study several coating systems, over several combinations of pressure and displacements amplitude. Among these tests, the fan coating system was also tested.

The tests were conducted on a flat-flat contact, using a newly developed test platform called SCITEK. This is a commercial test rig manufactured by SCITEK Consultants Ltd. [108], and commonly referred to simply as the SCITEK test platform. The concept of such configuration is the same as the DARTEC apparatus [7], [70]. The test contact arrangement consists of a central square prism of section 10 mm x 10 mm, with two other samples pressed on either side to achieve two flat-flat contact interfaces.

The test rig set up is shown in

Figure 5-7. The central specimen is reciprocated whilst a constant load is exerted to the lateral specimens.

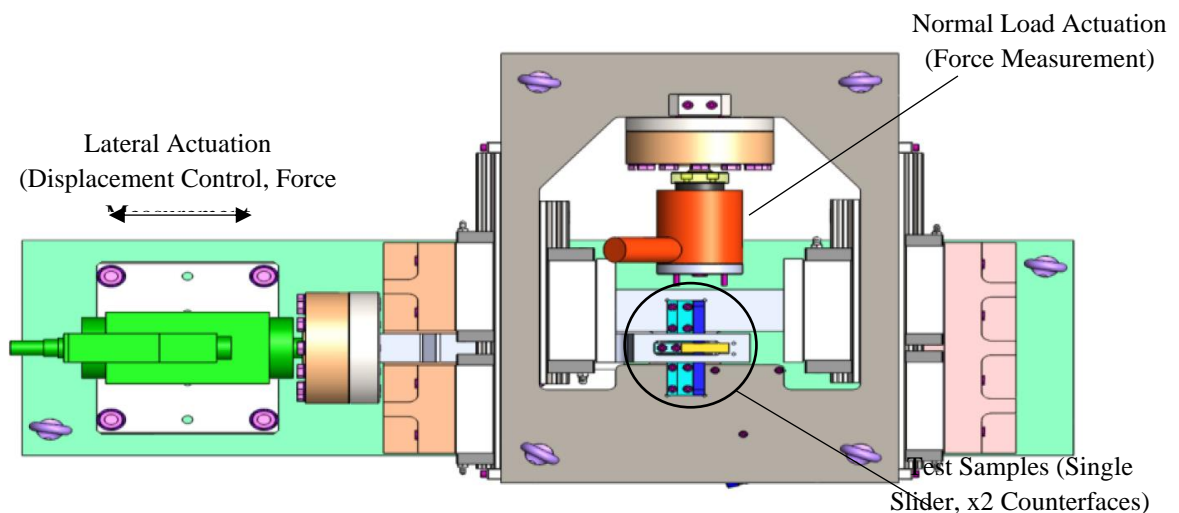


Figure 5-7: CAD model of the SCITEK test rig [108]

The samples and the test data were made available for three different average contact pressures (200, 350 and 500 MPa), each tested with a displacement amplitude of 0.200 mm, 0.125 mm and 0.050 mm. The test matrix included three repeats for each test configuration, however, only two repeats are hereby reported for some pressure and displacement combination as the data was provided whilst the testing at RR was ongoing.

### 5.2.2 University of Sheffield fan blade rig

Samples were manufactured from a Ti-6Al-4V grade 5 plate by electro discharge machining (EDM) and they will be grit-blasted and coated according to the Rolls-Royce procedure. As the EDM produces microstructural changes in the surface due to high thermal gradient, the grit blasting process is also important to remove the material affected by the process, which consists of a layer thinner than 100  $\mu\text{m}$  [109].

Fretting parameters will be 2.5 Hz and 300  $\mu\text{m}$  as for the tribometer tests for consistency. The test temperature will be set to 100  $^{\circ}\text{C}$  (estimated operating temperature) and held constant throughout the whole duration of the experiment using an environmental chamber. Tests will be carried out at 300 MPa contact pressure with some tests at 200 MPa in order to investigate the two main areas of the root described in Section 3.2.

## 5.3 Results

### 5.3.1 SCITEK

The tests were run until the coating showed high frictional behaviour ( $\text{CoF} \geq 0.4$ ) or until 20,000 cycles as shown in Figure 5-8. In the former case, a three-stage lubrication curve was observed, contrary to the ball-on-flat test arrangement where only two-stage curves were observed (Figure 4-19 in Section 4.3.2). Further, all the tests showed higher CoF at lower pressure during the secondary stage. As shown in the Figure, multiple repeats were also performed in each case to determine consistency of test outcome given the at times variable nature of low friction behaviour.

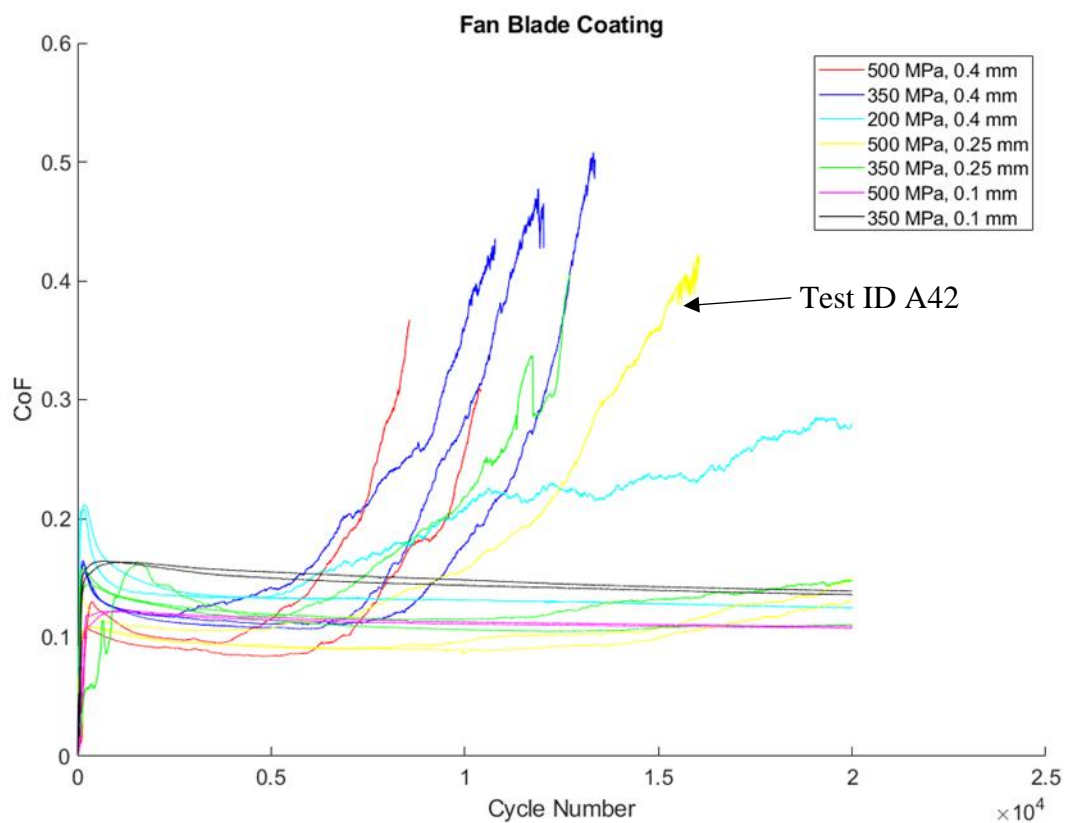


Figure 5-8: CoF of the fan blade coating system tested on the SCITEK rig tested by RR

It can be noted that failure does not always occur consistently for a given combination of test parameters. Whilst all specimens failed under some conditions (such as 500 MPa, 0.400 mm)

and showed good CoF progression repeatability, in other cases (500 MPa, 0.250 mm) a distinct outcome occurred with only a portion of the samples failed. A brief investigation of the worn samples is proposed in the next section to aid the analysis of the test results.

The samples showing unrepeatable behaviour were inspected under the SEM (see Section 3.1.1 for details). The tests chosen for further analysis are:

- Contact pressure = 500 MPa, displacement = 0.250 mm (Figure 5-9A-B)
- Contact pressure = 350 MPa, displacement = 0.250 mm (Figure 5-9C-D)

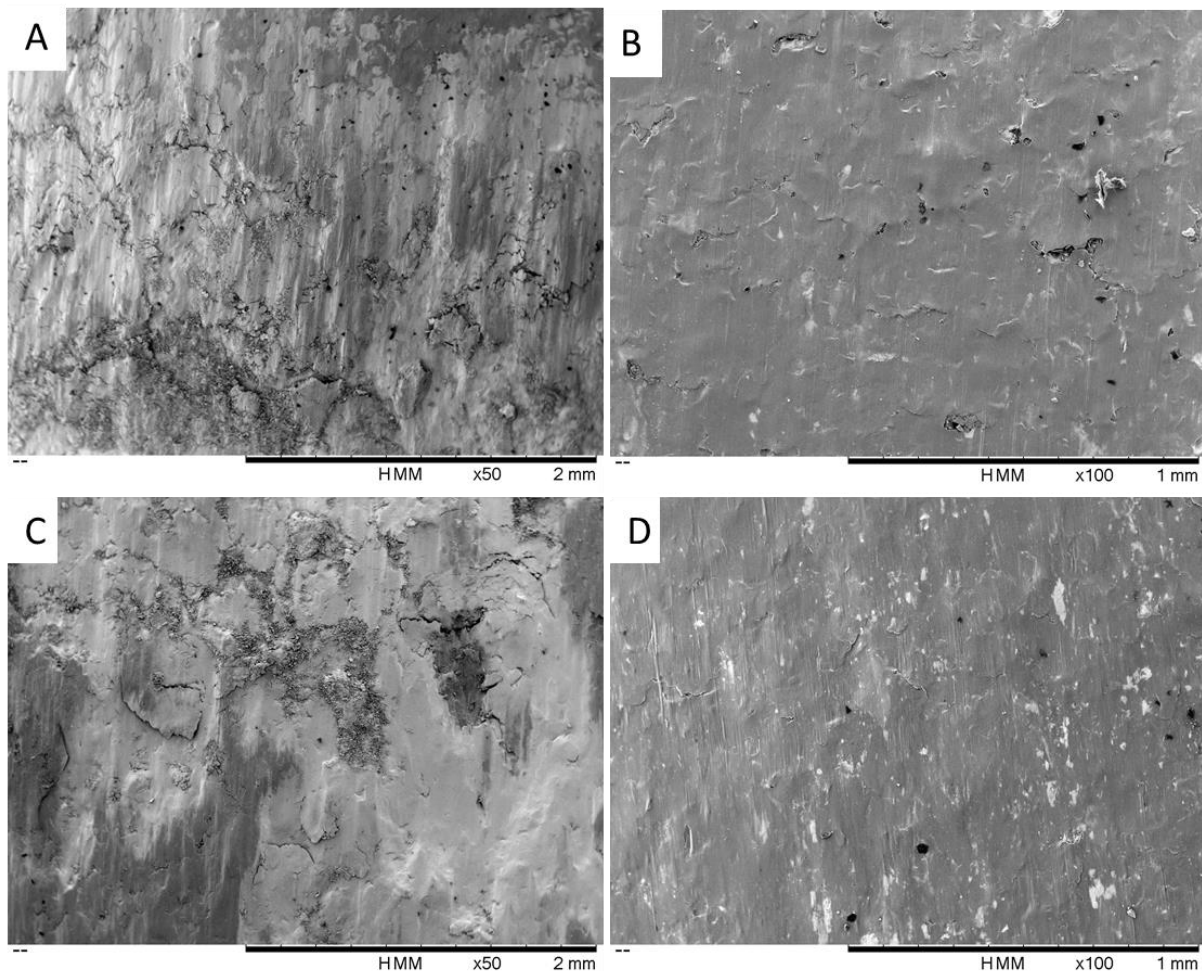


Figure 5-9: Contact pressure = 500 MPa, displacement = 0.250 mm A) Test ID 42 left specimen B) Test ID 43 left specimen, Contact pressure = 500 MPa, displacement = 0.250 mm C) Test ID 53 right specimen, D) Test ID 52 right specimen

As shown in Figure 5-9, there is a clear correlation between lubrication and surface features. A sintered layer formed on the surface of the low CoF tests (Figure 5-9B and Figure 5-9D), whereas high friction derived from a ploughed metal to metal interface (Figure 5-9A and Figure 5-9C) occurred on the tests that failed.

The samples were further characterised by profilometer. Having observed a large variability of the surface waviness in the ball-on-flat samples, it is of interest to assess if the SCITEK samples also differ among each other and, if differences can be correlated to the CoF progression.

A total of 6 profile measurements were performed on each side of the central specimens. In order to ensure a representative measurement of the tested area the measurements were taken in the unworn area in proximity of the wear scars: three just above and three just below. The profiles, oriented normally to the sliding direction, were 8 mm long, spaced 1 mm from each other, with the closest to the wear scar being 1 mm from the edge.

*The average roughness for the left and right specimens is shown in Figure 5-10. Test ID 41 and 43 exhibit similar CoF behaviour in Figure 5-8 yet have vastly different roughness. This means that for this set of specimens, different levels of roughness do not explain the differences seen in Figure 5-9A and B. Further analysis of the different roughness of the different tests that showed unrepeatable behaviour (for example Test ID 51,52,53) should be carried out to explore this further as it is difficult to draw conclusions from one set of specimens. Additionally, the waviness of the specimens should be explored.*

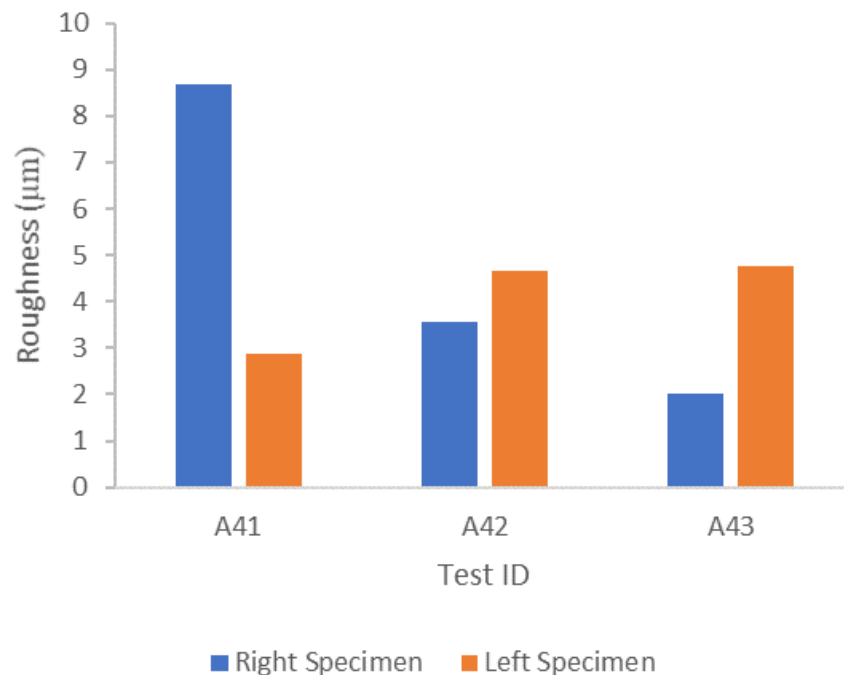


Figure 5-10: Roughness of the Left and Right specimens for Contact pressure = 500 MPa, displacement = 0.250 mm

*Figure 5-11 shows the results from testing using specimens solely coated with DFL without the bond coat present. The tests show much closer agreement to each other compared to the results presented in Figure 5-8. The CoF evolution is also much simpler that shown in Figure 5-8, after a short running-in period, it rises consistently as the coating is worn away. Decreasing contact pressure for the same displacement results in failure occurring quicker. Decreasing displacement for the same contact pressure results in the coating lasting longer.*

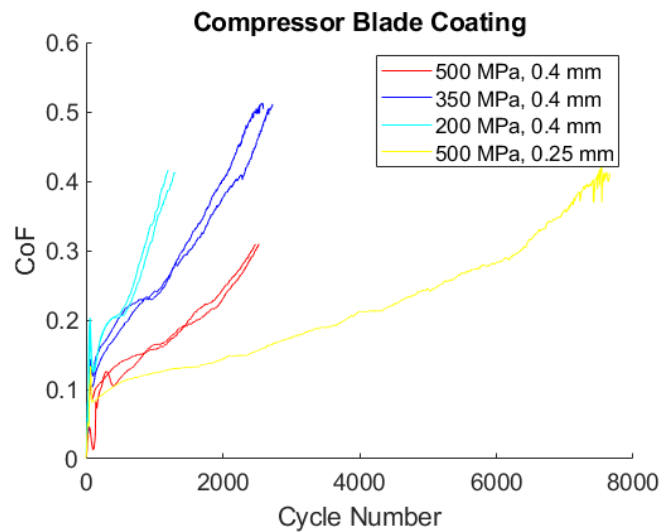


Figure 5-11- DFL only specimens (no bond coat) for variety of pressures and displacements

### 5.3.2 University of Sheffield fan blade rig

Figure 5-12 shows how the CoF changes as cycle number increases for different length tests. All these tests were at 300 MPa contact pressure and 150  $\mu\text{m}$  displacement amplitude. All the tests show an initial rise in CoF before decreasing to a steady point, this appears as a “hump” in the graph. This hump is apparent in Figure 5-8, but is much smaller on the SCITEK rig. The amount of cycles this hump lasts for is variable. Additionally, for one of the long tests the decrease in CoF did not occur (light blue line). The 10k tests were too short to establish a steady state. The 90k test was paused and specimens unloaded. This resulted in contact between the specimens being broken and any wear debris that was entrained in the contact was lost. This meant that when the specimens were brought back into contact wear occurred at a much higher rate and resulted in an increase in CoF. The 160k test (dark red line) showed a third stage where the CoF increased relating to the lubrication layer breaking down resulting in metal-metal contact. The variability between the tests is the subject of further analysis in this section and will be discussed fully in section 5.4.



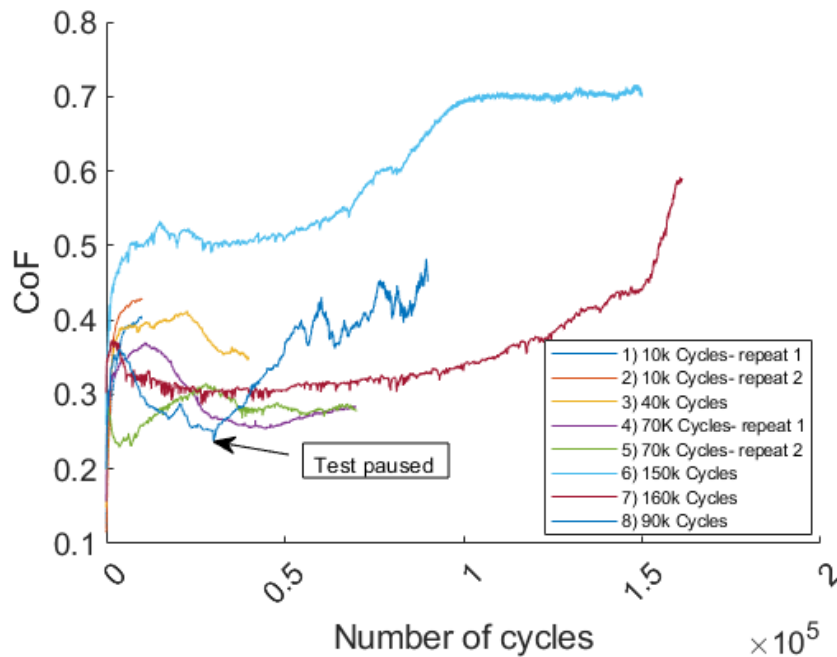


Figure 5-12: CoF evolution, nominal contact pressure 300 MPa, displacement amplitude 150  $\mu\text{m}$

Figure 5-13 shows the wear scars at the end of each test length at two different zoom levels. There is a clear progression in the wear mechanisms as the number of cycles increases. Initially, the platelet structure of the DFL is largely intact (Figure 5-13B). In Figure 5-13D the DFL layer has become more compacted and mixed with wear debris from the bond coat, there are also areas where the bond coat itself is showing through. Figure 5-13F shows more extensive DFL/bond coat compaction to form a larger glazed area. There are also larger areas of bond coat showing with some small cracks starting to appear. Finally, Figure 5-13H shows extensive cracking with only small remnants of the DFL and bond coat remaining at the edge of the contact. This is consistent the removal of the glazed area and the increase in CoF seen near the end of the test in Figure 5-12.

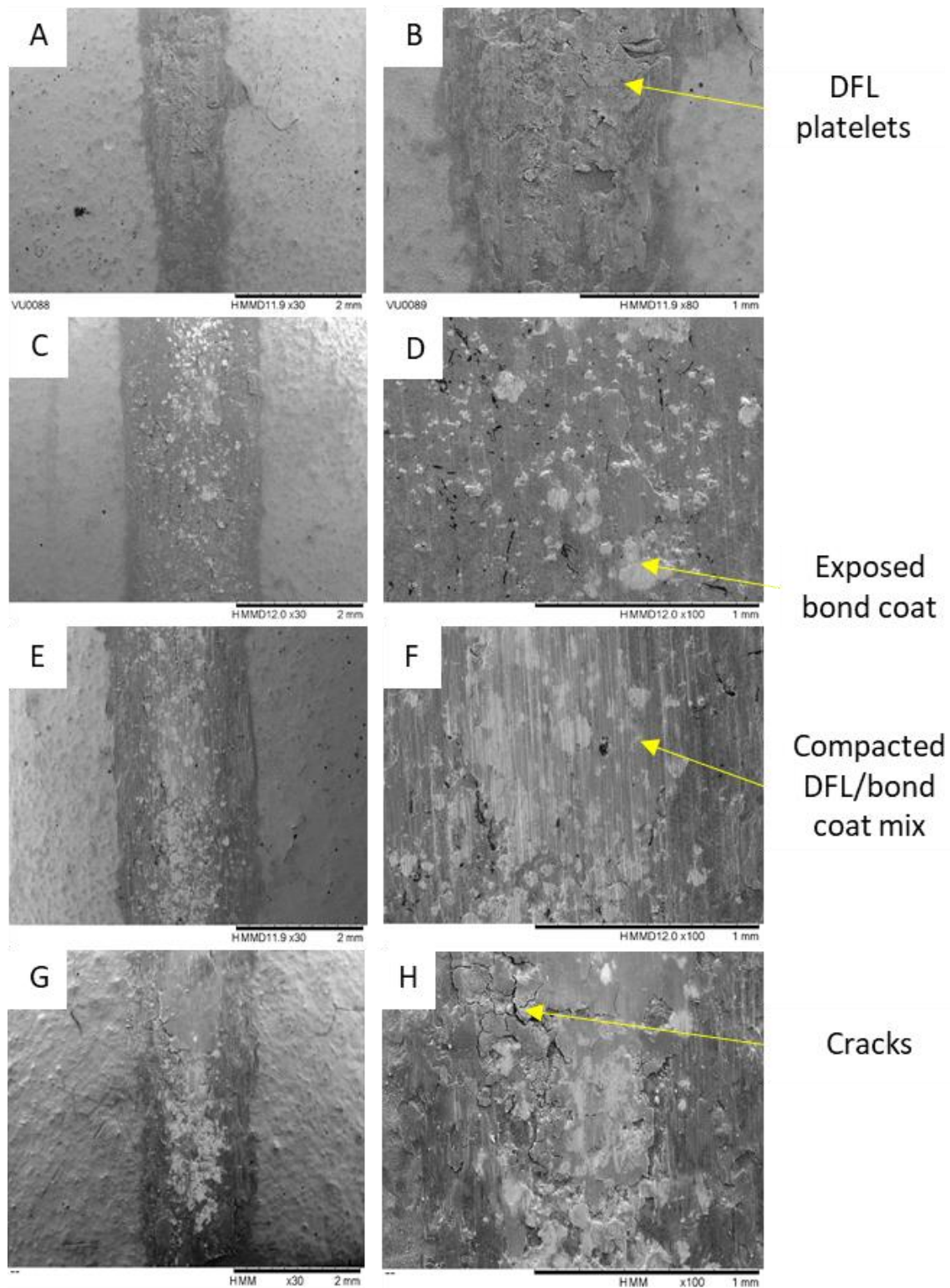


Figure 5-13: Wear scars for blade specimens at 300 MPa, 150  $\mu$ m tests (test numbers relate to numbers in Figure 5-12) A) Test 1- 10k cycles, 30x zoom, B) Test 1-10k cycles 100x zoom, C) Test 3- 40k cycles 30x zoom, D) Test 3- 40k cycles 100x zoom, E) Test 4- 70k cycles 30x zoom, F) Test4- 70k cycles 100x zoom, G) Test 7- 160k cycles 30x zoom, H) Test 7- 160k cycles 100x zoom

Figure 5-14 shows the results of EDX analysis of the blade specimen after 10k cycles. It shows that despite the surface appearing different there is a relatively consistent amount of DFL (along with an oxidation layer) remaining on the surface at the four areas tested. This matches the conclusion drawn from Figure 5-13A and B.

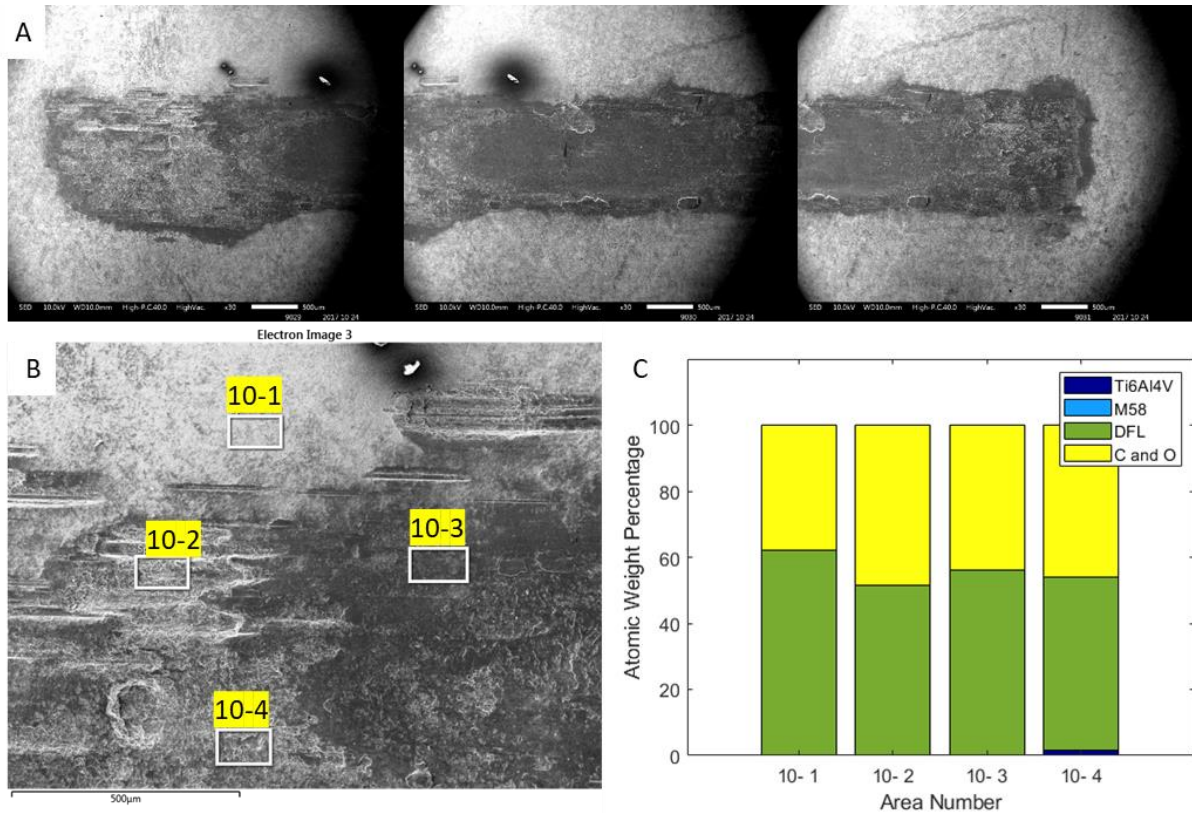


Figure 5-14: EDX analysis of blade specimens for 300 MPa, 150 µm tests after 10k cycles A) SEM image of whole wear scar, B) SEM image showing areas analysed C) composition of different areas

Figure 5-15 shows the results of EDX analysis of the blade specimen after 40k cycles. There are clear differences between the three areas analysed with area 40-1 and 40-2 in Figure 5-15B showing some bond coat is present at the surface as well as the DFL. Whereas 40-3 shows only DFL present. This area is at the edge of the wear scar so is likely to have less contact pressure applied to it compared to other areas. Additionally, some of the DFL from the higher wearing areas of the wear scar could have been pushed to edge of the contact. Again, this supports the findings in Figure 5-13C and D.

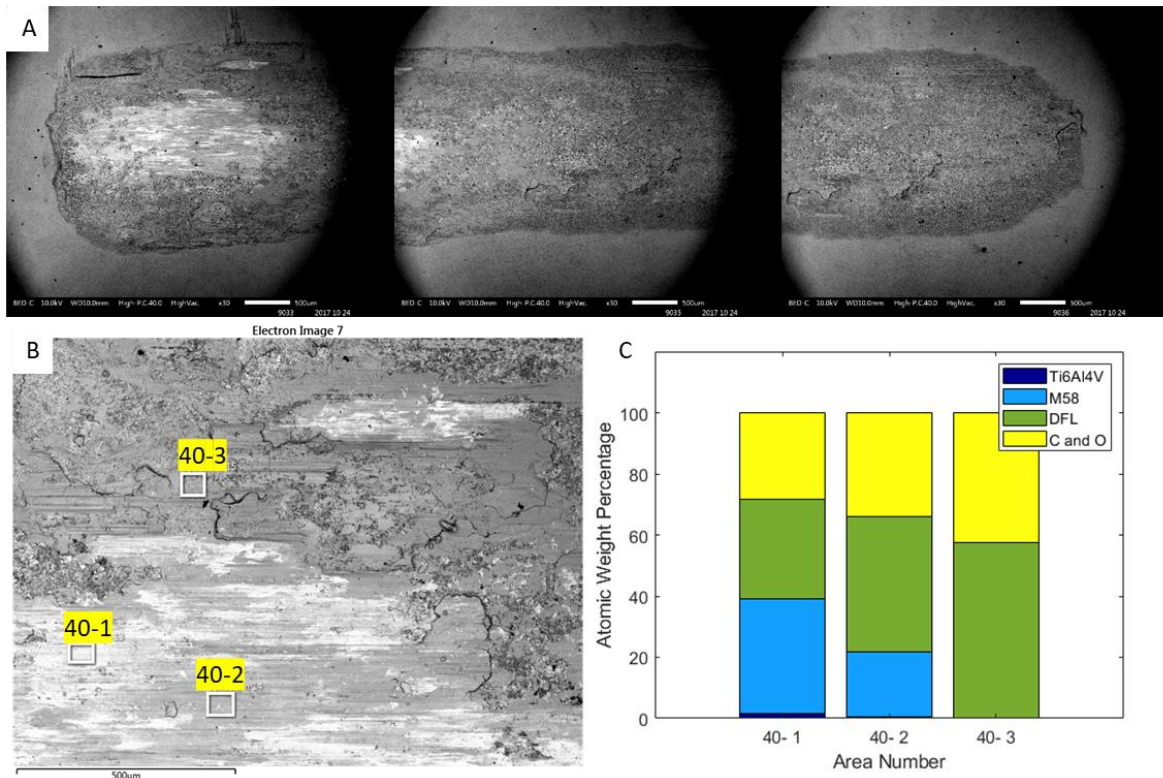


Figure 5-15: EDX analysis of blade specimens for 300 MPa, 150  $\mu\text{m}$  tests after 40k cycles A) SEM image of whole wear scar, B) SEM image showing areas analysed C) composition of different areas

Figure 5-16 shows the results of EDX analysis of the blade specimen after 70k cycles. It shows that there are some areas where the DFL and bond coat are in very small quantities and that the base alloy accounts for a large portion of the measurement (70-1 and 70-2). If the lubrication layer is thinner than the penetration depth of the measurement beam then the alloy will appear in the results. This means it is unclear if there is alloy under the surface of a very thin layer of lubrication. Area 70-3 shows a mix between the bond coat and DFL which is similar to some of the areas in Figure 5-15 (40-1 and 40-2). It also shows that there are areas where the DFL layer is present with no bond coat showing through (70-4) similar to 40-3 in Figure 5-15.

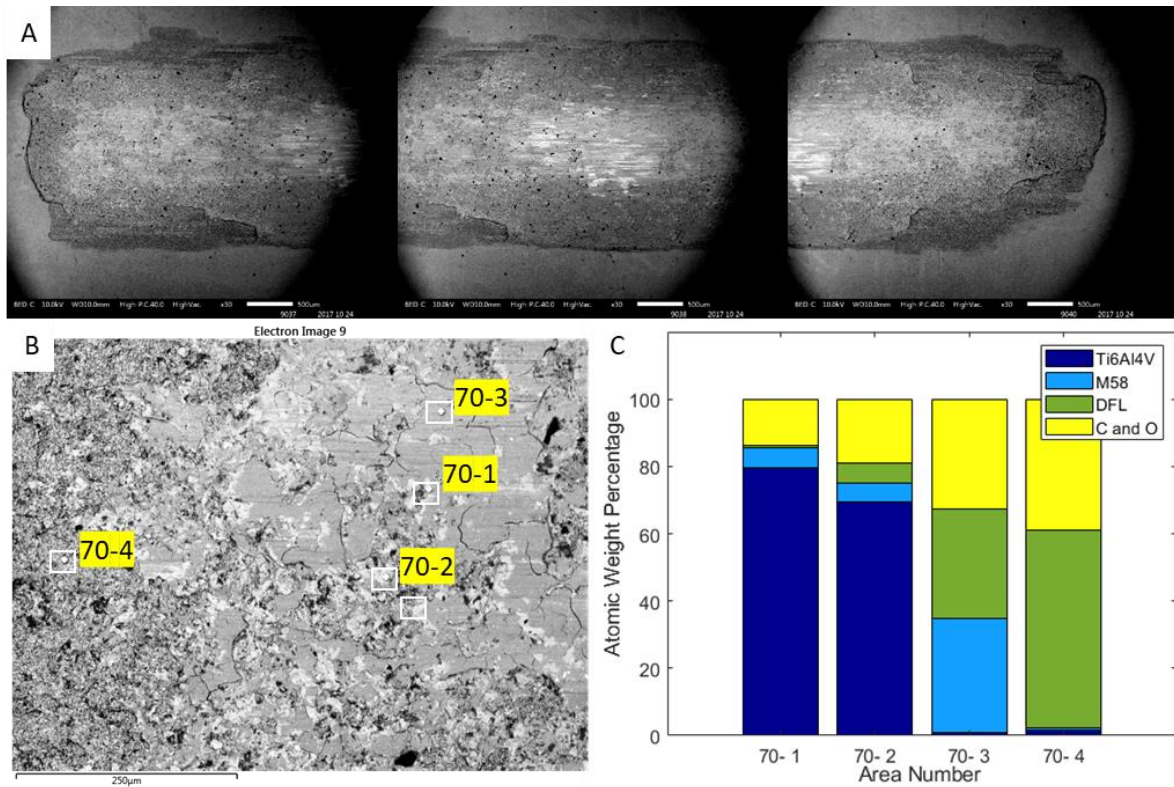


Figure 5-16: EDX analysis of blade specimens for 300 MPa, 150  $\mu\text{m}$  tests after 70k cycles A) SEM image of whole wear scar, B) SEM image showing areas analysed C) composition of different areas

Figure 5-17 shows the results of EDX analysis of the blade specimen after 90k cycles. As in the previous EDX analysis there are differences between the areas tested. 90-1 and 90-2 have some of the bond coat showing through (and some base alloy in 90-1) whereas 90-3 and 90-4 there is only DFL and oxidation layers. 90-3 and 90-4 are at the edge of the contact zone which means it has a lower contact pressure compared to the centre of the contact. This is similar results as seen in Figure 5-15. It should be noted that the 90k test was stopped halfway through the test and unloaded which made it perform differently to the other tests.

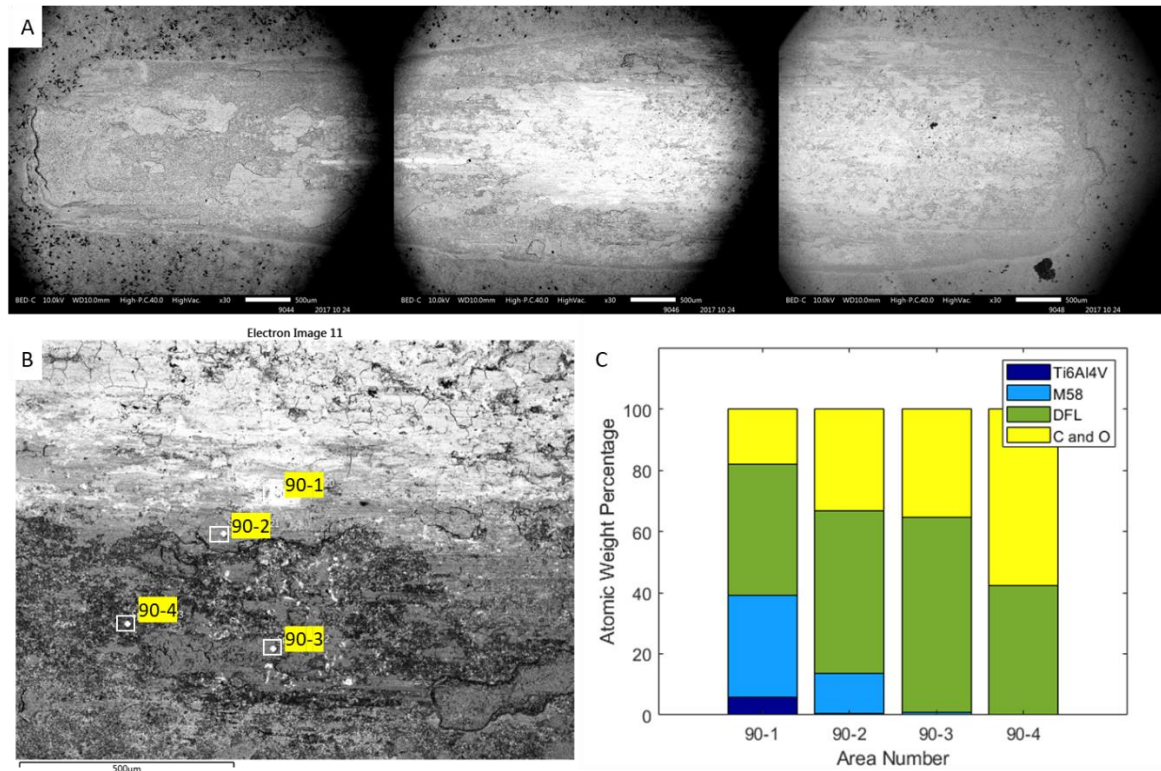


Figure 5-17: EDX analysis of blade specimens for 300 MPa, 150  $\mu\text{m}$  tests after 90k cycles A) SEM image of whole wear scar, B) SEM image showing areas analysed C) composition of different areas

The siting of the areas to be analysed in Figure 5-14- Figure 5-17 is an important factor. It can be seen in the SEM images of the whole wear scar that there are variations across it therefore the elemental analysis is useful to compare the make-up of those chosen points and identify what those features are but cannot be used to compare between the wear scars on a global level. So far, only the blade has been analysed, this is to try to ascertain the role the bond coat plays in forming the glazed layer. A Fischerscope XRF machine has been used to measure across the whole wear scar on both the left and right specimens and for the blade and the disc to gain greater understanding of the global make-up of the wear scar. The results of this analysis are shown in Figure 5-18. Initially, there is little reduction between 0 and 10k cycles on the blade, this is due to some DFL transfer from the disc to the blade. After 10k cycles, the amount of DFL on the blade decreases and the amount of bond coat showing increases. The DFL reduction also occurs on the disc, as it is worn away more Ti64 shows on the surface. There is also a small amount of bond coat transfer from the blade to the disc.

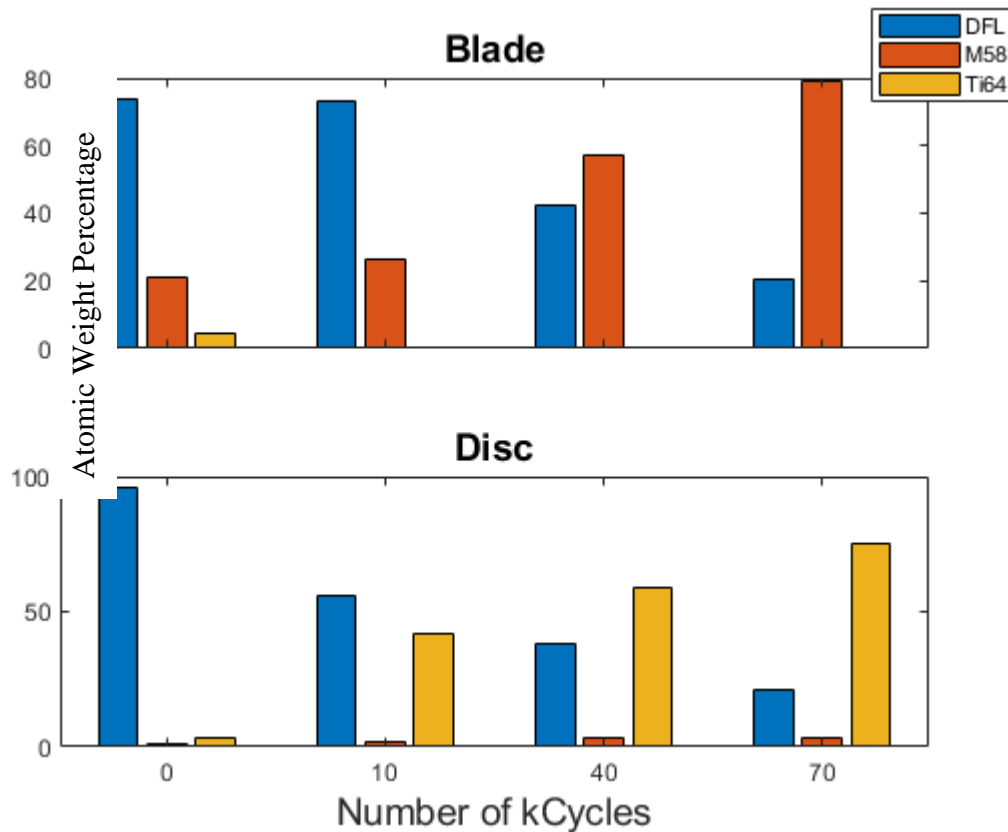


Figure 5-18: XRF averaged results for disc and compressor

Figure 5-19 shows cross-sections of both the blade and the disc at the end of differing amounts of cycles. The results correspond well with the results from SEM, EDX and XRF. After 10k cycles the blade coating system is largely intact (Figure 5-19A), some DFL has been removed from the disc (Figure 5-19B). After 40k cycles, the bond coat is exposed in places with DFL still present in valleys between bond coat asperities (Figure 5-19C) and there is very little DFL remaining on the disc (Figure 5-19D). After 70k cycles there is very little DFL remaining on the blade with mostly the bond coat showing (Figure 5-19E) and the disc shows a growth of a dull grey layer (Figure 5-19F). This is likely to be a mixture of DFL and bond coat wear debris transferring from the blade. After 90k cycles the bond coat has almost been completely removed from the blade (Figure 5-19G) with the remnants forming a dull grey layer as seen in Figure 5-19F. The disc shows some areas starved of lubrication as the grey layer has broken away (Figure 5-19H). As with the EDX results the location of the cross sections is important due to the SEM images showing variations within the wear scars.

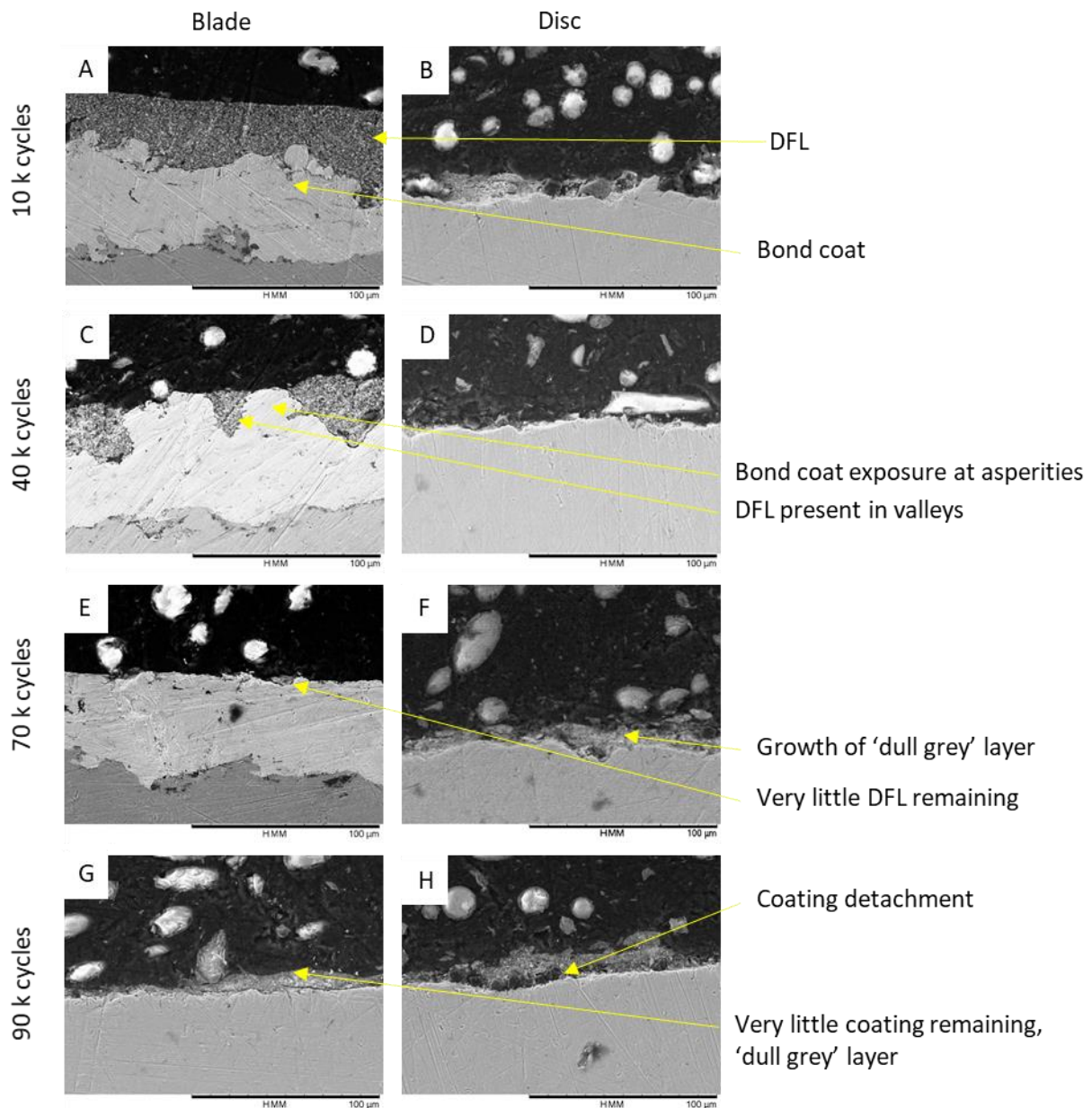


Figure 5-19: Cross-section images

Figure 5-20 shows how the CoF evolves for the two 300 MPa test presented in Figure 5-8 and two tests performed at 200 MPa at the same 150 μm displacement. The CoF shows similar performance for both the 200 MPa tests. There is an initial hump and then it remains low for the duration of the tests. This means that the coating is still performing well and lubricating the interface at the end of the test. The test shown in yellow does not have a hump and has a higher CoF compared to the purple line. As with the results from Figure 5-8, the variability will be discussed further in section 5.4. Further testing to attempt failure of lubrication at 200 MPa was planned, but not carried out.



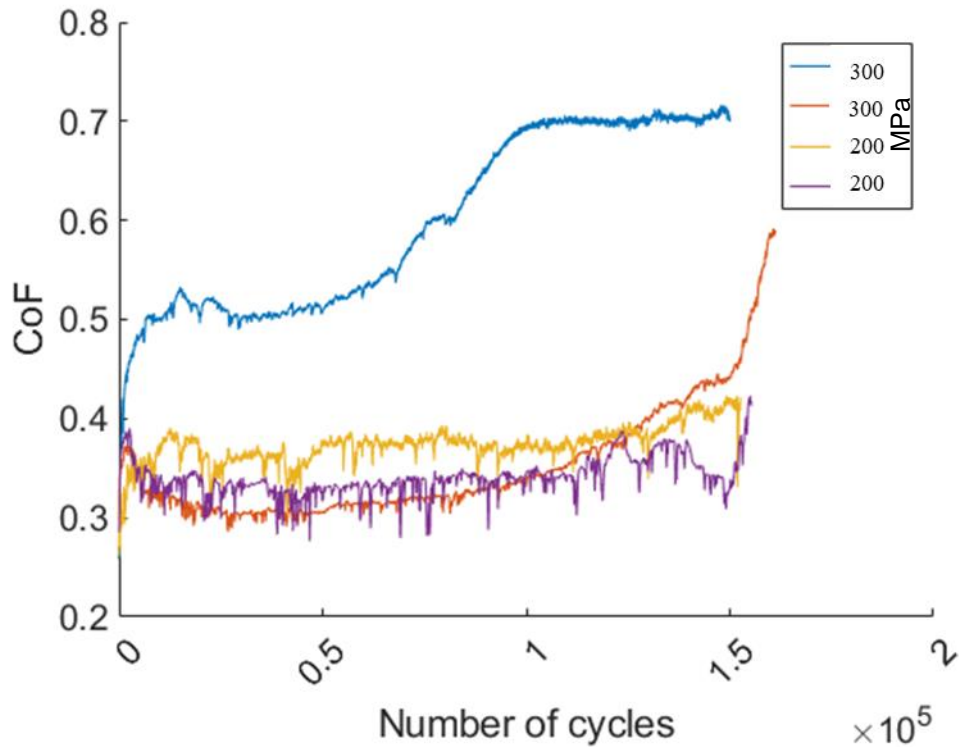


Figure 5-20: CoF evolution for 160k cycles for two different contact pressures

Figure 5-21 shows SEM images taken for the blade specimen from the results shown in Figure 5-20. The damage caused to the blade from the 300 MPa tests is more severe than for the 200 MPa tests. This is shown by obvious wear scar in Figure 5-21A and B compared to the less obvious scar in Figure 5-21C and D. This is expected due to the rise in CoF near the end of the test indicating that the lubrication layer was being worn away. Additionally, in Figure 5-21C and D there is less bond coat showing through and more areas of DFL/bond coat compaction still present. There are no signs of the cracks that are apparent in Figure 5-21B. This explains why the CoF is still low for the 200 MPa tests in Figure 5-20 as the DFL/bond coat compaction is still providing lubrication to the interface.

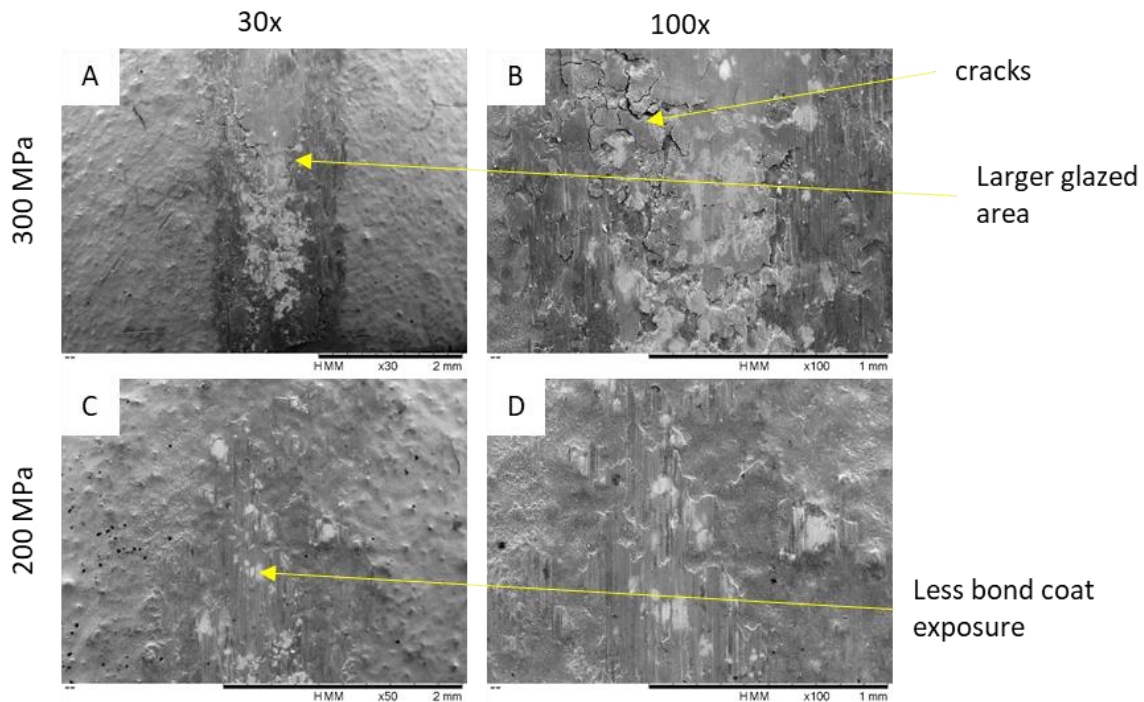


Figure 5-21: SEM images for the blade specimen for the test results shown in Figure 5-20 A) 300 MPa, 30x magnification B) 300 MPa, 100x magnification C) 200 MPa, 30x magnification D) 200 MPa, 100x magnification

## 5.4 Discussion

### 5.4.1 SCITEK

The results from Figure 5-8 are summarised in Table 9. *They show that at high displacements and the higher contact pressures the coating always fails. At low displacements the coating has not failed after 20,000 cycles. In the intermediate zone, on some repeats the coating fails and on others it does not. However, despite the coating always failing at some test conditions, there is variability in the length of time that the coating lasts for. The results shown in Figure 5-10 indicate that this variability in coating performance (both in terms of failure and in durability) is not caused by roughness. These roughness measurements were taken from one set of specimens and to confirm this finding more roughness measurements should be taken as well as waviness measurements but were not available at the time.*

Pressure (MPa)	Displacement (mm)	Number of Repeats	Failure Rate
500	0.200	2	100%
500	0.125	3	33%
500	0.050	2	0%
350	0.200	3	100%
350	0.125	3	33%
350	0.050	2	0%
200	0.200	2	50%

Table 9: Summary of the test results from Figure 5-8

Figure 5-11 presents results from tests with just a DFL layer (i.e. no bond coat between the alloy and DFL). The results are more consistent (although only two repeats per set of conditions) across the conditions tested. This suggests that the bond coat has an influence on the variability seen in Figure 5-8. This is supported by the findings in Chapter 4 that showed that the bond coat increased waviness of the surface. Additionally, the coatings in Figure 5-11 fail quicker than in Figure 5-8 suggesting that the bond coat and how it interacts with the DFL as wear occurs is an important mechanism to understand how to optimise the coatings performance. This conclusion is supported by the SEM images shown in Figure 5-9 where the low CoF, no failure test specimens surfaces had a sintered, glazed layer on the surface. Several tests were planned on the UoS fan blade rig with samples that had only a DFL layer applied to them to recreate these results but were not carried out.

The SCITEK rig uses flat contact geometry which is representative of the contact being investigated. However, any small misalignment of the test specimens could lead to local high-pressure areas, higher than specified by test parameters, which would lead to the coating being worn away quickly before the glazed surface has time to form. This could account for some of the variability seen. Furthermore, Chapter 4 identified that some batches of test samples for ball-on-flat tests were wavier than others. If variations in waviness also occurs with SCITEK samples then this would also have influence on the results and the variability.

#### 5.4.2 University of Sheffield fan blade rig

Figure 5-12 presents results from different length tests for the same test conditions. As with the SCITEK results there is significant variations on CoF between the different tests. From the SEM images shown in Figure 5-13 the mechanism behind the CoF evolution is clear. Initially, the DFL is worn away resulting in an increase in CoF, after a period (variable from test to test) CoF starts to decrease and a sintered, glazed layer starts to form. The composition of this layer is shown in Figure 5-15 and Figure 5-18 and it is clearly shown that the bond coat has an effect on the formation of this layer as it is part of its composition. The CoF is then relatively stable as the glazed layer provides lubrication to the interface. There is variation in the absolute value of CoF (as well as size of hump) between the different tests. This is caused by the different surface topography of the samples leading to slightly different glazed layers forming between tests. The topography changes the local contact pressure affecting the

*formation of the glazed layer. As this glazed layer is worn away the CoF starts to rise and eventually CoF rises sharply as the layer breaks down completely, resulting in metal-metal contact. The SEM, EDX and cross-section images support these conclusions.*

*The 90k cycle test in Figure 5-12 shows an interesting result. Initially, the CoF evolution is similar to the other tests, a rise in CoF followed by a decrease as the glazed layer starts to form. The CoF does not reach a stable period which mean that the layer is still forming. At this point the test was stopped and specimens taken out of contact which resulted in the wear debris being lost from the contact. When the test was resumed the CoF rose steadily, supporting the conclusion that the glazed layer had not formed properly and without it, the coating did not perform as well as the tests where the glazed layer was formed.*

*The EDX results presented in Figure 5-14-Figure 5-17 show that at the edge of the contact there is more DFL present. Due to the curved nature of the specimens, the edge of the blade has a lower contact pressure than the centre of the contact. This shows that a lower contact pressure does not provide the right conditions for the glazed layer to form. Additionally, worn DFL particles are likely to have been pushed to the edge of the interface by the curved nature of the specimens.*

*Figure 5-22 shows SEM images of the blade specimen surface at the end of the two 160k cycle tests (CoF evolution shown in Figure 5-12). Figure 5-22A and B are from the test which did not show the same evolution as the other tests (light blue line in Figure 5-12) whereas Figure 5-22C and D are from the test which did show similar evolution as the other tests (red line in Figure 5-12). The friction stays high throughout the test for Figure 5-22A and B. The remains of a glazed layer can be seen in Figure 5-22C and D whereas it cannot be seen in Figure 5-22A and B. This again shows why the formation of the glazed layer is important for effective lubrication of the interface as without it the CoF is significantly increased. Additionally, it shows the competing drivers in this process- if wear is too rapid then the DFL is worn away before the glaze can form, but wear is required to provide DFL particles for compaction and sintering. Therefore, it is hypothesised that there will be an optimum wear rate that allows glazing to occur.*

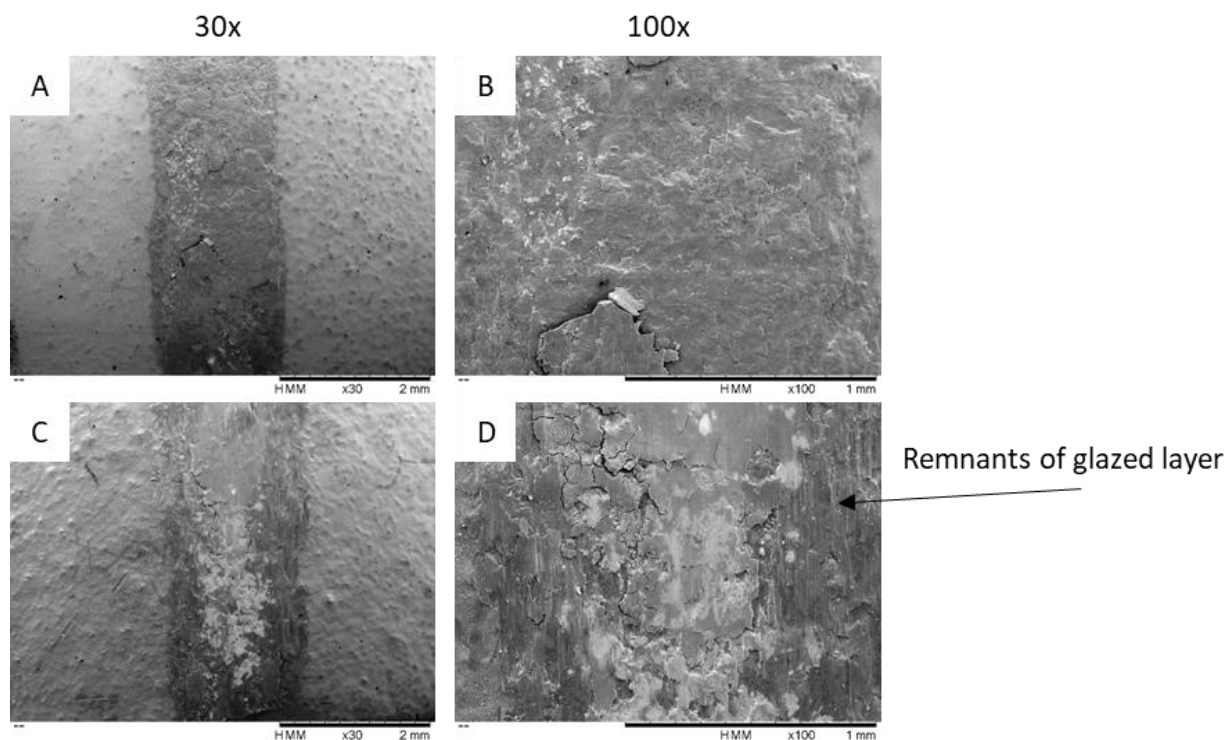


Figure 5-22: 160k tests from Figure 5-12, A) blue test 30x zoom, B) blue test 100x zoom, C) red test 30x zoom, D) red test 100x zoom

### 5.4.3 Comparisons of test rigs

*The CoF evolution of the new fan blade rig is similar to SCITEK. This is an improvement over the ball-on-flat tests which did not show the same evolution. However, the values are still different. Table 10 shows approximate CoF values for selected tests from the three test scales used in this work. The tests selected were best matched in terms of displacement and contact pressure. The CoF was qualitatively estimated from Figure 4-19, Figure 5-8 and Figure 5-12. SCITEK has the most representative contact geometry and has the most representative debris entrainment mechanism. Therefore, the SCITEK CoF are the most realistic. The UoS fan blade rig overcomes some of the limitations of ball-on-flat tests (detailed in 4.5.5) but is not quite as realistic as the SCITEK rig. The fact that the specimens are self-aligning is an advantage over the SCITEK rig as the test conditions can be more repeatable. As shown in Chapter 4, the curved nature of the samples means that the surface area is small relative to the surface topography compared to the SCITEK rig and the poor debris entrainment effects the glazing process by not providing DFL particles to be sintered. Figure 5-23 provides a summary of the advantages/disadvantages of the three test platforms. The main advantage of the UoS fan blade rig over SCITEK is that the curved geometry allows the specimens to self-align, overcoming any specimen alignment issues causing variability in the results.*

	<i>Contact Pressure (Mpa)</i>	<i>Displacement (<math>\mu</math>m)</i>	<i>Approximate CoF</i>
<i>Ball-on-Flat</i>	300	300	0.75
<i>Ball-on-Flat</i>	375	300	0.65
<i>UoS Fan Blade</i>	300	150	0.31
<i>SCITEK</i>	350	100	0.16
<i>SCITEK</i>	350	250	0.12
<i>SCITEK</i>	350	400	0.12

Table 10: Comparison of test rigs from selected tests

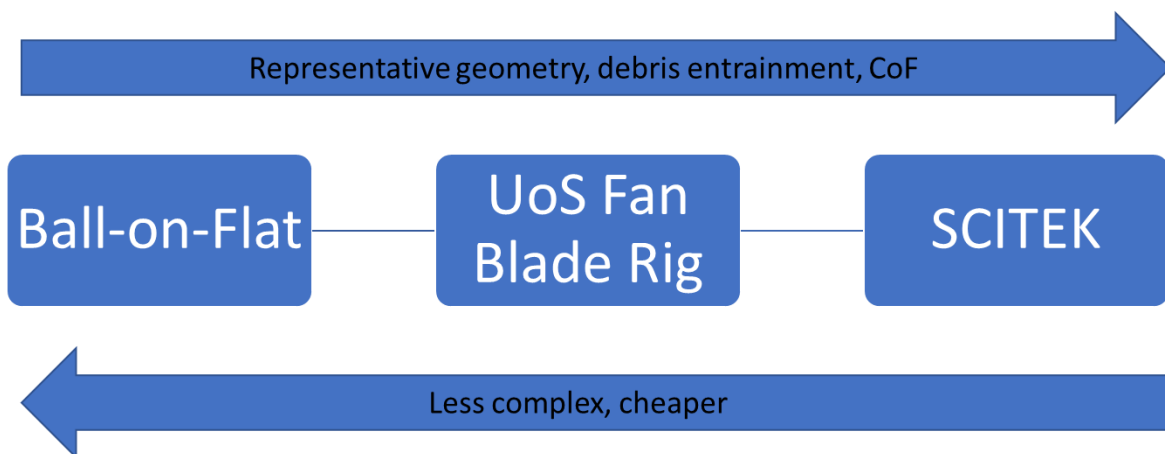


Figure 5-23: Summary of different test platforms advantages/disadvantages

#### 5.4.4 Conditions affecting sintered layer

*It is clear from the results presented in this chapter that the formation of the glazed layer greatly enhances the coating effectiveness by both providing a lower CoF and increased durability than DFL on its own. Therefore, by finding the conditions that allow this glazed layer to form the coating can be tailored to optimise the formation. The glazed layer needs severe enough conditions (high pressure, high displacement) to allow DFL but if the conditions are too severe then the coating will be stripped away before it is able to form the layer.*

The effect of surface topography is that it provides high contact pressure locally – these high-pressure spots serve two purposes: they increase the wear rate and thus the debris availability, and they promote the layer formation.

*The tests were carried out using one bond coat and one bond coat thickness. The literature review carried out in Chapter 2 identified that bond coat research is currently lacking. Changing bond coat thicknesses or materials (along with modifying surface topography) are areas which the UoS fan blade could investigate further. Ensuring topography, layer thickness and layer attachment to specimens is consistent between tests/repeats is key to reducing variability between tests and improving confidence in the results.*

## 5.5 Summary

*The work presented in this chapter can be broken down into the following summary:*

- *A new fan blade rig has been developed to overcome the limitations of ball-on-flat geometries*
- *Comparison of the new rig to an existing Rolls Royce test platform has shown that it shows similar coating behaviour although the values of CoF are higher.*
- *The bond coat has been identified as key in forming a glazed layer with the DFL to provide improved CoF and durability. The formation of this layer is seen in the CoF evolution as “hump” at the start of the test followed a period of low CoF.*
- *Contact pressure and displacement also influence the formation of this layer. If they are too low, it does not form and if they are too high then the coating is stripped away before it can form.*
- *Surface topography is likely to have caused the variation seen in the test results due to it forming high pressure spots on a local level. On high pressure tests these spots lead to even greater pressure and result in conditions too severe to form the layer. On low pressure tests these spots help formation of the layer by increasing the pressure to a point where layer formation can occur.*

## **6 Coating condition monitoring**

The current maintenance strategy for the fan blade coating adopted by Rolls-Royce has been detailed in chapter 2. All the fan blades must be removed from the disc to permit access to the root and disc surfaces to apply the PL470 for re-lubrication. The process is carried out on a preventive maintenance basis and therefore regardless of the state of the coating.

The possibility of inspecting the coating in-situ, non-destructively would allow Rolls-Royce to perform re-lubrication maintenance on a condition-based approach. This would produce an economic advantage by cutting down the costs due to unnecessary coating top-ups.

Many non-destructive techniques have been used to monitor coating conditions. For example, Raman spectroscopy has been successfully applied for coating thickness measurements [110]. Other methods such as infrared thermal wave imaging have been applied to the automotive industry to inspect the state of thermal barrier coatings. However, these approaches require direct access to the coated surface in order to perform a measurement. Ultrasound techniques could represent possible solutions to adopt as they do not necessarily require the sensor to be applied on the surface to be inspected. Ultrasonic inspections are already being routinely carried out on power generation gas turbines.

The purpose of this chapter is to present an experimental plan to assess feasibility of coating condition monitoring through their use. A novel method will be used, which is based on the interference of multiple reflections of a wave into a component created by sending a continuous signal. This method was chosen as it offers higher sensitivity than the conventional approaches. Preliminary experiments will involve instrumenting ball on flat tests to monitor the progression on the coating damage during the tests and, ultimately, the implementation on the test rig will be attempted.

### **6.1 Conventional ultrasound methods**

Ultrasound is mechanical vibrations that propagate at frequencies above the human audible range ( $>20$  kHz) and can be generated by applying a variable tension to ultrasonic sensors (piezoelectric materials). Waves propagate at a certain velocity and attenuate through a medium depending on the properties of the material. When a wave reaches the interface between two mediums, part of the signal is transmitted and part is reflected back (Figure 6-1) depending on the acoustic impedance of the materials. Wave phase shift may also occur at the interface.



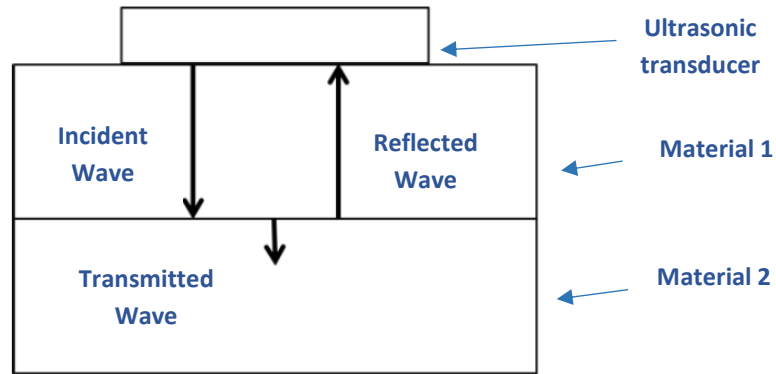


Figure 6-1: Ultrasound reflection and transmission at interface

The reflection coefficient,  $R$ , is defined to quantify the amount of wave reflected as the ratio between the reflected and the incident wave ( $A_I/A_R$ ). For perfectly bonded components the reflection coefficient is a function of the acoustic impedance of the materials,  $z_1$  and  $z_2$ .

$$R = \frac{z_1 - z_2}{z_1 + z_2}$$

Equation 6-1

The acoustic impedance of solid materials is function of material density,  $\rho$ , and the velocity,  $c$ , at which the sound propagates into it:

$$z = \rho c$$

Equation 6-2

Conventional methods consist on pulsing a signal and recording the reflected wave. The ratio between the amplitude of incident wave and the reflected wave (which is  $R$ ) contains information about the properties of the material at the interface as it is a function of its acoustic impedance.

The measurement of the length of a component is also possible, by measuring and processing the time of flight (time taken by the wave to travel twice through the length of the component).

## 6.2 STAMINA

STAMINA (STANDING wave Measurement of INterfaces and lAyers) is a novel method used to measure properties of interfaces and layers [111]. It can be used to measure the thickness or viscosity of a fluid layer on a surface, thermal expansion, length, deflection and loss of material. The main advantage of the method is higher sensitivity than conventional pulse-echo techniques.

The method relies on standing wave formation to achieve high sensitivity. The incident wave is reflected when it reaches the measurement interface and then again at the solid-transducer interface, these waves constructively and destructively interfere within the component forming the standing wave, as shown in Figure 6-2. The amplitude of the standing wave increases with each reflection of the continuous wave, which however is decreased by attenuation until a steady state is reached.

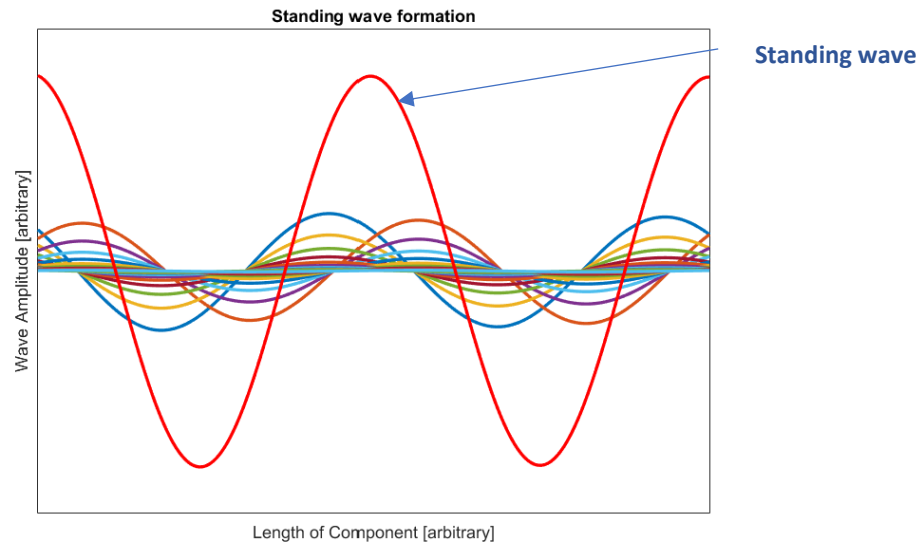


Figure 6-2: Standing wave formation

A mathematical model of the wave superimposition has been proposed in the STAMINA patent [111]. The model describes the evolution of the wave as it propagates through the structure, attenuates and reflects at the interfaces (Figure 6-3).

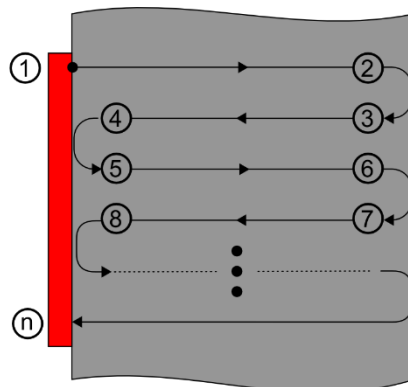


Figure 6-3: Propagation and reflection of a continuous ultrasonic wave

After having travelled for  $n$  times from the transducer surface to the measurement interface and back again to the transducer, the wave impacting on the transducer expressed as a complex number is:

$$A_0 e^{-i[\omega(\frac{2nL}{c}-t)-n\theta-(n-1)\theta']} e^{2nL\alpha} R^n R'^{n-1}$$

**Equation 6-3 [111]**

where  $A_0$  is the initial amplitude of the wave,  $\omega$  is the angular frequency,  $c$  is the velocity of the sound into the component,  $\alpha$  is the attenuation coefficient and  $t$  is the time at which the wave was emitted. The reflection coefficient and phase shift between the component and the medium present at the surface are expressed as  $R$  and  $\theta$  respectively, and those at the component-transducer interface are denoted as  $R'$  and  $\theta'$ .

The overall wave sensed by the transducer when stationary conditions are reached, can be expressed at a given time as:

$$A_0 \sum_{n=1}^{\infty} e^{-i[\omega(\frac{2nL}{c}-t)-n\theta-(n-1)\theta']} e^{2nL\alpha} R^n R'^{n-1}$$

**Equation 6-4 [111]**

This is the signal that is acquired and used for the measurement. It is a function of the component properties as well as of the reflection coefficient at the measurement surface.

The practical application of the method involves driving the transducer by sweeping through a certain range of frequencies and recording the system response at each frequency. The changes of the signal amplitude at a given frequency are related to the reflection coefficient variations and therefore to the conditions at the interface (e.g. presence or absence of a medium, viscosity of the fluid on the surface). Changes in the geometric parameters (such as thickness or elongation of the component, thickness of a surface layer) affect the resonance frequency values and they can also be accurately measured with the method.

### 6.3 Wear measurement

The coating degradation process involves loss of material due to wear. For this reason, the first objective of this part of the project will focus on measuring wear. STAMINA is particularly appropriate here due to its high sensitivity. Assuming the removal of material takes place by removal of flat layers, the amount of wear can be related to the changes of the thickness of the component, which influences the magnitude of the resonant frequencies of the system. The first order resonant frequency  $f$  for a component of thickness  $L$  is:

$$f = \frac{c}{2L}$$

**Equation 6-5**

As the thickness of the component changes by  $\Delta L$  due to material loss, the resonant frequency changes by  $\Delta f$ :

$$f + \Delta f = \frac{c}{2(L + \Delta L)}$$

Equation 6-6

Substituting Equation 6-5 into Equation 6-6 and rearranging to make  $\Delta L$  the subject:

$$\Delta L = -\frac{2L^2\Delta f}{c + 2\Delta fL}$$

Equation 6-7

As in most of the cases  $2\Delta fL \ll c$ , the equation can be approximated as:

$$\Delta L = -\frac{2L^2\Delta f}{c}$$

Equation 6-8

Equation 6-8 denotes that a reduction of the component thickness ( $\Delta L < 0$ ) corresponds to an increment of the resonant frequency ( $\Delta f > 0$ ).

By acquiring the frequency spectrum before and after material removal and comparing them, it is possible to measure  $\Delta f$  and therefore obtain  $\Delta L$ . Figure 6-4 shows qualitatively this comparison where it can be observed that resonant frequency of order  $n$  will be shifted by  $n$  times  $\Delta f$ . By measuring  $n\Delta f$  rather than  $\Delta f$  higher accuracy is achieved.

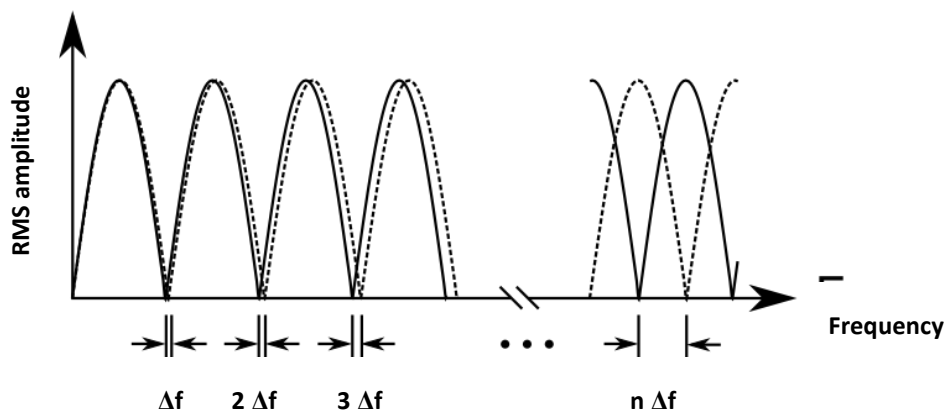


Figure 6-4: Comparison of frequency spectrums.

## 6.4 Experimental plan

*This approach will be applied to wear quantification. In order to isolate the effect of coating removal, flat rectangular specimens with the coating applied were produced by Rolls-Royce. Samples were manufactured to the dimensions required for wear testing in the Bruker Universal Mechanical Tester (UMT) as specified in Sections 4.1 and 4.2.*

Two 10 MHz transducers were bonded to the bottom of the metallic specimens using a strain gauge, glue, and cured at 120°C for 3 hours under a compressive force. The transducers were placed adjacent to each other as a pitch catch ultrasonic arrangement was chosen for this technique. A pitch catch arrangement is adopted as the technique permits the comparison of a pulsed wave method and the STAMINA ultrasonic methodology. When using the STAMINA ultrasonic method, one transducer is required to generate the standing wave, and the other is required to acquire the waveform. A schematic is shown in (Figure 6-5)

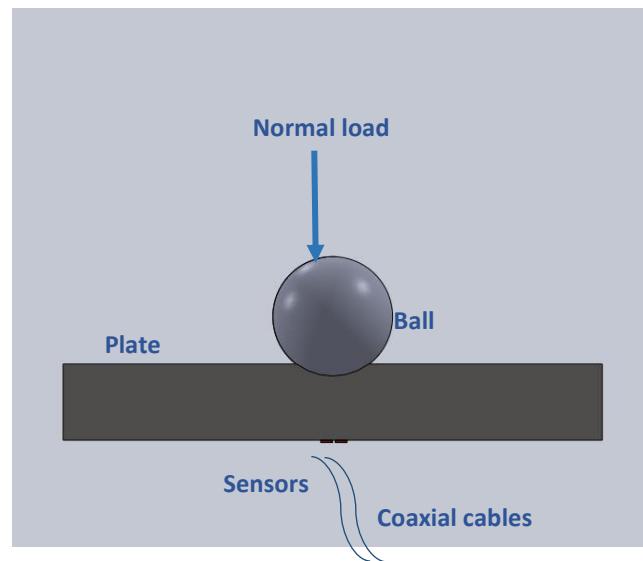


Figure 6-5: Instrumented ball on flat test schematic (cross-section)

A PicoScope 5000 series device, which functions as both signal generator and oscilloscope, is used to operate the transducers. This hardware was controlled through a computer via a LabView program developed in-house, programmed to drive the sender with a sweep of frequencies and record the response from the receiver.

*The plate was positioned within the UMT and secured in place. In this condition, the specimen is unworn and in the new state, hence an ultrasonic measurement was initially taken. This first ultrasonic measurement is taken as the reference signal, as a means of comparison with subsequent measurements once wear has taken place. Signals were captured every 1k cycles of the tribometer up to 5k, then every 5k cycles to 90k. A pulse of 10 MHz using the conventional ultrasound method was used to measure the layer. The test was carried out using a normal force of 700 N.*

The motion must be interrupted, and the ball removed from the contact as its presence affects the signal. The thermodynamic aspects of the system also influence the measurements. The mechanical energy introduced into the contact is dissipated into heat, resulting in thermal expansion of the component. However, bulk heating is unlikely to occur in this simple test, but it is important to keep in mind for more complex testing where heating of components may occur. It is vital to perform all the acquisition at the same temperature as expansion tends to

compensate the thickness reduction due to wear, therefore if heating of the materials is an issue in testing then calibration of the differing temperatures would need to be performed. Allowing the specimen to return to room temperature after test interruption could represent a methodology to adopt. A calibration against temperature may also represent a possibility.

Analysis of the change to the signals will show the progression of the wear and could eventually be used for estimating the residual life of the coating. Ultimately, the blade-disc specimens' interface could be instrumented within the test rig.

## 6.5 Trial Results

*Figure 6-6 the first reflection of the signal after the number of cycles of the tribometer given in the legend.*

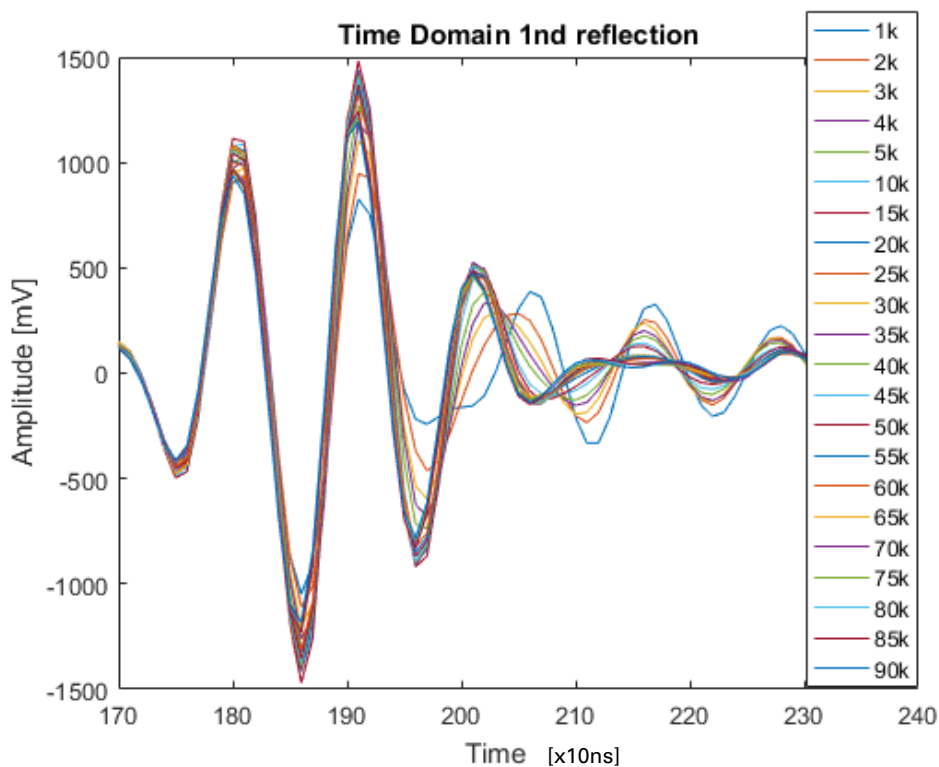


*Figure 6-6: The first ultrasonic reflection in the time domain taken after the number of cycles indicated in the legend.*

*The temporal location of the peaks in the signal is determined by the layer thickness. The presence of the layer on the surface of the specimen acts to introduce a second reflective interface. Two reflections occur, one at the specimen-layer interface and the one at the layer-air interface. If the layer is a quarter wavelength thick (at the centre frequency of the wave incident upon the interfaces), the reflections are 180° out of phase and so destructively*

interfere. This is seen in the frequency domain as a dip in the signal around 9.8MHz, as shown in Figure 6-7.

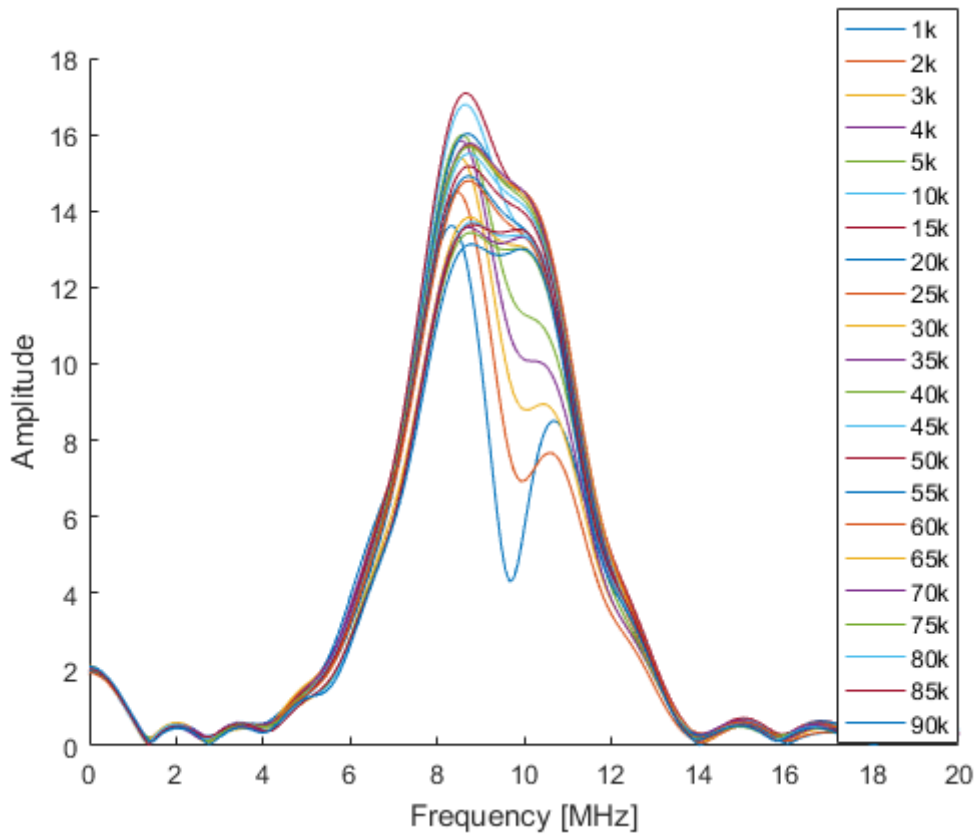


Figure 6-7: FFT of the Chirp signal after each number of cycles

## 6.6 Analysis

The dip in Figure 6-7 permits the calculation of the thickness of the surface coating. If the resonant dip is around 9.8 MHz and the speed of sound in the surface coating is known, the following equation can then be used to determine the coating thickness (from Equation 6-5):

$$L_c = \frac{nc_c}{4f} \tag{Equation 6-9}$$

where  $L_c$  is the thickness of the coating,  $n$  is a natural integer equal to the order of the dip,  $c_c$  is the speed of sound in the coating, and  $f$  is the frequency between consecutive dips. The dip becomes less prominent, and the amplitude of the wave increases as the number of cycles of the tribometer increases. As wear of the layer occurs, its thickness decreases. Since the speed of sound of the layer is fixed, the quarter wavelength frequency increases, which is observed as the dip moving to a higher frequency with increasing cycle number.

The key to calculating an accurate thickness is knowing the exact speed of sound in the materials used, i.e. speed of sound in the alloy, bond coat, DFL and any surface layer that

forms. This is challenging as this is a new application of ultrasound measurement, so these values are not known. There is some literature on speed of sound in MoS<sub>2</sub> [112]–[114] however the results are varied due to different deposition techniques etc. For the purposes of this analysis, estimates have been made based on standard tables and uncertainty has been plotted to show the effects of changes to the speed of sound. Figure 6-8 shows the results for speed of sound of 7500 ± 500 m/s which is based on literature results for MoS<sub>2</sub> [112]–[114]. The total thickness of the coating is in the region of 200 μm which matches well with expected results. However, the wear results are not as expected, showing negative wear (i.e. thickness of layer increasing). This is caused by an incorrect speed of sound. As shown in Chapter 4 and 5 the DFL layer initially wears, then compact and mix with wear debris from exposed bond coat to form a glaze. During this compaction and glazing process, the speed of sound will change due to the different materials forming it.

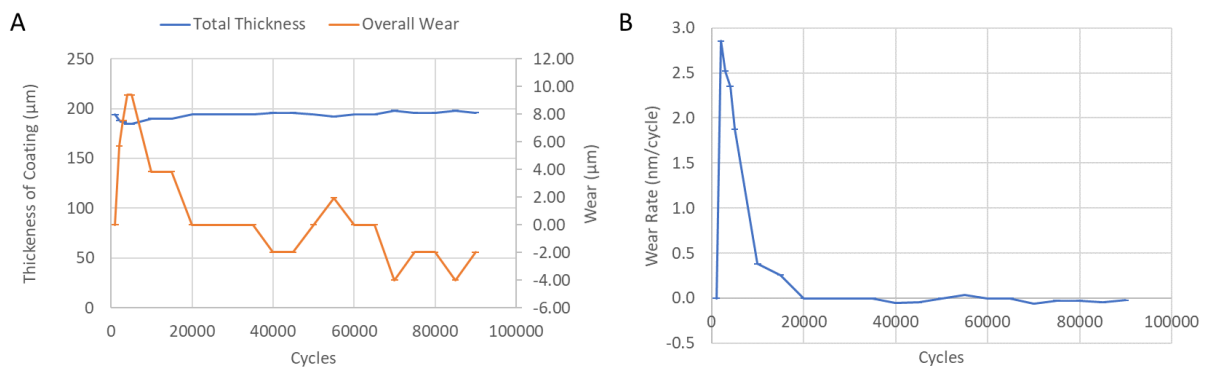


Figure 6-8: For speed of sound = 7500 ± 500 m/s A) thickness and wear of coating B) wear rate

Figure 6-9 shows how the atomic weight percentages change as the number of cycles increase. This graph is created from the data in Figure 5-18 and extrapolated. Whilst this data is from the fan blade rig and the tests in this chapter are from ball-on-flat tests it provides data that shows how the makeup of the glazed layer changes and therefore by using a weighted average how the speed of sound changes as the test increases. Table 11 shows the values for speed of sound that were used for each part of the coating. Table 12 shows the values of speed of sound that were used for each cycle



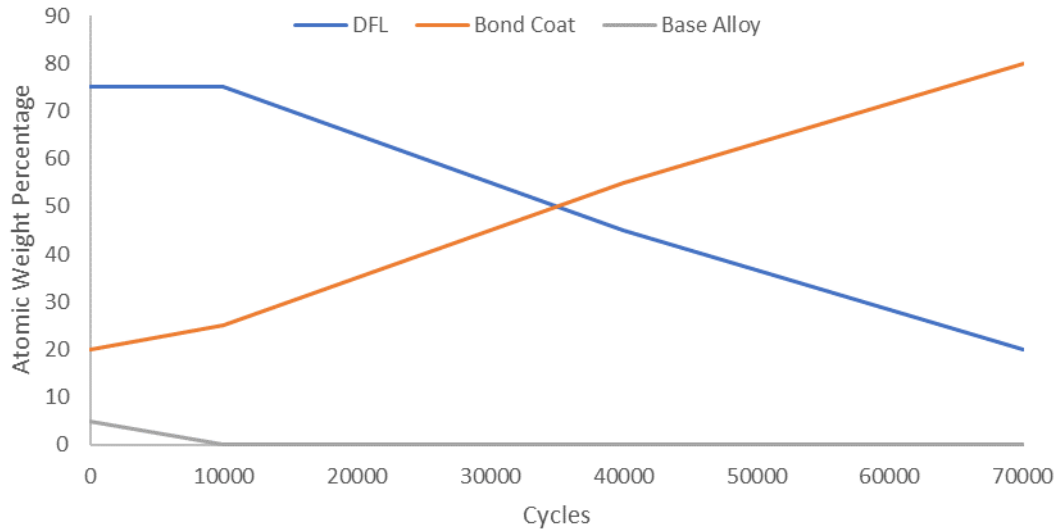


Figure 6-9: Atomic weight percentages from Figure 5-18

	<i>Speed of Sound (m/s)</i>	<i>Upper Bound (m/s)</i>	<i>Lower Bound (m/s)</i>
<i>DFL</i>	<i>7500</i>	<i>8000</i>	<i>7000</i>
<i>Bond Coat</i>	<i>5126</i>	<i>5626</i>	<i>4626</i>
<i>Base Alloy</i>	<i>6070</i>	<i>6570</i>	<i>5570</i>

Table 11: Speed of sound figures used in further analysis for the different materials

Table 12 shows the values of speed of sound that were used for each cycle based on Table 11 and Figure 6-9.

Cycles	Speed of Sound (m/s)	Upper Bound (m/s)	Lower Bound (m/s)
1000	6954	7454	6454
2000	6954	7454	6454
3000	6954	7454	6454
4000	6954	7454	6454
5000	6954	7454	6454
10000	6907	7407	6407
15000	6805	7305	6305
20000	6703	7203	6203
25000	6601	7101	6101
30000	6500	7000	6000
35000	6398	6898	5898
40000	6296	6796	5796
45000	6194	6694	5694
50000	6076	6576	5576
55000	5957	6457	5457
60000	5838	6338	5338
65000	5720	6220	5220
70000	5601	6101	5101
75000	5482	5982	4982
80000	5363	5863	4863
85000	5245	5745	4745
90000	5126	5626	4626

Table 12: Speed of sound values used for different cycles

Figure 6-10 shows the coating thickness and the wear of the coating based on frequency analysis from Figure 6-7 incorporating speed of sound levels from Table 12. As before the coating thickness is in the right magnitude. The overall wear is as expected showing that the thickness of the coating gradually decreases. The overall wear is 45  $\mu\text{m}$  at the end of the test. This suggests that there is still coating present on the surface and that the base alloy has not been exposed. This is supported by the CoF results presented in Figure 4-19 and Figure 4-21 for similar conditions which show that the CoF is relatively stable and has not risen at the end of the test. The CoF results also support the high initial wear rate as the CoF increases before dropping as the glaze forms. The high initial wear rate is the DFL being worn away before the glaze has formed which provides a stable CoF and low wear rate. The decrease in wear shown in Figure 6-10A is an interesting result and could be caused by the jump in measurement interval from 1000 cycles to 5000 intervals. For future tests the short interval should be maintained to evaluate the region when the glaze is first forming and once the wear rate has stabilised the recording interval can be increased. The influence of speed of sound is shown by uncertainty bars in the figure. For the wear and wear rate the speed of sound has little effect

on the results and even for the total thickness of the coating the uncertainty bars are still in a range that is acceptable.

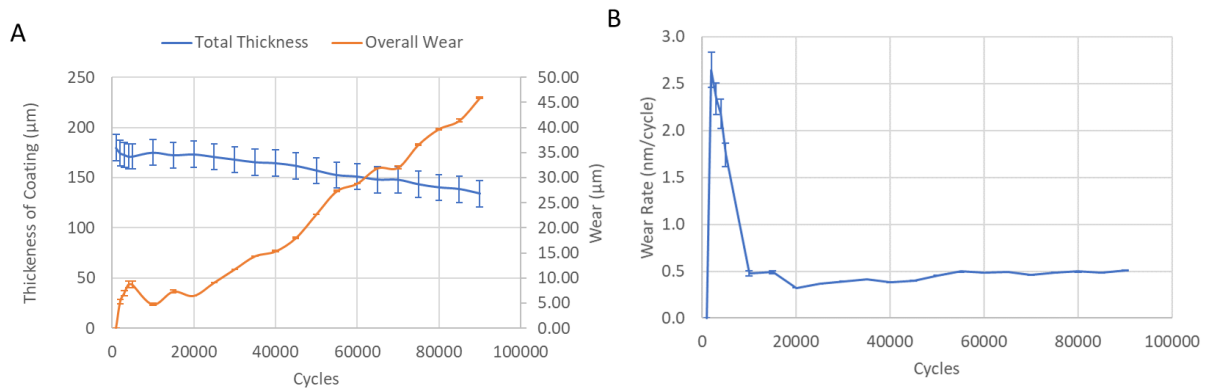


Figure 6-10: For speed of sound from Table 12 A) Thickness and wear of coating B) wear rate

## 6.7 Conclusion

*This initial test showed that, given the speed of sound of the coating, a means of measuring its residual thickness by monitoring the frequency of the resonant dip could be feasible using Equation 6-9. This work shows how a conventional pulsed technique can measure the thickness of the coating. Although the data shown is only from one test, so repeats are necessary to confirm the findings.*

*This is a promising step and shows how ultrasound could be used to measure residual coating thickness during inspection and eventually be a real-time condition monitoring system. There are some limitations to this method that need to be considered and are areas for future work:*

- *The ball needed to be removed for an accurate measurement. For a true in-situ condition monitoring system, this would need to be overcome. STAMINA may be able to overcome this limitation as the increased accuracy may be able to show the ball-coating interface*
- *Thermal effects of the contact affect the readings. If this method is used for an engine, measurements are likely to be taken at a variety of temperatures. How much the temperature affects the readings is an area for research. The system could then be calibrated depending on the temperature at that point in time.*
- *Ball-on-flat geometry is dissimilar to a real engine. A next step is to incorporate this method on the test rig developed in Chapter 5.*

## 7 Conclusions

*The work presented in this thesis has fulfilled the aims of the project as detailed in Section 1.2. A comprehensive review of the literature showed that there were gaps surrounding the fundamental understanding of how fretting causes failure of the fan blade/disc contact. Partly this is the result of testing being performed on unrealistic geometries due to the complex nature of the fan blade. There has also been extensive testing with titanium alloys and MoS<sub>2</sub> but there is little research on the part the bond coat plays in the lubrication mechanism. These were gaps that this thesis focussed on.*

*Analysis of the service blade in Chapter 3 yielded understanding of the changes that the coating system undergoes during service. This is key to designing laboratory tests that mimic the changes as closely as possible to gain confidence that the laboratory conclusions will still hold for a real fan blade. Visual inspection of the blade identified three regions that looked different, they were identified as: edge of contact areas, low load areas and high load areas. SEM analysis showed that the edge of contact had as applied and lightly worked DFL surface. Low load areas showed some damage and light working of the DFL surface. High load areas had a cracked, platelet structure on the surface with some craters where platelets had been detached. This structure is caused by compaction and sintering of DFL particles. Cross-sectional analysis showed that the DFL in low load areas was worn away suggesting that pressure has an influence on how the coating transforms and performs. The thickness of the platelets in the high load areas is larger than the as applied DFL. This suggests that there could be material transfer from the low load areas, from the disc to the blade or from relubrication. Overall, the coating was still providing lubrication to the contact due to DFL still being present on the surface.*

*Analysis of failed biaxial samples also showed that pressure affects the way the coating behaves. Failure of the specimens occurred at edge of blade regions where the contact pressure was the highest. In these areas DFL starvation led to high CoF and adhesive behaviour. Some areas of the biaxial samples were similar to the service blade (areas BA and BC) where compaction and sintering of the DFL occurred, this is shown in the surface and cross-sectional analysis. In other areas of the samples, the bond coat was exposed and detached. These areas represent progression of the damage mechanism from the areas where DFL is still present. Relubrication of the samples mid test occurred but it was difficult to identify any differences in the layers or what effect this had on the samples.*

*Overall, Chapter 3 has provided information on how the coating develops. Different areas of the specimens/blade show different characteristics caused by pressure differences. This highlights that pressure is a key parameter in determining how the coating performs. The areas of the specimen and blade for further analysis were identified by visual inspection which means there is a qualitative nature to this investigation which should be noted when drawing conclusions.*

*Ball-on-flat tests in Chapter 4 provided insight into the lubricating mechanism of the coating. The lubrication was shown to perform better at higher pressures and did not reach failure of the whole contact area for any of tests (although some cracking observed at the highest contact pressures). This is due to the surface topography and rapid pressure drop caused by wear to the ball. The main mechanism causing the low CoF was the compaction and sintering of the DFL into a layer and this was more prevalent as contact pressure was increased. This agrees with the work covered already in Chapter 3. There were similarities in the mechanism observed on the blade root and the results seen in the ball-on-flat tests. There was a small amount of compaction of DFL into a layer at low pressure and as the pressure increased, so did the amount of compaction. At the highest test pressures, cracks and fracturing of the layer could be observed, just like what was seen in the blade root. The platelet structure was more obvious in the blade than in the ball-on-flat specimens. Differences are expected due to:*

- *Larger pressure gradient in the ball-on-flat tests, a result of the test geometry*
- *LCF is simulated, HCF is not*
- *Small contact area resulting in less particle entrainment*
- *Small contact area also results in small contact area to asperity size ratio*
- *Environmental conditions are different resulting*
- *No relubrication occurred*

*Further similarities were identified between the high-pressure tests and the high load areas on the service blade root. This shows that these tests were showing the same pressure effects as seen in an actual blade-disc interface. Analysis of the wear scars showed they were made up of as-applied DFL, loose DFL particles, DFL layer, exposed bond coat and out of contact areas. At high pressure there is more debris pushed out of the contact as well as more compacted DFL and exposed bond coat.*

*The CoF in the ball-on-flat tests was higher than expected. This is due to a bow wave forming caused by the compliance of the specimen's substrate. In the literature this can account for as much as 70% of the measured tangential force [107]. The poor debris entrainment also means that there is limited amount of DFL particles available to form the glaze that provides low CoF. Additionally, the gross slide regime should occur for the  $Q^*/P$  ratio to be representative of CoF and this is not the case for the two higher pressure tests.*

*Surface topography was also shown to affect the results. Two batches of samples with different waviness were tested and whilst CoF evolutions shows similar progression the absolute values vary from 0.45 to 0.7. Rougher specimens also produced more irregular shaped wear scars and more bond coat exposure. This is due to the rougher samples resulting in less asperities being in the initial contact leading to higher local contact pressures. This higher contact pressure leads to more DFL compaction and behaves similar to a smoother specimen at a higher nominal contact pressure. Specimens with no bond coat were found to have a smaller range of waviness. This led to more regular shaped wear scars. Additionally, the samples with bond coat were shown to have a lower CoF for the duration of the test. This highlights the*

*important role that the bond coat plays in the lubrication mechanism. It provides a lower CoF and therefore better lubrication but at the expense of surface topography. Across the length of a blade root, this variation in surface can lead to larger variations in contact pressure compared to a smoother surface.*

*To further understand the surface topography effects, a contact model was developed to estimate the contact pressure on macro asperities. The model extracts the surface topography from 3D imaging and applies Hertz theory, and Jackson and Green model to the contacting macro asperities. There are several assumptions of this model:*

- *Contacting asperities are modelled as hemispherical caps*
- *Curvature of the sphere specimen is neglected*
- *Roughness components are neglected, this model focusses on surface waviness*
- *Summits of the asperities are at the same height and are subjected to the same deformation*
- *High wear tests cannot be analysed as the asperities have worn down to form one single contact patch*
- *Mechanical properties of Ti-6Al-4V were used, ignoring coating properties*

*Jackson and Green calculations showed contact pressures on the asperities of 1.60-1.97 GPa. Clearly, this is significantly higher than the nominal contact pressure of 300 MPa. This shows why behaviour associated with higher nominal contact pressures was seen at lower nominal contact pressure tests with rough samples. The asperities estimated to have higher contact pressures showed increased bond coat exposure and increased glazed layer. This corresponds well with previous observations regarding pressure and its effect on the wear scar.*

*Ball-on-flat tests concentrate pressure in a way other configurations cannot. This highlighted how continued low pressure does not form a glazed surface and accentuated the lack of debris entrainment and surface topography. Whilst this configuration is less realistic than the real case, it enabled key learning points to help guide the future, more realistic tests and support conclusions derived from this later testing. To overcome the limitations described for the ball-on-flat a new fan blade test rig was developed. This test platform (described in Chapter 5) incorporates two disc specimens either side of a blade specimen to provide a simplified blade-disc interface. The rig can reproduce LCF and control environmental conditions. The contact arrangement is a line contact due to the curvature of the specimens, analogous to cylinder on cylinder contact. This arrangement limits misalignment and achieves high contact stress at moderate normal loads.*

*Results from Rolls Royce SCITEK test rig were provided by Rolls Royce for analysis. These results allowed validation of the new fan blade rig. The SCITEK rig has a flat-flat test geometry so results are not directly comparable. Results showed variability in whether the coating failed and the durability of the coating if it did fail. A sintered layer was found on the specimens from the tests which did not fail. Roughness was not found to be a cause of the variability. Tests on*

*specimens without the bond coat showed better repeatability and a much shorter test length before failure, indicating that the bond coat introduces variability and increases lubrication performance.*

*Results on the fan blade rig showed variability in performance. Testing was performed at 300 MPa. An initial rise in CoF was followed by a decrease to a steady state, followed finally by a sharp rise in CoF as the coating failed. Overall the CoF values on this rig were more realistic than ball-on-flat tests but not as low as expected from literature or from the SCITEK tests. This is due to the contact geometry but since the CoF evolution and wear characteristics are as expected and the specimens are self-aligning, the tests are representative of a real fan blade root-disc interface. This means that this test rig can be used to further evaluate the coating.*

*Tests were stopped at different points to analyse how the coating was evolving at different stage. The specimens were analysed using SEM, EDX and XRF. These tests provide insight into the lubrication mechanism. The coating initially starts to wear (causing the rise in CoF). Once wear progresses and asperities of the bond coats starts to show through, the DFL wear particles mix with bond coat particles and are compacted and sintered to form a glazed layer. It is this glazed layer that provides the low CoF for the sustained period before cracks start to form and it breaks down causing a sharp rise in CoF. XRF analysis showed that the ratio of DFL to bond coat exposure decreased as the test progressed. EDX analysis showed that the area of the contact that was compacted into a glazed layer was made up of bond coat as well as DFL. This analysis shows that the bond coat plays an important role in the formation of the glaze and explains the rise and decrease in the CoF as it takes time for the glazed layer to form. However, the role it plays is not understood. Does the bond coat layer directly contribute to the formation of the sintered layer due to its material properties and interaction with DFL? Or does it simply provide surface topography that assists in achieving the glazed layer and by default some bond coat ends up in the glazed layer due to wear. There was one test that behaved differently to the others and had a higher CoF. The SEM analysis showed that the glazed layer did not form in this test highlighting that this layer needs to form to provide a low CoF. Tests at 200 MPa showed that the layer was still present after 160,000 cycles and a longer test period would be needed to cause failure at this pressure.*

*The ultrasonic method for measuring coating thickness described in Chapter 6 is a promising start to developing a condition monitoring system. Only one test was carried out using the ball-on-flat test platform described in Chapter 4 so more extensive testing is required to confirm these initial findings and develop the method further. Analysing the frequency changes during testing has provided coating thicknesses of a sensible magnitude and appropriate wear. Speed of sound in the coating is a key parameter for the coating thickness to be accurate. Approximations were used in this analysis as reliable data was not available and uncertainty was plotted on the graphs. A complication for this analysis is that the makeup of the glazed layer changes and so for an accurate speed of sound value, the ratio of DFL to bond coat and the elements present on the surface is required at each measurement point to calculate an accurate speed of sound in the coating. Despite this, the initial results have shown promise and there is scope for future development of this method.*

*Overall this study shows that contact pressure is a key component in forming a glazed layer from the as-applied coating and that the surface topography (enhanced by the bond coat) plays its part in changing the contact pressure at the local interfaces. The analysis of the failed blade root slot in Chapter 3 identified three distinct regions with only the high load region showing similar surface characteristics to the glazed layer seen in this work. If glazing only occurs locally, and the rest of the interface has a lower contact pressure causing wear to occur without the glazed layer forming, then the blade fails quickly due to wear of the coating. Whereas, if glazing can occur across the blade root on a global level, the fan blade will last longer due to the low CoF and protective nature of the glaze. This could be achieved by modifying surface topography to be rougher in low pressure areas of the blade root interface (to increase contact pressure where conditions are not severe enough to cause glazing) and smoother in high contact pressure areas of the blade root interface (to lower contact pressure where conditions are too severe for glazing to occur). From the analysis in Figure 3-5, Area 2 could have rougher surfaces than in Area 3 to promote the glaze forming in these areas and provide a life extension to the fan blade.*

## **7.1 Future Directions**

*There are several areas that this work can be developed further. The new University of Sheffield Fan Blade rig has been shown that it is representative of the real blade root-disc interface. This means that it can be used for further investigations. Currently, one displacement and load has been investigated. Varying these parameters would gain more information about how the coating evolves in the different areas of the blade root. Failure of the coating at these lower contact pressures and testing with no bond coat are two areas of interest initially. The testing with no bond coat allows further validation of the test rig against SCITEK as well as understanding the lubrication performance of the countersurface of the blade root-disc interface. The literature review identified a gap where there is little work focussing on the bond coat. This test rig can be used to fill this gap and develop greater understanding of the bond coats effect on forming the glazed layer.*

*The work in this thesis showed that the glazed layer is key to providing a low CoF so investigations can be carried out to determine the optimum parameters (surface topography, layer thicknesses, contact pressure etc.) to promote formation of this glazed layer. For example, is it beneficial to have high roughness bond coat to provide exposure of the bond coat asperities sooner in the wear process? Another example would be to determine the optimum contact pressure to achieve the glazing process as if it is too low, the glaze does not form and if it is too high, then the lubrication layer is worn away without the glaze forming. This could lead to a blade root that has a variation in surface topography. In the part of the root that is at low pressure, the surface waviness can be increased to increase the contact pressure promoting glaze formation. The areas of the blade where the contact pressure is too high can be smoother to reduce the pressure back to the optimum range for the glazed layer to form. The exact role of the bond coat in the glazing process can also be evaluated by creating the appropriate surface topography without the bond coat present to determine if the bond coat itself contributes in the glazing process. The current literature detailed in Chapter 2 suggested*



*that the transformation of the DFL is more important, however this work has identified that the bond coat plays a role in the formation of the glazing and this role needs to be fully understood to optimise the coating.*

*The test rig can also be used to understand the re-lubrication effect and mechanism. Chapter 3 of this thesis showed that inconsistent relubrication layer thickness and interlayer detachment might be an issue, but it was difficult to draw conclusions from the analysis without being able to analyse the blade during service. Therefore, interrupted tests (similar to those in detailed in Chapter 5) can be carried out on the test rig with relubrication to see the effect that this has.*

*The ultrasound work in Chapter 6 showed a promising start but there is a large amount of work required to develop this method further. Firstly, speed of sound measurements in the bond coat and DFL need to be carried out in order to provide accurate values for the analysis. Post test measurements can be validated by cross-sections of samples to compare real and prediction thickness values, and to gain an estimation of speed of sound through a glazed layer. Since the work in this thesis showed that the fan blade rig is a nice balance between realistic conditions and ease of analysis/use of the rig, the ultrasound method should be incorporated into this test rig rather than relying on ball-on-flat tests. STAMINA, rather than the conventional pulsed method may also yield more accurate measurements of the coating, so efforts should be made to utilise this method. The environment chamber on the fan blade rig also allows temperature control to understand the effect of it on the thickness measurements, and calibration at different temperatures to be carried out. This would lead to ultrasound being used as an NDT to assess how much coating was left during inspections to save time and money re-lubricating or replacing the coating if it is still performing effectively.*

## References

- [1] Rolls-Royce plc, *The Jet Engine*. Rolls-Royce, 2005.
- [2] S. P. Zhu, P. Yue, Z. Y. Yu, and Q. Wang, "A combined high and low cycle fatigue model for life prediction of turbine blades," *Materials (Basel)*, vol. 10, no. 7, pp. 1–15, 2017.
- [3] S. a. Namjoshi and S. Mall, "Fretting behavior of Ti-6Al-4V under combined high cycle and low cycle fatigue loading," *Int. J. Fatigue*, vol. 23, pp. 455–461, 2001.
- [4] D. S. Wei, S. H. Yuan, and Y. R. Wang, "Failure analysis of dovetail assemblies under fretting load," *Eng. Fail. Anal.*, vol. 26, pp. 381–396, 2012.
- [5] M. Ciavarella and G. Macina, "New results for the fretting-induced stress concentration on Hertzian and flat rounded contacts," *Int. J. Mech. Sci.*, vol. 45, no. 3, pp. 449–467, 2003.
- [6] R. Rajendran, "Gas turbine coatings - An overview," *Eng. Fail. Anal.*, vol. 26, pp. 355–369, 2012.
- [7] S. Beale, "Precision engineering for future propulsion and power systems: a perspective from Rolls-Royce.," *Philos. Trans. R. Soc. A Math. Phys. Eng. Sci.*, vol. 370, no. 1973, pp. 4130–53, 2012.
- [8] A. M. Korsunsky, A. R. Torosyan, and K. Kim, "Development and characterization of low friction coatings for protection against fretting wear in aerospace components," *Thin Solid Films*, vol. 516, no. 16, pp. 5690–5699, 2008.
- [9] T. N. Rhys-Jones and T. N. Cunningham, "The influence of surface coatings on the fatigue behaviour of aero engine materials," *Surf. Coatings Technol.*, vol. 42, pp. 13–19, 1990.
- [10] Australian Transport Safety Bureau, "Examination of a Failed Fan Blade Rolls-Royce RB211 Trent 892 Turbofan Engine Boeing 777-300, A6-EMM," pp. 1–21, 2002.
- [11] S. Fouvry, C. Paulin, and S. Deyber, "Impact of contact size and complex gross-partial slip conditions on Ti-6Al-4V/Ti-6Al-4V fretting wear," *Tribol. Int.*, vol. 42, no. 3, pp. 461–474, 2009.
- [12] "Personal communication with Pattinson G." 2017.
- [13] B. Garrison, "High cycle fatigue (HCF) science and technology program 2002 annual report," *Report*, no. January 2002, 2000.
- [14] V. Fridrici, S. Fouvry, and P. Kapsa, "Fretting wear behavior of a Cu–Ni–In plasma coating," *Surf. Coat. Technol.*, vol. 163, pp. 429–434, 2003.
- [15] G. R. Y. N. Sabeya, J. Y. Paris, and J. Denape, "Fretting wear of a coated titanium alloy under free displacement," *Wear*, vol. 264, no. 3–4, pp. 166–176, 2008.
- [16] P. C. Patnaik, M. R. Pishva, J. E. Elder, W. Doswell, and R. Thamburaj, "Repair and life extension of titanium alloy fan blades in aircraft gas turbines," *Proc. ASME Turbo Expo*, vol. 5, no. ii, 1989.
- [17] W. T. Becker *et al.*, "ASM Handbook," *Fail. Anal. Prev.*, vol. 11, pp. 79–217, 2002.
- [18] J. Dobromirski, "Variables of Fretting Process: Are There 50 of Them? BT - Variables of Fretting Process: Are There 50 of Them?," 1992.
- [19] O. Vingsbo and S. Söderberg, "On fretting maps," *Wear*, vol. 126, no. 2, pp. 131–147, 1988.
- [20] S. Fouvry, P. Duó, and P. Perruchaut, "A quantitative approach of Ti-6Al-4V fretting damage: Friction, wear and crack nucleation," *Wear*, vol. 257, no. 9–10, pp. 916–929, 2004.
- [21] V. Fridrici, S. Fouvry, P. Kapsa, and P. Perruchaut, "Impact of contact size and geometry on the lifetime of a solid lubricant," *Wear*, vol. 255, no. 7–12, pp. 875–882, 2003.
- [22] P. Kapsa, "Tribocorrosion of Passive Metals and Coatings," S. M. Dieter Landolt, Ed.

- Woodhead Publishing, 2011, pp. 100–117.
- [23] G. X. Chen and Z. R. Zhou, “Study on transition between fretting and reciprocating sliding wear,” *Wear*, vol. 250–251, no. PART 1, pp. 665–672, 2001.
- [24] R. D. Mindlin, “No Title,” *Appl. Mech.*, no. 16, p. 269, 1949.
- [25] S.-H. Jeong, S.-J. Yong, and Y.-Z. Lee, “Friction and Wear Characteristics Due to Stick-Slip under Fretting Conditions,” *Tribol. Trans.*, vol. 50, no. 4, pp. 564–572, 2007.
- [26] a. L. Mohd Tobi, J. Ding, G. Bandak, S. B. Leen, and P. H. Shipway, “A study on the interaction between fretting wear and cyclic plasticity for Ti-6Al-4V,” *Wear*, vol. 267, no. 1–4, pp. 270–282, 2009.
- [27] C. H. Hager, J. H. Sanders, and S. Sharma, “Characterization of mixed and gross slip fretting wear regimes in Ti6Al4V interfaces at room temperature,” *Wear*, vol. 257, no. 1–2, pp. 167–180, 2004.
- [28] Z. R. Zhou and L. Vincent, “Mixed fretting regime,” *Wear*, vol. 181–183, no. PART 2, pp. 531–536, 1995.
- [29] S. Fouvry, P. Kapsa, and L. Vincent, “Analysis of sliding behaviour for fretting loadings: determination of transition criteria,” *Wear*, vol. 185, no. 1–2, pp. 35–46, 1995.
- [30] and G. H. M. Varenberg, I. Etsion\*, “Slip index: a new unified approach to fretting,” *Eur. Sci. Ed.*, vol. 17, pp. 35–37, 2014.
- [31] M. H. Zhu and Z. R. Zhou, “On the mechanisms of various fretting wear modes,” *Tribol. Int.*, vol. 44, no. 11, pp. 1378–1388, 2011.
- [32] C. H. Hager, J. H. Sanders, and S. Sharma, “Unlubricated gross slip fretting wear of metallic plasma-sprayed coatings for Ti6Al4V surfaces,” *Wear*, vol. 265, no. 3–4, pp. 439–451, 2008.
- [33] N. M. Everitt, J. Ding, G. Bandak, P. H. Shipway, S. B. Leen, and E. J. Williams, “Characterisation of fretting-induced wear debris for Ti-6Al-4 V,” *Wear*, vol. 267, no. 1–4, pp. 283–291, 2009.
- [34] S. A. NAMJOSHI, S. MALL, V. K. JAIN, and O. JIN, “Fretting fatigue crack initiation mechanism in Ti-6Al-4V,” *Fatigue & Fract. Eng. Mater. Struct.*, vol. 25, no. 10, pp. 955–964, 2002.
- [35] C. D. Lykins, S. Mall, and V. Jain, “Evaluation of parameters for predicting fretting fatigue crack initiation,” *Int. J. Fatigue*, vol. 22, no. 8, pp. 703–716, 2000.
- [36] C. Paulin, S. Fouvry, and S. Deyber, “Wear kinetics of Ti-6Al-4V under constant and variable fretting sliding conditions,” *Wear*, vol. 259, no. 1–6, pp. 292–299, 2005.
- [37] R. Cortez, S. Mall, and J. R. Calcaterra, “Investigation of variable amplitude loading on fretting fatigue behavior of Ti-6Al-4V,” *Int. J. Fatigue*, vol. 21, no. 7, pp. 709–717, 1999.
- [38] M. Ciavarella and G. Demelio, “A review of analytical aspects of fretting fatigue, with extension to damage parameters, and application to dovetail joints,” *Int. J. Solids Struct.*, vol. 38, no. 10–13, pp. 1791–1811, Mar. 2001.
- [39] R. Rajasekaran and D. Nowell, “Fretting fatigue in dovetail blade roots: Experiment and analysis,” *Tribol. Int.*, vol. 39, no. 10, pp. 1277–1285, 2006.
- [40] D. S. Wei, Y. R. Wang, and X. G. Yang, “Analysis of failure behaviors of dovetail assemblies due to high gradient stress under contact loading,” *Eng. Fail. Anal.*, vol. 18, no. 1, pp. 314–324, 2011.
- [41] A. Durelli, J. Dally, and W. Riley, “Stress and strength studies on turbine blade attachments,” *Proc. SESA*, no. 1, 1958.
- [42] V. Parks and R. Sanford, “Photoelastic and holographic analysis of a turbine-engine component,” *Exp. Mech.*, no. September, pp. 328–334, 1978.
- [43] G. B. Sinclair, N. G. Cormier, J. H. Griffin, and G. Meda, “Contact Stresses in Dovetail Attachments: Finite Element Modeling,” *J. Eng. Gas Turbines Power*, vol. 124, no. 1,

- p. 182, 2002.
- [44] L. Gallego, B. Fulleringer, S. Deyber, and D. Nélias, “Multiscale computation of fretting wear at the blade/disk interface,” *Tribol. Int.*, vol. 43, no. 4, pp. 708–718, 2010.
  - [45] D. Nowell, D. Dini, and D. a. Hills, “Recent developments in the understanding of fretting fatigue,” *Eng. Fract. Mech.*, vol. 73, no. 2, pp. 207–222, 2006.
  - [46] K. Anandavel and R. V. Prakash, “Effect of three-dimensional loading on macroscopic fretting aspects of an aero-engine bladedisc dovetail interface,” *Tribol. Int.*, vol. 44, no. 11, pp. 1544–1555, 2011.
  - [47] H. Murthy, G. Harish, and T. N. Farris, “Efficient Modeling of Fretting of Blade/Disk Contacts Including Load History Effects,” *J. Tribol.*, vol. 126, no. 1, p. 56, 2004.
  - [48] S. Marsh, “Preventing Fretting Fatigue in Blade Dovetail Roots by Modifying Geometry of Contact Surfaces,” *Power Transm. Eng.*, pp. 44–49, 2013.
  - [49] V. Sabelkin, S. A. Martinez, S. Mall, S. Sathish, and M. P. Blodgett, “Effects of shot-peening intensity on fretting fatigue crack-initiation behaviour of Ti-6Al-4V,” *Fatigue Fract. Eng. Mater. Struct.*, vol. 28, no. 3, pp. 321–332, 2005.
  - [50] A. King, A. Steuwer, C. Woodward, and P. J. Withers, “Effects of fatigue and fretting on residual stresses introduced by laser shock peening,” *Mater. Sci. Eng. A*, vol. 435–436, pp. 12–18, 2006.
  - [51] Y. Fu, J. Wei, and A. W. Batchelor, “Some considerations on the mitigation of fretting damage by the application of surface-modification technologies,” *J. Mater. Process. Technol.*, vol. 99, no. 1, pp. 231–245, 2000.
  - [52] Y. Qiu and B. J. Roynance, “The effect of lubricant additives on fretting wear,” in *Lubrication Engineering*, 1992, pp. 801–808.
  - [53] Y. Ye, J. Chen, and H. Zhou, “An investigation of friction and wear performances of bonded molybdenum disulfide solid film lubricants in fretting conditions,” *Wear*, vol. 266, no. 7–8, pp. 859–864, 2009.
  - [54] R. L. J. and R. C. (NASA) Bill, “Fretting in aircraft turbine engines,” 1974.
  - [55] T. Spalvins, “Lubrication with Sputtered MoS<sub>2</sub> Films: Principles, Operation, Limitations,” *NASA Tech. Memo. 105292*, 1991.
  - [56] P. Stoyanov, H. W. Strauss, and R. R. Chromik, “Scaling effects between micro- and macro-tribology for a Ti-MoS<sub>2</sub> coating,” *Wear*, vol. 274–275, pp. 149–161, 2012.
  - [57] A. Castellanos-Gomez, M. Poot, G. A. Steele, H. S. J. Van Der Zant, N. Agra?<sup>†</sup>, and G. Rubio-Bollinger, “Elastic properties of freely suspended MoS<sub>2</sub> nanosheets,” *Adv. Mater.*, vol. 24, no. 6, pp. 772–775, 2012.
  - [58] a. Savan, E. Pflüger, P. Voumard, a. Schröer, and M. Simmonds, “Modern solid lubrication: Recent developments and applications of MoS<sub>2</sub>,” *Lubr. Sci.*, vol. 12, no. 2, pp. 185–203, 2000.
  - [59] M. Dallavalle, N. Sändig, and F. Zerbetto, “Stability, dynamics, and lubrication of MoS<sub>2</sub> platelets and nanotubes,” *Langmuir*, vol. 28, no. 19, pp. 7393–400, 2012.
  - [60] T. Hu, Y. Zhang, and L. Hu, “Tribological investigation of MoS<sub>2</sub> coatings deposited on the laser textured surface,” *Wear*, vol. 278–279, pp. 77–82, 2012.
  - [61] V. Bellido-González *et al.*, “Tribological behaviour of high performance MoS<sub>2</sub> coatings produced by magnetron sputtering,” *Surf. Coatings Technol.*, vol. 97, no. 1–3, pp. 687–693, 1997.
  - [62] W. O. Winer, “Molybdenum disulfide as a lubricant: A review of the fundamental knowledge,” *Wear*, vol. 10, no. 6, pp. 422–452, 1967.
  - [63] X. Li, Y. Gao, J. Xing, Y. Wang, and L. Fang, “Wear reduction mechanism of graphite and MoS<sub>2</sub> in epoxy composites,” *Wear*, vol. 257, no. 3–4, pp. 279–283, 2004.
  - [64] R. L. Fusaro, “Lubrication and Failure Mechanisms of Molybdenum Disulphide Films - Effect of Substrate Roughness,” no. December, 1978.

- [65] R. L. Fusaro, "Lubrication and Failure Mechanisms of Molybdenum Disulphide Films - Effect of Atmosphere," no. December, 1978.
- [66] K. J. Wahl, M. Belin, and I. L. Singer, "A triboscopic investigation of the wear and friction of MoS<sub>2</sub> in a reciprocating sliding contact," *Wear*, vol. 214, no. 2, pp. 212–220, 1998.
- [67] J. Xu, M. H. Zhu, Z. R. Zhou, P. Kapsa, and L. Vincent, "An investigation on fretting wear life of bonded MoS<sub>2</sub> solid lubricant coatings in complex conditions," *Wear*, vol. 255, no. 1–6, pp. 253–258, 2003.
- [68] J. Xu, Z. R. Zhou, C. H. Zhang, M. H. Zhu, and J. B. Luo, "An investigation of fretting wear behaviors of bonded solid lubricant coatings," *J. Mater. Process. Technol.*, vol. 182, no. 1–3, pp. 146–151, 2007.
- [69] K. Kim and A. M. Korsunsky, "Fretting damage of Ni-MoS<sub>2</sub> coatings: Friction coefficient and accumulated dissipated energy evolutions," *Proc. Inst. Mech. Eng. Part J J. Eng. Tribol.*, vol. 224, no. 11, pp. 1173–1180, 2010.
- [70] K. Kim and A. M. Korsunsky, "Effects of imposed displacement and initial coating thickness on fretting behaviour of a thermally sprayed coating," *Wear*, vol. 271, no. 7–8, pp. 1080–1085, 2011.
- [71] O. Jin and S. Mall, "Effects of independent pad displacement on fretting fatigue behavior of Ti-6Al-4V," *Wear*, vol. 253, no. 5–6, pp. 585–596, 2002.
- [72] S. A. Namjoshi, S. Mall, V. K. Jain, and O. Jin, "Fretting fatigue crack initiation mechanism in Ti-6Al-4V," *Fatigue Fract. Eng. Mater. Struct.*, vol. 25, no. 10, pp. 955–964, 2002.
- [73] M. R. Vazirisereshk, A. Martini, D. A. Strubbe, and M. Z. Baykara, "Solid lubrication with MoS<sub>2</sub>: A review," *Lubricants*, vol. 7, no. 7, 2019.
- [74] D. J. Stokes, *Principles and Practice of Variable Pressure Environmental Scanning Electron Microscopy (VP-ESEM)*. Chichester, UK: John Wiley & Sons, Ltd.
- [75] Y. Wang, F. Xie, S. Ma, and L. Dong, "Review of surface profile measurement techniques based on optical interferometry," *Optics and Lasers in Engineering*, vol. 93. Elsevier Ltd, pp. 164–170, 01-Jun-2017.
- [76] D. Shindo and T. Oikawa, "Energy dispersive X-ray spectroscopy," *Japanese J. Tribol.*, vol. 51, no. 1, pp. 33–38, 2006.
- [77] K. Barman, K. T. Voisey, P. H. Shipway, and G. Pattinson, "Fretting wear behaviour of MoS<sub>2</sub> dry film lubricant," pp. 2–7.
- [78] A. R. Lansdown, "Molybdenum Disulphide Lubrication," 1974.
- [79] F. H. Stott, "The role of oxidation in the wear of alloys," *Tribol. Int.*, vol. 31, no. 1–3, pp. 61–71, 1998.
- [80] G. Tronci and S. M. B. Marshall, "Frictional Behaviour of Coated Self-locking Aerospace Fasteners," no. January, 2017.
- [81] I. L. Singer, R. N. Bolster, J. Wegand, S. Fayeulle, and B. C. Stupp, "Hertzian stress contribution to low friction behavior of thin MoS<sub>2</sub> coatings," *Appl. Phys. Lett.*, vol. 57, no. 10, pp. 995–997, 1990.
- [82] F. Abbasi, G. H. Majzoobi, and M. M. Barjesteh, "Developing a new experimental set up to study fretting fatigue behavior under cyclic contact loading," *Proc. Inst. Mech. Eng. Part J J. Eng. Tribol.*, vol. 232, no. 7, pp. 837–850, 2018.
- [83] K. Barman, P. H. Shipway, K. T. Voisey, and G. Pattinson, "Evolution of damage in MoS<sub>2</sub>-based dry film lubricants (DFLs) in fretting wear—The effect of DFL thickness and contact geometry," *Prog. Org. Coatings*, vol. 105, pp. 67–80, 2017.
- [84] K. L. Johnson, K. Kendall, and A. D. Roberts, "Surface Energy and the Contact of Elastic Solids," *Proc. R. Soc. A Math. Phys. Eng. Sci.*, vol. 324, no. 1558, pp. 301–313, 1971.

- [85] A. R. Warmuth, W. Sun, and P. H. Shipway, “The roles of contact conformity , temperature and displacement amplitude on the lubricated fretting wear of a steel-on-steel contact Subject Category : Subject Areas :,” 2016.
- [86] H. R. Hertz, “Über die Berührung fester elastischer Körper (on the contact of elastic solids),” *J. für die reine und Angew. Math.*, vol. 92, pp. 156–171, 1882.
- [87] H. Hertz, ““Über die Berührung fester elastischer Körper,”” *J. für die Reine und Angew. Math.*, vol. 92, pp. 156–171, 1882.
- [88] D. Bowden, F. P. & Tabor, *The Friction And Lubrication Of Solids*. Oxford, 1986.
- [89] J. Archard, “Elastic Deformation and the Laws of Friction,” in *Royal Society of London. Series A, Mathematical and Physical Sciences.*, 1957, vol. 243, no. 1233.
- [90] A. W. B. R.D.Gibson, “The elastic contact of a rough surface,” *Wear*, vol. 35, no. 1, pp. 87–111, 1975.
- [91] J. A. Greenwood and J. B. P. Williamson, “Contact of Nominally Flat Surfaces,” *Proc. R. Soc. A Math. Phys. Eng. Sci.*, vol. 295, no. 1442, pp. 300–319, 1966.
- [92] J. a. Greenwood and J. H. Tripp, “The Elastic Contact of Rough Spheres,” *J. Appl. Mech.*, vol. 34, no. 1, p. 153, 1967.
- [93] D. Maugis, “On the Contact and Adhesion of Rough Surfaces,” *J. Adhes. Sci. Technol.*, vol. 10, pp. 161–175, 1996.
- [94] and T. Fuller, K. N. G., “The Effect of Surface Roughness on the Adhesion of Elastic Solids,” in *Proc. R. Soc.*, 1975, pp. 327– 342.
- [95] Y. P. Derjaguin, BV and Muller, VM and Toporov, “Effect of contact deformations on the adhesion of particles,” *J. Colloid Interface Sci.*, vol. 53, no. 2, pp. 314–326, 1975.
- [96] Abbott, E. J., and Firestone, F. A., “Specifying Surface Quality-A Method Based on Accurate Measurement and Comparison,” *Mech. Eng.*, vol. 55, pp. 569–572, 1933.
- [97] B. Bhushan, “Contact mechanics of rough surfaces in tribology: multiple asperity contact,” *Tribol. Lett.*, vol. 4, no. 1, pp. 1–35, 1998.
- [98] M. Ramesh *et al.*, “Micro and macro contact mechanics for interacting asperities,” *Tribol. Int.*, vol. 31, no. 1, pp. 47–58, 2006.
- [99] S. J. Cole and R. S. Sayles, “A numerical model for the contact of layered elastic bodies with real rough surfaces,” vol. 108, no. July 1986, 2009.
- [100] R. L. Jackson, “A Finite Element Study of Elasto-Plastic Hemispherical,” vol. 127, no. April, pp. 343–354, 2005.
- [101] L. Kogut and I. Etsion, “Elastic-Plastic Contact Analysis of a Sphere and a Rigid Flat,” *J. Appl. Mech.*, vol. 69, no. 5, p. 657, 2002.
- [102] T. Street, “Spherical indentation of elastic-plastic solids,” no. October 1998, pp. 2707–2728, 1999.
- [103] R. L. Jackson and I. Green, “A statistical model of elasto-plastic asperity contact between rough surfaces,” *Tribol. Int.*, vol. 39, no. 9, pp. 906–914, Sep. 2006.
- [104] R. L. Jackson and I. Green, “A finite element study of elasto-plastic hemispherical contact against a rigid flat,” *J. Tribol.*, vol. 127, no. 2, pp. 343–354, Apr. 2005.
- [105] R. I. Amaro, R. C. Martins, J. O. Seabra, N. M. Renevier, and D. G. Teer, “Molybdenum disulphide/titanium low friction coating for gears application,” *Tribol. Int.*, vol. 38, no. 4, pp. 423–434, 2005.
- [106] V. Fridrici, S. Fouvry, and P. H. Kapsa, “Fretting wear behavior of a Cu-Ni-In plasma coating,” *Surf. Coatings Technol.*, vol. 163–164, pp. 429–434, 2003.
- [107] A. M. Abodena, “An Investigation into the Effect of Coolants ’ Composition , Concentration and Cutting Conditions on the Coefficient of Friction and Ultrasonic Reflection Coefficient during Turning of Aluminium 6082-T6,” no. June, 2015.
- [108] “Commercial Test Rig,” *Internal Source*. [Online]. Available: <http://scitekconsultants.co.uk/about/>. [Accessed: 20-Feb-2020].

- [109] H. Sidhom, F. Ghanem, T. Amadou, G. Gonzalez, and C. Braham, “Effect of electro discharge machining (EDM) on the AISI316L SS white layer microstructure and corrosion resistance,” *Int. J. Adv. Manuf. Technol.*, vol. 65, no. 1–4, pp. 141–153, 2013.
- [110] T. Sovány, K. Nikowitz, G. Regdon, P. Kása, and K. Pintye-Hódi, “Raman spectroscopic investigation of film thickness,” *Polym. Test.*, vol. 28, no. 7, pp. 770–772, 2009.
- [111] M. B. Mills, R., Dwyer-Joyce, R.S., Marshall, “Continuous Wave Ultrasound for Analysis of a Surface,” 1522677.2, 2015.
- [112] W. Zhang, Z. Huang, and W. Zhang, “Two dimensional semiconductors with possible high room temperature mobility,” 2014.
- [113] T. Kim, D. Ding, J.-H. Yim, Y.-D. Jho, and A. J. Minnich, “Elastic and thermal properties of free-standing molybdenum disulfide membranes measured using ultrafast transient grating spectroscopy,” *Cit. APL Mater.*, vol. 5, p. 86105, 2017.
- [114] G. Zhu *et al.*, “Tuning thermal conductivity in molybdenum disulfide by electrochemical intercalation,” *Nat. Commun.*, vol. 7, Oct. 2016.
- [115] T. D. O. Vale *et al.*, “Methodology for Structural Integrity Analysis of Gas Turbine Blades.”
- [116] A. A. Akay, D. Çöker, A. Kayran, and E. Gürses, “Experimental study and finite element analysis of dovetail attachments,” *ASME Int. Mech. Eng. Congr. Expo. Proc.*, vol. 1, no. November, 2017.
- [117] B. Yang, “Blade containment evaluation of civil aircraft engines,” *Chinese J. Aeronaut.*, vol. 26, no. 1, pp. 9–16, 2013.

## A. Appendix- Tables from Marcello's draft

This Appendix includes tables that Marcello included in his draft.

### A.1. Literature Review

#### A.1.1. Section 2.2.3 Fretting in dovetail joints

Stress and strength studies on turbine blade attachment [41]  1958	Studied stress with experimentally (photoelasticity) Experimental work – this is more focused to understanding stress field more than fretting behaviour – does not seem to be worth citing in thesis
Photoelastic and Holographic analysis of a turbine-engine component [42] 1978	<ul style="list-style-type: none"> <li>• Studied stress with photoelasticity</li> </ul>
Contact Stresses in Dovetail Attachments: FEM [43] 2006	<ul style="list-style-type: none"> <li>• Fine mesh to estimate stresses more accurately than previous work</li> <li>• Pressure profile across blade</li> </ul>
A review of analytical aspects of fretting fatigue, with extensions to damage parameters, and application to dovetail joints  2000 – Could not manage to import this into Mendeley – see copy in folder	Quite technical – analytical studies of fretting fatigue
Recent developments in understanding fretting fatigue [45] 2006	Consider, for example, the flat and rounded contact depicted in Fig. 11a, which gives a similar contact pressure to that in the dovetail (Fig. 3).
Fretting fatigue in dovetail blade roots: Experiment and analysis [39]	Good for contact stress distribution
Analysis of failure behaviour of dovetail assemblies due to high gradient stress under contact loading [40] 2010	
Effect of three-dimensional loading on macroscopic fretting aspects of an aero-engine blade/disc interface [46] 2011	
Methodology for Structural Integrity Analysis of Gas Turbine Blades [115] 2011	
Failure analysis of dovetail assembly under fretting loads [4] 2012	



Experimental study and FEA of dovetail attachments [116]	Particularly critical is the high stress gradient occurring near the edge of the contact
Experimental work – instrumented Inconel 2D replica of fan blade (straing gauges and DIC)	
2017	

Table 13- From section 2.2.3

Given the complexity of the dovetail geometry, most of the studies have been carried out on a simplified 2D geometry of the joint. An interesting test setup is the 2D biaxial test rig A biaxial test rig applies loads to two opposing blade specimens representing the centrifugal forces in an engine. The opposing blade specimens are mounted onto a central disk specimen which is also subjected to load which simulates the disk expansion. HCF loads are also applied via mechanical shaker units which represent blade vibration [45].

- A 2D biaxial test rig developed in Oxford represents
- This is still used and a samples tested with it

Experimental works and FEM simulations have been mostly conducted on a 2D simplify geometry

- Prediction of life methods with results
- Advanced 3D methods (e.g. Anandavel) – mention to RR models
- 3D studies with results

#### A.1.2. Section 2.3.5- Alternatives

Ti–MoS2 coatings [56]	
Blade containment evaluation of civil aircraft engines [117]	Cite the importance of blade containment.
Precision engineering for future propulsion and power systems: a perspective for Rolls-Royce [7]	Biaxial test rig – test condition and results
Failure analysis of dovetail assemblies under fretting load [4]	There are two keys to evaluating the fretting fatigue life of dovetail assemblies: one is determining the high stress gradients at the edge of the contact zone under complex loading by means of numerical methods, especially the finite element method (FEM); the other is finding suitable

	parameters to correlate with fretting fatigue life to improve predictive accuracy. In fact, fretting fatigue has been one of the cost sources relating to HCF [ref].
<a href="https://www.slideshare.net/egajunior/trent-1000-presentation">https://www.slideshare.net/egajunior/trent-1000-presentation</a>	Presentation with Trent 1000 overview – contains engine specs and different facts.
Fretting behaviour of [3]ti64 under combined HCF and LCF	Therefore, a complex interaction between high- cycle and low-cycle fatigue leads to fretting-fatigue induced failure in turbine disks.
Unlubricated gross slip fretting wear of metallic plasma-sprayed coatings for Ti64 surfaces [32]	Therefore, the development of new coatings, coating processes, and lubricants that are able to reduce fretting damage and withstand the hostile engine environment will provide significant reductions in maintenance costs. In
[66]	The friction stability has been attributed to replenishment of the contact by transfer of worn MoS <sub>2</sub> [3, 4, 9] from lubricant reservoirs [6,10] and to the need for only a few layers of MoS <sub>z</sub> to sustain low $\mu$ [11].
	There may be as many as 50 factors [ref] that can affect the fretting behavior of materials, in which contact pressure, coefficient of friction, slip amplitude, and cyclic axial stress are relatively important.

Table 14- From Section 2.3.5

Repair and life extension [16]	The latter (CuNiIn) is a soft coating designed to inhibit fretting of the Ti-6Al-4V substrate by reducing the shear loads transmitted to the surface of the substrate due to the fretting action. The															
Fretting wear of a coated titanium alloy under free displacement [15]	CuNiIn coating topped with a polymer bonded solid lubricant MoS <sub>2</sub> [14,15]. This latter solution gives a dual advantage: firstly, the CuNiIn coating has a great capacity of accommodation by plastic deformation which limits nucleation and the propagation of cracks [16–18]; secondly, the polymer bonded lubricant molybdenum disulphide MoS <sub>2</sub> favours sliding and decreases the coefficient of friction [19,20].															
[32]	Al-Bronze are also used as fretting protection															
[11]	<p>Table 1 Mechanical properties of Ti-6Al-4V and Cu-Ni-In</p> <table border="1"> <thead> <tr> <th>Material</th> <th>Ti-6Al-4V</th> <th>Cu-Ni-In</th> </tr> </thead> <tbody> <tr> <td>Elastic modulus (GPa)</td> <td>119</td> <td>60</td> </tr> <tr> <td>Poisson ratio</td> <td>0.29</td> <td>0.15</td> </tr> <tr> <td>Yield stress (MPa)</td> <td>970</td> <td></td> </tr> <tr> <td>Vickers hardness</td> <td>360 HV<sub>0.3</sub></td> <td>170 HV<sub>0.3</sub></td> </tr> </tbody> </table>	Material	Ti-6Al-4V	Cu-Ni-In	Elastic modulus (GPa)	119	60	Poisson ratio	0.29	0.15	Yield stress (MPa)	970		Vickers hardness	360 HV <sub>0.3</sub>	170 HV <sub>0.3</sub>
Material	Ti-6Al-4V	Cu-Ni-In														
Elastic modulus (GPa)	119	60														
Poisson ratio	0.29	0.15														
Yield stress (MPa)	970															
Vickers hardness	360 HV <sub>0.3</sub>	170 HV <sub>0.3</sub>														

Table 15- CuNiIn table in Section 2.3.5

## A.2. Section 5.4 Discussion

The results are summarised below

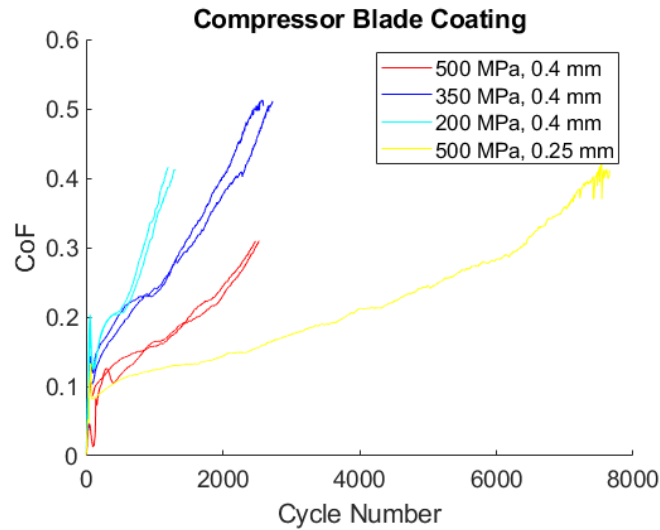
Table 16: Summary of the test results from Figure 5-8.

Pressure (MPa)	Displacement (mm)	Number of Repeats	Failure Rate
500	0.200	2	100%
500	0.125	3	33%
500	0.050	2	0%
350	0.200	3	100%
350	0.125	3	33%
350	0.050	2	0%
200	0.200	2	50%

- Discuss that roughness is not likely to be an issue

- Discuss that the rig is also not likely

Whilst certain combination of load and displacement showed a repeatable CoF evolution, some others were identified as critical in such regards.



### A.3. Section 5.3 Results

#### 300 MPa tests

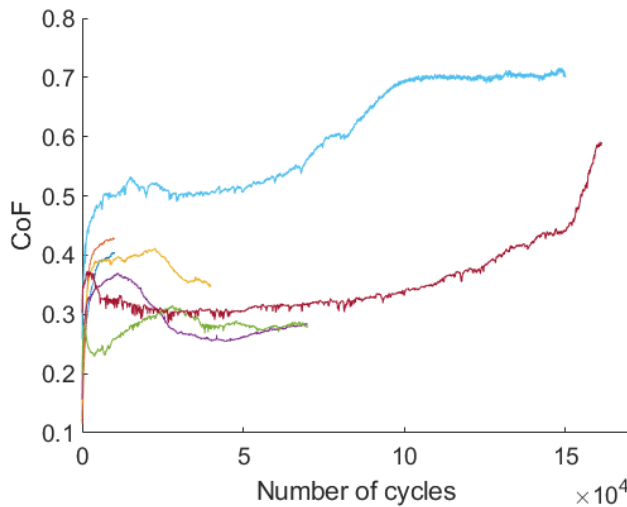


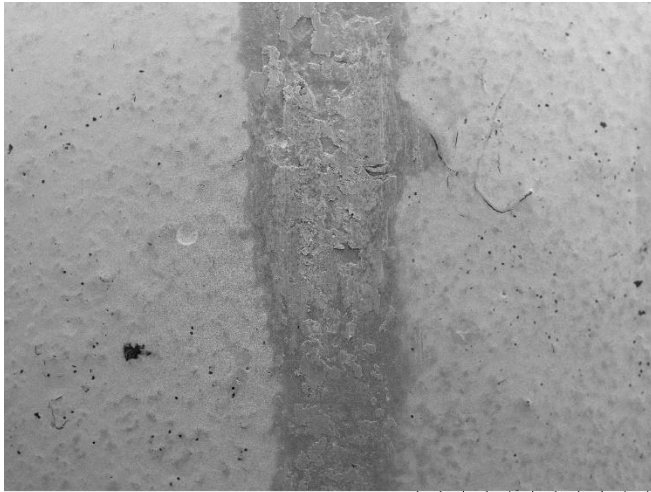
Figure 0-1: CoF evolution on test Rig: nominal contact pressure 300MPa, displacement amplitude 0.15mm.

Wear scar profile available in rig folder

#### Wear progression

10kcycles

The top-view of the



VU0088

HMMD11.9 x30 2 mm

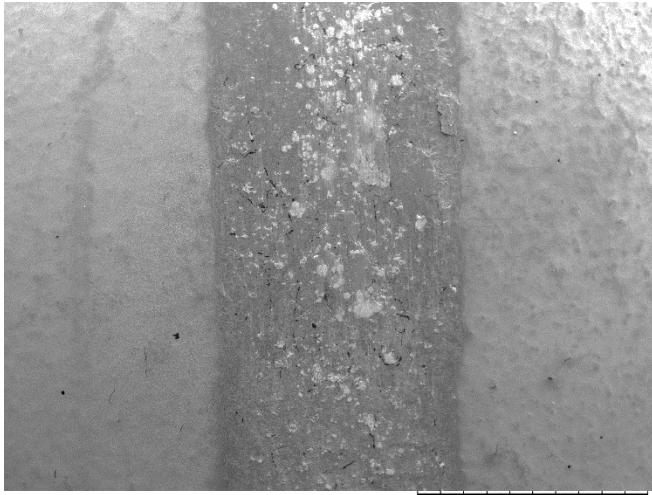


VU0089

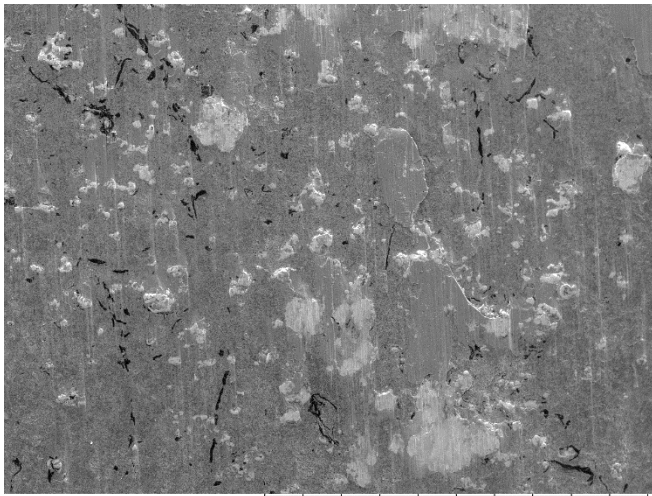
HMMD11.9 x80 1 mm

Figure 0-2: Blade surface: 300MPa, 150µm, 10 kcycles.

40 kcycles



HMMD12.0 x30 2 mm



HMMD12.0 x100 1 mm

Figure 0-3: Blade surface: 300MPa, 150 $\mu$ m, 40 kcycles.

70 kcycles



HMMD12.0 x100 1 mm



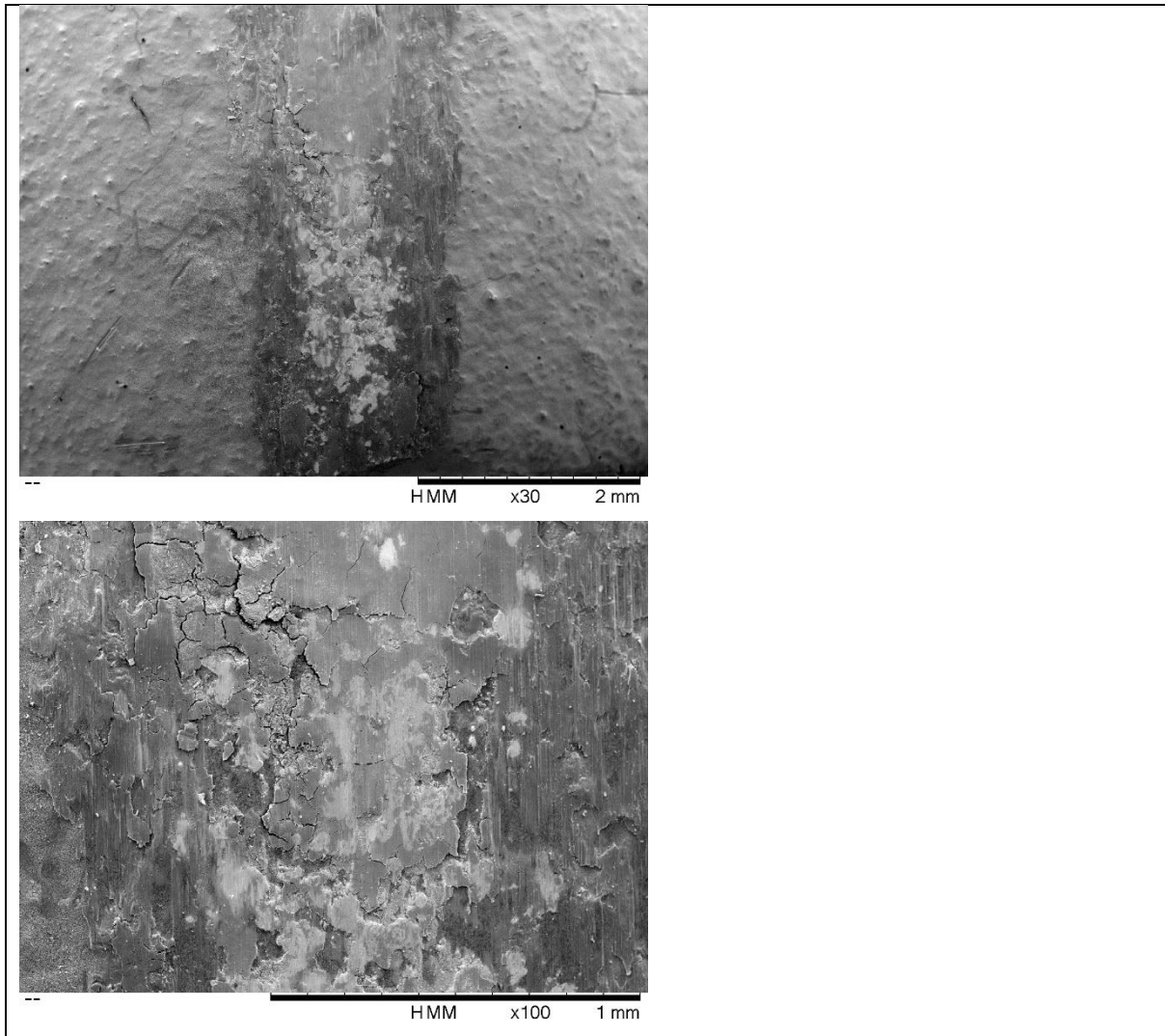
HMMD11.9 x30 2 mm

160k



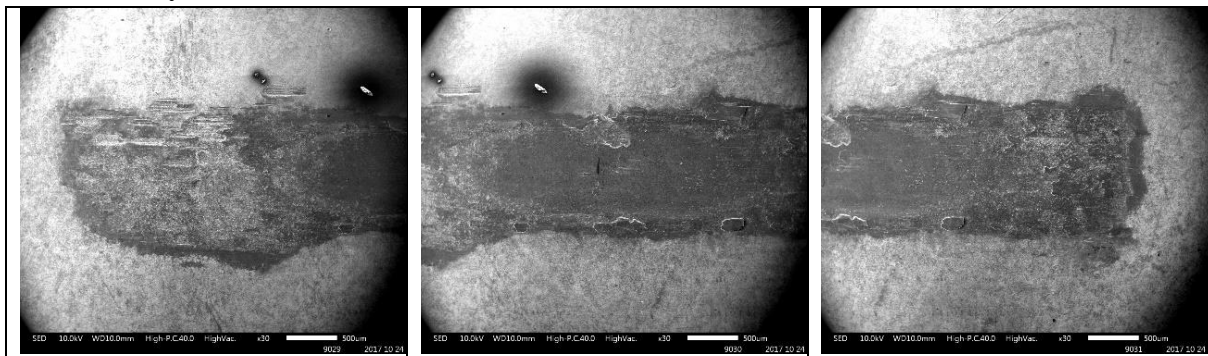
HMMD12.0 x100 1 mm

Failure

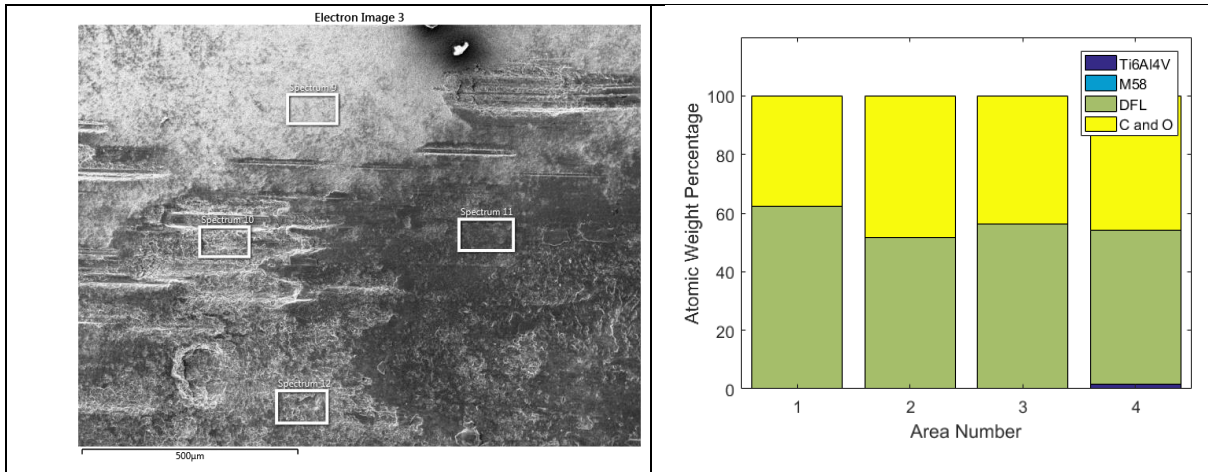


## Discs EDX

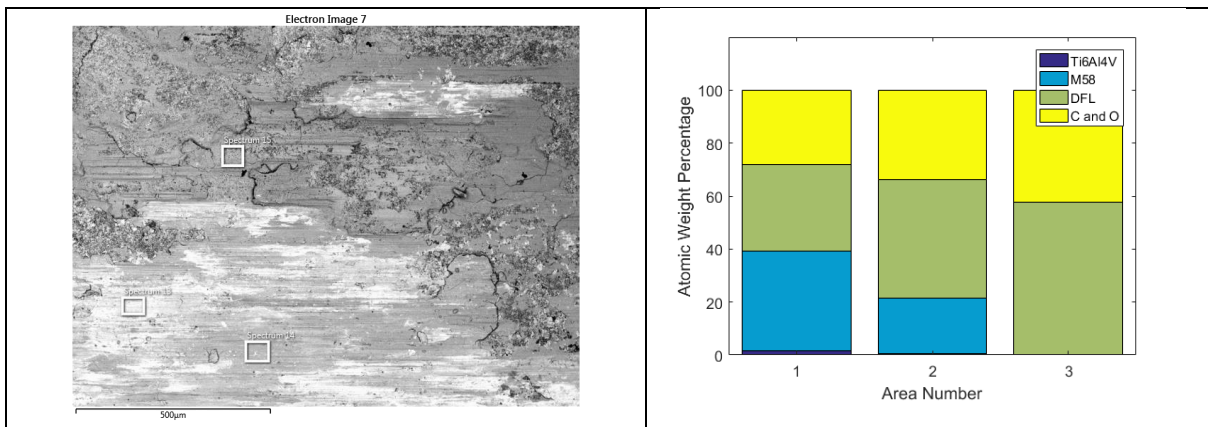
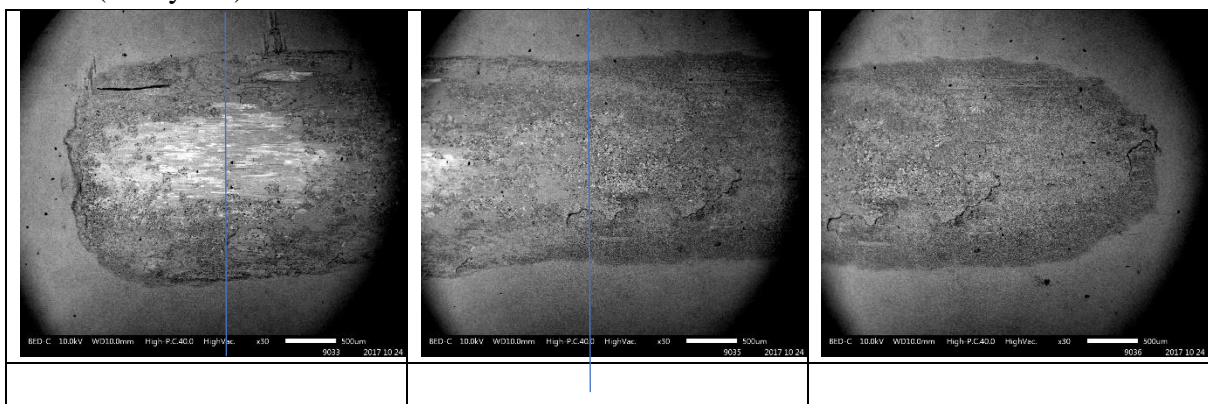
Disc 2 (10kcycles)



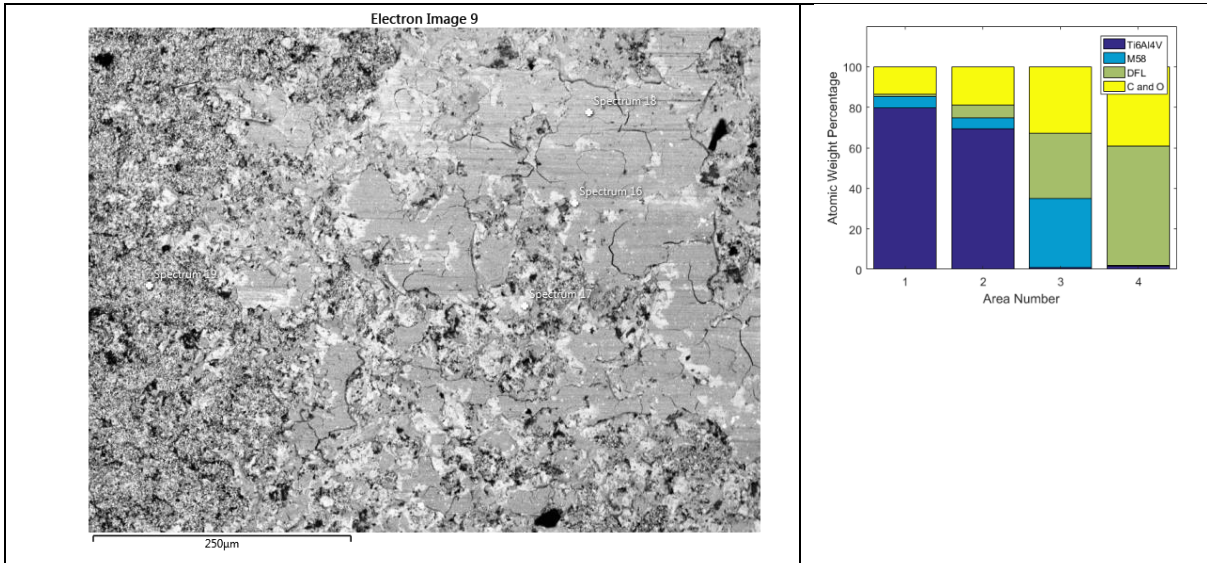
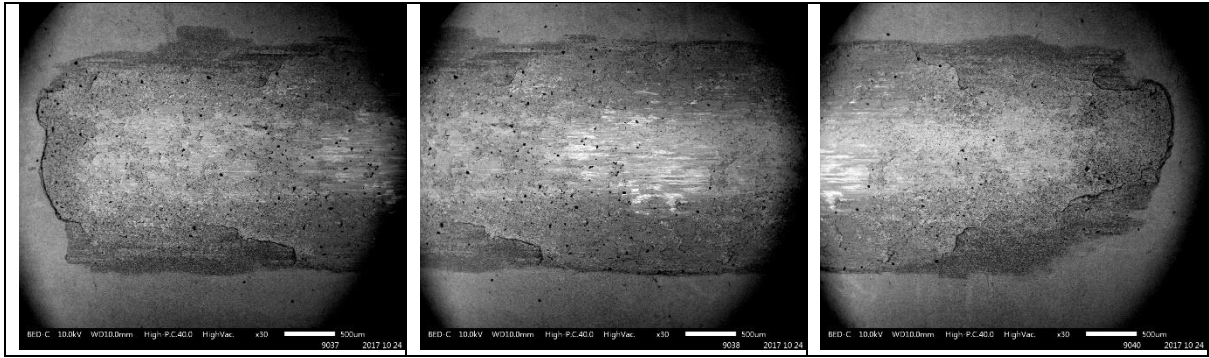




Disc 3 (40kcycles)

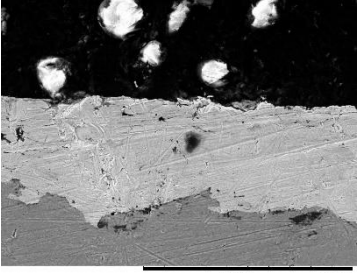
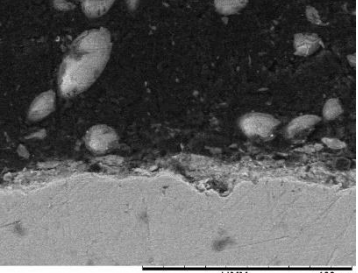
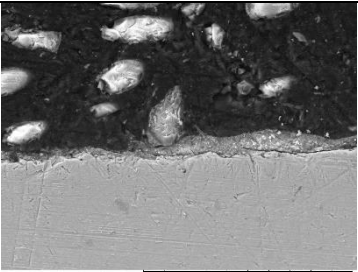
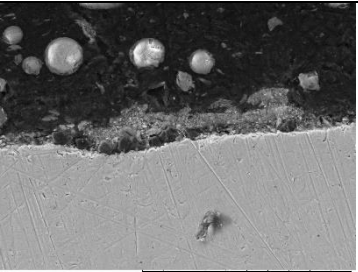


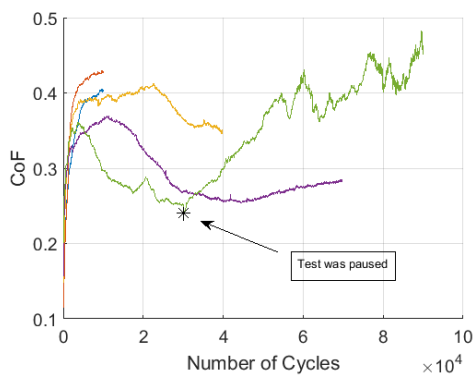
Disc4 (70k)



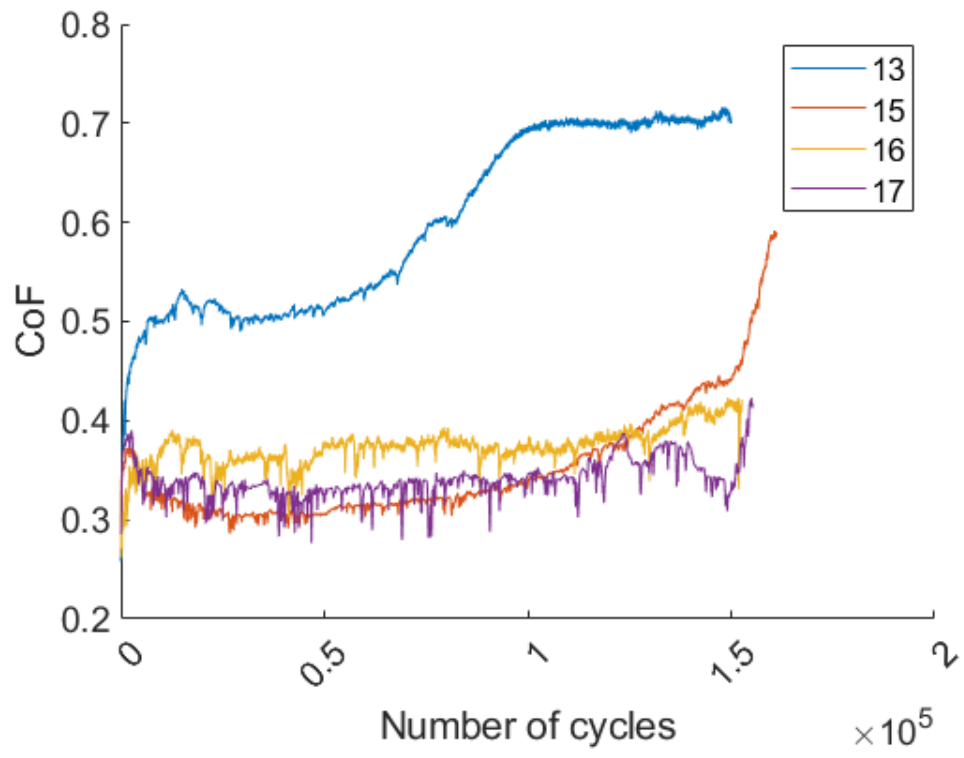
### Cross-section imaging

	Blade	Disc	
10 kcycles			<ul style="list-style-type: none"> <li>• Blade coating system looks nearly intact</li> <li>• Removal of MoS2 from disc</li> </ul>
40 kcycles			<ul style="list-style-type: none"> <li>• M58 Asperities exposed on Blade</li> <li>• Very limited amount of MoS2 on disc</li> </ul>

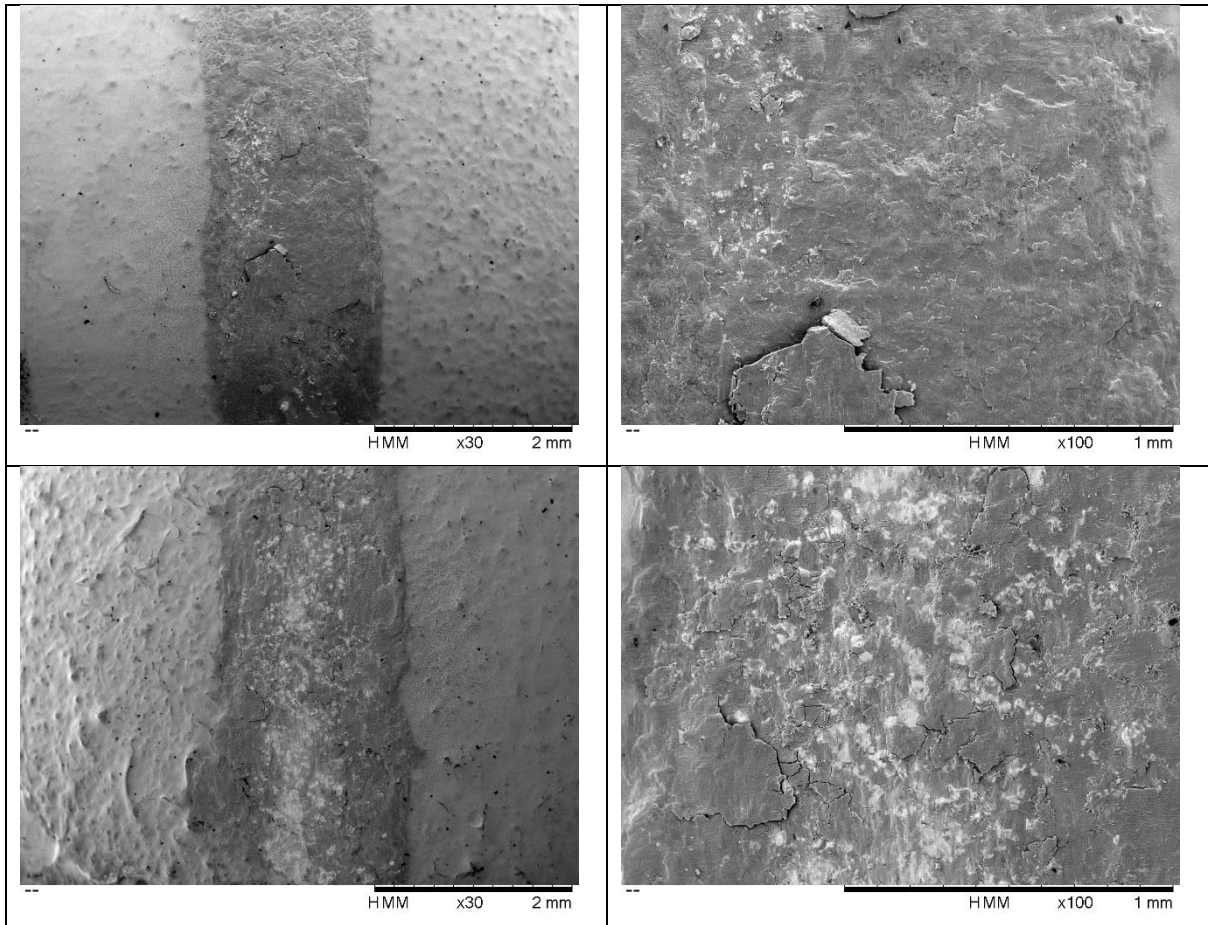
70 kcycles			<ul style="list-style-type: none"> <li>• Mostly M58 left on blade, with very limited amount of DFL on valleys</li> <li>• Disc showed mixture of areas like this (layer?) and areas as 40k</li> </ul>
90 kcycles			<ul style="list-style-type: none"> <li>• M58 almost completely removed with dull layer on surface (to be EDX'd)</li> <li>• Disc – some part completely starved and some other present same layer found in blade</li> </ul>



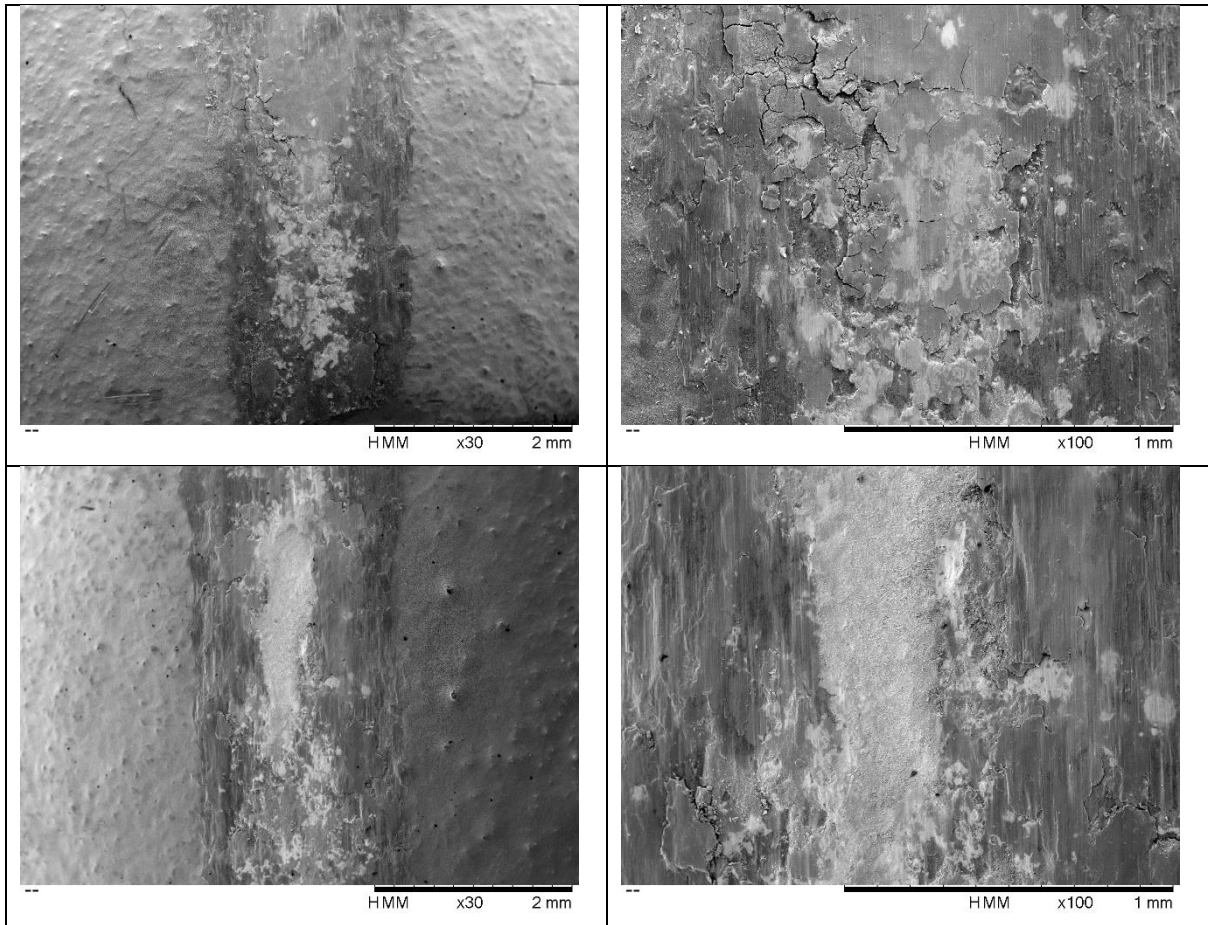
### 300 MPa vs 200MPa



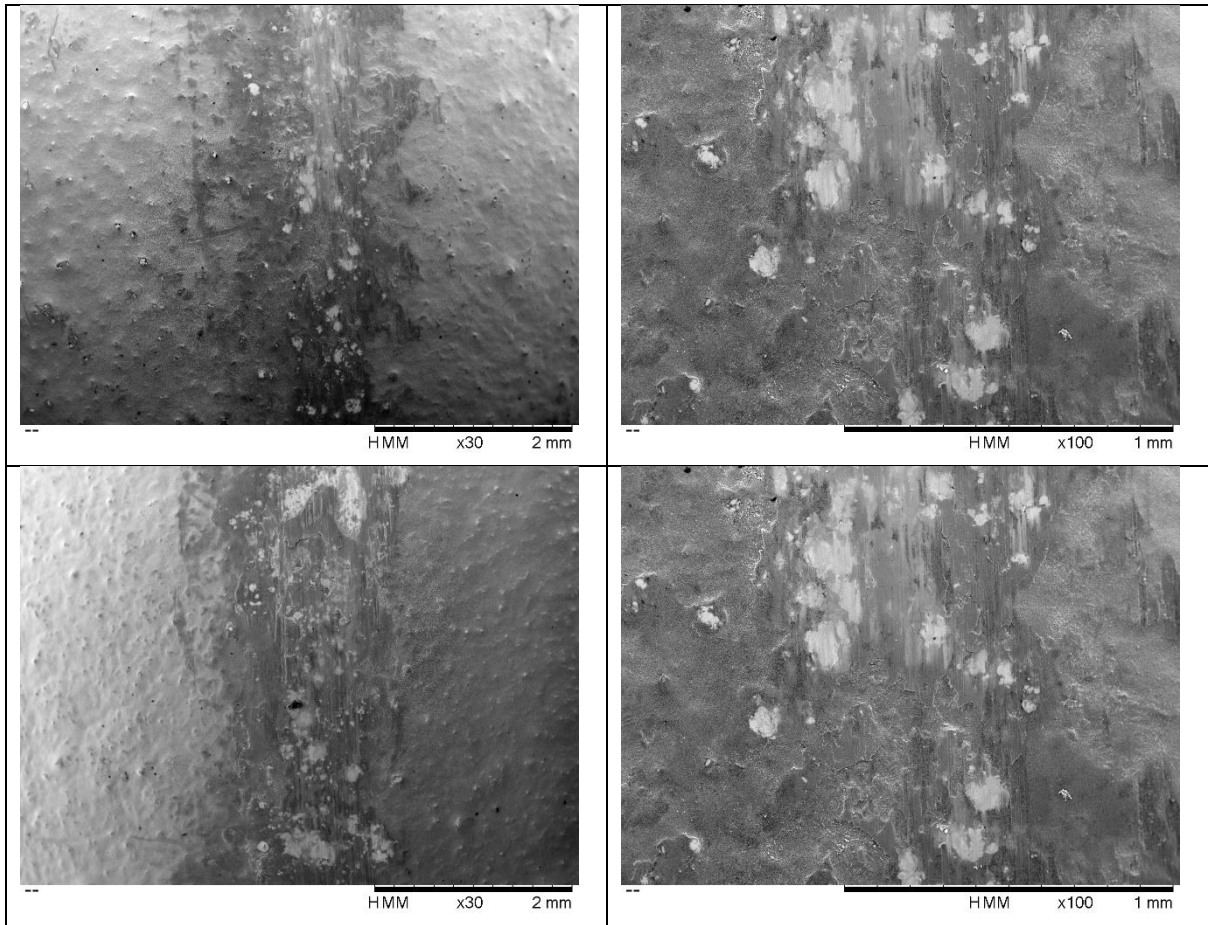
Test 13



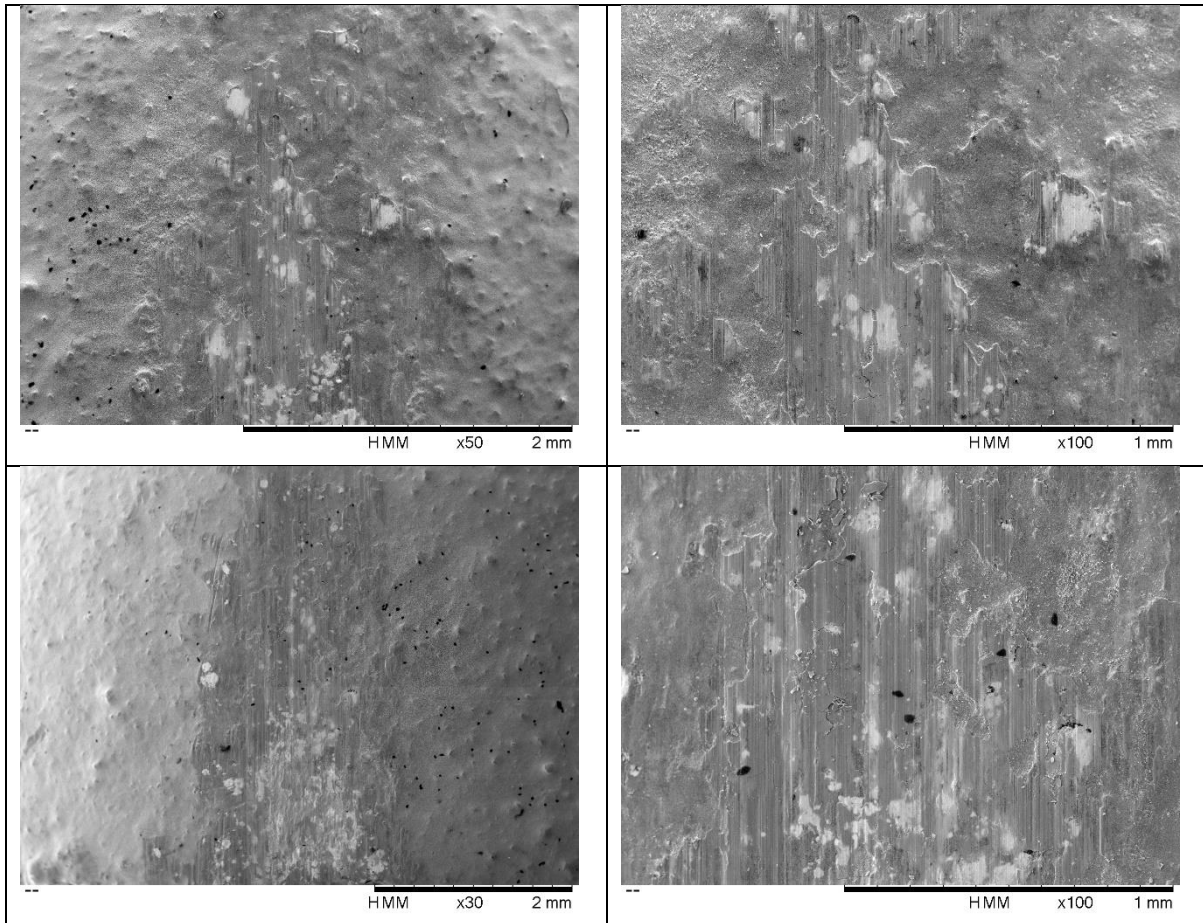
Test 15



Test 16



## Test 17



### A.4. Section 5.4 Discussion

Secondly, the amount of substrate exposure is also increased at higher contact pressure, and many researchers have suggested that MoS<sub>2</sub> lubricates better when is intermixed with metal.

#### Effect of the bond coat

The effect of the surface topography provides high contact pressure locally – these high-pressure spots serve two purposes: they increase the wear rate and thus the debris availability, and they promote the layer formation.

It needs to be able to glaze before the wear is too secure and the contact locks up.

## B. Appendix- Modelling Theory

### B.1. Hertz Theory

Assumptions:

- The surfaces are continuous, non-conforming and the effect of the roughness is negligible



- The stress is within the materials elastic limit and the material are homogenous
- The contact area is significantly smaller than the characteristic dimension of the bodies
- The contact is frictionless and no tangential force acts on the surfaces

Hertz derived the equations to obtain the dimension of the contact area of two bodies being pressed against each other, under a given normal load. In the case of the contact between a sphere and an elastic half-space, the radius of the contact area,  $a$ , is given by the following equation:

$$a = \sqrt[3]{\frac{3PR}{4E^*}} \quad (0.1)$$

where  $P$  is the normal load applied (N),  $R$  is the radius of the sphere (m), and  $E^*$  is the reduced modulus (Pa) that is defined by the relationship below:

$$\frac{1}{E^*} = \frac{1 - \nu_1^2}{E_1} + \frac{1 - \nu_2^2}{E_2} \quad (0.2)$$

with  $E_1$  and  $E_2$  being the Young's modulus of the sphere and the half-space and  $\nu_1$  and  $\nu_2$  indicating the Poisson's ratio.